Second Harmonic Generation
at Liquid/Liquid Interfaces

THÈSE

présentée à la Faculté des sciences de l'Université de Genève
pour obtenir le grade de Docteure ès sciences, mention interdisciplinaire

par

Jihad SISSAOUI

de

Beni Mellal (Maroc)

"God made the bulk; surfaces were invented by the devil."

Wolfgang Pauli

Abstract

Second harmonic generation at liquid/liquid interfaces

Liquid interfaces, which are boundaries between two isotropic media, hold pivotal importance across various scientific disciplines. Despite their significance, studying these interfaces presents a notable challenge due to their 'buried' nature. This thesis primarily focuses on enhancing our understanding of liquid/liquid interfaces, benefiting from the unique capabilities of Surface Second Harmonic Generation (SSHG). Owing to the cancellation of the SHG process in centrosymmetric media like bulk liquids, the signal originates only from the interface region where the symmetry is broken, making SSHG a robust tool for investigating surface properties and dynamics on an ultrafast timescale.

This work has two main objectives: firstly, we use molecular probes to elucidate various interfacial properties such as charge, friction, and aggregation. Secondly, we strive to understand how these interfacial properties impact chemical reactivity.

Key studies within this work include investigating the effects of room-temperature ionic liquids on the adsorption of a cationic probe at the dodecane/water interface, examining the impact of confinement on the isomerization dynamics of an azobenzene dye, namely methyl orange, and exploring the excited-state properties of a porphyrin–fullerene dyad and its porphyrin analogue at the dodecane/water interface.

The findings from these investigations enhance our growing understanding of liquid interfaces, offering valuable insights.

Résumé

Génération de seconde harmonique aux interfaces liquide/liquide.

Les interfaces liquides, qui sont des frontières entre deux milieux isotropes, ont une importance cruciale dans diverses disciplines scientifiques. Malgré leur importance, l'étude de ces interfaces présente un défi notable en raison de leur nature 'enfouie'. Cette thèse se concentre principalement sur l'amélioration de notre compréhension des interfaces liquide/liquide, en bénéficiant des capacités uniques de la Génération de Second Harmonique de Surface (SSHG). En raison de l'annulation du processus SHG dans des milieux centrosymétriques comme les liquides, le signal provient uniquement de la région de l'interface où la symétrie est rompue, ce qui fait de la SSHG un outil robuste pour étudier les propriétés de surface et les dynamiques à une échelle de temps ultra-rapide.

Ce travail a deux objectifs principaux : premièrement, nous utilisons des sondes moléculaires pour élucider diverses propriétés interfaciales telles que la charge, la friction et l'agrégation. Deuxièmement, nous nous efforçons de comprendre comment ces propriétés interfaciales influencent la réactivité chimique.

Les études clés de ce travail incluent l'investigation des effets des liquides ioniques à température ambiante sur l'adsorption d'une molécule qui fait office de sonde cationique à l'interface eau/dodécane, l'examen de l'impact du confinement sur la dynamique d'isomérisation d'un colorant azobenzène et l'exploration des propriétés à l'état excité d'un dyade porphyrine-fullerène et de son analogue qui consiste en une porphyrine à l'interface eau/dodécane.

Les résultats de ces investigations améliorent notre compréhension des interfaces liquides, offrant des perspectives précieuses.

Remerciements

Je tiens à exprimer ma profonde gratitude envers mon directeur de thèse, Prof. Éric Vauthey. Sa patience et ses conseils ont été essentiels à chaque étape de ce travail. Plus que tout, je suis profondément reconnaissante pour l'opportunité qu'il m'a accordée et pour sa capacité à instiller confiance et assurance quand j'en avais le plus besoin.

Je tiens également à remercier les membres du jury, Prof. Pierre-François Brevet et Prof. Gaelle Martin-Gassin, pour avoir accepté de s'engager comme experts lors de la soutenance de cette thèse.

Mes remerciements vont à Sophie Jacquemet, toujours souriante et d'une aide inestimable dans les démarches administratives.

Un grand merci à Didier Frauchiger pour ses compétences techniques impressionnantes qui bénéficient à l'ensemble du groupe. Sa disponibilité et son aide ont été précieuses.

À chaque membre du groupe, des visages du passé à ceux d'aujourd'hui, je tiens à exprimer ma gratitude. Vous m'avez non seulement soutenue, mais aussi transmis de précieuses connaissances. Nos moments partagés restent gravés en moi. Chacun d'entre vous a laissé une trace dans le récit de ma vie.

Je tiens à remercier chaque personne avec qui j'ai partagé un éclat de rire, une discussion sincère ou un simple moment de complicité. Nos pauses déjeuner, où les sujets les plus légers côtoyaient parfois l'absurde, et ces instants volés autour d'un café ou d'un thé, ont été les petites étincelles qui ont illuminé mes journées. Ces moments, bien que fugaces, ont tissé des liens forts et m'ont offert un répit face à l'intensité du quotidien. À vous qui lisez ceci et reconnaissez nos moments partagés, sachez combien vous avez compté pour moi. Ces instants ont été précieux pour mon cœur. Ils sont les pages marquées d'un livre souvent complexe, témoignant de la beauté et de la chaleur de notre camaraderie.

À celui dont les souvenirs et les leçons demeurent vivants en moi, et dont la voix, résonnante encore à mes oreilles, guide chacun de mes pas : telle une étoile lointaine qui, malgré l'obscurité enveloppante de la nuit, persiste à briller. Ces échos évoquent simultanément la chaleur d'un souvenir cher et la douleur d'une absence amère.

Enfin, à ma petite famille, le pilier silencieux de cette aventure, chaque page de cette thèse porte l'empreinte de votre soutien, de vos sacrifices et de votre foi inébranlable en moi. Vous êtes le doux refrain qui berce ma vie, le rappel constant que, face à chaque défi, une tribu fidèle est toujours là, veillant sur moi jour et nuit, avec un amour qui jamais ne faiblit.

Contents

To my dear family . . .

Chapter 1

Introduction and Thesis Aim

1.1 Historical Overview

The field of surface nonlinear optics has its roots in the broader discipline of nonlinear optics, which emerged alongside the invention of the laser. Within this field, surface nonlinear optics represents a specialized branch that has garnered significant attention and research interest. It offered an intriguing combination of exploring fundamental physics and providing practical applications in the vast domain of surface science and technology.

The development of nonlinear optics happened concurrently with the creation of the ruby laser. Franken and his colleagues first documented the observation of the optical second-harmonic generation (SHG) phenomenon in quartz crystals [1]. This initial discovery stimulated an influx of research in SHG, leading to the development of theoretical models to better understand its underlying physics. The concept of wave mixing in nonlinear media was established by Armstrong et al. [2]. Bloembergen and Pershan further contributed to the field by including necessary boundary conditions in the theory, which enabled a more accurate depiction of how nonlinear waves transmit and reflect at interfaces [3].

The high sensitivity of the SHG process was first identified by Brown and Matsuoka in 1969. Their research showed a strong SHG signal from an Ag film deposited under vacuum [4]. A similar observation was later made by Chen and his team when they studied Na deposition on clean Ge surfaces [5]. Despite these initial findings, which clearly suggested the considerable potential of SHG in surface studies, this area was not extensively explored until the 1980s. While the remarkable surface sensitivity of SHG was recognized, there might have been reservations about its applicability, and the incomplete understanding of surface nonlinearity may have hindered further advancements during that period.

Interest in second-order nonlinear effects at surfaces was sparked by the study of surface enhancement effects, particularly surface-enhanced Raman scattering. It was demonstrated that the Raman output from molecular adsorbates on a roughened silver surface could be significantly stronger than that from a smooth surface [6]. This discovery attracted substantial interest from chemists and physicists in the late 1970s, as they anticipated enormous potential applications of the effect. Similar

1

to Raman, it was discovered that the surface SHG process could also be increased by several orders of magnitude [7]. It was subsequently realized that SHG could be used as a probe for observing surface reactions, including the adsorption and desorption processes of molecules on a roughened metal surface, with a sensitivity extending to a fractional monolayer [8]. The development of SHG and second-order nonlinear optics as probes of surfaces and interfaces has been rapidly advancing ever since.

The work of Chen et al. and Heinz et al. demonstrated the potential for surface-specific spectroscopy through the resonant SHG process [9]. SHG could be used to get spectral and orientational information about a monolayer of organic molecules adsorbed on a substrate through the determination of independent elements of surface nonlinear susceptibility [10]. Analyzing the experimental results allowed for the refinement of SHG theory and helped establish SHG as a surface probe [11], making the potential of surface SHG apparent. As an optical technique, it was used to probe liquid/air interfaces [12] [13] and any interface accessible by light, including buried interfaces such as solid/liquid interfaces or liquid/liquid interfaces [14][15] [16]. This latter interfaces are the main focus of this thesis.

1.2 Investigating Liquid Interfaces: From Fundamental Properties to Chemical Reactivity

Liquid interfaces, such as air/liquid, solid/liquid, and liquid/liquid, are ubiquitous and crucial in numerous scientific areas and technological applications [17]. They play key roles in a variety of processes, ranging from biological phenomena [18] to chemical extractions [19, 20]. For instance, in molecular biology, water interfaces are vital to processes like protein adsorption [21, 22]. Similarly, in industrial chemistry, interfaces influence the formation and stability of emulsions [23] and the rate of specific chemical reactions can drastically increase in emulsions or on water interfaces [24, 25]. These interfaces also have significant implications for future renewable energy systems, such as electrochemical energy conversion and storage [26].

The characteristics of liquid interfaces fundamentally differ from those of the bulk liquid phase. While molecules in the bulk liquid phase are randomly oriented, with their behavior being defined by properties like viscosity and polarity, the asymmetry of forces at liquid interfaces results in anisotropy in molecular orientation, leading to distinct properties. This unique anisotropy indicates that photochemistry at interfaces could significantly deviate from that in bulk phases, highlighting the necessity for a comprehensive understanding of interfaces.

Despite their importance, studying liquid interfaces presents significant challenges due to their 'buried' nature within condensed media, making it difficult to access these boundary regions without disrupting the surrounding environment. Furthermore, the experimental signal from the interface can be orders of magnitude

smaller than the spectroscopic signal from the bulk phase due to the higher number of molecules, complicating the extraction of precise information about the interface.

To circumvent these challenges, techniques like Second Harmonic Generation (SHG) have been developed. SHG is particularly potent in the field of surface nonlinear optics due to its inherent sensitivity to surface properties and its unique ability to generate a signal exclusively from the interface. This allows selective probing of these interfaces, overcoming the aforementioned challenges.

Most studies use SSHG to investigate the orientation of molecules and adsorbates at the surface or interface. By studying the polarization dependence of the SHG signal, one can infer the orientation of molecules at the interface. Additionally, Time Resolved SSHG (TR-SSHG) can measure the dynamics of processes occurring at interfaces on an ultrafast timescale.

In our group, over the years, we have developed a setup that allows for polarization-resolved SSHG, TR-SSHG, and interfacial spectrum measurement using a tunable probe. Initial investigations focused on learning more about interfacial properties using appropriate molecular probes. For example, triphenylmethane dyes, like malachite green, have been used as friction probes, as their S_1 excited state decays non-radiatively through the torsional motion of the phenyl rings, which strongly depends on the viscosity [27, 28]. Other properties such as hydrogen bonding of interfacial water and ion adsorption at water interfaces were also investigated [29–31]. Mechanosensitive probes were also used to investigate lateral pressure and order at dodecane/phospholipids/water interfaces [32].

The aim of this thesis can be broadly defined by the goal of investigating the properties of liquid/liquid interfaces. This work continues in the same direction as my predecessors' in the pursuit of a more comprehensive understanding of interfacial properties and their effects on chemical reactivity. Primarily, two approaches are employed. The first approach involves using a molecular probe to report on various interfacial properties such as interfacial charge, friction, and aggregation. In the second approach, we are interested in understanding how these interfacial properties influence chemical reactivity. In both cases, to make reliable interpretations - especially of TR-SSHG measurements - the first step typically involves gaining a thorough understanding of the excited state dynamics of the system in solution. Therefore, SSHG measurements and various bulk measurements go often hand in hand.

1.3 Thesis Roadmap

This thesis journey is initiated with Chapter 2, where we lay the necessary theoretical foundations and outline the experimental methodology, providing a solid groundwork for our investigations.

Chapter 3 focuses on how room-temperature ionic liquids (ILs) affect the adsorption of malachite green (MG) at the dodecane/water interface. It reveals that the interface's concentration and overall charge depend on the ionic constituents. In Chapter 4, we investigate another triphenylmethane dye, crystal violet (CV), as an alternative probe for malachite green at liquid/liquid interfaces. Chapter 5 further explores its photophysics, with a specific focus on the electronic absorption band of crystal violet (CV). We uncover the role of torsional disorder in broadening its absorption band and study the behavior of symmetric and symmetry-broken molecules in different environments through experiments and computations.

Chapter 6 delves into the influence of confinement on the isomerization dynamics and yields of an azobenzene dye, methyl orange. Three systems—CTAC, DPPC, and CB[7]—are used to understand how confinement impacts the photophysics of the dye in both liquid/liquid interfaces and the bulk.

Chapter 7 continues the investigation, focusing on the excited-state properties of a porphyrin–fullerene dyad and its porphyrin analogue at the dodecane/water interface. We observe the interaction of these molecules at the interface and detect hints of intermolecular electron transfer processes in their dynamics and spectra.

In the appendices, you'll find some additional experimental results related to amphiphilic dyes at the dodecane/phospholipid interface (Appendix A) as well as detailed experimental procedures (Appendix B). A comprehensive list of the symbols and abbreviations used throughout the thesis is provided at the end of this manuscript.

Bibliography

(1)   Franken, P. A.; Hill, A. E.; Peters, C. W.; Weinreich, G. *Phys. Rev. Lett.* **1961**, *7*, 118–119.

(2)   Armstrong, J. A.; Bloembergen, N.; Ducuing, J.; Pershan, P. S. *Phys. Rev.* **1962**, *127*, 1918–1939.

(3)   Bloembergen, N.; Pershan, P. S. *Phys. Rev.* **1962**, *128*, 606–622.

(4)   Brown, F.; Matsuoka, M. *Phys. Rev.* **1969**, *185*, 985–987.

(5)   Chen, J. M.; Bower, J. R.; Wang, C. S.; Lee, C. H. *Opt. Commun.* **1973**, *9*, 132–134.

(6)   Fleischmann, M.; Hendra, P. J.; McQuillan, A. J. *Chem. Phys. Lett.* **1974**, *26*, 163–166.

(7)   Chen, C. K.; de Castro, A. R. B.; Shen, Y. R. *Phys. Rev. Lett.* **1981**, *46*, 145–148.

(8)   Chen, C. K.; Heinz, T. F.; Ricard, D.; Shen, Y. R. *Phys. Rev. Lett.* **1981**, *46*, 1010–1012.

(9)   Heinz, T. F.; Chen, C. K.; Ricard, D.; Shen, Y. R. *Phys. Rev. Lett.* **1982**, *48*, 478–481.

(10)   Heinz, T. F.; Tom, H. W. K.; Shen, Y. R. *Phys. Rev. A* **1983**, *28*, 1883–1885.

(11)   Guyot-Sionnest, P.; Chen, W.; Shen, Y. R. *Phys. Rev. B* **1986**, *33*, 8254–8263.

(12)   Goh, M. C.; Hicks, J. M.; Kemnitz, K.; Pinto, G. R.; Heinz, T. F.; Eisenthal, K. B.; Bhattacharyya, K. *J. Phys. Chem.* **1988**, *92*, 5074–5075.

(13)   Rao, Y.; Comstock, M.; Eisenthal, K. B. *J. Phys. Chem. B* **2006**, *110*, 1727–1732.

(14)   Uchida, T.; Yamaguchi, A.; Ina, T.; Teramae, N. *J. Phys. Chem. B* **2000**, *104*, 12091–12094.

(15)   Tamburello-Luca, A. A.; Hébert, P.; Brevet, P. F.; Girault, H. H. *J. Chem. Soc., Faraday Trans.* **1996**, *92*, 3079–3085.

(16)   Brevet, P. F.; Girault, H. H. In *Amphiphiles at Interfaces*, ed. by Texter, J., Steinkopff: Darmstadt, 1997, pp 1–9.

(17)   Volkov, A. G., *Liquid Interfaces In Chemical, Biological And Pharmaceutical Applications*; CRC Press: 2001; 878 pp.

(18)   Tamerler, C. *JOM* **2015**, *67*, 2480–2482.

(19)   Watarai, H. *Trends Anal. Chem.* **1993**, *12*, 313–318.

(20)   Scoppola, E.; Watkins, E. B.; Campbell, R. A.; Konovalov, O.; Girard, L.; Dufrêche, J.-F.; Ferru, G.; Fragneto, G.; Diat, O. *Angew. Chem. Int. Ed.* **2016**, *55*, 9326–9330.

(21)   Pinholt, C.; Hartvig, R. A.; Medlicott, N. J.; Jorgensen, L. *Expert Opin Drug Deliv* **2011**, *8*, 949–964.

(22)   Mitropoulos, V.; Mütze, A.; Fischer, P. *Adv. Colloid Interface Sci.* **2014**, *206*, 195–206.

(23)   Wilde, P. J. *Curr. Opin. Colloid Interface Sci* **2000**, *5*, 176–181.

(24)   Klijn, J. E.; Engberts, J. B. F. N. *Nature* **2005**, *435*, 746–747.

(25)   Kusaka, R.; Nihonyanagi, S.; Tahara, T. *Nat. Chem.* **2021**, *13*, 306–311.

(26)   Shin, H.; Yoo, J. M.; Sung, Y.-E.; Chung, D. Y. *JACS Au* **2022**, *2*, 2222–2234.

(27)   Fita, P.; Punzi, A.; Vauthey, E. *J. Phys. Chem. C* **2009**, *113*, 20705–20712.

(28)   Fedoseeva, M.; Richert, S.; Vauthey, E. *Langmuir* **2012**, *28*, 11291–11301.

(29)   Fita, P.; Fedoseeva, M.; Vauthey, E. *Langmuir* **2011**, *27*, 4645–4652.

(30)   Fita, P.; Fedoseeva, M.; Vauthey, E. *J. Phys. Chem. A* **2011**, *115*, 2465–2470.

(31)   Richert, S.; Mosquera Vazquez, S.; Grzybowski, M.; Gryko, D. T.; Kyrychenko, A.; Vauthey, E. *J. Phys. Chem. B* **2014**, *118*, 9952–9963.

(32)   Licari, G.; Beckwith, J. S.; Soleimanpour, S.; Matile, S.; Vauthey, E. *Phys. Chem. Chem. Phys.* **2018**, *20*, 9328–9336.

Chapter 2

Theoretical Framework and Experimental Methodology

2.1 General Photophysics and Photochemistry

2.1.1 Light Propagation in Vacuum

Light is an electromagnetic wave consisting of an electric field $\mathbf{E}$ and a magnetic field $\mathbf{B}$, which oscillate in time and space, and are perpendicular to each other [1]. In the classical description, the properties of such a wave are described by Maxwell's equations (Equation 2.1). In the case of propagation in a vacuum, they are written as:

$$\nabla \cdot \mathbf{E} = 0 \tag{2.1a}$$

$$\nabla \cdot \mathbf{B} = 0 \tag{2.1b}$$

$$\nabla \times \mathbf{E} = -\frac{\partial \mathbf{B}}{\partial t} \tag{2.1c}$$

$$\nabla \times \mathbf{B} = \mu_0 \varepsilon_0 \frac{\partial \mathbf{E}}{\partial t} \tag{2.1d}$$

Here, $\mathbf{E}$ and $\mathbf{B}$ are the electric and magnetic field vectors, respectively, while μ_0 and ε_0 are the permeability and permittivity of the vacuum, respectively. $\nabla\cdot$ denotes the divergence operator and $\nabla\times$ represents the curl operator. The last two equations, $\nabla \times \mathbf{E} = -\frac{\partial \mathbf{B}}{\partial t}$ and $\nabla \times \mathbf{B} = \mu_0 \varepsilon_0 \frac{\partial \mathbf{E}}{\partial t}$, describe how changing electric and magnetic fields induce each other. These relationships underlie the wave nature of light, enabling its propagation through space as a self-sustaining electromagnetic wave.

The wave equation for the electric field $\mathbf{E}$ in a vacuum can be derived from the curl of Faraday's law in Maxwell's equations:

$$\nabla \times (\nabla \times \mathbf{E}) = -\mu_0 \varepsilon_0 \frac{\partial^2 \mathbf{E}}{\partial t^2} \tag{2.2}$$

By using vector calculus identities ($\nabla \times (\nabla \times \mathbf{V}) = \nabla(\nabla \cdot \mathbf{V}) - \nabla^2 \mathbf{V}$ and the fact that $\nabla \cdot \mathbf{E} = 0$ in a vacuum, we can simplify this to the wave equation:

$$\nabla^2 \mathbf{E} - \mu_0 \varepsilon_0 \frac{\partial^2 \mathbf{E}}{\partial t^2} = \nabla^2 \mathbf{E} - \frac{1}{v_\phi^2} \frac{\partial^2 \mathbf{E}}{\partial t^2} = 0 \tag{2.3}$$

Equation 2.3 shows that electromagnetic waves propagate as transverse waves with a phase velocity v_ϕ. In a vacuum, $v_\phi = c = \frac{1}{\sqrt{\mu_0 \varepsilon_0}}$, where c is the speed of light in a vacuum.

One evident solution for Equation 2.3 is the harmonic wave, expressed as:

$$\mathbf{E}(\mathbf{r}, t) = \mathbf{E}_0 \cos(\mathbf{k} \cdot \mathbf{r} - \omega t + \phi) \tag{2.4}$$

Here, $\mathbf{E}_0$ is the electric field vector representing the amplitude and phase information of the wave; $\mathbf{k}$ is the wave vector, indicating the direction and magnitude of wave propagation; $\mathbf{r}$ is the position vector in three-dimensional space; ω is the angular velocity of the wave; t represents time, and ϕ is the phase angle, which represents the initial phase of the wave at $t = 0$.

In vacuum, the magnitude of the wave vector $\mathbf{k}$ is related to the wavelength λ of the wave and the angular frequency ω by $k = \frac{2\pi}{\lambda}$, and the wave propagates at the speed of light $c = \frac{1}{\sqrt{\mu_0 \varepsilon_0}}$. A representation of transverse EM Wave traveling in the direction of the x-axis, having Electric field E and magnetic field B is pictured in Figure 2.1
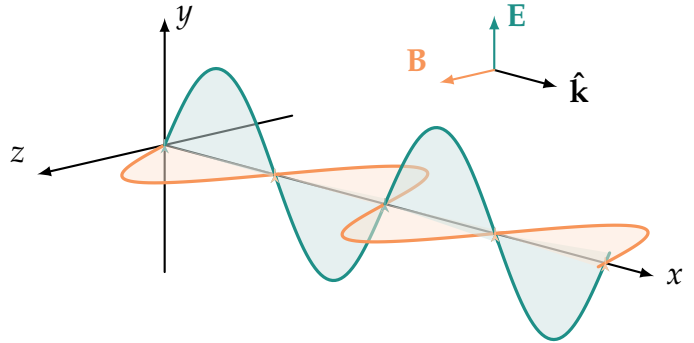

Figure 2.1: Electric and magnetic fields of an electromagnetic wave

2.1.2 Propagation of Electromagnetic Waves in Dielectric Media

When an electromagnetic wave interacts with a dielectric material, the electric field of the wave distorts the electron clouds of the molecules within the material. This distortion often results in a displacement of the electrons relative to the positively charged nuclei, creating a dipole moment, referred to as an *induced dipole*.

The dipole moment p can be mathematically linked to the electric field $\mathbf{E}$ by:

$$p = \alpha \mathbf{E} \tag{2.5}$$

where α denotes the molecular polarizability. It should be noted that polarizability is a tensor quantity and represents its ability to respond to an external electric field by developing an induced electric dipole moment.

The induced dipole moments of all the molecules are combined to create the *macroscopic polarization* **P** of the material, which signifies the dipole moment per unit volume:

$$\mathbf{P} = \epsilon_0 \tilde{\chi} \cdot \mathbf{E} \tag{2.6}$$

Here, **E** represents the electric field, and $\tilde{\chi}$ denotes the electric susceptibility tensor. The electric susceptibility tensor, as a second-rank tensor, describes the material's linear response to an external electric field. In the case of anisotropic materials, the electric susceptibility tensor can be formulated as:

$$\tilde{\chi} = \begin{bmatrix} \chi_{xx} & \chi_{xy} & \chi_{xz} \\ \chi_{yx} & \chi_{yy} & \chi_{yz} \\ \chi_{zx} & \chi_{zy} & \chi_{zz} \end{bmatrix} \tag{2.7}$$

Each component χ_{ij} represents the response of the material to an electric field along the i-th direction when an electric field is applied in the j-th direction. Notably, the electric susceptibility tensor can be complex, with both real and imaginary components playing significant roles. The complex nature of the tensor becomes especially relevant when considering the optical properties and responses of the material.

The oscillating charges in the material also generate electromagnetic radiation, which can in turn affect the incident radiation. This interaction is described by Maxwell's equations for a dielectric medium. In a source-free region (i.e., no free charges or currents), these equations can be written as:

$$\nabla \times \mathbf{E} = -\frac{\partial \mathbf{B}}{\partial t} \tag{2.8}$$

$$\nabla \times \mathbf{H} = \frac{\partial \mathbf{D}}{\partial t} \tag{2.9}$$

where **E** is the electric field, **B** is the magnetic field, **H** is the auxiliary magnetic field, and **D** is the electric displacement field.

The electric field **E** is related to the electric displacement field **D** through the relation:

$$\mathbf{D} = \epsilon_0 \mathbf{E} + \mathbf{P} = \epsilon_0 (1 + \tilde{\chi}) \cdot \mathbf{E} \tag{2.10}$$

where ϵ_0 is the permittivity of free space, **P** is the polarization, and $\tilde{\chi}$ is the electric susceptibility tensor.

Incorporating these relations, we can derive the wave equation for the electric field in a dielectric medium in the same way as for Equation 2.3:

$$\nabla^2 \mathbf{E} - \mu_0 \epsilon_0 (1 + \tilde{\chi}) \frac{\partial^2 \mathbf{E}}{\partial t^2} = 0 \tag{2.11}$$

By analogy with Equation 2.3, one can deduce the phase velocity in the medium: $\tilde{v}_\phi = [\mu_0 \varepsilon_0 (1 + \tilde{\chi})]^{-1/2}$.

The optical susceptibility is usually expressed in terms of the complex refractive index $\tilde{n}$ as follow:

$$\tilde{n} = \frac{v_\phi(\text{ vacuum })}{\tilde{v}_\phi(\text{ material })} = (1 + \tilde{\chi})^{1/2} \tag{2.12}$$

The real and imaginary parts of the complex refractive index $(\tilde{n} = n + iK)$ are related to the material's dispersion and absorption properties, respectively. The real part n represents the refractive index of the material, which determines the speed of light in the medium, and can be defined as $n = \frac{c}{v_\phi}$ where v_ϕ is the phase velocity in the material (the real part of $\tilde{v}_\phi$). The imaginary part K is called the attenuation constant, and describes how the light wave is attenuated (absorbed) as it travels through the material. In a non-absorbing medium, the value of K is zero. This indicates that the medium does not exhibit any absorption of light as it propagates through the material.

In electromagnetic theory, waves are a fundamental way through which energy and momentum travel through space. These waves have oscillating electric and magnetic fields and carry energy from their source to distant locations.

Irradiance, often denoted by I, is a measure of the power of electromagnetic radiation received per unit area. It is an important concept when discussing the propagation of light or electromagnetic waves in general. This quantity can be understood as the density of power projected onto a surface.

For a harmonic plane wave in a non-absorbing medium, the irradiance can be directly related to the square of the amplitude of the electric field associated with the wave in that medium. Mathematically, this can be expressed as:

$$I = \frac{1}{2} \epsilon v \mathbf{E}_0^2 \tag{2.13}$$

where I is the irradiance, ϵ is the permittivity of the medium, v is the phase velocity of the wave, and $\mathbf{E}_0$ is the amplitude of the electric field.

This relationship tells us that the irradiance of a light wave is proportional to the square of the amplitude of the electric field. Hence, light waves with larger electric fields carry more power per unit area.

2.1.3 Absorption and Emission of Electromagnetic Radiation

A two-level system is a simplified model often used to understand the absorption of light by a molecule [2]. In this model, the molecule has only two electronic energy levels: the ground state and an excited state, labeled 1 and 2, with energies E_1 and E_2 $(E_1 < E_2)$, respectively. Initially, the system is in the lower state. When the system interacts with light whose energy matches the energy difference between these two levels, the possible processes are illustrated in Figure 2.2.
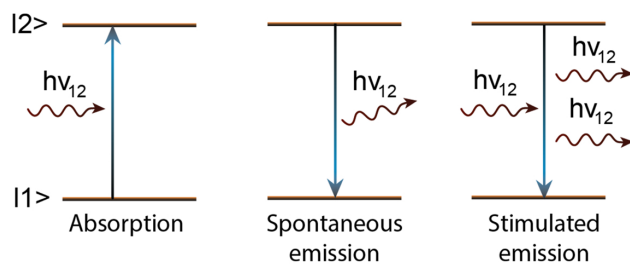
Figure 2.2: Interaction of a two-level system with a radiation field.

The system can be excited to the upper state by the absorption of a photon with energy:

$$\nu_{12} = \frac{E_2 - E_1}{h} \tag{2.14}$$

This transition is referred to as $2 \leftarrow 1$. In the kinetic model formalism, the rates of change of the populations N_1 and N_2 in the two states can be written as:

$$-\frac{\mathrm{d}N_1^{(\mathrm{abs})}}{\mathrm{d}t} = \frac{\mathrm{d}N_2^{(\mathrm{abs})}}{\mathrm{d}t} = B_{12}\rho\left(\nu_{12}\right)N_1 \tag{2.15}$$

where $\rho\left(\nu_{12}\right)$ is the photon density, and B_{12} is the Einstein coefficient for absorption. This depends on the properties of the system, particularly the wave functions of states 1 and 2, but not on the temperature.

Once the system is in the excited state, it can spontaneously decay to the initial state $1 \leftarrow 2$, emitting light at the same frequency ν_{12} as the one defined above. It can also be described kinetically as follows:

$$\frac{\mathrm{d}N_1^{(\mathrm{sp.\ em.})}}{\mathrm{d}t} = -\frac{\mathrm{d}N_2^{(\mathrm{sp.\ em.})}}{\mathrm{d}t} = A_{21}N_2 \tag{2.16}$$

This process is called spontaneous emission due to the absence of any external trigger or perturbation that induces the emission process. A_{21} is the Einstein coefficient for spontaneous emission. It represents the probability of a molecule in the excited state (2) spontaneously undergoing a transition to the lower energy state (1) and emitting a photon without any external influence. It characterizes the intrinsic tendency of an excited atom or molecule to return to a lower energy state and release its excess energy in the form of a photon.

The relationship between the Einstein coefficient for spontaneous emission and the fluorescence lifetime is as follows:

$$\tau_f = \frac{1}{A_{21}} \tag{2.17}$$

The last process that can occur is stimulated emission, where the light induces a transition $1 \leftarrow 2$. This can be described as follows:

11

$$\frac{dN_1^{\text{(stim.em.)}}}{dt} = -\frac{dN_2^{\text{(stim.em.)}}}{dt} = B_{21}\rho\left(\nu_{12}\right)N_2 \tag{2.18}$$

The emitted photon has the same energy, direction, and phase as the incident photon. This process is used, for example, in lasers.

2.1.4 Measurable Quantities in Spectroscopy

The attenuation of an optical wave when propagating through an absorbing medium can be described as follows:

$$\frac{dI(x)}{dx} = -\zeta I(x) \tag{2.19}$$

where:

- $\frac{dI(x)}{dx}$ represents the rate of decrease in the intensity of the optical wave as it propagates through the medium, with x being the distance traveled.

- $I(x)$ is the intensity of the optical wave at the distance x from the source.

- ζ is the absorption coefficient of the medium. It represents the measure of how strongly the medium absorbs light as it passes through.

This equation is a first-order linear differential equation that describes the exponential decay of the optical wave's intensity with distance in an absorbing medium. The solution to this equation is given by:

$$I(x) = I_0 \cdot e^{-\zeta x} \tag{2.20}$$

where I_0 is the initial intensity of the optical wave at $x = 0$. As the wave propagates through the medium ($x > 0$), its intensity decreases exponentially due to absorption.

The Beer-Lambert law can be derived from this equation. We introduce the concept of absorbance A, which is related to the intensity of light transmitted through the sample. The absorbance is defined as the negative logarithm (base 10) of the ratio of the initial intensity I_0 to the transmitted intensity $I(x)$:

$$A = -\log_{10}\left(\frac{I(x)}{I_0}\right) \tag{2.21}$$

Substituting the expression for $I(x)$ from the previous solution, we get:

$$A = -\log_{10}\left(\frac{I_0 \cdot e^{-\zeta x}}{I_0}\right) = \zeta x \tag{2.22}$$

The Beer-Lambert law states that the absorbance (A) of a sample is directly proportional to the product of the concentration (c) (usually expressed in mol/L or M) of

the absorbing species in the sample, the path length (d) of the light through the sample, and ε, which is the molar absorptivity or molar absorption coefficient. This takes into account the specific properties of the absorbing species and the wavelength of light used in the measurement.

$$A = \varepsilon \cdot c \cdot d \tag{2.23}$$

The absorbance A relates to the attenuation coefficient K, mentioned earlier, through the following relation:

$$K = \frac{\ln 10 \cdot A \cdot \lambda}{4\pi d} \tag{2.24}$$

Fate of Excited Molecules

Organic molecules typically have two primary electronic states : singlet states, where all electrons are spin-paired, and triplet states, characterized by the presence of one set of unpaired electron spins. The molecules enter one of the vibrational levels within an excited state (Figure 2.3). The probability of finding the molecule in a particular excited singlet state, denoted as S_n, depends on transition probabilities and the excitation wavelength, governed by the interaction between the electron involved in the transition and the electric field of the excitation light.
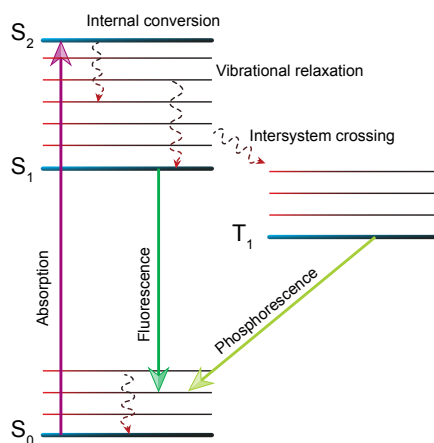

Figure 2.3: Jablonski diagram depicts the radiative (represented by solid arrows) and non-radiative (indicated by dashed arrows) processes for excited closed-shell molecules.

Upon excitation to higher singlet states, molecules undergo rapid *internal conversion* to higher vibrational levels of the first excited singlet state S_1. The excess vibrational energy is quickly dissipated via a process known as *vibrational relaxation*. These non-radiative processes are fast and bring the molecule to the lowest vibrational level of the excited electronic state. *Internal conversion* from high excited states

to the lowest excited state is common enough that fluorescence, if it occurs, will originate from S_1. This is known as Kasha's rule. However, there are exceptions to this rule.

Fluorescence can occur through spontaneous emission of a photon, in accordance with the Franck-Condon principle. This vertical transition to higher excited vibrational levels of the electronic ground state (S_0) is followed by vibrational relaxation until thermal equilibrium, dictated by the Boltzmann distribution, is reached. This gives rise to the mirror image characteristic of the absorption and the emission spectra, although this is not always the case as it may depend on other factors such as the molecule's structure and its environment. The fact that the fluorescence occurs from the lowest singlet excited state often results in the fluorescence spectrum being at longer wavelengths (lower energy) than the absorption spectrum. The difference between the position of the absorption and emission maxima is called Stokes shift.

For certain molecules, a radiationless transition between electronic states of different spin multiplicities, for example from a singlet to a triplet state, is possible. This process is referred to as *intersystem crossing*. Emission from the triplet is also possible (phosphorescence) and occurs on much longer time scales since it originates from a spin-forbidden transition.

By monitoring the decrease of spontaneous emission with time, one can obtain the radiative rate constant k_{rad}, which is the molecular equivalent of the Einstein coefficient for emission A_{21}. This decrease would give an exponential decay as follows:

$$I^{fl}(t) = I_0^{fl} 10^{-k_{fl}t} \qquad (2.25)$$

Here, I_0^{fl} is the initial fluorescence intensity, and $I^{fl}(t)$ is the fluorescence intensity at time t. The S_1 state decays monoexponentially to the ground state through fluorescence. The rate at which this fluorescence occurs is represented by the rate constant k_{fl}. This rate constant includes contributions not only from radiative processes (characterized by k_{rad}), but also from any non-radiative processes (such as internal conversion or intersystem crossing), with the rate constant expressed as $k_{fl} = k_{rad} + \sum_{\text{non-rad proc.}} k_{\text{non-rad}}$. Fluorescence lifetimes can be measured with various techniques, for example by Time Correlated Single Photon Counting (TCSPC) or by fluorescence up-conversion.

In general, excited-state populations, after being excited by electromagnetic radiation, can be investigated through numerous time-resolved spectroscopic techniques. These methodologies can track dynamic phenomena over timescales from femtoseconds to microseconds. The time duration of the perturbation used to excite the system into the excited state must be shorter than the timescale of the process being studied. As such, it's essential to use advanced lasers capable of generating brief optical pulses.

For instance, Transient Absorption (TA) spectroscopy can attain time resolutions

on the order of femtoseconds, enabling the detection of various states such as emissive, non-emissive, and 'dark' states. However, TA and similar techniques, like broadband fluorescence upconversion, do not strictly conform to the principles of linear spectroscopy. The foundational principles of these techniques are rooted in the field of nonlinear optics, due to the fact that the system's response is not directly proportional to the intensity of the incident light.

2.2 Nonlinear Spectroscopy

Earlier, we saw that the polarization $\mathbf{P}$ is linearly dependent on the applied electric field as shown in Equation 2.6.

In the presence of a strong electric field, the polarization $\mathbf{P}$ can no longer be considered linearly proportional to the electric field $\mathbf{E}$ [3]. In this case, it can be expressed as a series expansion of the form:

$$\mathbf{P} = \mathbf{P}^L + \mathbf{P}^{NL} = \varepsilon_0 \left[\underline{\chi}^{(1)} \cdot \mathbf{E} + \underline{\chi}^{(2)} \cdot \mathbf{E} \cdot \mathbf{E} + \underline{\chi}^{(3)} \cdot \mathbf{E} \cdot \mathbf{E} \cdot \mathbf{E} + ... \right] \tag{2.26}$$

Here, higher-order phenomena depending on the second, the third, etc., power of the electric field start to be important. $\underline{\chi}^{(1)}$ is the linear optical susceptibility and corresponds to the susceptibility at low intensity. $\underline{\chi}^{(2)}$ is the second-order nonlinear optical susceptibility tensor and it is a third-rank tensor containing $3^3 = 27$ elements. $\underline{\chi}^{(3)}$ is the third-order nonlinear optical susceptibility and it is a fourth-rank tensor with 3^4 elements. In the following, we will only focus on the phenomena which depend on the second-order polarization.

In the presence of optical pulses, the generated electric field is non negligible compared to the existing one between the nuclei and the electron, therefore, the properties of the material are modified. $\underline{\chi}^{(2)}$ then represents the variation of the optical susceptibility with the electric field:

$$\chi^{(2)} = \frac{\partial \chi}{\partial E} \tag{2.27}$$

In this work, only the nonlinear phenomena of the second order are of interest to us (i.e., the second term of the Equation 2.26). In its most generalized form, it is expressed as a multipole series expansion as follows [4]:

$$\mathbf{\Pi}^{(2)} = \mathbf{P}^{(2)} - \nabla \cdot \mathbf{Q}^{(2)} + \frac{\mu_0}{i\omega} \nabla \times \mathbf{M}^{(2)} + \dots \tag{2.28}$$

In this work, we apply the electric dipole approximation and neglect the quadrupole and magnetic term (second and third term respectively). The electric displacement is given in Equation 2.10. We can then derive the wave equation for the nonlinear second-order processes:

$$\nabla \times (\nabla \times \mathbf{E}) - \nabla^2 \mathbf{E} + \varepsilon_0 \mu_0 \tilde{\varepsilon}_r \frac{\partial^2 \mathbf{E}}{\partial t^2} + \mu_0 \frac{\partial^2 \mathbf{P}}{\partial t^2} = 0 \tag{2.29}$$

In the case of second harmonic generation (SHG) where two waves at a frequency ω interact in a material to generate a new wave at 2ω, the general solution for Equation 2.29 scales as [4]:

$$I^{(2)}(2\omega) \propto l^2 \left(\mathrm{sinc}(\Delta \mathbf{k} l/2)\right)^2 I^2(\omega) \tag{2.30}$$

Where l is the optical path length in a material where the fundamental beam is in phase with the nonlinear signal. $\Delta \mathbf{k} = 2\mathbf{k}(\omega) - \mathbf{k}(2\omega)$ is the phase mismatch between the nonlinear induced polarization and the propagating electric field in the material. If $\Delta \mathbf{k}$ is small, the two waves remain more or less in phase over a long distance.

To achieve phase matching in a nonlinear optical process, one can use various techniques, such as adjusting the angle or temperature of the crystal to alter the wave vectors $\mathbf{k}(\omega)$ and $\mathbf{k}(2\omega)$. Additionally, birefringent or quasi-phase-matching structures can be employed to compensate for the phase mismatch and enhance the conversion efficiency under certain conditions. Proper phase matching is essential for optimizing the performance of nonlinear optical devices, such as frequency doublers, optical parametric amplifiers, and parametric oscillators.

In the ideal case, $\Delta \mathbf{k} = 0$ (perfect phase matching) and the conversion efficiency is the highest. The coherence length can be defined as:

$$l_{\mathrm{c}} = \frac{2\pi}{\Delta k} \tag{2.31}$$

This defines the coherence length (l_{c}) as the distance over which the phase mismatch (Δk) is equal to 2π. In other words, it is the length over which the waves remain in phase and interact coherently, leading to efficient energy conversion in nonlinear optical processes. When the propagation distance exceeds the coherence length, the efficiency of the conversion process decreases due to the increasing phase mismatch.

2.2.1 Second Harmonic Generation

The strength of the second harmonic signal depends essentially on the magnitude of the second order susceptibility $\underline{\chi}^{(2)}$, and in the case of SHG, the polarization is written as follows:

$$\mathbf{P}_{NL}^{(2)}(2\omega) = \varepsilon_0 \underline{\chi}^{(2)} \mathbf{E}(\omega)\mathbf{E}(\omega) \tag{2.32}$$

This tensor is around 12 orders of magnitude smaller than the linear susceptibility tensor $\underline{\chi}^{(1)}$, but it significantly increases when in resonance with an optical transition of the material. The measurement of the variation of the SHG signal corresponds to the variation of $\left|\chi^{(2)}\right|^2$, and thus one can measure the spectrum at one photon or two photon resonances of the non-linear material.

SHG can only be generated from non-centrosymmetric media. This is an important rule as it significantly reduces the number of media where this process can happen. Indeed, in centrosymmetric media such as liquids, gases, and certain crystalline classes, second-order processes like SHG are forbidden in the electric dipole approximation. To explain this, let's consider two electric fields propagating in a medium with possessing inversion symmetry. The first order of the non-linear polarization is given by Equation 2.32. If the media is centrosymmetric, the sign of $\chi^{(2)}$ is not affected. However, the incident and the harmonic field are affected. The second order polarization can be written in this case as:

$$-\mathbf{P}^{(2)}(2\omega) = \varepsilon_0 \underline{\chi}^{(2)}[-\mathbf{E}(\omega)][-\mathbf{E}(\omega)] = \varepsilon_0 \underline{\chi}^{(2)} \mathbf{E}^2(\omega) \tag{2.33}$$

This implies that $\mathbf{P}^{(2)}(2\omega) = -\mathbf{P}^{(2)}(2\omega)$, which can be satisfied only in case $\underline{\chi}^{(2)} = 0$. This means that no second-order process such as SHG can take place in centrosymmetric media.

At the interfaces between two centrosymmetric media, the symmetry is broken, so the signal we get is only generated from the interface. This is the basic idea of surface second harmonic generation.

2.2.2 Classical Description of Non-Linear Susceptibility

The Lorentz oscillator model offers a classical interpretation that helps us understand the fundamental characteristics of linear and nonlinear optical phenomena, eliminating the necessity for more intricate quantum mechanical perspectives. In this model, a molecule is seen as consisting of electrons (with mass m and charge $-e$) and a nucleus bound together by an attractive force. The potential $U(x)$, which represents the force between an electron and a nucleus, is expressed as a series expansion in terms of the distance x separating these two particles and can be written as follows:

$$U(x) = \frac{1}{2}kx^2 + \frac{1}{3}ax^3 + \frac{1}{4}bx^4 + \dots \tag{2.34}$$

with k, a and b constants. The electron moves within an attractive central force field (which is the derivative of the potential), taking on the following form:

$$F = -\frac{dU(x)}{dx} = -(kx + ax^2 + bx^3 + \dots) \tag{2.35}$$

To effectively handle resonances and prevent singularities, a frictional force, γ, is incorporated. The equation of motion for the free system can then be formulated as:

$$m\frac{d^2x}{dt^2} + 2m\gamma\frac{dx}{dt} + kx + ax^2 + bx^3 + \dots = 0 \tag{2.36}$$

In the context of a medium where an incoming electromagnetic wave is propagating, this electromagnetic wave, E(t), disturbs the electron-nucleus system via

Coulomb forces. Taking into account all the preceding components, the equation of motion can be presented as follows:

$$m\frac{d^2x}{dt^2} + 2m\gamma\frac{dx}{dt} + kx + ax^2 + bx^3 + ... = -eE(t) \tag{2.37}$$

In the harmonic approximation, only the first term of the force in Equation 2.35 is considered. This approximation is only applicable for weak fields, which result in small displacements of the electron from its equilibrium position. For stronger fields, higher terms need to be taken into account.

The solution to Equation 2.37 requires a perturbative treatment and is expressed as a series expansion of the displacement x, with a parameter λ representing the strength of the perturbation:

$$x(t) = \sum_{i=1}^{\infty} \lambda^i x^{(i)}(t) \tag{2.38}$$

By replacing the external field $E(t)$ with $\lambda E(t)$ in Equation 2.37, the equation for the first order of λ is:

$$\frac{d^2x^{(1)}}{dt^2} + 2\gamma\frac{dx^{(1)}}{dt} + \frac{k}{m}x^{(1)} = -\frac{e}{m}E(t) \tag{2.39}$$

This has a solution:

$$x^{(1)}(t) = -\frac{e}{2m}\frac{E(\omega)e^{-i\omega t}}{\left[\omega_0^2 - \omega^2 - 2i\gamma\omega\right]} - c.c. \tag{2.40}$$

Here, it's important to note that the external electric field was expressed using the complex notation:

$$E(t) = \frac{1}{2}\left[E(\omega)e^{-i\omega t} + E^*(\omega)e^{i\omega t}\right] \tag{2.41}$$

Moreover, the resonance frequency $\omega_0 = \sqrt{k/m}$ of a free system was used. Assuming N independent electron-nucleus systems per unit volume, the total polarization induced in the medium, according to Equation 2.40, can be formulated as:

$$P^{(1)}(t) = -Nex^{(1)}(t) = \frac{Ne^2}{2m}\frac{E(\omega)e^{-i\omega t}}{\left[\omega_0^2 - \omega^2 - 2i\gamma\omega\right]} + c.c. \tag{2.42}$$

This equation illustrates that the induced dipole oscillates in time, reflecting the displacement of the electron.

By comparing Equations 2.6 and 2.42, the linear susceptibility can be expressed as:

$$\tilde{\chi}^{(1)}(\omega) = \frac{Ne^2}{\varepsilon_0 m}\frac{1}{\left[\omega_0^2 - \omega^2 - 2i\gamma\omega\right]} \tag{2.43}$$

This formulation is under the assumption that the polarization follows the form:
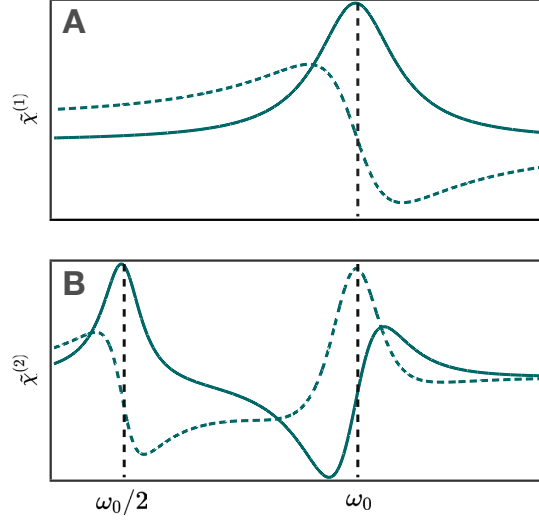
Figure 2.4: Variation of (A) linear and (B) second-order susceptibility with incident frequency. The real and imaginary parts are represented by dotted and solid lines, respectively.

$$P^{(1)}(t) = \frac{1}{2}\left\{P^{(1)}(\omega)e^{-i\omega t} + P^{(1)^*}(\omega)e^{i\omega t}\right\} \tag{2.44}$$

When an external field is much more intense, one has to include an additional nonlinear term of the displacement expansion into the equation of motion as the displacement cannot be taken as a linear function of the applied electric field. Equation 2.39 now becomes:

$$\frac{d^2x}{dt^2} + 2\gamma\frac{dx}{dt} + \frac{k}{m}x + \frac{a}{m}x^2 = -\frac{e}{m}E(t) \tag{2.45}$$

Applying the perturbation treatment once again, but at the second order of λ and using Equation 2.41 for the electric field, we get:

$$x^{(2)}(t) = -\frac{ae^2}{m^2}\frac{[E(\omega)]^2 e^{-2i\omega t}}{[\omega_0^2 - 4\omega^2 - 4i\gamma\omega]\,[\omega_0^2 - \omega^2 - 2i\gamma\omega]^2} - c.c. \tag{2.46}$$

In a similar way to the previous expression, we can extract the macroscopic second order polarization. Using the same procedure used in the previous section, the expression of the second order polarization becomes:

$$P^{(2)}(t) = -Nex^{(2)}(t) = \frac{Nae^3}{4m^2}\frac{[E(\omega)]^2 e^{-2i\omega t}}{[\omega_0^2 - 4\omega^2 - 4i\gamma\omega]\,[\omega_0^2 - \omega^2 - 2i\gamma\omega]^2} + c.c. \tag{2.47}$$

To give an expression of the second order macroscopic susceptibility of the system, we use the expression of the second order macroscopic susceptibility of the media as follows:

$$P^{(2)}(2\omega) = \frac{1}{4}\varepsilon_0\chi^{(2)}(2\omega;\omega,\omega)E^\omega E^\omega \tag{2.48}$$

The macroscopic nonlinear susceptibility can be written as:

$$\tilde{\chi}^{(2)}(2\omega;\omega,\omega) = \frac{Nae^3}{\varepsilon_0 m^2}\frac{1}{\left[\omega_0^2 - 4\omega^2 - 4i\gamma\omega\right]\left[\omega_0^2 - \omega^2 - 2i\gamma\omega\right]^2} \tag{2.49}$$

We observe that $\chi^{(2)}$ has two resonance frequencies, at the fundamental frequency ω_0 and at the harmonic frequency $\omega_0/2$ (Figure 2.4B). $\chi^{(2)}$ also scales with the coefficient a, which is related to the strength of the nonlinearity. This classical description outlines the main features of the nonlinear susceptibility.

2.2.3 Symmetry Properties of the Susceptibility

For second harmonic generation, we will focus on the nonlinear susceptibility tensor $\chi^{(2)}$. This tensor has 27 elements (that can be complex). Practically, the number of these elements can be reduced if one considers certain symmetry arguments. In the previous section, the *inversion symmetry* was already mentioned. This argument implies that second harmonic generation occurs only where the centrosymmetry of the media is broken, typically at surfaces and interfaces. Here, we consider other symmetry properties that will be relevant to reduce the number of $\chi^{(2)}$ elements [3, 4].

Let's consider this general expression of the first-order nonlinear polarization:

$$\mathbf{P}^{(2)}(\omega) = \varepsilon_0\tilde{\chi}_{ijk}^{(2)}(\omega,\omega_1,\omega_2)\mathbf{E}_j(\omega_1)\mathbf{E}_k(\omega_2) \tag{2.50}$$

with $\omega = \omega_1 + \omega_2$

Intrinsic permutation symmetry states that the last two indices, namely j, k of the $\chi^{(2)}$ tensor, can be permuted if the corresponding frequencies are also permuted accordingly:

$$\chi_{ijk}^{(2)}(\omega,\omega_1,\omega_2) = \chi_{ikj}^{(2)}(\omega,\omega_2,\omega_1) \tag{2.51}$$

This symmetry reduces the total number of the nonlinear susceptibility tensor elements from 27 to 18 independent elements. It could be interpreted physically as it is impossible to give any precedence of a field over another one. In the case of SHG, the two incoming fields have the same frequency, so the two last indices can be permuted without interchanging the frequencies.

Symmetry in lossless media: Far from resonance, the $\chi^{(2)}$ tensor becomes real. In this case, full permutation symmetry applies, meaning all the indices of the second-order susceptibility tensor can be permuted while simultaneously interchanging the frequencies accordingly with $\omega = \omega_1 + \omega_2$. This translates as follows:

$$\chi_{ijk}^{(2)}\left(\omega_1+\omega_2,\omega_1,\omega_2\right)=\chi_{jki}^{(2)}\left(-\omega_1,\omega_2,-\omega_1-\omega_2\right) \tag{2.52}$$

Kleinman symmetry is closely related to the previous symmetry. The frequencies of light involved are all much less than the resonant frequencies of the material. In this case, the indices of the tensor elements can be permuted without permutation of the corresponding frequencies. Here, the susceptibility is no longer a function of the frequency. As a result, we get:

$$\chi_{ijk}^{(2)}=\chi_{jik}^{(2)} \tag{2.53}$$

Combining this with the intrinsic permutation symmetry, we get:

$$\chi_{ijk}^{(2)}=\chi_{jki}^{(2)}=\chi_{kij}^{(2)}=\chi_{jik}^{(2)}=\chi_{kji}^{(2)}=\chi_{ikj}^{(2)} \tag{2.54}$$

This reduces the number of independent elements to 10 elements.

The last type of symmetry that we consider is *spatial symmetry*. This is based on Neumann's principle [5], which states that the symmetry elements of any physical property of a crystal, including its tensor properties, must include at least the symmetry elements of the point group of the crystal. These symmetries allow for further reduction of the number of independent elements of $\chi^{(2)}$. If we consider an interface between two liquids where X and Y are in the plane of this interface and Z is perpendicular to the interface plane. The phenomena that take place in the (XY) plane don't depend on the orientation of the surface according to the X or Y plane. Such system has a $C_{\infty v}$ point group symmetry, and these spatial symmetries allow for further reduction of the number of independent elements of the $\chi^{(2)}$ to three elements as follows:

$$\begin{aligned}\chi_{xxz}^{(2)}=\chi_{yzy}^{(2)}=\chi_{yyz}^{(2)}=\chi_{xzx}^{(2)}\\ \chi_{zxx}^{(2)}=\chi_{zyy}^{(2)}\\ \chi_{zzz}^{(2)}\end{aligned} \tag{2.55}$$

Other types of point group symmetries, along with their respective non-zero tensor elements, can be found in literature.

2.2.4 Modelisation of SHG Response

The Three-Layers Model

The Three-Layer Model in Second Harmonic Generation (SHG) seeks to explain the optical phenomenon by dividing the material into different regions, each contributing differently to the overall SHG response. The model is represented in Figure 2.5. This model accounts for the interface of two media, each having specific optical properties and implicitly a surface dielectric constant [4, 6]. Different models have
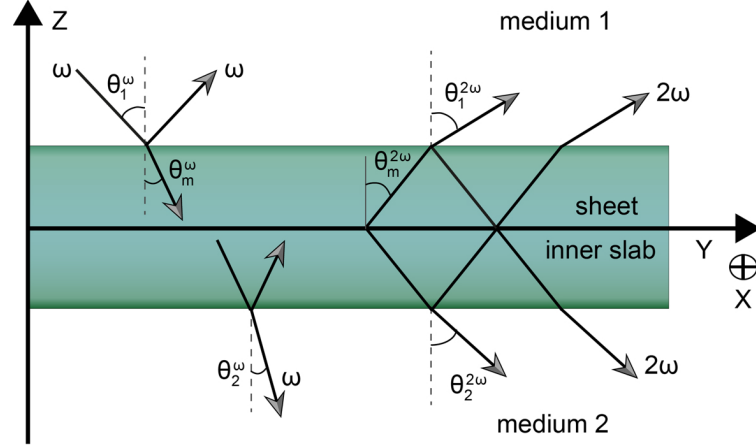
Figure 2.5: Three-layer model geometry for surface second harmonic generation. A nonlinear polarization sheet is embedded in a thin linear slab, which is itself immersed between two linear bulk media.

been derived to include the optical dielectric constant of the sheet of nonlinear polarization. The model we use here assigns an optical dielectric constant to the sheet, which is embedded in a thin slab of vanishing thickness possessing its dielectric constant (ε_m). This slab is also embedded between two media representing the bulk phases with ε_1 and ε_2 as dielectric constants, respectively. This model can be of great advantage if there is resonant SHG and leaves some flexibility in the description of liquid/liquid interfaces [7].

Here, the fundamental electric field is hitting the linear slab from medium 1 at an angle of incidence denoted as θ_1^ω. In this scenario, it is assumed that only one reflection from the interior of the slab is accounted for. Furthermore, the incident electric field is broken down into two perpendicular vectors. These vectors are represented as $\hat{s}$ and $\hat{p}$. Here, $\hat{p}$ lies in the plane of incidence while $\hat{s}$ is perpendicular to it. This is mathematically represented as:

$$\mathbf{E}(\omega) = E_s(\omega)\hat{s} + E_p(\omega)\hat{p} \tag{2.56}$$

To further model the properties of the incident light, we introduce a polarization angle γ. The components of the field are then expressed as:

$$E_s(\omega) = E(\omega)\sin\gamma, \tag{2.57a}$$

$$E_p(\omega) = E(\omega)\cos\gamma e^{i\delta} \tag{2.57b}$$

In these equations, δ represents the dephasing angle between $E_s(\omega)$ and $E_p(\omega)$. When $\delta = 0°$, the wave is linearly polarized. Additionally, $\gamma = 0°$ corresponds to p-polarized waves (parallel to the plane of incidence), while $\gamma = 90°$ corresponds to s-polarized waves (perpendicular to the plane of incidence).

Next, we determine the electric field amplitudes using the Fresnel coefficients for the propagation of light between two media. Fresnel factors tell how an electromagnetic wave interacts with a boundary of two different materials. These coefficients influence the strength of the generated second harmonic signal and its distribution between the reflected and transmitted waves. For these calculations, we approximate $n_i \sim \sqrt{\varepsilon_i}$. The Fresnel coefficients for reflection and transmission are:

$$r_{12}^s = \frac{n_1 \cos\theta_1 - n_2 \cos\theta_2}{n_1 \cos\theta_1 + n_2 \cos\theta_2} \tag{2.58a}$$

$$r_{12}^p = \frac{n_2 \cos\theta_1 - n_1 \cos\theta_2}{n_2 \cos\theta_1 + n_1 \cos\theta_2} \tag{2.58b}$$

and

$$t_{12}^s = \frac{2n_1 \cos\theta_1}{n_1 \cos\theta_1 + n_2 \cos\theta_2} \tag{2.59a}$$

$$t_{12}^p = \frac{2n_2 \cos\theta_1}{n_2 \cos\theta_1 + n_1 \cos\theta_2} \tag{2.59b}$$

For this work, we consider measurements taken under total internal reflection (TIR) geometry. This is operative when the incidence angle exceeds the critical angle, calculated via Snell's law as:

$$\theta_{1,critic.}^\omega = \arcsin\frac{n_2^\omega}{n_1^\omega} \tag{2.60}$$

Polarization Dependence of the SH Signal

Our primary focus is on the nonlinear Second Harmonic Generation (SSHG) intensity at frequency 2ω. The intensity is described by Equation 2.61, where the variables with subscripts 1 and m indicate the upper dodecane phase and the liquid/liquid interface, respectively [4, 8–10]. The bulk medium 2 is an aqueous solution, usually containing the dye responsible for the nonlinear response.

$$I_{\text{SSHG}} = \frac{\omega^2}{8\varepsilon_0 c^3} \frac{\left(\varepsilon_1^{2\omega}\right)^{1/2}}{\varepsilon_1^\omega \left(\varepsilon_m^{2\omega} - \varepsilon_1^\omega \sin^2\theta_1^\omega\right)} \left|\underline{\chi}^{(2)}\right|^2 I_{\text{pr}}^2 \tag{2.61}$$

Based on the system symmetries shown in the previous section, in the case of a liquid/liquid interface, only three independent nonzero tensor elements are needed to describe the experimental observations. These elements are $\chi_{xxz}^{(2)}$, $\chi_{zxx}^{(2)}$, and $\chi_{zzz}^{(2)}$.

Our SSHG setup allows us to study the SSHG intensity's dependence on the polarization angle of the probe beam, γ ($\gamma = 0°$, 45° and 90°, and the second harmonic signal component, Γ ($\Gamma = 0°$, 45° and 90° for p, m and s components). The Equation 2.62 demonstrates this relationship [4]:

$$I_{SSHG}(\gamma, \Gamma) = C \left| a_1\chi^{(2)}_{XXZ} \sin 2\gamma \sin \Gamma + \left(a_2\chi^{(2)}_{XXZ} + a_3\chi^{(2)}_{ZXX} + a_4\chi^{(2)}_{ZZZ}\right) \cos^2\gamma \cos\Gamma + \right.$$
$$\left. + a_5\chi^{(2)}_{ZXX} \sin^2\gamma \cos\Gamma \right|^2 I^2_{pr}$$

$$(2.62)$$

where C is a constant based on solvents and the probe wavelength, I_{pr} is the probe field intensity, and $a_1..., a_5$ are optical coefficients. These coefficients depend on the Fresnel factors and were calculated as described in the literature. For our system, the following values were used:

$$n_{1,dod} = 1.42, \quad n_{2,water} = 1.33, \quad n_m = 1.378.$$

n_m was calculated as the average of the refractive indices of water n_2 and dodecane n_1 [11].

Polarization curves or polarization-resolved SSHG measurements carried out in this work were measured by varying the probe beam polarization γ using a $\lambda/2$ waveplate and setting the output polarization with the help of an analyzer to three different output polarizations $\Gamma = 0°, 45°$, and $90°$. This allowed extracting the relative magnitude and sign of the three susceptibility elements. Equation 2.63 derives from Equation 2.62 and allows us to calculate the susceptibility elements' ratios using a least-squares curve fitting analysis of the data.

$$I_{SSHG}(\gamma, 0°) \propto \left| \left(a_2\chi^{(2)}_{XXZ} + a_3\chi^{(2)}_{ZXX} + a_4\chi^{(2)}_{ZZZ}\right) \cos^2\gamma + a_5\chi^{(2)}_{ZXX} \sin^2\gamma \right|^2 \quad (2.63a)$$

$$I_{SSHG}(\gamma, 45°) \propto \left| a_1\chi^{(2)}_{XXZ} \sin 2\gamma + \left(a_2\chi^{(2)}_{XXZ} + a_3\chi^{(2)}_{ZXX} + a_4\chi^{(2)}_{ZZZ}\right) \cos^2\gamma \right.$$
$$\left. + a_5\chi^{(2)}_{ZXX} \sin^2\gamma \right|^2$$

$$(2.63b)$$

$$I_{SSHG}(\gamma, 90°) \propto \left| a_1\chi^{(2)}_{XXZ} \sin 2\gamma \right|^2 \quad (2.63c)$$

2.2.5 Determining the Molecular Orientation of Molecules at the Interface

The orientation of molecules at an interface can be determined through the analysis of a SH signal that is generated by these molecules. If the molecules at the interface orient randomly, the second-order nonlinear susceptibility $\chi^{(2)}$ will be equal to zero. This indicates that the molecules have a preferential orientation, although the likelihood of them aligning perfectly is quite slim due to the non-rigid nature of their environment. Instead, we can infer an orientational distribution of these molecules,
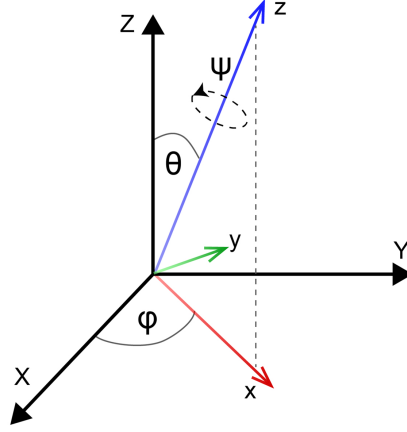
Figure 2.6: Euler angles: we have both lab (X, Y, Z) and molecular (x, y, z) reference frames. The angle of rotation around the interface normal is denoted by ϕ, θ represents the angle between the interface normal and the molecular axis, and ψ signifies the angle of rotation around the molecular axis.

centered around a specific out-of-plane angle, symbolized as θ. The relative magnitude of the $\chi^{(2)}$ elements extracted from polarization-resolved measurements describes the macroscopic second order response of the system in the laboratory frame. The hyperpolarizability tensor $\overset{\leftrightarrow}{\beta}$ is a third-rank tensor and can be considered as the microscopic counterpart of the nonlinear susceptibility. It represents the molecular property that initiates the second harmonic response. The number of relevant elements of the hyperpolarizability tensor can be obtained from quantum mechanical calculations, for example. These elements are given in the molecular frame. This is represented in Figure 2.6

The macroscopic second-order nonlinear susceptibility depends on the hyperpolarizability tensor $\overset{\leftrightarrow}{\beta}$ as follows:

$$\overset{\leftrightarrow}{\chi}^{(2)} = \frac{1}{\varepsilon_0} N \langle \overset{\leftrightarrow}{T} \rangle \overset{\leftrightarrow}{\beta} \tag{2.64}$$

N is the number of chromophores which generate the second harmonic response and $\overset{\leftrightarrow}{T}$ is the transformation tensor that allows to go from the molecular frame to the laboratory frame.

To simplify the transformation tensor $\overset{\leftrightarrow}{T}$, we introduced two assumptions. First, we considered the interface's invariance under rotations around the surface normal, which led to a uniform distribution of angles ϕ. Second, we fixed the distribution of the angle ψ to a specific value or assumed a uniform distribution. This simplified the dependence of the nonlinear susceptibility on the hyperpolarizability.

The rotations around the three Euler angles θ, ϕ, and ψ can be formulated in matrix notation as follows:

$$R_\phi = \begin{bmatrix} \cos\phi & -\sin\phi & 0 \\ \sin\phi & \cos\phi & 0 \\ 0 & 0 & 1 \end{bmatrix} \quad \phi \in [0, 2\pi] \tag{2.65a}$$

$$R_\theta = \begin{bmatrix} 1 & 0 & 0 \\ 0 & \cos\theta & -\sin\theta \\ 0 & \sin\theta & \cos\theta \end{bmatrix} \quad \theta \in [0, \pi] \tag{2.65b}$$

$$R_\psi = \begin{bmatrix} \cos\psi & -\sin\psi & 0 \\ \sin\psi & \cos\psi & 0 \\ 0 & 0 & 1 \end{bmatrix} \quad \psi \in [0, 2\pi] \tag{2.65c}$$

Most studies in the literature involve axial molecules with a charge transfer character along the molecular axis. Under these conditions, the dominant element of the hyperpolarizability tensor, β_{zzz}, is the one aligned along the primary molecular axis z. As a result, the macroscopic susceptibility and microscopic hyperpolarizability are related to each other by the following equations:

$$\chi_{ZZZ}^{(2)} = N\langle\cos^2\theta\rangle\beta_{zzz} \tag{2.66}$$

$$\chi_{ZXX}^{(2)} = \chi_{XXZ}^{(2)} = \frac{1}{2}N\langle\sin^2\theta\cos\theta\rangle\beta_{zzz} \tag{2.67}$$

This reduces the number of independent tensor elements to two. This is very convenient, since the tilt angle θ (between the transition dipole moment and the normal to the interface (Z in the lab frame)) can be extracted without prior knowledge of N, the number of molecules at the interface. This can simply be done by taking the ratio of the two tensor elements, in this case $\chi_{ZZZ}^{(2)}$ and $\chi_{ZXX}^{(2)}$.

Assuming that molecular orientation can be described only by the tilt angle θ and only two tensor elements of β are nonzero, an orientational parameter, D, can be expressed as [4, 12, 13]:

$$D = \frac{\chi_{zzz}^{(2)} - \chi_{zxx}^{(2)} + \chi_{xzx}^{(2)}}{\chi_{zzz}^{(2)} + 3\chi_{xzx}^{(2)} - \chi_{zxx}^{(2)}} = \frac{\langle\cos^3(\theta)\rangle}{\cos\theta} \tag{2.68}$$

This parameter can be directly calculated from the measured elements of $\chi^{(2)}$.

In the case where one tensor element of β is dominant, which is the case for molecules with a charge transfer character, the above expression becomes:

$$D = \frac{\chi_{zzz}^{(2)}}{\chi_{zzz}^{(2)} + 2\chi_{xzx}^{(2)}} = \frac{\langle\cos^3(\theta)\rangle}{\cos\theta} \tag{2.69}$$

If we consider a Dirac distribution of the angles at the interface, the expression further simplifies to:
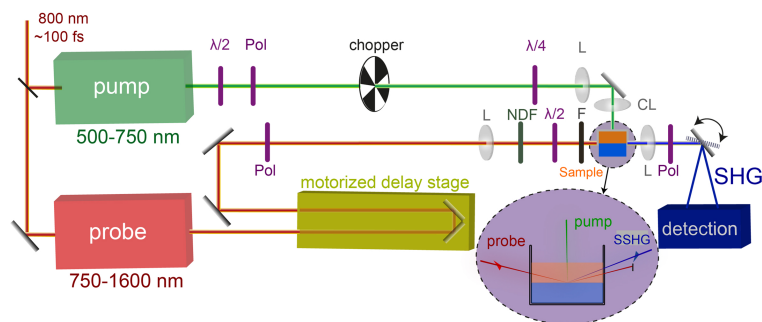
Figure 2.7: Instrumentation for TR-SSHG employed in this study. ($\lambda/2$, half-wave plate; *Pol*, polarizer; *L*, lens; *CL*, cylindrical lens; *NDF*, neutral density filter; *F*, Filter).

$$D = \cos^2 \theta \qquad (2.70)$$

This narrow distribution was assumed for the work shown in this thesis. A more realistic approach is to assume that the molecules at the interface orient with a certain distribution. This distribution can be determined using MD simulations. This approach was, for example, applied in Chapter 7, where porphyrin dyads were investigated.

2.2.6 Experimental Apparatus

A schematic drawing of the setup used for Surface Second Harmonic Generation (SSHG) is shown in Figure 2.7 [14]. The apparatus is based on an amplified Ti:Sapphire amplifier (Solstice, Spectra-Physics) centered at 800nm with pulses of around 100 fs. It powers a collinear optical parametric amplifier (TOPAS-C, Light Conversion) which generates probe pulses of around 100fs and 1-2 µJ, centered around a specific wavelength (usually in the near-infrared region). The probe pulse wavelength is tunable between 750nm and 1600nm. Scanning multiple wavelengths while recording the signal allows for the measurement of the SSHG spectrum, enabling the identification of the resonances of the dye (one photon and two-photon resonance). In this work, the SSHG spectra were given as the square root of the SH intensity to scale with the concentration of the dye at the interface. The probe pulses were focused on the sample using a lens and hit the interface at an angle of about 70°, corresponding to the angle of total internal reflection. The polarization of the probe beam was controlled with a $\lambda/2$ waveplate mounted on a rotary stage, whereas the second harmonic signal polarization was selected using a wire-grid polarizer. The SSHG signal at half the wavelength of the probe was separated from the reflected fundamental probe light using a combination of irises and band-pass filters.

This setup also allows for time-resolved measurements. For this purpose, pump pulses were generated using a two-stage non-collinear optical parametric amplifier (TOPAS White, Light Conversion) powered by the same Ti:Sapphire amplifier. The

pump wavelength can also be tuned according to the excitation needs of the investigated dye. The pump pulses were circularly polarized to avoid in-plane photoselection and were focused on the interface using a spherical and a cylindrical lens to match the shape of the probe pulse. To correct for fluctuations of the probe beam intensity, a chopper was used to reduce the pump pulse repetition rate by a factor of 2 relative to the probe pulse. The reflected SH signal was directed onto the spectrograph entrance slit by using a mirror mounted on a galvanometer oscillating at the same frequency (500 Hz). The SH signals coming from the pumped and non-pumped sample hit different spots on the CCD camera and were measured separately. The time-resolution of the apparatus is about 1 ps, mainly due to the employed geometry.

Bibliography

(1) Hecht, E., *Optics*; Pearson: 2016; 722 pp.

(2) Haar, D. T., *The Old Quantum Theory: The Commonwealth and International Library: Selected Readings in Physics*; Elsevier: 2016; 217 pp.

(3) Boyd, R. W., *Nonlinear Optics*; Elsevier: 2008; 635 pp.

(4) Surface Second Harmonic Generation - - Pierre-François Brevet (EAN13 : 9782880743451) EPFL Press, https://www.epflpress.org/produit/374/9782880743451/surface-second-harmonic-generation (accessed 06/19/2023).

(5) Bhagavantam, S.; Pantulu, P. V. *Proc. Indian Acad. Sci.* **1967**, *66*, 33–39.

(6) Brevet, P. F. *J. Chem. Soc., Faraday Trans.* **1996**, *92*, 4547–4554.

(7) Brevet, P. F.; Girault, H. H. In *Amphiphiles at Interfaces*, ed. by Texter, J., Steinkopff: Darmstadt, 1997, pp 1–9.

(8) Nagatani, H.; Piron, A.; Brevet, P.-F.; Fermín, D. J.; Girault, H. H. *Langmuir* **2002**, *18*, 6647–6652.

(9) Rinuy, J.; Piron, A.; Brevet, P. F.; Blanchard-Desce, M.; Girault, H. H. *Chem. Eur. J.* **2000**, *6*, 3434–3441.

(10) Eisenthal, K. B. *Chem. Rev.* **1996**, *96*, 1343–1360.

(11) Wang, H.; Borguet, E.; Eisenthal, K. B. *J. Phys. Chem. B* **1998**, *102*, 4927–4932.

(12) Zhang, W.-k.; Zheng, D.-s.; Xu, Y.-y.; Bian, H.-t.; Guo, Y.; Wang, H.-f. *J. Chem. Phys.* **2005**, *123*, 224713.

(13) Rao, Y.; Tao, Y.-s.; Wang, H.-f. *J Chem Phys* **2003**, *119*, 5226–5236.

(14) Licari, G. L. Second Harmonic Generation Applied to Biomimetic Interfaces, University of Geneva, 2018.

Chapter 3

Probing Liquid Interfaces with Room-Temperature Ionic Liquids Using the Excited-State Dynamics of a Cationic Dye

Article
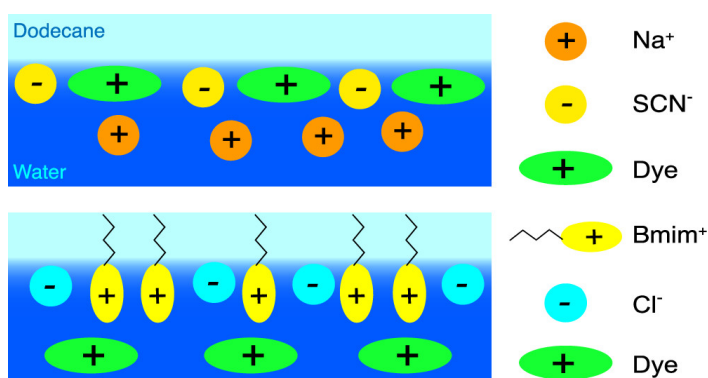
Probing Liquid Interfaces with Room-Temperature Ionic Liquids Using the Excited-State Dynamics of a Cationic Dye

Jihad Sissaoui,[†] Darya S. Budkina,[†] and Eric Vauthey*

Cite This: *J. Phys. Chem. B* 2020, 124, 10546−10555

Read Online

ACCESS | Metrics & More | Article Recommendations | Supporting Information

ABSTRACT: Interfaces with room-temperature ionic liquids (ILs) play key roles in many applications of these solvents, but our understanding of their properties is still limited. We investigate how the addition of ILs in the aqueous subphase affects the adsorption of the cationic dye malachite green at the dodecane/water interface using stationary and time-resolved surface second harmonic generation. We find that the interfacial concentration of malachite green depends crucially on the nature of both anionic and cationic constituents. This concentration reports on the overall charge of the interface, which itself depends on the relative interfacial affinity of the ions. Our results reveal that the addition of ILs to the aqueous subphase has similar effects to the addition of conventional salts. However, the IL cations have a significantly higher propensity to adsorb than small inorganic cations. Furthermore, the IL constituents show a synergistic effect, as the interfacial concentration of each of them also depends on the interfacial affinity of the other.
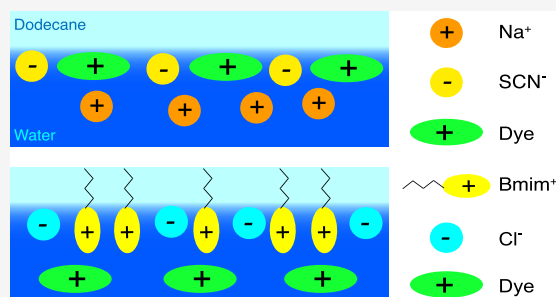
INTRODUCTION

Over the past years, room-temperature ionic liquids (ILs) have attracted considerable attention due to their unique properties that make them promising substitutes of conventional organic solvents in many applications.[1−3] The latter include multiphase bioreactors,[4−7] absorption of volatile organic pollutants,[8−13] as well as energy conversion and storage.[14−16] Therefore, significant effort is being invested to reach a comprehensive understanding of these liquids.[17−23] As many of the above applications of ILs involve surfaces and interfaces, knowledge of the interfacial properties and behavior of these liquids is necessary as well. Various techniques were applied to study interfaces with ionic liquids.[24] For example, surface tension and surface potential studies of air/IL interfaces revealed an increase of the surface tension with the strength of the anion−cation interactions.[25,26] Atomic force microscopy demonstrated that most investigated ionic liquids form a layered structure at solid interfaces.[27] The specific arrangement at the interface can be complex due to the interplay between Coulomb forces and steric effects. Adding water, for example, at a low concentration causes the formation of nanostructures, whereas at a high water concentration, the solution behaves more like a conventional electrolyte.[28]

Investigating the interfaces with standard spectroscopic methods is challenging, as the signal originating from interfaces is usually buried in that from the bulk. This complication is not present in second-order nonlinear spectroscopic techniques, such as surface sum-frequency generation (SSFG) and second harmonic generation (SSHG),[29−31] because the second-order

nonlinear optical susceptibility vanishes in centrosymmetric media but not at interfaces.

IL interfaces have been mostly investigated by SSFG.[32−41] For example, ILs at various interfaces have been thoroughly studied by Baldelli and co-workers.[40] Their studies show that the nonpolar part of the ions, e.g., the alkyl chain of typical imidazolium cations, orient preferentially toward the air-(vacuum) phase, while the charges remain in the liquid, where there are better stabilized. SSFG studies at solid/liquid interfaces suggest that ions at the interfaces organize into a single layer and that orientation beyond this layer is negligible. However, the presence of impurities or other solvents can induce a change in the structure of interfaces.[40]

SSHG studies of interfaces with ILs are scarcer.[42,43] This is due to the fact that most ILs absorb in the UV and are prone to contain impurities absorbing at longer wavelengths. Therefore, the electronic resonance enhancement of the SSHG might arise from the impurities and not only from the IL itself. However, Nishi and co-workers synthesized an IL with a cation, 1-dodecyl-4-phenylpyridinium ($C_{12}ppy^+$), characterized by a large first hyperpolarizability, and performed

10546

Chapter 3. Probing Liquid Interfaces with Room-Temperature Ionic Liquids Using the Excited-State Dynamics of a Cationic Dye

SSHG studies at air/IL and water/IL interfaces.[42] Their results suggest that the dodecyl chain of $C_{12}ppy^+$ points toward air at the air/IL interface and protrudes away from water at the water/IL interface. However, comparing the affinity of several ions using this approach is difficult because these ions have different second-order nonlinear properties and/or may require SSHG measurements at different probe wavelengths. These problems do not arise with nonresonant SSHG, as demonstrated in a recent investigation on air/IL interfaces, which revealed an increased ordering at the interface with increasing alkyl chain length of the imidazolium cation.[43]

An alternative approach is to use a molecular probe with a strong SSHG response and a high sensitivity to the presence of ions at the interface. Over the past years, we have been applying this principle with several ionic dyes to investigate salt effects at both air/water[44] and alkane/water interfaces.[45−48] Depending on the charge and affinity of a given ion for the interface, the ionic probe dye is either attracted or repelled from the interfacial region. The change of probe dye concentration at the interface, which reflects the interfacial affinity of the ion, can then be monitored by measuring the variation of the SSHG intensity. A more efficient approach is to measure the excited-state dynamics of this dye using time-resolved (TR) SSHG. Indeed, the formation of molecular aggregates increases with the interfacial concentration of the dye, leading to distinct excited-state decay dynamics.

We report here on our investigation of dodecane/water interfaces with various concentrations of ILs in the aqueous phase. To probe the interfacial affinity of these ionic liquids for the interface, we measured the excited-state dynamics of the cationic dye malachite green (MG, Chart 1) using TR-SSHG.

Chart 1. Malachite Green and the ILs/Salts Constituents
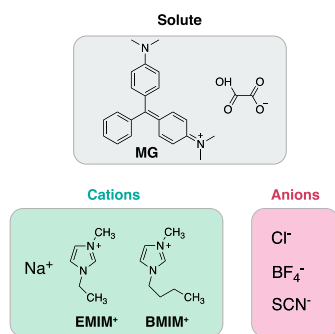
MG is characterized by a large first hyperpolarizability, which makes it an often-used SSHG probe.[49−53] MG is also a well-known viscosity probe as its excited-state lifetime both in bulk liquids and at interface increases with increasing local friction.[54−57] TR-SSHG studies of MG at liquid interfaces revealed that its ground-state recovery dynamics is bimodal, with a fast (ca. 1−2 ps) viscosity-dependent component and a slow one (~20 ps), whose amplitude increases with the bulk MG concentration.[56] The fast component reflects the ultrafast nonradiative decay of the MG excited state associated with large-amplitude motion of its phenyl groups, whereas the slow component is due to the decay of excited aggregates. The relative amplitude of the slow component was found to be very sensitive to the presence of salts in the aqueous sub-phase.[44,45,47]

Six imidazolium ILs, as well as three sodium salts were investigated (Chart 1 and Table S1). The two IL cations differ by the length of one of the alkyl chains, whereas the anions have been selected according to the Hofmeister series, which sort the ions relative to their salting-in or salting-out properties.[58−62] Therefore, the affinity of the cations for the interface is anticipated to increase with increasing alkyl chain length, i.e., in the order $Na^+ < EMIM^+ < BMIM^+$, whereas that of the anion should increase in the order $Cl^- < BF_4^- < SCN^-$.

Our results reveal that these variations of anionic and cationic constituents have a very strong effect on the adsorption properties of these ILs at the dodecane/water interface.

■ METHODS

Samples. Malachite green (MG) oxalate was purchased from Alfa Aesar. The ionic liquids 1-ethyl-3-methylimidazolium tetrafluoroborate (EMIMBF$_4$) and 1-ethyl-3-methylimidazolium thiocyanate (EMIMSCN) were obtained from Iolitec, whereas 1-butyl-3-methylimidazolium tetrafluoroborate (BMIMBF$_4$), 1-ethyl-3-methylimidazolium chloride (EMIMCl), 1-butyl-3-methylimidazolium chloride (BMIMCl), as well as dodecane (99%) were from Acros Organics. 1-Butyl-3-methylimidazolium thiocyanate (BMIMSCN) and the sodium salts NaCl, NaBF$_4$, and NaSCN were obtained from Sigma-Aldrich. All of the compounds were used without further purification.

MG was dissolved in Milli-Q water at a 10^{-5} M concentration for all experiments. The pH of all samples was kept around 3−4 by adding acetic acid. Under these conditions, MG is in a monocationic form. The samples for SSHG measurements were prepared by pouring the aqueous MG solution without or with specific IL or salt concentration in a $2 \times 2 \times 2$ cm^3 cubic quartz cell and then adding dodecane on the top as an upper phase. All measurements were performed at room temperature. Electronic absorption spectra, measured with a Varian Cary 50 Bio spectrophotometer before and after SSHG experiments, did not point to significant degradation of the sample.

Surface Second Harmonic Generation. *Experimental Setup.* The SSHG setup has been described in detail before.[47,63] It is based on an amplified Ti:sapphire system (Solstice, Spectra-Physics) and can be transformed into a TR-SSHG setup by adding a pump pulse channel that can be delayed with respect to the SSHG probe pulse. The SSHG probe pulses (100 fs, 0.7 μJ, and 130 μm $\times$ 340 μm spot size at the interface) were generated with a collinear optical parametric amplifier (Topas C, Light Conversion) and were focused onto the interface with an angle of incidence of about 70°, corresponding to the conditions for total internal reflection. A possible second harmonic signal caused by the optics was eliminated using a long-pass filter located in front of the sample. The polarization was controlled with a half-wave plate. The reflected pulses went through a series of irises, filter and spectrograph to eliminate the reflected probe light before reaching a charge-coupled device (CCD) camera (Newton 920, Andor). No signal could be detected at dodecane/water or dodecane/water + IL interface in the absence of the MG dye.

Polarization-Selective SSHG. For polarization-selective measurements, the polarization angle of the incident beam at 800 nm, γ, was controlled with a half-wave plate mounted on a motorized rotary stage and a given polarization component

of the steady-state SSHG signal was selected using a wire-grid polarizer.[64] The conventional notation for the polarization is used: *p* for parallel polarization with respect to the plane of incidence and *s* for perpendicular polarization. The resulting signal intensity is denoted I_{SS}.

Steady-State SSHG Spectra. Steady- state SSHG spectra were recorded by scanning the wavelength of the SSHG probe pulses with 5 nm steps. The resulting spectra recorded at the liquid interfaces were corrected using the SSHG spectrum from an aluminium mirror.[64] The spectra were recorded at $\gamma = 75°/p$ polarization geometry, to have good signal from both the sample and the mirror. The resulting spectral intensity is denoted I_{SS}.

Time-Resolved SSHG. The pump pulses for the TR-SSHG measurements were at 615 nm (80 fs, 0.8 μJ, and 180 μm × 500 μm spot size at the interface) and were generated with a noncollinear optical parametric amplifier (Topas White, Light Conversion). As illustrated in Figure 1, this wavelength
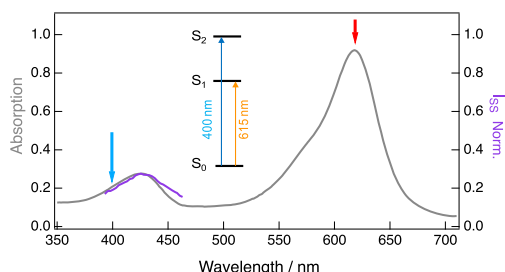
Figure 1. Stationary absorption spectrum of MG in water (gray) and SSHG spectrum of MG at the dodecane/water interface (purple). The inset shows an energy-level scheme of MG with the wavelength of the pump pulse and of the SSHG signal.

corresponds to the $S_1 \leftarrow S_0$ transition of MG. These pulses were circularly polarized to avoid photoselection and were focused on the interface from the top using a combination of spherical and cylindrical lenses and overlapped with the probe pulses at 800 nm. As a consequence, the SSHG signal is resonant with the $S_2 \leftarrow S_0$ transition of MG (Figure 1). No dependence on the probe wavelength was observed between 800 and 900 nm. The TR-SSHG profiles were recorded using the s/p polarization, where the signal intensity is the highest. No significant dependence of the dynamics on the polarization was observed. To correct for the fluctuations of the probe beam intensity, a chopper was used to reduce the pump pulse repetition rate by a factor of 2 relative to the probe pulse. The reflected second harmonic signal was directed onto the spectrograph entrance slit using a mirror mounted on a galvanometer oscillating at the same frequency (500 Hz). The SSHG signals coming from the pumped and the un-pumped sample hit different spots on the CCD camera and were measured separately. The TR-SSHG profiles were processed by taking the square root of the SSHG intensity of the pumped signal divided by the intensity of the un-pumped signal. The so-obtained time profiles were then intensity normalized to −1, since in the present measurements, photoexcitation always resulted in a decrease of the SSHG intensity.[64] As the SSHG signal is resonant with the $S_2 \leftarrow S_0$ transition of MG, the resulting signal, $S(t)$, directly reflects the photoinduced changes of the ground-state population.

RESULTS

Interfaces with EMIMBF$_4$. *Steady-State SSHG.* We start with the results obtained with the dodecane/water−EMIMBF$_4$ interface, since both the EMIM$^+$ cation and the BF$_4^-$ anion are anticipated to have an intermediate affinity for the interface. Addition of different amounts of EMIMBF$_4$ in aqueous solutions of MG does not lead to a significant change in the electronic absorption spectrum (Figure S1). This rules out the formation of MG aggregates in bulk solution, which results in a broadening of the $S_1 \leftarrow S_0$ absorption band.[44]

Figure 2 depicts steady-state SSHG spectra in the 400−460 nm region recorded at the dodecane/water interface with
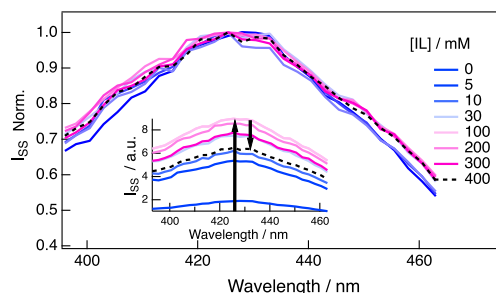

Figure 2. Intensity-normalized stationary SSHG spectra recorded at the dodecane/water interface with different EMIMBF$_4$ concentrations in the aqueous subphase. Inset: non-normalized spectra (error on I_{SS}: ±2.5%).

different amounts of EMIMBF$_4$ in the aqueous subphase. Without IL, the SSHG spectrum matches relatively well the $S_2 \leftarrow S_0$ absorption band of MG (Figure 1), in agreement with the electronic resonance enhancement of the signal. Upon addition of the EMIMBF$_4$, the intensity of the SSHG spectrum first increases up to a concentration of 100 mM and then decreases. Intensity normalization points to a slight spectral broadening in the presence of the IL that could be indicative of the formation of MG aggregates at the interface. This broadening remains constant even at the IL concentrations at which the SSHG intensity decreases.

The dependence of the SSHG intensity on the EMIMBF$_4$ concentration is confirmed by polarization-selective measurements. Figure 3 shows the SSHG intensity measured at the s/p polarization as a function of EMIMBF$_4$ concentration. The steady-state signal intensity increases continuously to reach a maximum value, I_{SS}^{max}, at ∼100 mM IL. At that concentration, which will be designated as c_{SS}^{max}, the steady-state SSHG intensity is larger than that measured without IL by a factor of about 10. The signal decreases when the concentration exceeds c_{SS}^{max} but with a weaker dependence than the rise. The γ/p polarization profiles obtained by measuring the p component of the SSHG signal as a function of the polarization angle of the incoming probe beam, γ, are depicted in the inset. Although the intensity of these profiles changes upon addition of IL, their shape remains constant, pointing to minor change in the orientation of the dye molecules at the interface. Proper determination of the orientation requires analysis of both γ/p and γ/s profiles.[65−68] However, the γ/s profile measured without IL exhibits four peaks of alternating intensity (Figure S2) and, consequently, cannot be described using the standard procedure based on the dipolar electric approximation and assuming an achiral interface, which predicts peaks of identical
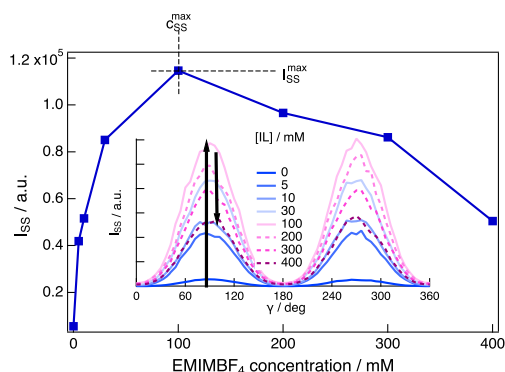
Figure 3. Dependence of the SSHG intensity at 400 nm and s/p polarization on the concentration of EMIMBF$_4$ in the aqueous subphase. The concentrations c_{SS}^{max} above which the intensity decreases, as well as the maximum steady-state SSHG intensity, I_{SS}^{max}, are indicated with the dashed lines. Inset: γ/p polarization profiles at different IL concentrations (error on I_{SS}: ±2.5%).

Figure 4. Normalized TR-SSHG profiles, $S(t)$, at 400 nm measured upon 615 nm excitation of MG at the dodecane/water interface with different concentrations of EMIMBF$_4$. Inset: dependence of the amplitudes of the fast and slow components on the IL concentration. The concentration c_{TR}^{max} at which the amplitudes plateau as well as A_{slow}^{max} are indicated with dashed lines.

intensity. The shape of these γ/s profiles did not change significantly upon addition of IL, confirming a minor effect of the IL on the orientation. Therefore, further analysis including additional elements of the second-order nonlinear susceptibility tensor, associated with, e.g., chirality and magnetic dipole interaction,[69] was not carried out.

Time-Resolved SSHG. An alternative approach to follow the change of dye concentration at the interface is to look at the aggregates, whose propensity to be formed increases with MG concentration. As shown above, their SSHG spectra do not differ sufficiently from that of the monomeric dye to differentiate these two species. However, MG aggregates are characterized by a significantly longer excited-state lifetime than the monomer, due to the inhibition of large-amplitude motion in the former.[56] Therefore, we performed TR-SSHG measurements to monitor the effect of ILs on the formation of aggregates.

Upon excitation at 615 nm in the $S_1 \leftarrow S_0$ absorption band of MG, the SSHG signal at 400 nm, resonant with the $S_2 \leftarrow S_0$ transition, decreases due to the depletion of the ground-state population. The subsequent increase of the SSHG intensity reflects the recovery of the ground-state population. In the absence of IL in the aqueous phase, the normalized signal reflecting the photoinduced population dynamics, $S(t)$, can be reproduced by the convolution of the instrument response function, simulated with a Gaussian function, and a biexponential function with 1.7(± 0.2) ps and ca. 10−15 ps time constants, in agreement with previous investigations.[55−57] The fast component originates from the ultrafast nonradiative decay of the S_1 state of MG, whereas the slow component arises from the excited-state decay of aggregates. The relative amplitude of the slow component, A_{slow}, increases with the bulk concentration of MG (Figure S3).[56] At the 10^{-5} M MG concentration used further on, A_{slow} is below 0.1 (Tables S2−S10). As illustrated in Figure 4, addition of EMIMBF$_4$ leads to slowing down of the recovery dynamics. This effect is the strongest up to ~50 mM IL. Above this concentration, that we will designate as c_{TR}^{max}, the changes in the TR-SSHG dynamics are almost negligible.

The $S(t)$ profiles measured in the presence of IL could be reproduced using the convolution of a Gaussian function with
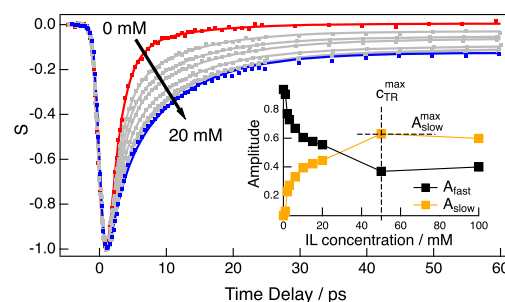
the sum of three exponential functions. Indeed, the fit of the slow component required two exponential functions, one with a time constant around 10−15 ps, which was fixed to 12 ps, and the other with a time constant ≫300 ps, much larger than the 0−300 ps temporal window of the TR-SSHG experiment. The shorter time constant, due to the decay of the excited monomers, ranges between 1.7 and 2.8 ps and does not exhibit any clear correlation with EMIMBF$_4$ concentration (Table S2 and Figure S4). The slow component can be attributed to the excited-state decay of MG aggregates. The need to use two exponential functions for a proper fit can be explained by the presence of aggregates of different sizes. The inset of Figure 4 depicts the variation of the amplitudes of the fast and slow components, A_{fast} and A_{slow}, upon addition of IL. Here, A_{slow} is the sum of the relative amplitudes of the 12 ps and ≫300 ps exponentials. This picture shows that A_{slow}, which is below 0.1 without IL, increases continuously up to 0.6 at $c_{TR}^{max} \sim 50$ mM IL and then remains almost constant at higher concentrations. This result confirms the increase of the interfacial concentration of MG in the presence of EMIMBF$_4$ deduced from the stationary SSHG measurements. As the concentration of MG increases, aggregation becomes more favorable and the TR-SSHG dynamics slows down. Although the stationary SSHG intensity decreases at high concentrations of IL, the TR-SSHG profile remains almost constant.

No SSHG signal could be observed at the dodecane/IL interface. This effect is mostly due to the fact that the interfacial region is not as well defined as with the dodecane/water system because of the decrease of the surface tension with pure IL subphase.[70]

Tuning of the Anion. The same series of experiments as those described above for EMIMBF$_4$ were repeated with other ILs consisting of the same EMIM$^+$ cation but with different anions, namely, Cl$^-$ and SCN$^-$. Qualitatively similar changes as those measured with BF$_4^-$ were observed: addition of IL leads to an increase of the intensity of the SSHG spectra and of the peaks of the polarization profiles as well as to a slowing down of the TR-SSHG dynamics. However, the magnitude of these changes was found to exhibit a significant dependence on the anion.

Figure 5 shows the change of the SSHG intensity at s/p polarization upon addition of EMIM$^+$-based ILs with different anions. These dependences have been normalized to the maximum intensity to better distinguish the concentration,
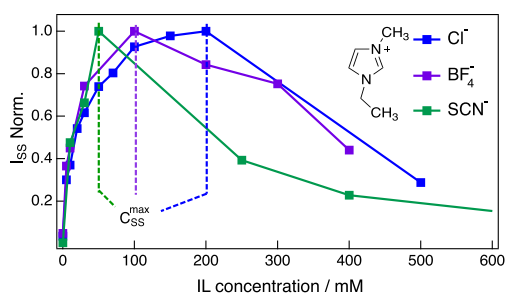
Figure 5. Effect of the anion on the change of the steady-state SSHG signal intensity upon addition of $EMIM^+$-containing ILs. The concentrations c_{SS}^{max} above which the intensity decreases are indicated with dashed lines. Non-normalized dependences are depicted in Figure S5.

c_{SS}^{max}, above which the SSHG intensity goes down again. This concentration decreases in the order $Cl^- > BF_4^- > SCN^-$. The non-normalized data are presented in Figure S5. Comparison of absolute signal intensities with different ILs has to be done with some caution, because these experiments were not always carried with exactly the same conditions, due to daily variations of probe pulse characteristics. Despite this, the results suggest that the maximum SSHG intensity reached upon adding a given IL, I_{SS}^{max}, is the largest with EMIMSCN, and the smallest with EMIMCl. Therefore, the effect of the anion on I_{SS}^{max} increases in the order $Cl^- < BF_4^- < SCN^-$. The anion dependence on I_{SS}^{max} is opposite to that on c_{SS}^{max}.

This trend observed with the stationary SSHG intensity is also visible with the TR-SSHG profiles. As illustrated in Figure 6, the slowing down of the dynamics increases in the order $Cl^- < BF_4^- < SCN^-$. Similar to the plot shown in the inset of Figure 4, the relative amplitudes A_{fast} and A_{slow} plateau above c_{TR}^{max} (Figure S6). The anion dependence of this concentration
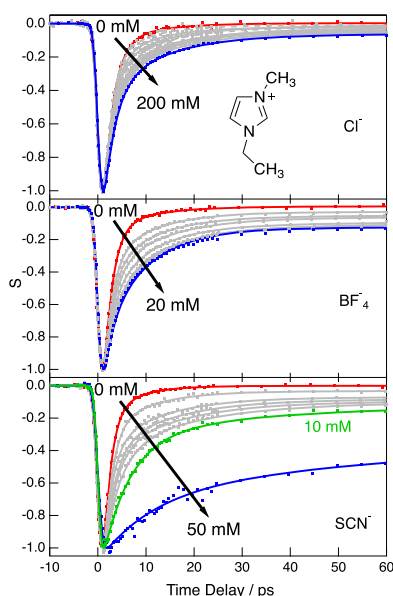
Figure 6. Normalized TR-SSHG profiles with different concentrations of $EMIM^+$-containing ILs.

as well as of the maximum value of the slow amplitude, A_{slow}^{max}, are depicted in Figure 7.
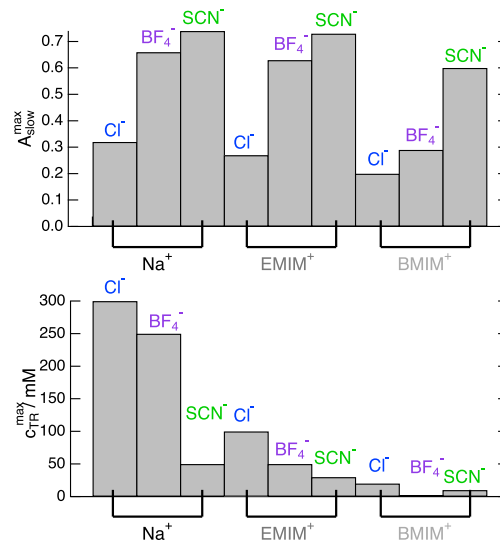
Figure 7. Effect of the anion on the TR-SSHG profiles. A_{slow}^{max}: maximum amplitude of the slow TR-SSHG component; c_{TR}^{max}: concentration above which the TR-SSHG dynamics remains almost unchanged. Error on A_{slow}^{max}: ±0.05; error on c_{TR}^{max}: ±15%.

With EMIMCl, A_{slow} remains below 0.3, whereas it goes up to 0.6 with EMIMBF$_4$ and above 0.7 with EMIMSCN. Moreover, the plateau is reached at $c_{TR}^{max} \sim$ 100 mM EMIMCl, whereas only $c_{TR}^{max} \sim$ 30 mM EMIMSCN is required.

Interestingly, c_{TR}^{max} and c_{SS}^{max} are of similar magnitudes. Furthermore, both concentrations show qualitatively the same anion dependence. Similarly, A_{slow}^{max} and the maximum steady-state SSHG intensity, I_{SS}^{max}, exhibit also a similar dependence on the anion, which is opposite to that of c_{TR}^{max} and c_{SS}^{max}. This suggests that c_{TR}^{max} and A_{slow}^{max} deduced from the TR-SSHG data reflect the same phenomena as c_{SS}^{max} and I_{SS}^{max}, respectively. The advantage of using the TR-SSHG data is that, contrary to the steady-state SSHG results, these time profiles, $S(t)$, are not sensitive to experimental conditions (pulse irradiance, angle of incidence, etc.).

Figures 7, S7, and S8 reveal that A_{slow}^{max} and c_{SS}^{max} exhibit the same dependence on the anion with the $BMIM^+$- and Na^+-based ILs/salts. This order is the same as the Hofmeister series for the anion affinity for interfaces.[58,60]

The same order is observed with c_{TR}^{max} and c_{SS}^{max} upon addition of Na^+ salts. However, in the case of the $BMIM^+$ ILs, their order is different, with BF_4^- having a stronger effect than SCN^-. As discussed below, the amplitude of the anion effect with the $BMIM^+$ ILs is much smaller than that with the other cations.

Tuning of the Cation. We now consider how the nature of the cationic constituent, i.e., Na^+, $EMIM^+$, or $BMIM^+$, affects the steady-state SSHG and the TR-SSHG signals. Again, addition of all ILs/salts, irrespective of their constituents, resulted in an increase of the steady-state SSHG intensity followed by a decrease, with a small broadening of the SSHG spectrum but without significant change in the shape of the polarization profiles. Figure 8 shows the normalized changes of
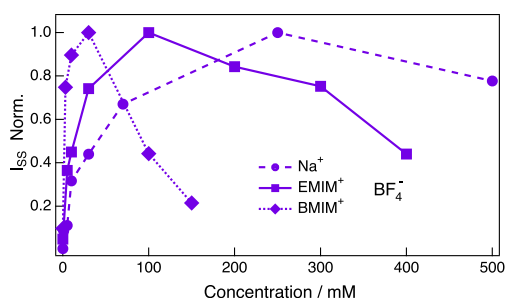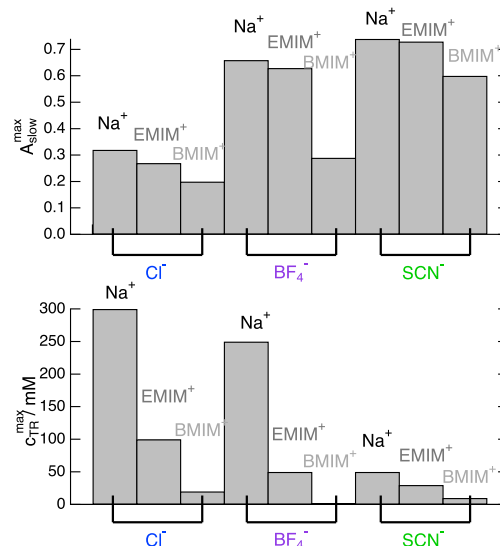
Figure 8. Effect of the cation on the change of the stationary SSHG signal intensity upon addition of BF_4^--containing ILs/salts. The non-normalized dependences are depicted in Figure S10.

the SSHG intensity at s/p polarization upon addition of BF_4^--containing ILs/salts, the non-normalized SSHG data being depicted in Figure S9. The concentration, c_{SS}^{max}, above which the SSHG intensity goes down depends significantly on the cation. For example, the maximum intensity is reached at 300 mM $NaBF_4$ and 30 mM $BMIMBF_4$. Thus, c_{SS}^{max} decreases in the order $Na^+ > EMIM^+ > BMIM^+$.

However, the largest maximum SSHG intensity, I_{SS}^{max}, is observed upon adding $NaBF_4$, whereas the smallest one is found with $BMIMBF_4$. Therefore, the effect of the cation on I_{SS}^{max} increases in the order $BMIM^+ < EMIM^+ < Na^+$. Similar cation dependence was measured with ILs/salts containing Cl^- and SCN^- (Figures S10 and S11).

This trend is opposite to that observed with the anions, where the largest I_{SS}^{max} was detected with the anion having the smallest c_{SS}^{max}.

The nature of the cation has also a significant effect on the TR-SSHG profiles as illustrated in Figures 9 and S12. The highest sensitivity to the addition of ILs was found with the $BMIM^+$ cation. Indeed, A_{slow} more than doubles upon addition of less than 0.1 mM $BMIMBF_4$, whereas about 10 and 50 times
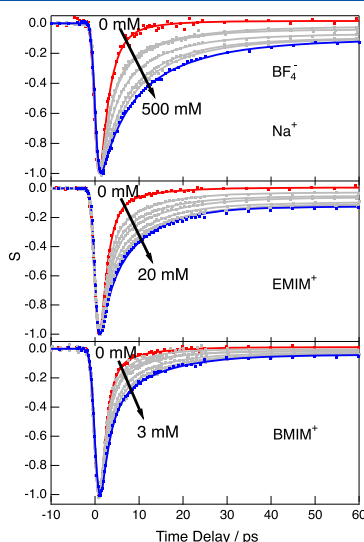
Figure 9. Normalized TR-SSHG profiles with different concentrations of BF_4^--containing ILs/salts.

as much $EMIMBF_4$ and $NaBF_4$ are needed. However, A_{slow} levels off at very small $BMIMBF_4$ concentrations, and does not go beyond 0.3. By contrast, A_{slow} exceeds 0.6 with the other two cations (Figures 10 and S12).

Figure 10. Effect of the cation on the TR-SSHG profiles. A_{slow}^{max}: maximum amplitude of the slow TR-SSHG component; c_{TR}^{max}: concentration above which the TR-SSHG dynamics remains almost unchanged. Error on A_{slow}^{max}: ±0.05; error on c_{TR}^{max}: ±15%.

The concentration at which A_{slow} plateaus, c_{TR}^{max}, decreases in the order $Na^+ > EMIM^+ > BMIM^+$, similarly to c_{SS}^{max} (Figure 10). This order corresponds to the increasing affinity of the cation toward the interface. This behavior is opposite to that of the anions, where A_{slow}^{max} increases with increasing interfacial affinity (Figure 7).

Figure 10 indicates that the cation effect observed with the ILs/salts containing Cl^- and SCN^- is qualitatively the same as that found with the BF_4^- ILs/salts. However, the amplitude of this dependence is markedly weaker with SCN^- than with the other two anions.

■ DISCUSSION

The above results reveal that the addition of any of the nine ILs/salts results in an increase of the SSHG signal due to MG and in a slowing down of the TR-SSHG dynamics. The increase of the stationary SSHG intensity can be attributed to an increase of the number of MG molecules contributing to the signal. It can have two main origins: (i) a higher interfacial concentration of dyes and (ii) a thicker region of the aqueous subphase with an orientational anisotropy of the dye molecules.

The latter effect could be due to the presence of a static electric field associated with the charged constituents of the ILs at the interface.[71,72] This is an electric-field induced second harmonic process that depends on the third-order nonlinear electric susceptibility.[73,74] Although this phenomenon could explain the increase of the steady-state SSHG intensity upon addition of IL/salt, its contribution to the effects observed here with MG should only be minor for several reasons. First, this

process should not affect the concentration of MG and, thus, should not favor the formation of aggregates, as observed in the TR-SSHG profiles. Second, its strength should scale with the IL concentration and, thus, the signal intensity should not decrease above a certain concentration as found here. Third, its strength should increase with the affinity of the ions for the interface, and consequently this process cannot explain the decrease of the SSHG intensity observed when going from Na$^+$ to EMIM$^+$ and to BMIM$^+$.

By contrast, an increase of the MG concentration near the interface upon addition of IL is consistent with all of the effects observed in both steady-state SSHG and the TR-SSHG measurements.

This increase of MG concentration upon addition of ILs/salts can be explained by the cationic nature of this dye and its attraction toward the interfacial region because of the presence of ions of opposite charge at the interface. For example, the slowing down of the TR-SSHG dynamics, observed by going from Cl$^-$ to BF$_4^-$ and SCN$^-$, can be explained by the increasing affinity of these anions toward the interface. Therefore, addition of SCN$^-$-containing ILs results in a relatively high interfacial concentration of anions that enhances the adsorption of the cationic dyes through Coulombic attraction. This in turn favors aggregation, leading to a slowing down of the TR-SSHG dynamics.

Figure 7 indicates that the amplitude of the anion effect depends itself on the cation. The strongest slowing down of the TR-SSHG dynamics is always observed with SCN$^-$ but becomes less marked by going from NaSCN to EMIMSCN and to BMIMSCN. The same trend is observed with the other anions. This decrease can be explained by the different affinities of the cations toward the interface. Na$^+$ stands approximately in the middle of the Hofmeister series of cations.[58,75] Because of their large size and organic nature, both EMIM$^+$ and BMIM$^+$ can be expected to be more hydrophobic than Na$^+$ and hence adsorb more at the interface. Finally, the butyl chain of BMIM$^+$ makes it more amphiphilic than EMIM$^+$. The presence of IL cations at the interface has an opposite electrostatic effect on MG than that of anions and should repel these dyes toward the bulk. This effect was reported upon addition of cetyltrimethylammonium bromide.[47] In this case, the presence of the cationic surfactant at the interface resulted in a decrease of the concentration of MG, hence to a smaller SSHG signal.

Addition of any IL always leads to an increase of the MG concentration near the interface. If the interactions between MG and the IL ions were purely electrostatic, this would mean that the interface is always negatively charged and, consequently, that the three anions used here have a higher affinity toward the interface than the three cations. It is however highly doubtful that the affinity toward the interface of an amphiphilic molecule like BMIM$^+$ is smaller than that of Cl$^-$, which sits in the middle of the Hofmeister series of anions.[60] Therefore, addition of BMIMCl should lead to a preferential adsorption of BMIM$^+$ and, thus, to a globally positive interface. The fact that the interfacial concentration of MG increases even under this condition suggests that other interactions than the Coulombic repulsion are operative. Given the structure of EMIM$^+$ and BMIM$^+$, dispersive interactions between these cations and MG as well as hydrophobic effects could counterbalance Coulomb repulsion and still enhance the adsorption of MG. The same combination of effects is responsible for the aggregation of MG.

In summary, the dependence of the slowing down of the TR-SSHG dynamics of both anions and cations is consistent with their affinity toward the interfaces. However, these dependences do not give any information about the relative affinities of anions and cations.

Some insight into this relative affinity can be obtained from the anion and cation dependences of the concentration c_{TR}^{max}, above which the TR-SSHG profiles remain almost unchanged. This concentration coincides also with the concentration above which the stationary SSHG signal decreases. The fact that the stationary signal decreases, whereas the SSHG profile stays constant, could be explained by a competition for adsorption between the MG dyes and the IL ions.[76−78] If the IL ions have a higher interfacial affinity than MG, the adsorption of the dye is hampered above a certain concentration, that should coincide with c_{TR}^{max}, at which most of the adsorption sites are occupied by the IL ions. This should lead to a decrease of the stationary SSHG intensity as MG is somehow repelled from the interface. The fact that the TR-SSHG dynamics do not change significantly suggests that the concentration of MG close to the interface remains high. However, the MG dyes being further from the interface, their orientational anisotropy is lower and, thus, the SSHG intensity smaller. A similar effect was reported upon addition of sodium dodecyl sulfate (SDS) surfactants.[47] There, the decrease of the stationary intensity was found to occur above 3 mM SDS only, in agreement with the strong affinity of this surfactant toward the dodecane/water interface. Higher concentrations are required with the ILs and salts. However, Figure 10 reveals that with both Cl$^-$- and BF$_4^-$-containing ILs/salts, c_{TR}^{max} decreases dramatically when going from Na$^+$ to the two imidazolium cations. This strongly suggests that the affinity of these two IL cations for the interface is larger than that of Cl$^-$ and BF$_4^-$.

With SCN$^-$-containing ILs/salts, this decrease of c_{TR}^{max} is much less pronounced as this concentration remains small with all three cations. In this case, the propensity of SCN$^-$ and the two imidazolium cations to adsorb at the interface does not differ enough to allow for any conclusion. Indeed, Figure 7 shows that the effect of anion on c_{TR}^{max} is the most pronounced for the cation with the lowest interfacial affinity, here Na$^+$. Similarly, the effect of cation is the strongest with the anion having the lowest interfacial affinity, here Cl$^-$ (Figure 10).

CONCLUSIONS

Using electronic SSHG, we could compare the interfacial behavior of nine different ILs/salts using a single probe molecule, MG. This approach is much simpler than the direct probing of the constituents, which requires knowledge of their nonlinear properties.[79,80]

This investigation revealed that the addition of ILs to the aqueous subphase has a similar effect on the water/dodecane interface than that of conventional salts. In other words, the aqueous subphase with the IL behaves like an electrolyte. The main difference with conventional salts is the nature of the cations, which are made bulky in ILs to ensure a melting point below room temperature. Because of this, these cations are significantly less hydrophilic than atomic cations and have thus a relatively high propensity to adsorb at the interface. By comparison with previous studies,[45,47] the interfacial affinity of these IL cations is between those of atomic cations and cationic surfactants like cetyltrimethylammonium. Our results also indicate that the interfacial concentration of these cations

depends on the counterion and can be enhanced when using an anion such as SCN^-, which has itself a high propensity to adsorb at the interface. Both constituents of the IL have thus a synergistic effect. These different interfacial affinities of the constituents of ILs could be advantageously used to fine-tune the properties of liquid interfaces.

■ ASSOCIATED CONTENT

ⓢ Supporting Information

The Supporting Information is available free of charge at https://pubs.acs.org/doi/10.1021/acs.jpcb.0c07803.

> Viscosity of the ionic liquids, details on the analysis of the TR-SSHG profiles, and additional data (PDF)

■ AUTHOR INFORMATION

Corresponding Author

Eric Vauthey − *Department of Physical Chemistry, University of Geneva, 1211 Geneva 4, Switzerland;* ⓞ orcid.org/0000-0002-9580-9683; Email: eric.vauthey@unige.ch

Authors

Jihad Sissaoui − *Department of Physical Chemistry, University of Geneva, 1211 Geneva 4, Switzerland*

Darya S. Budkina − *Department of Physical Chemistry, University of Geneva, 1211 Geneva 4, Switzerland*

Complete contact information is available at:
https://pubs.acs.org/10.1021/acs.jpcb.0c07803

Author Contributions

[†]J.S. and D.S.B. contributed equally to this work.

Notes

The authors declare no competing financial interest.
The data can be downloaded from https://doi.org/10.5281/zenodo.3999111.

■ ACKNOWLEDGMENTS

■ REFERENCES

(1) Welton, T. Room-Temperature Ionic Liquids. Solvents for Synthesis and Catalysis. *Chem. Rev.* **1999**, *99*, 2071−2084.

(2) Wilkes, J. S. A Short History of Ionic Liquids-from Molten Salts to Neoteric Solvents. *Green Chem.* **2002**, *4*, 73−80.

(3) Welton, T. Ionic Liquids: a Brief History. *Biophys. Rev.* **2018**, *10*, 691−706.

(4) Quijano, G.; Couvert, A.; Amrane, A.; Darracq, G.; Couriol, C.; Le Cloirec, P.; Paquin, L.; Carri, D. Potential of ionic liquids for VOC absorption and biodegradation in multiphase systems. *Chem. Eng. Sci.* **2011**, *66*, 2707−2712.

(5) Guihéneuf, S.; Castillo, A. S. R.; Paquin, L.; Biard, P.-F.; Couvert, A.; Amrane, A. *Production of Biofuels and Chemicals with Ionic Liquids*; Springer Netherlands: Dordrecht, 2014; Vol. *1*, pp 305−337.

(6) Nguyen, T.-V.-N.; Rodriguez Castillo, A. S.; Guihéneuf, S.; Biard, P.-F.; Paquin, L.; Amrane, A.; Couvert, A. Toluene Degradation in a Two-Phase Partitioning Bioreactor Involving a Hydrophobic Ionic Liquid as a Non-Aqueous Phase Liquid. *Int. Biodeterior. Biodegrad.* **2017**, *117*, 31−38.

(7) Rodriguez Castillo, A.-S.; Biard, P.-F.; Guihéneuf, S.; Paquin, L.; Amrane, A.; Couvert, A. Assessment of VOC Absorption in Hydrophobic Ionic Liquids: Measurement of Partition and Diffusion Coefficients and Simulation of a Packed Column. *Chem. Eng. J.* **2019**, *360*, 1416−1426.

(8) Rogers, R. D.; Seddon, K. R. Ionic Liquids−Solvents of the Future? *Science* **2003**, *302*, 792−793.

(9) Chiappe, C.; Pieraccini, D. Ionic Liquids: Solvent Properties and Organic Reactivity. *J. Phys. Org. Chem.* **2005**, *18*, 275−297.

(10) Weingärtner, H. Understanding Ionic Liquids at the Molecular Level: Facts, Problems, and Controversies. *Angew. Chem., Int. Ed.* **2008**, *47*, 654−670.

(11) Quijano, G.; Couvert, A.; Amrane, A.; Darracq, G.; Couriol, C.; Le Cloirec, P.; Paquin, L.; Carri, D. Absorption and Biodegradation of Hydrophobic Volatile Organic Compounds in Ionic Liquids. *Water, Air, Soil Pollut.* **2013**, *224*, No. 1528.

(12) Guihéneuf, S.; Castillo, A. S. R.; Paquin, L.; Biard, P.-F.; Couvert, A.; Amrane, A. In *Production of Biofuels and Chemicals with Ionic Liquids*; Fang, Z.; Smith, J.; Richard, L.; Qi, X., Eds.; Biofuels and Biorefineries; Springer Netherlands: Dordrecht, 2014; pp 305−337.

(13) Rodriguez Castillo, A. S. R.; Guihéneuf, S.; Biard, P.-F.; Paquin, L.; Amrane, A.; Couvert, A. Physicochemical Properties of some Hydrophobic Room-Temperature Ionic Liquids Applied to Volatile Organic Compounds Biodegradation Processes. *J. Chem. Technol. Biotechnol.* **2018**, *93*, 215−223.

(14) Watanabe, M.; Thomas, M. L.; Zhang, S.; Ueno, K.; Yasuda, T.; Dokko, K. Application of Ionic Liquids to Energy Storage and Conversion Materials and Devices. *Chem. Rev.* **2017**, *117*, 7190−7239.

(15) Kar, M.; Tutusaus, O.; MacFarlane, D. R.; Mohtadi, R. Novel and Versatile Room Temperature Ionic Liquids for Energy Storage. *Energy Environ. Sci.* **2019**, *12*, 566−571.

(16) Karuppasamy, K.; Vikraman, D.; Hwang, I.-T.; Kim, H.-J.; Nichelson, A.; Bose, R.; Kim, H.-S. Nonaqueous Liquid Electrolytes Based on Novel 1-Ethyl-3-methylimidazolium bis (nonafluorobutane-1-sulfonyl imidate) Ionic Liquid for Energy Storage Devices. *J. Mater. Res. Technol.* **2020**, *9*, 1251−1260.

(17) Handy, S. T. Room temperature ionic liquids: Different classes and physical properties. *Curr. Org. Chem.* **2005**, *9*, 959−988.

(18) Hapiot, P.; Lagrost, C. Electrochemical Reactivity in Room-Temperature Ionic Liquids. *Chem. Rev.* **2008**, *108*, 2238−2264.

(19) Castner, E. W.; Margulis, C. J.; Maroncelli, M.; Wishart, J. F. Ionic Liquids: Structure and Photochemical Reactions. *Annu. Rev. Phys. Chem.* **2011**, *62*, 85−105.

(20) Fayer, M. D. Dynamics and structure of room temperature ionic liquids. *Chem. Phys. Lett.* **2014**, *616−617*, 259−274.

(21) Nagasawa, Y.; Miyasaka, H. Ultrafast solvation dynamics and charge transfer reactions in room temperature ionic liquids. *Phys. Chem. Chem. Phys.* **2014**, *16*, 13008−13026.

(22) Araque, J. C.; Hettige, J. J.; Margulis, C. J. Modern Room Temperature Ionic Liquids, a Simple Guide to Understanding Their Structure and How It May Relate to Dynamics. *J. Phys. Chem. B* **2015**, *119*, 12727−12740.

(23) Benedetto, A. Room-temperature ionic liquids meet bio-membranes: the state-of-the-art. *Biophys. Rev.* **2017**, *9*, 309−320.

(24) Wang, Y.-L.; Li, B.; Sarman, S.; Mocci, F.; Lu, Z.-Y.; Yuan, J.; Laaksonen, A.; Fayer, M. D. Microstructural and Dynamical Heterogeneities in Ionic Liquids. *Chem. Rev.* **2020**, *120*, 5798−5877.

(25) Freire, M. G.; Carvalho, P. J.; Fernandes, A. M.; Marrucho, I. M.; Queimada, A. J.; Coutinho, J. A. P. Surface Tensions of Imidazolium Based Ionic Liquids: Anion, Cation, Temperature and Water Effect. *J. Colloid Interface Sci.* **2007**, *314*, 621−630.

(26) Tariq, M.; Freire, M. G.; Saramago, B.; Coutinho, J. A. P.; Canongia Lopes, J. N.; Rebelo, L. P. N. Surface Tension of Ionic Liquids and Ionic Liquid Solutions. *Chem. Soc. Rev.* **2012**, *41*, 829−868.

(27) Rodenbücher, C.; Wippermann, K.; Korte, C. Atomic Force Spectroscopy on Ionic Liquids. *Appl. Sci.* **2019**, *9*, No. 2207.

(28) Qiao, R. Water at ionic liquids-solid interfaces. *Curr. Opin. Electrochem.* **2019**, *13*, 11−17.

(29) Shen, Y. R. Surface Properties Probed by Second-Harmonic and Sum-Frequency Generation. *Nature* **1989**, *337*, 519−525.

(30) Richmond, G. L. Molecular Bonding and Interactions at Aqueous Surfaces as Probed by Vibrational Sum Frequency Spectroscopy. *Chem. Rev.* **2002**, *102*, 2693−2724.

(31) Eisenthal, K. B. Liquid Interfaces Probed by Second-Harmonic and Sum-Frequency Spectroscopy. *Chem. Rev.* **1996**, *96*, 1343−1360.

(32) Baldelli, S. Influence of Water on the Orientation of Cations at the Surface of a Room-Temperature Ionic Liquid: A Sum Frequency Generation Vibrational Spectroscopic Study. *J. Phys. Chem. B* **2003**, *107*, 6148−6152.

(33) Rivera-Rubero, S.; Baldelli, S. Influence of Water on the Surface of Hydrophilic and Hydrophobic Room-Temperature Ionic Liquids. *J. Am. Chem. Soc.* **2004**, *126*, 11788−11789.

(34) Fitchett, B. D.; Conboy, J. C. Structure of the Room-Temperature Ionic Liquid/SiO2 Interface Studied by Sum-Frequency Vibrational Spectroscopy. *J. Phys. Chem. B* **2004**, *108*, 20255−20262.

(35) Sung, J.; Jeon, Y.; Kim, D.; Iwahashi, T.; Seki, K.; Iimori, T.; Ouchi, Y. Gibbs Monolayer of Ionic Liquid+H$_2$O Mixtures Studied by Surface Tension Measurement and Sum-Frequency Generation Spectroscopy. *Colloids Surf., A* **2006**, *284−285*, 84−88.

(36) Rivera-Rubero, S.; Baldelli, S. Surface Characterization of 1-Butyl-3-methylimidazolium Br⁻, I⁻, PF$_6$⁻, BF$_4$⁻, (CF$_3$SO$_2$)$_2$N⁻, SCN⁻, CH$_3$SO$_3$⁻, CH$_3$SO$_4$⁻, and (CN)$_2$N- Ionic Liquids by Sum Frequency Generation. *J. Phys. Chem. B* **2006**, *110*, 4756−4765.

(37) Rollins, J. B.; Fitchett, B. D.; Conboy, J. C. Structure and Orientation of the Imidazolium Cation at the Room-Temperature Ionic Liquid/SiO$_2$ Interface Measured by Sum-Frequency Vibrational Spectroscopy. *J. Phys. Chem. B* **2007**, *111*, 4990−4999.

(38) Baldelli, S.; Bao, J.; Wu, W.; Pei, S.-s. Sum Frequency Generation Study on the Orientation of Room-Temperature Ionic Liquid at the Graphene−Ionic Liquid Interface. *Chem. Phys. Lett.* **2011**, *516*, 171−173.

(39) Martinez, I. S.; Santos, C.; Baldelli, S. Structural Study at the Gas-Liquid Interface of 1-Alkyl-3-Methylimidazolium Alkylsulfates Using Surface Potential Measurements. *ChemPhysChem* **2012**, *13*, 1818−1824.

(40) Baldelli, S. Interfacial Structure of Room-Temperature Ionic Liquids at the Solid−Liquid Interface as Probed by Sum Frequency Generation Spectroscopy. *J. Phys. Chem. Lett.* **2013**, *4*, 244−252.

(41) Peñalber-Johnstone, C.; Gabriela, A.; Plechkova, N. V.; Bahrami, M.; Ghaed-Sharaf, T.; Ghatee, M. H.; Seddon, K. R.; Baldelli, S. Sum Frequency Generation Spectroscopy of Tetraalkyl-phosphonium Ionic Liquids at the Air-Liquid Interface. *J. Chem. Phys.* **2018**, *148*, No. 193841.

(42) Nishi, N.; Ishimatsu, R.; Yamamoto, M.; Kakiuchi, T. Orientation of 1-Dodecyl-4-phenylpyridinium Ions Constituting an Ionic Liquid at the Ionic Liquid|Water Interface Studied by Second Harmonic Generation. *J. Phys. Chem. C* **2007**, *111*, 12461−12466.

(43) Costa, R.; Pereira, C. M.; Silva, A. F.; Brevet, P.-F.; Benichou, E. Ordering and Nonideality of AirIonic Liquid Interfaces in Surface Second Harmonic Generation. *J. Phys. Chem. B* **2020**, *124*, 3954−3961.

(44) Punzi, A.; Martin-Gassin, G.; Grilj, J.; Vauthey, E. Effect of Salt on the Excited-State Dynamics of Malachite Green in Bulk Aqueous Solutions and at Air/Water Interfaces: a Femtosecond Transient Absorption and Surface Second Harmonic Generation Study. *J. Phys. Chem. C* **2009**, *113*, 11822−11829.

(45) Fedoseeva, M.; Fita, P.; Punzi, A.; Vauthey, E. Salt Effect on the Formation of Dye Aggregates at Liquid/Liquid Interfaces Studied by Time-Resolved Surface Second Harmonic Generation. *J. Phys. Chem. C* **2010**, *114*, 13774−13781.

(46) Fedoseeva, M.; Richert, S.; Vauthey, E. Excited-State Dynamics of Organic Dyes at Liquid-Liquid Interfaces. *Langmuir* **2012**, *28*, 11291−11301.

(47) Fedoseeva, M.; Fita, P.; Vauthey, E. Excited-State Dynamics of Charged Dyes at Alkane/Water Interfaces in the Presence of Salts and Ionic Surfactants. *Langmuir* **2013**, *29*, 14865−14872.

(48) Fedoseeva, M.; Letrun, R.; Vauthey, E. Excited-State Dynamics of Rhodamine 6G in Aqueous Solution and at the Dodecane/Water Interface. *J. Phys. Chem. B* **2014**, *118*, 5184−5193.

(49) Meech, S. R.; Yoshihara, K. Picosecond Dynamics at the Solid−Liquid Interface: a Total Internal Reflection Time-Resolved Surface Second-Harmonic Generation Study. *Chem. Phys. Lett.* **1990**, *174*, 423−427.

(50) Wang, H.; Yan, E. C. Y.; Borguet, E.; Eisenthal, K. B. Second Harmonic Generation from the Surface of Centrosymmetric Pparticles in Bulk Solution. *Chem. Phys. Lett.* **1996**, *259*, 15−20.

(51) Liu, Y.; Yan, E. C. Y.; Eisenthal, K. B. Effects of Bilayer Surface Charge Density on Molecular Adsorption and Transport across Liposome Bilayers. *Biophys. J.* **2001**, *80*, 1004−1012.

(52) Jen, S.-H.; Gonella, G.; Dai, H.-L. The Effect of Particle Size in Second Harmonic Generation from the Surface of Spherical Colloidal Particles. I: Experimental Observations. *J. Phys. Chem. A* **2009**, *113*, 4758−4762.

(53) Song, J.; Kim, M. W. Second Harmonic Generation Study of Malachite Green Adsorption at the Interface between Air and an Electrolyte Solution: Observing the Effect of Excess Electrical Charge Density at the Interface. *J. Phys. Chem. B* **2010**, *114*, 3236−3241.

(54) Ippen, E. P.; Shank, C. V.; Bergman, A. Picosecond Recovery Dynamics of Malachite Green. *Chem. Phys. Lett.* **1976**, *38*, 611−614.

(55) Shi, X.; Borguet, E.; Tarnovsky, A. N.; Eisenthal, K. B. Ultrafast Dynamics and Structure at Aqueous Interfaces by Second Harmonic Generation. *Chem. Phys.* **1996**, *205*, 167−178.

(56) Fita, P.; Punzi, A.; Vauthey, E. Local Viscosity of Binary Water +Glycerol Mixtures at Liquid/Liquid Interfaces Probed by Time-Resolved Surface Second Harmonic Generation. *J. Phys. Chem. C* **2009**, *113*, 20705−20712.

(57) Sen, P.; Yamaguchi, S.; Tahara, T. Ultrafast Dynamics of Malachite Green at the Air-Water Interface Studied by Femtosecond Time-Resolved Electronic Sum Frequency Generation (TR-ESFG): an Indicator for Local Viscosity. *Faraday Discuss.* **2010**, *145*, 411−428.

(58) Hofmeister, F. Zur Lehre von der Wirkung der Salze. *Arch. Exp. Pathol. Pharmakol.* **1888**, *24*, 247−260.

(59) Kunz, W.; Lo Nostro, P.; Ninham, B. W. The Present State of Affairs with Hofmeister Effects. *Curr. Opin. Colloid Interface Sci.* **2004**, *9*, 1−18.

(60) Zhang, Y.; Cremer, P. S. Interactions between Macromolecules and Ions: the Hofmeister Series. *Curr. Opin. Chem. Biol.* **2006**, *10*, 658−663.

(61) Pegram, L. M.; Record, M. T. Thermodynamic Origin of Hofmeister Ion Effects. *J. Phys. Chem. B* **2008**, *112*, 9428−9436.

(62) Lo Nostro, P.; Ninham, B. W. Hofmeister Phenomena: An Update on Ion Specificity in Biology. *Chem. Rev.* **2012**, *112*, 2286−2322.

(63) Richert, S.; Mosquera Vazquez, S.; Grzybowski, M.; Gryko, D. T.; Kyrychenko, A.; Vauthey, E. Excited-State Dynamics of an Environment-Sensitive Push-Pull Diketopyrrolopyrrole: Major Differences between the Bulk Solution Phase and the Dodecane/Water Interface. *J. Phys. Chem. B* **2014**, *118*, 9952−9963.

(64) Licari, G.; Brevet, P.-F.; Vauthey, E. Fluorescent DNA Probes at Liquid/Liquid Interfaces Studied by Surface Second Harmonic Generation. *Phys. Chem. Chem. Phys.* **2016**, *18*, 2981−2992.

(65) Heinz, T. F.; Chen, C. K.; Ricard, D.; Shen, Y. R. Spectroscopy of Molecular Monolayers by Resonant Second-Harmonic Generation. *Phys. Rev. Lett.* **1982**, *48*, 478−481.

(66) Dick, B. Irreducible Tensor Analysis of Sum- and Difference-Frequency Generation in Partially Oriented Samples. *Chem. Phys.* **1985**, *96*, 199−215.

(67) Brevet, P.-F. *Surface Second Harmonic Generation*; Presses polytechniques et universitaires romandes: Lausanne, 1997.

(68) Simpson, G. J.; Rowlen, K. L. An SHG Magic Angle: Dependence of Second Harmonic Generation Orientation Measurements on the Width of the Orientation Distribution. *J. Am. Chem. Soc.* **1999**, *121*, 2635−2636.

(69) Martin-Gassin, G.; Benichou, E.; Bachelier, G.; Russier-Antoine, I.; Jonin, C.; Brevet, P. F. Compression Induced Chirality in Dense Molecular Films at the Air/Water Interface Probed by

Second Harmonic Generation. *J. Phys. Chem. C* **2008**, *112*, 12958−12965.

(70) Law, G.; Watson, P. R. Surface Tension Measurements of N-Alkylimidazolium Ionic Liquids. *Langmuir* **2001**, *17*, 6138−6141.

(71) Zhao, X.; Ong, S.; Eisenthal, K. B. Polarization of Water Molecules at a Charged Interface. Second Harmonic Studies of Charged Monolayers at the Air/Water Interface. *Chem. Phys. Lett.* **1993**, *202*, 513−520.

(72) Eftekhari-Bafrooei, A.; Borguet, E. Effect of Electric Fields on the Ultrafast Vibrational Relaxation of Water at a Charged Solid-Liquid Interface as Probed by Vibrational Sum Frequency Generation. *J. Phys. Chem. Lett.* **2011**, *2*, 1353−1358.

(73) Finn, R. S.; Ward, J. F. Measurements of Hyperpolarizabilities for some Halogenated Methanes. *J. Chem. Phys.* **1974**, *60*, 454−458.

(74) Levine, B. F.; Bethea, C. G. Second and Third Order Hyperpolarizabilities of Organic Molecules. *J. Chem. Phys.* **1975**, *63*, 2666−2682.

(75) Flores, S. C.; Kherb, J.; Konelick, N.; Chen, X.; Cremer, P. S. The Effects of Hofmeister Cations at Negatively Charged Hydrophilic Surfaces. *J. Phys. Chem. C* **2012**, *116*, 5730−5734.

(76) Wang, H.; Troxler, T.; Yeh, A.-G.; Dai, H.-L. In Situ, Nonlinear Optical Probe of Surfactant Adsorption on the Surface of Microparticles in Colloids. *Langmuir* **2000**, *16*, 2475−2481.

(77) Sahu, K.; Eisenthal, K. B.; McNeill, V. F. Competitive Adsorption at the Air-Water Interface: A Second Harmonic Generation Study. *J. Phys. Chem. C* **2011**, *115*, 9701−9705.

(78) Licari, G.; Cwiklik, L.; Jungwirth, P.; Vauthey, E. Exploring Fluorescent Dyes at Biomimetic Interfaces with Second Harmonic Generation and Molecular Dynamics. *Langmuir* **2017**, *33*, 3373−3383.

(79) Petersen, P. B.; Saykally, R. J.; Mucha, M.; Jungwirth, P. Enhanced Concentration of Polarizable Anions at the Liquid Water Surface: SHG Spectroscopy and MD Simulations of Sodium Thiocyanate. *J. Phys. Chem. B* **2005**, *109*, 10915−10921.

(80) Petersen, P. B.; Saykally, R. J. On the Nature of Ions at the Liquid Water Surface. *Annu. Rev. Phys. Chem.* **2006**, *57*, 333−364.

SUPPORTING INFORMATION:

Probing Liquid Interfaces with Room-Temperature Ionic Liquids Using the Excited-State Dynamics of a Cationic Dye

Jihad Sissaoui,[†,‡] Darya S. Budkina,[†,‡] and Eric Vauthey[*,†]

†*Department of Physical Chemistry, University of Geneva, 30 Quai Ernest-Ansermet,*

Geneva, Switzerland

‡*Contributed equally to this work*

E-mail: eric.vauthey@unige.ch

Contents

List of Figures

S3

List of Tables

S4

45

S1 Viscosity of the ionic liquids

Table S1: Viscosity of the ILs at the 25 °C

	EMIM Cl⁻	EMIM BF₄⁻	EMIM SCN⁻	BMIM Cl⁻	BMIM BF₄⁻	BMIM SCN⁻
Viscosity / cP (25° C)	Melting point 70° C	33.8	24.7	Melting point 65° C	104	35.9

S2 Multiexponential analysis of the TR-SSHG data

The best-fit parameters obtained from multiexponential analysis of the TR-SSHG profiles, $S(t)$, upon addition of different amounts of IL/salt are listed in the following tables. τ_2 was fixed to $12\,\mathrm{ps}$ and $\tau_3 >> 300\,\mathrm{ps}$. $A_{\text{fast}} = A_1$ and $A_{\text{slow}} = A_2 + A_3 = 1 - A_{\text{fast}}$.

Table S2: EMIMBF₄

conc (mM)	0	1	2	3	6	10	15	20	50	100	250	600	1000
τ_1	1.9	2	2	2.1	2.3	2.6	2.8	2.6	3.3	3.6	2.3	2.1	2.7
A_1	94	90.8	77	73	66.9	60.6	57.8	55.5	36.9	38.5	37.7	44.5	69.3

Table S3: EMIMCl

conc (mM)	0	5	10	20	30	40	50	70	100	150	200	500	1000
τ_1	2.1	1.9	2.1	2.1	2.2	2.3	2.3	2.3	2.4	2.4	2.6	2.4	2.4
A_1	94.6	91.1	88	83.6	80.6	78.8	76.2	74.3	73.5	76.4	70.7	68.5	71.9

Table S4: EMIMSCN

conc (mM)	0	0.1	0.5	1	2	5	10	30	50	250	400	1000
τ_1	1.8	1.9	1.9	2.2	2.2	2.5	2.3	3	2.9	2.6	5	3.1
A_1	95	86.6	75.8	70	66.4	56.5	57.7	26.8	21.1	26.6	29.1	75.5

S5

Table S5: NaCl

conc (mM)	0	5	10	50	100	300	500
τ_1	2.0	2	2.1	2.2	2.6	2.5	2.3
A_1	92.6	87.7	83.6	76.5	73.9	67.6	67.2

Table S6: NaBF$_4$

conc (mM)	0	1	3	5	10	30	70	250	500
τ_1	2.5	2.3	2.5	2.4	3	3.6	4.1	3	3.3
A_1	98	81.9	73.8	73.5	60.8	47.7	41.6	27.4	34

Table S7: NaSCN

conc (mM)	0	0.1	0.5	1	2	5	10	50	250
τ_1	1.5	2	2.3	2.1	2.2	2.4	2.9	3.3	6.2
A_1	92.6	87.7	70.7	64	56.6	45.4	36.3	26	28.7

Table S8: BMIMCl

conc (mM)	0	1	3	5	10	20	50	100	250	500
τ_1	1.8	1.8	1.8	1.9	2.1	2.2	1.9	2.3	2	1.9
A_1	93.9	91.5	89.8	86.8	85.8	79.8	83.2	77.1	77.5	85.9

Table S9: BMIMBF$_4$

conc (mM)	0	0.05	0.1	0.2	0.5	1	2	3	6	20
τ_1	1.6	1.7	2	1.9	2.1	2.3	2.4	2.4	1.7	1.6
A_1	92.6	91.6	89.1	86.4	80.8	75.8	71.2	72.3	70.5	66.3

Table S10: BMIMSCN

conc (mM)	0	0.1	0.5	1	3	10	50	100
τ_1	1.9	1.8	2	1.7	2	2.1	1	3.7
A_1	94.1	76.7	68.8	71	52	41.6	13.4	41.2

S6

S3   Additional data

S3.1   EMIMBF$_4$
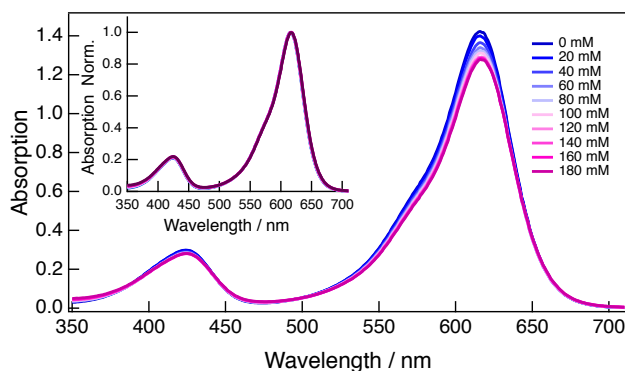
Figure S1: Steady-state electronic absorption spectra of MG with various amount of EMIMBF$_4$ in water. Inset: normalised spectra.
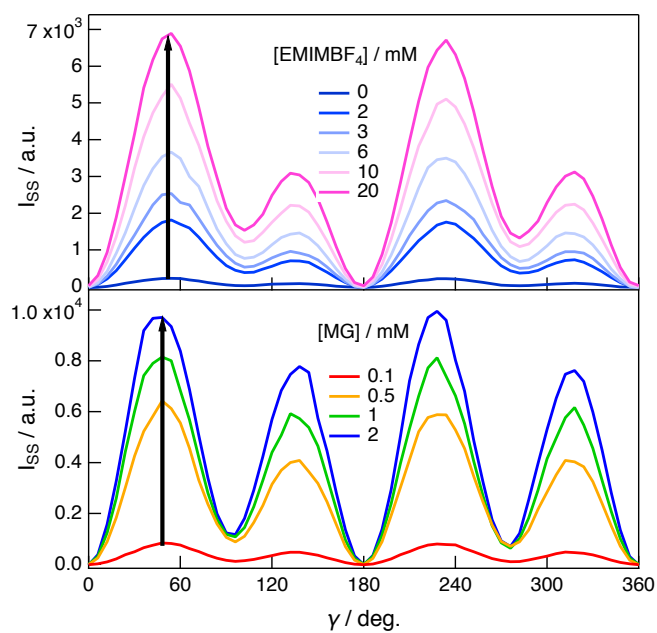
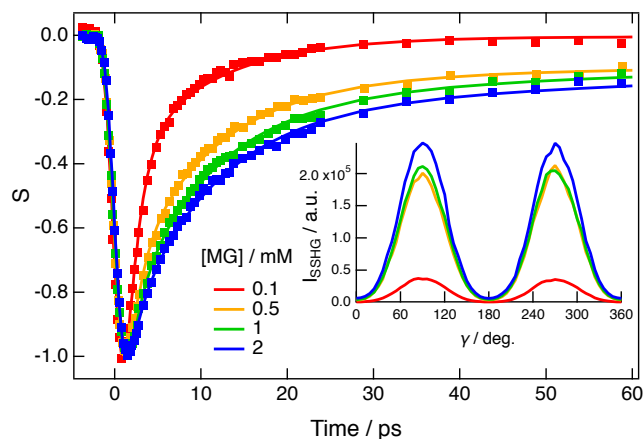Figure S2: γ/s polarisation profiles at different MG concentrations (bottom) and upon addition of various amounts EMIMBF$_4$ (top).

S7

48

Figure S3: Normalised TR-SSHG profiles, $S(t)$, at $400\,\mathrm{nm}$ measured upon $615\,\mathrm{nm}$ excitation of MG at the dodecane/water interface with different MG concentrations (symbols) and best biexponential fits. Inset: γ/p polarisation profiles at different MG concentrations.
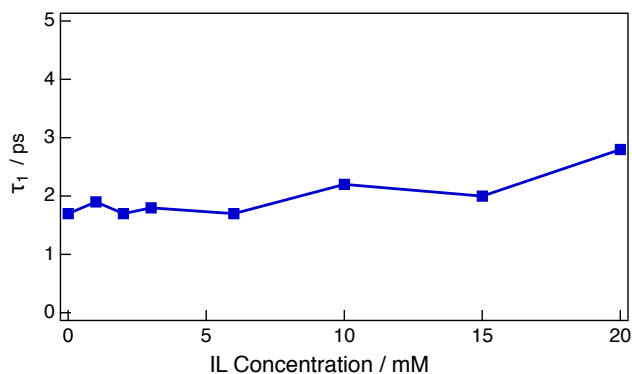
Figure S4: Shortest time constant, τ_1, obtained from the multiexponential analysis of the TR-SSHG profiles measured at different concentrations of EMIMBF$_4$.

S8

49

S3.2 Tuning of the anion
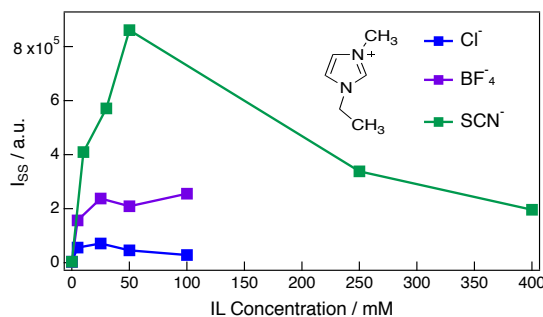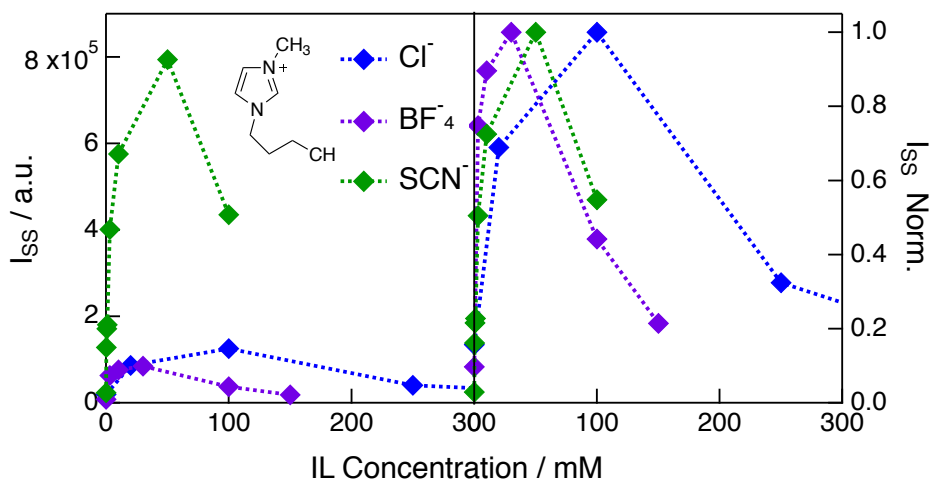

Figure S5: Effect of the anion on the change of the stationary SSHG signal intensity upon addition of $EMIM^+$-containing ILs. These dependences differ somewhat from the normalised dependences shown in the main text (Figure 5). The reason is that the data shown here have been recorded during the same day with the same experimental parameters. In Figure 5 (main text), the individual data sets contain more points but were not all recorded during the same day.
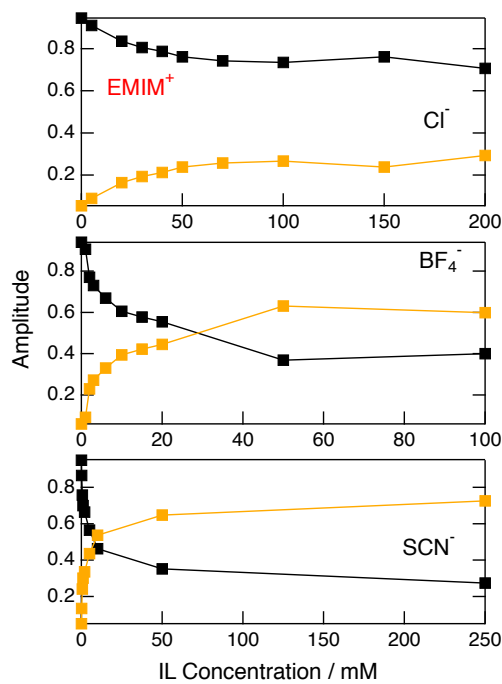
Figure S6: Effect of the anion on the amplitudes A_{fast} and A_{slow} obtained from the analysis of the TR-SSHG profiles in $EMIM^+$-containing ILs.

S9

50
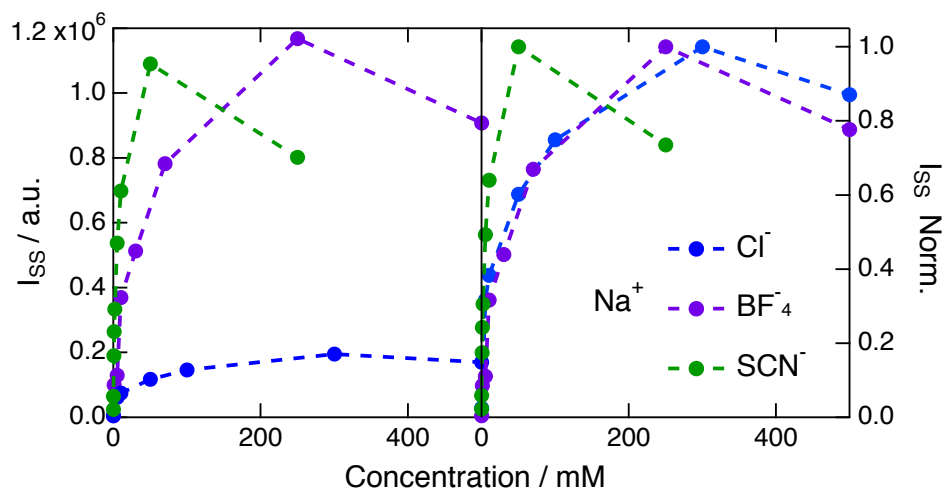
Figure S7: Left: effect of the anion on the change of the steady-state SSHG signal intensity upon addition of Na^+-containing salts. Right: same as left after intensity normalisation.

Figure S8: Left: effect of the anion on the change of the steady-state SSHG signal intensity upon addition of $BMIM^+$-containing ILs. Right: same as left after intensity normalisation.
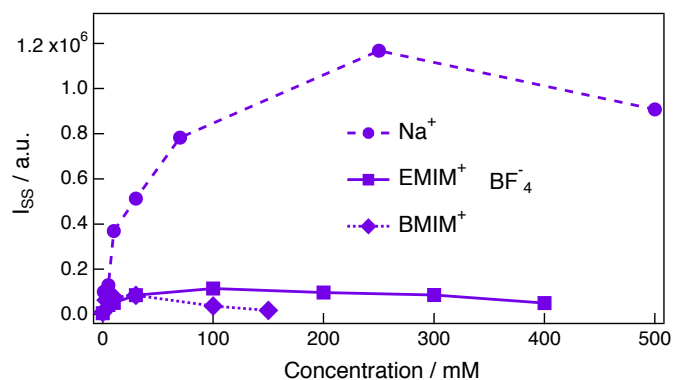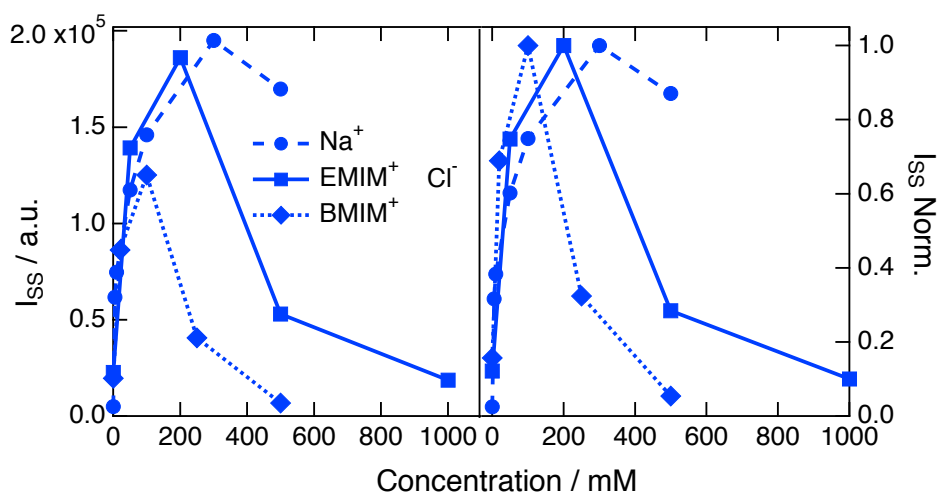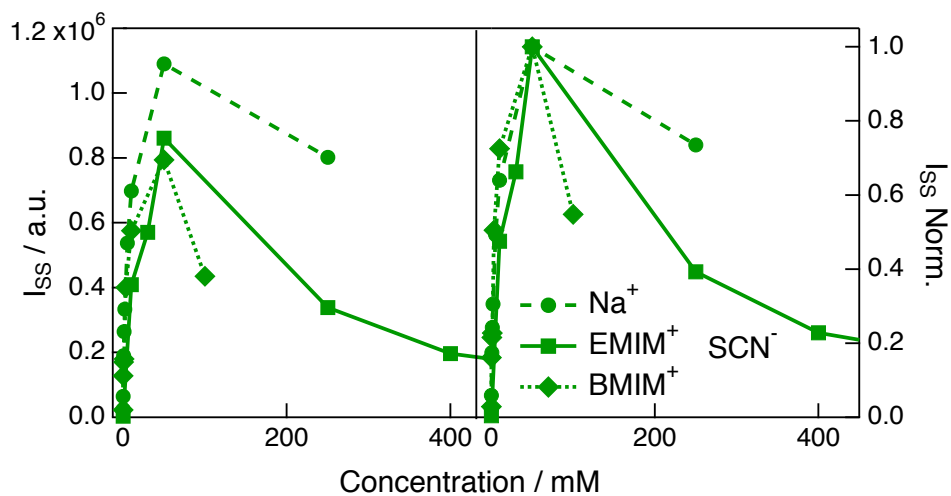
S10

51

S3.3   Tuning of the cation

Figure S9: Effect of the cation on the change of the steady-state SSHG signal intensity upon addition of BF_4^--containing ILs/salts.

Figure S10: Effect of the cation on the change of the steady-state SSHG signal intensity upon addition of Cl^--containing ILs/salts.

S11

Figure S11: Effect of the cation on the change of the stationary steady-state signal intensity upon addition of SCN^--containing ILs/salts.
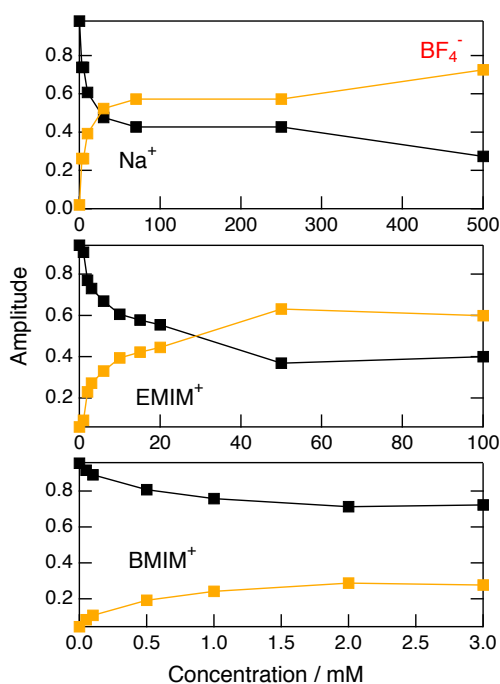

Figure S12: Effect of the cation on the amplitudes A_{fast} and A_{slow} obtained from the analysis of the TR-SSHG profiles in BF_4^--containing ILs.

S12

53

Chapter 4

Crystal Violet as an Alternative Probe to Malachite Green

4.1   Introduction

In the previous chapter, Chapter 3, our study centered around the interfacial behavior of room temperature ionic liquids at the water/dodecane interface. We investigated their influence on the excited state dynamics of an organic dye, Malachite Green (MG), using SSHG techniques. One problem we faced was the irregular shape of the MG polarization curves, which are not yet fully understood: Upon closer examination of the s curve, we observed that it had four peaks of alternating intensity and two minima that differed from zero. Consequently, this pattern cannot be described using the standard assumption of the dipolar electric approximation for an achiral interface, which predicts peaks of equal intensity and four minima equal to zero.

MG, one of the most popular dyes used in SHG studies, has been employed to probe the chemical physics of the interfacial region at air/liquid, solid/liquid, and liquid/liquid interfaces. [1–12]. The polarization-resolved curves found in the literature are mostly for air/liquid [9] or silica/liquid [6] interfaces. The reported polarization curves in these cases did not show any irregular shapes. Although studies of MG at water/alkane interfaces exist [4, 13], we could not find any polarization curves in the literature to compare with our results.

However, a study on 4-(4-(dihexadecylamino)styryl)-N-methylpyridinium iodide (DiA) films, formed at the air-water interface in a Langmuir trough with a high average surface density, reported polarization curves that were similar. Full data analysis required going beyond the electric dipole approximation and introducing magnetic contributions. At high surface coverage, the film revealed chirality arising from the formation of molecular aggregates. This chirality was demonstrated to arise from the coupling between the electric and magnetic fields [14]. However, applying this model to our data did not prove fruitful. The situation in our case is quite different, as we don't expect any chiral signatures at the interface; thus, the explanation must be sought elsewhere.

Following our observations with MG, we became interested in other probes that could potentially produce more straightforward polarization curves and allow us to further explore these interfacial behaviors. We turned to Crystal Violet (CV), another triphenylmethane dye. Despite the structural differences between CV, which carries three dimethylamino groups attached to its phenyl rings, and MG, which is characterized by two dimethylamino groups and one phenol group, we expect similar photophysical behaviors from both dyes. In this small chapter, we present some of the results obtained with CV at the interface. Surprisingly, CV did not display the same irregularities seen in the MG polarization curves, prompting further investigation into the factors causing these differences.
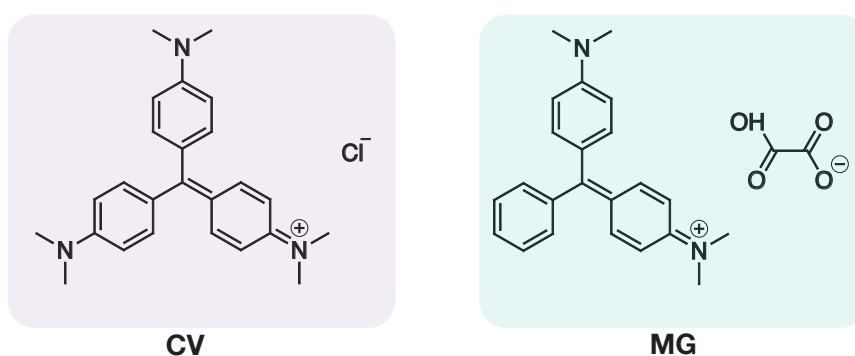

Figure 4.1: Structure of Crystal Violet (CV) and Malachite Green (MG)

4.2 Experimental Results

Figure 4.2 shows the normalized electronic absorption spectra of MG and CV in water. For MG, the band centered at 618 nm corresponds to the $S_1 \leftarrow S_0$ transition, whereas the band at 425 nm results from the $S_2 \leftarrow S_0$ transition. CV, on the other hand, shows an intense band at 590 nm with a shoulder on its blue side.
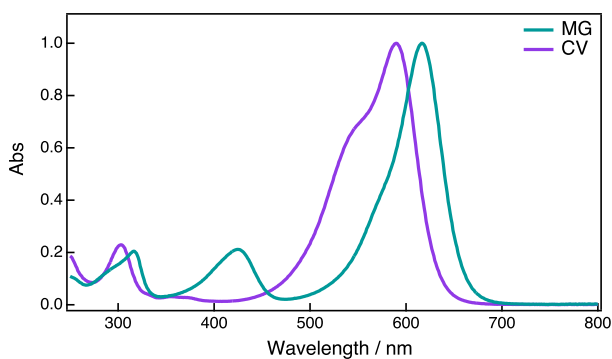

Figure 4.2: Normalised electronic absorption spectra of MG and CV in water.

Polarization curves obtained for MG at the dodecane/water interface are shown in Figure 4.3. The experiment was conducted at 840nm. We observe an irregular shape of the s polarization in the right figure. Consequently, the data obtained from these measurements could not be used to determine the orientational parameters.
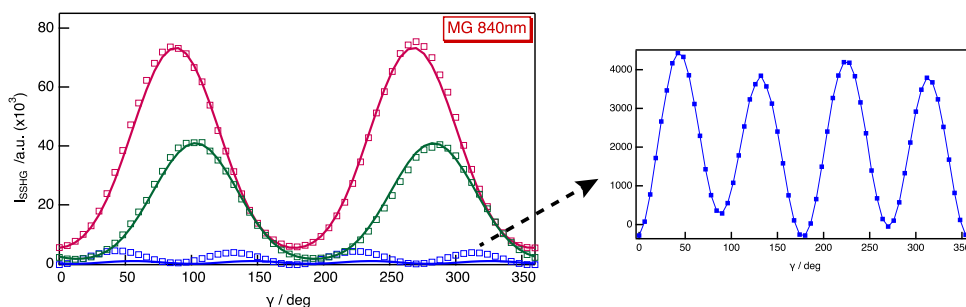
Figure 4.3: Polarization-resolved SH profiles recorded at p (red), s (blue), and 45 (green) geometries at 840nm with MG at a concentration of 10uM. The figure on the right is a zoom-in on the s component of the SSHG signal.

Similarly, the polarization curves shown in Figure 4.4 were measured for CV at the dodecane/water interface at 840 nm.
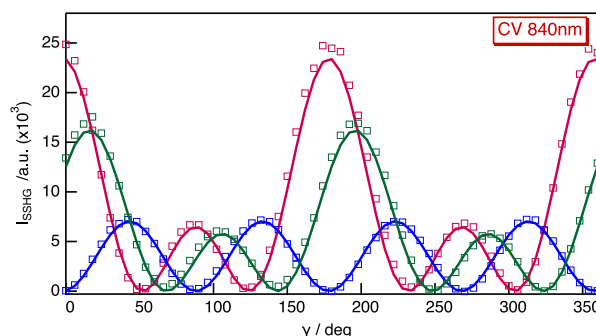

Figure 4.4: Polarization-resolved SH profiles recorded at p (red), s (blue), and 45 (green) geometries at 840 nm with CV at a concentration of 10uM.

The two dyes are expected to have different symmetries: CV, where the three phenyl rings have an amino group as a substituent, should have a D_{3h} symmetry, with the ground state being non-degenerate and the excited state two-fold degenerate. In contrast, MG, where one of the phenyl rings has no substituent, should have a C_{2v} symmetry.

To determine the molecular orientation, we extract information on the second-order susceptibility tensors from the measured polarization curves. In our study, these elements can be reduced to χ_{ZZZ}, χ_{ZXX}, and χ_{XXZ} as shown in Chapter 2.

Assuming that CV has a D_{3h} symmetry, with the ground state being non-degenerate and the excited state two-fold degenerate, this would lead to vanishing values of the hyperpolarizability tensor, and therefore no SHG signal would be expected. However, we do observe an SHG signal, suggesting the presence of molecules with broken symmetry at the interface and, therefore, with nonvanishing values of the hyperpolarizability tensor, for example. Nevertheless, if we assume three non-zero elements for the hyperpolarizability tensor: β_{ZZZ}, β_{ZXX}, and β_{XXZ}, our data analysis indicates that β_{XXZ} is two orders of magnitude larger than the other two elements.

Assuming a random distribution function for the angle ψ, this yields a tilt angle $\theta = 44.8° \pm 0.5°$. This tilt angle represents the angle between the surface normal (Z) and the molecular plane, which in this case is also the molecular symmetry axis. This angle is quite close to the value of $\theta = 41° \pm 1°$ determined by Shi et al. for MG at the octane/water interface using the null angle technique[4].

Upon examining the absorption spectrum of CV (Figure 4.2), we find that CV does not absorb at 420nm (the harmonic frequency of the probe wavelength at 840nm). Nonetheless, the recorded SHG signal was quite intense.

To gain a better understanding of the spectrum of CV at the interface, SHG measurements were carried out by varying the probe wavelength between 790nm to 1350nm. The SHG spectrum was measured for both CV and MG at the cyclohexane-D12/water interfaces due to the specific spectral properties of dodecane in the 1200 nm region (for more details, please refer to Appendix B). The spectra were measured at two sets of polarizations: ($\gamma = 90°$/p) and ($\gamma = 45°$/s) and are shown in Figure 4.5.

(a)

(b)

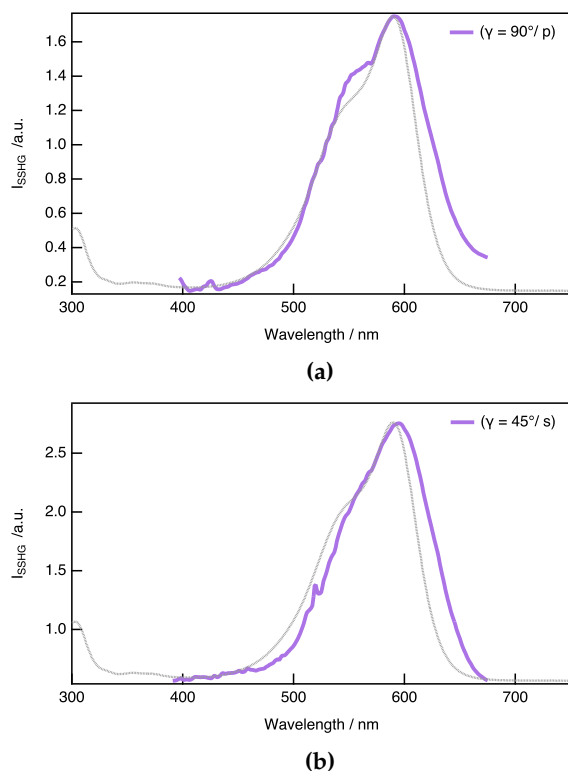**Figure 4.5:** SSHG spectra of CV at the cyclohexane-D12/water interface at two different sets of polarizations: $\gamma = 90°$/p (a) and $\gamma = 45°$/s (b). The electronic absorption spectrum of CV in water is shown for comparison (in gray).

We observe that the SSHG spectra nicely replicate the absorption band in water, suggesting a signal enhancement via a two-photon resonance. The band appears slightly broader on the red side of the spectrum, and no noticeable shift is observed.

The spectrum measured at the $\gamma = 90°/p$ polarization set shows a feature resembling a shoulder, which is at roughly the same wavelength where the shoulder is observed in the electronic absorption spectrum.

The spectrum of MG was also measured under the same conditions. For a C_{2v} molecule like malachite green, there are two optical bands in the visible region. The $S_0 \leftarrow S_2$ transition is parallel to the C_{2v} (z-axis) and the lower energy band corresponding to the $S_0 \leftarrow S_1$ transition lies along the x-axis which is perpendicular to the z-axis in the same molecular plane.

Here as well, the SHG spectrum nicely reproduces the two bands observed in the steady-state electronic absorption spectrum. The ratio between the two bands $(S_1 \leftarrow S_0)$ and $(S_2 \leftarrow S_0)$ changes with different sets of polarizations. At these polarization combinations, the spectrum is proportional to χ_{zxx} for $\gamma = 90°/p$ and to χ_{xxz} for $\gamma = 45°/s$. This alternation is probably due to the fact that these bands are associated with two trnasition dipoles with different orientations relative to the interface. Therefore the resonance enhancement occurs at different sets of polarization.

we have two transition dipoles with different orientations relative to the interface. Depending on where we probe, we are more sensitive to one than the other.
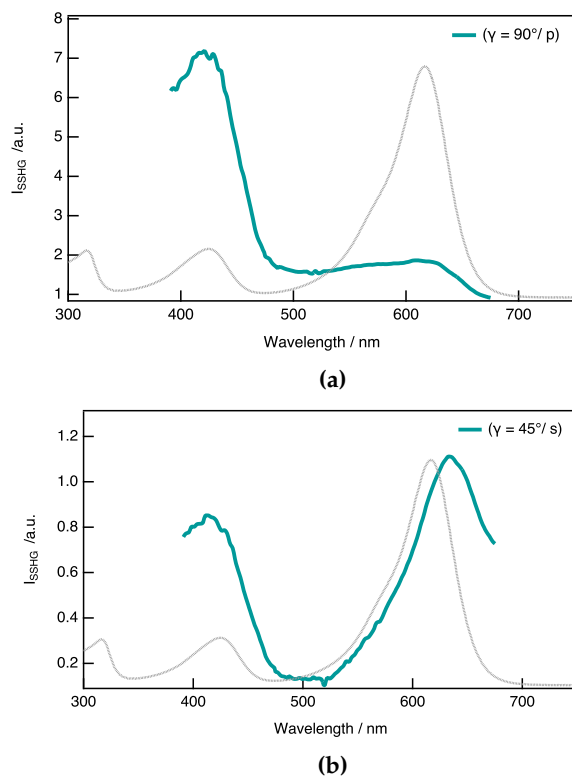

(a)

(b)

Figure 4.6: SSHG spectra of MG at the cyclohexane-D12/water interface at two different sets of polarizations: $\gamma = 90°/p$ (a) and $\gamma = 45°/s$ (b). The electronic absorption spectrum of MG in water is shown for comparison (in gray).

We were curious to measure the polarization curves upon probing at 1320nm,

which coincides with the $S_1 \leftarrow S_0$ transition at low energy. The results obtained are shown in Figure 4.7.
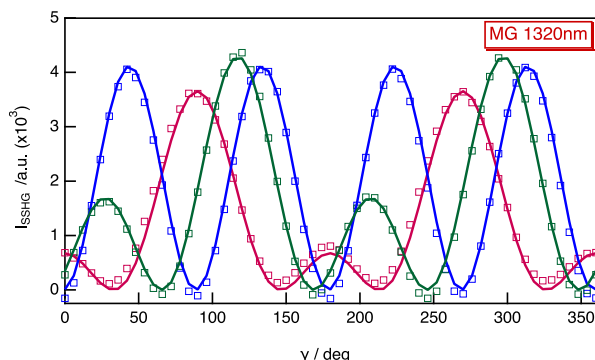

Figure 4.7: Polarization-resolved SH profiles recorded at p (red), s (blue), and 45 (green) geometries at 1320 nm with MG at a concentration of 100uM.

Shi et al. demonstrated that, within the wavelength range considered (corresponding to the $S_0 \leftarrow S_1$ transition), the molecular polarizability predominantly arises from β_{xxz}, with a smaller contribution from β_{zxx} [4]. Thus, we could consider both β_{zxx} and β_{xxz} as contributions to the molecular polarizability. This leads to a tilt angle between the surface normal (Z) and the molecular axis (z) of $\theta = 42° \pm 0.4°$, which agrees well with the value of $\theta = 41° \pm 1°$of reported in the literature for MG at the octane/water interface by Shi et al. [4].

In the preceding chapter, we discussed that one method for tracking dye concentration variations at the interface involves studying the aggregates. The likelihood of the aggregates formation is directly proportional to the concentration of MG. These aggregates are distinct from monomers, primarily due to their substantially longer excited-state lifetimes which arise from the inhibition of large-amplitude motion of the phenyl substituents. Consequently, we conducted TR-SSHG experiments to observe the influence of ILs on aggregate formation.
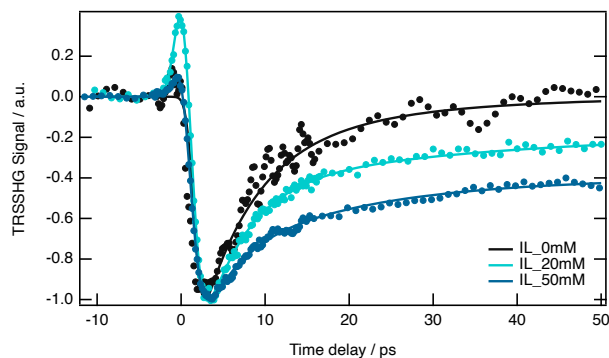

Figure 4.8: Time-resolved SSHG signal profiles recorded at 860 nm after 590nm excitation of CV at the dodecane/water interface in the presence of EMIMSCN.

CV is expected to exhibit the same behavior as MG, as it also undergoes very efficient nonradiative deactivation associated with the large amplitude motion of the phenyl substituents. To verify this, we monitored the effect of adding an IL (EMIM-SCN) to the aqueous phase containing CV. The TR-SSHG profiles were recorded by exciting at 590 nm and probing at 840 nm using the $\gamma = 0°$/p polarization set, where the signal intensity is the highest. Similarly to MG, there is a slowing down of the TR-SSHG dynamics upon addition of the IL. The fast component most likely originates from the ultrafast nonradiative decay of the CV monomers, whereas the slow component arises from the excited-state decay of aggregates.

The TR-SSHG profiles show a prompt rise at time zero, which is more visible with a 20mM concentration of IL, indicative of an increase in the SSHG intensity upon excitation followed by a fast decay to a negative value and then a recovery of the signal to zero. In Figure 4.5, we see that the stationary SHG intensity is very weak because we are far from the absorption band maximum. On the other hand, previous transient absorption measurements in bulk solutions revealed the presence of a $S_n \leftarrow S_1$ absorption band at 430nm. As a consequence, the positive sign can be ascribed to a $S_n \leftarrow S_1$ resonance enhancement.
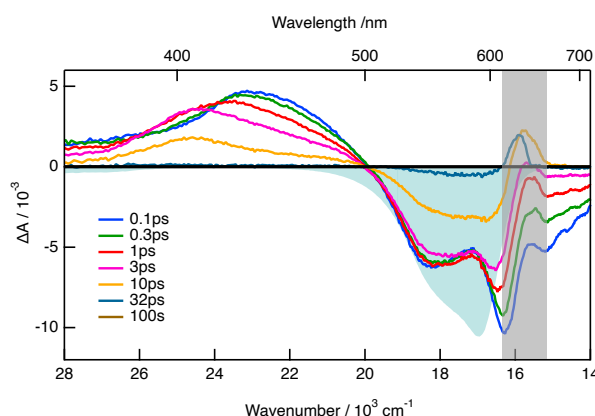

Figure 4.9: Transient absorption spectra recorded at various time delays after 615 nm excitation of CV in butanol. The shaded areas are the negative stationary spectra.

4.3 Conclusion

Due to the irregular polarization curves measured with MG, we shifted our focus to CV, another triphenylmethane dye, hoping to obtain more interpretable results. The polarization curves obtained from CV were regular and could be analyzed using the model described in Chapter 2. TR-SSHG measurements yielded similar quantitative results to those obtained with MG, as detailed in Chapter 3, suggesting CV could serve as a viable alternative to MG.

Despite these findings, the reasons why CV, a molecule with D_{3h} symmetry, produces SHG signal remains uncertain. Either the molecule possesses an intrinsic

high molecular NLO-hyperpolarizability even in its symmetric form, as discussed by Zyss et al. [15], or the symmetry of the molecule is broken due to anisotropic forces at the interface. Any assumptions regarding dominant hyperpolarizability tensors and their impact on interface orientation should, therefore, be taken with a grain of salt.

The observed high-energy shoulder in the electronic absorption spectrum of CV has been a subject of debate, with several studies investigating this spectral feature [16–23]. Explanations range from symmetry breaking that lifts the degeneracy of the S_1 state to the existence of either two ground states or two excited states isomers. Some studies suggest a combination of these models to explain the shoulder's presence [24].

Our subsequent chapter will delve into the investigation of the origin of this spectral shoulder, employing a combination of stationary and time-resolved spectroscopy techniques. Complementing these experimental approaches, we will also use quantum chemical calculations. Through this multifaceted approach, we will show that this shoulder is due to the $S_2 \leftarrow S_0$ of symmerty broken molecules. This explanation is consistent with the SHG spectrum, where we observe a more pronounced shoulder. This observation aligns with our expectation that molecules with broken symmetry should have a larger molecular hyperpolarizability β

Bibliography

(1) Meech, S. R.; Yoshihara, K. *Chem. Phys. Lett.* **1990**, *174*, 423–427.

(2) Meech, S. R.; Yoshihara, Keitaro. *J. Phys. Chem.* **1990**, *94*, 4913–4920.

(3) Morgenthaler, M. J. E.; Meech, S. R. *Chem. Phys. Lett.* **1993**, *202*, 57–64.

(4) Shi, X.; Borguet, E.; Tarnovsky, A. N.; Eisenthal, K. B. *Chem. Phys.* **1996**, *205*, 167–178.

(5) Srivastava, A.; Eisenthal, K. B. *Chem. Phys. Lett.* **1998**, *292*, 345–351.

(6) Kikteva, T.; Star, D.; Leach, G. W. *J. Phys. Chem. B* . **2000**, *104*, 2860–2867.

(7) Song, J. *J. Phys. Chem. B* **2010**, *114*, 3236–3241.

(8) Nowakowski, P. J.; Woods, D. A.; Bain, C. D.; Verlet, J. R. R. *J. Chem. Phys.* **2015**, *142*, 084201.

(9) Gassin, P.-M.; Martin-Gassin, G.; Prelot, B.; Zajac, J. *Chem. Phys. Lett.* **2016**, *664*, 50–55.

(10) Punzi, A.; Martin-Gassin, G.; Grilj, J.; Vauthey, E. *J. Phys. Chem. C* **2009**, *113*, 11822–11829.

(11) Fedoseeva, M.; Fita, P.; Punzi, A.; Vauthey, E. *J. Phys. Chem. C* **2010**, *114*, 13774–13781.

(12) Tyson, A. L.; Woods, D. A.; Verlet, J. R. R. *J. Chem. Phys.* **2018**, *149*, 204201.

(13) Eisenthal, K. B. *J. Phys. Chem.* **1996**, *100*, 12997–13006.

(14) Martin-Gassin, G.; Benichou, E.; Bachelier, G.; Russier-Antoine, I.; Jonin, Ch.; Brevet, P. F. *J. Phys. Chem. C* **2008**, *112*, 12958–12965.

(15) Zyss, J.; Van, T. C.; Dhenaut, C.; Ledoux, I. *Chem. Phys.* **1993**, *177*, 281–296.

(16) Lewis, G. N.; Magel, T. T.; Lipkin, D. *J. Am. Chem. Soc.* **1942**, *64*, 1774–1782.

(17) Korppi-Tommola, J.; Kolehmginen, E.; Sal, E. . *number* **1984**, *104*.

(18) Barker, C. C.; Bridge, M. H.; Stamp, A. *J. Chem. Soc.* **1959**, 3957–3963.

(19) Looney, C. W.; Simpson, W. T. **1954**, *76*.

(20) Lueck, H. B.; McHale, J. L.; Edwards, W. D. *J. Am. Chem. Soc.* **1992**, *114*, 2342–2348.

(21) Maruyama, Y.; Ishikawa, M.; Satozono, H. *J. Am. Chem. Soc.* **1996**, *118*, 6257–6263.

(22) Ishikawa, M.; Ye, J. Y.; Maruyama, Y.; Nakatsuka, H. *J. Phys. Chem. A* **1999**, *103*, 4319–4331.

(23) Lewis, L. M.; Indig, G. L. *Dyes Pigm.* **2000**, 10.

(24) Lovell, S.; Marquardt, B. J.; Kahr, B. *J. Chem. Soc., Perkin Trans. 2* **1999**, 2241–2247.

Chapter 5

Torsional Disorder, Symmetry Breaking, and the Crystal Violet Shoulder Controversy
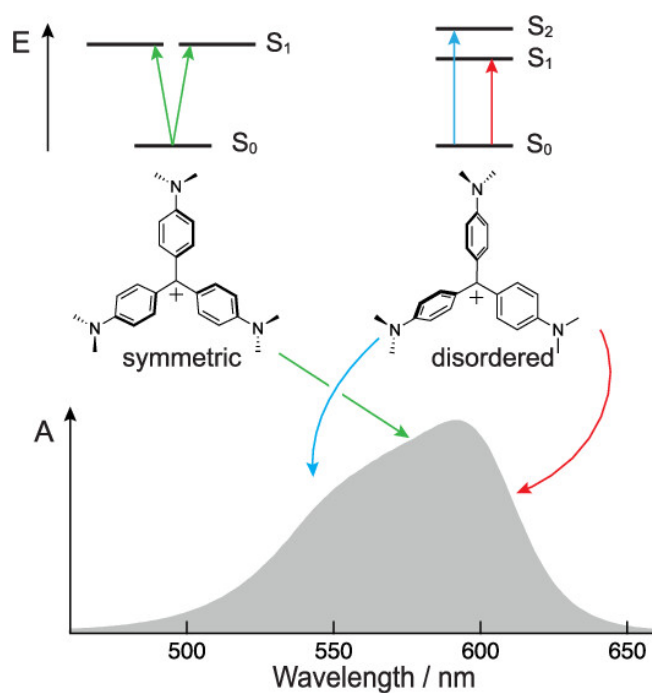
Letter

Torsional Disorder, Symmetry Breaking, and the Crystal Violet Shoulder Controversy

Jihad Sissaoui, Darya S. Budkina, and Eric Vauthey*

Read Online

ACCESS | Metrics & More | Article Recommendations | Supporting Information

ABSTRACT: The nature of the lowest-energy electronic absorption band of crystal violet (CV) and particularly the origin of its high-energy shoulder have been debated since the middle of the past century. The most recent studies invoke a splitting of the S_1 state upon symmetry breaking induced by interactions with the solvent and/or the counterion. Using a combination of stationary and time-resolved polarized spectroscopy together with quantum-chemical calculations, we show that torsional disorder in the ground-state results in an inhomogeneous broadening of the absorption band of CV. The center of the band is mostly due to symmetric molecules with a degenerate S_1 state, whereas the edges originate from transitions to the S_1 and S_2 states of distorted symmetry-broken molecules. Transient-absorption measurements with different excitation wavelengths reveal that these two groups of molecules interconvert rapidly in liquid but not in a rigid environment.
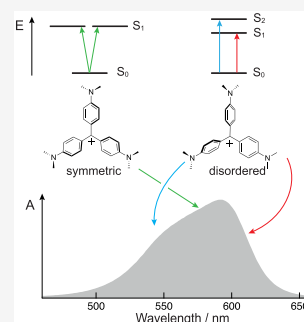
Additionally to their numerous technological applications,[1] triphenylmethane (TPM) dyes have been widely used in spectroscopy to investigate the influence of symmetry and structural relaxation on properties as diverse as nonlinear optical response,[2−6] and ultrafast nonradiative transitions.[7−14] Among these dyes, crystal violet, CV, has attracted considerable attention because of the peculiar shape of its lowest-energy absorption band, characterized by a prominent shoulder on its blue side. As thoroughly reviewed by Lovell et al.,[15] the origin of this shoulder has been highly debated since the work of Lewis and co-workers in 1942,[16] who proposed the existence of an equilibrium between two CV conformers, a symmetric propeller-shaped one and another with one of the branches twisted in the opposite direction. Based on quantum-chemical calculations and polarized resonance Raman measurements,[17] the shoulder was later on explained in terms of symmetry breaking, which lifts the degeneracy of the S_1 state. Over the years, numerous studies on CV were rationalized with either the two ground-states or the two excited-states models,[8,18−22] until Lovell et al. proposed that a combination of both models would be consistent with the ensemble of experimental data.[15] Symmetry breaking has mostly been ascribed to interactions with the solvent and/or the counterion.[17,22−24] The twist coordinate, known to play a crucial role in the excited-state dynamics of TPM dyes, was also invoked, but more rarely.[10,21] From simulations of the absorption band of CV in methanol with an essential-state model, Campo et al. concluded that the shoulder is not only due to symmetry-breaking induced by the solvent field but has also a vibronic origin.[6] A recent two-dimensional electronic-vibrational spectroscopic study of CV in alcohols supports neither the two conformers model nor the solvent/counterion interaction model.[14]

Low barrier for torsion in conjugated molecules, like those containing phenyl−ethynyl building blocks, results in structural disorder at room temperature,[25−28] which can lead to a inhomogeneous broadening of the $S_1 \leftarrow S_0$ absorption band. In such cases, the excited-state dynamics may depend on the excitation wavelength.[29−31] Interestingly, faster ground-state recovery dynamics were reported upon red-edge excitation of CV.[8,10] Based on this, we wondered whether torsional disorder could also be at the origin of the shoulder of the absorption band of CV. Here, using stationary and time-resolved spectroscopy with polarization control, combined with quantum-chemical calculations, we show that there is indeed a distribution of ground-state geometries, that includes symmetric and symmetry-broken, torsionally disordered, structures. These two forms are characterized by distinct absorption spectra and can also be differentiated by their fluorescence anisotropy as well as by their transient dichroism. Our results provide an unambiguous answer to a long-standing controversy.

Quantum-chemical calculations of CV at the DFT level (CAM-B3LYP/6-31G(d,p))[32] in the gas phase and in water (polarizable continuum model) point to a symmetric D_3

ground-state geometry with the three arms twisted by about 33° relative to the molecular plane (Figure S1). Figure 1 shows
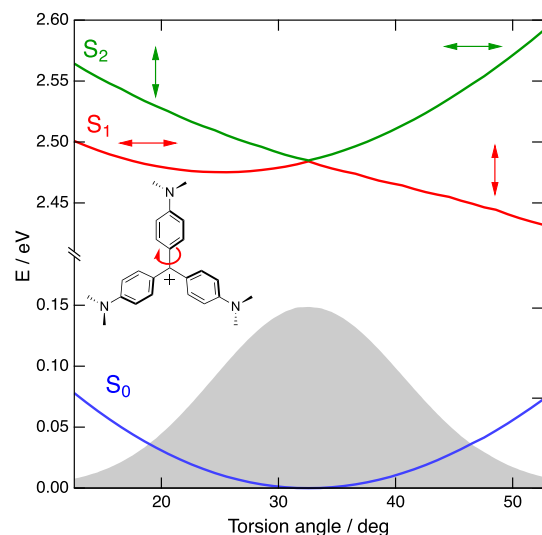

Figure 1. Calculated energy (CAM-B3LYP/6-31G(d,p)) of the ground and Franck−Condon S_1 and S_2 states of CV along the torsional coordinate and population distribution at room temperature (gray). The direction of the transition dipoles is represented by double arrows.

how the ground-state energy increases upon varying the twist angle of one branch while letting the other coordinates relax. These calculations suggest a 20° wide (fwhm) Gaussian distribution of this angle at room temperature and, thus, significant torsional disorder. Time-dependent (TD) DFT calculations were then performed along the same torsional coordinate. In agreement with previous reports,[6,17] the $S_1 \leftarrow S_0$ transition is degenerate at the symmetric D_3 structure, with the transition dipole moments oriented along perpendicular directions. Further on, this state will be designated as S_1^{D3}. Upon symmetry breaking, S_1^{D3} split into two states: S_1^{SB} and S_2^{SB} are located at lower and higher energy, respectively. These calculations predict a significant dependence of the $S_1^{SB} \leftarrow S_0$ and $S_2^{SB} \leftarrow S_0$ transition energies on the twist angle and thus inhomogeneous broadening (Figure 1). Consequently, the lowest-energy absorption band of CV should comprise the degenerate $S_1^{D3} \leftarrow S_0$ transition of the symmetric subpopulation and both the $S_1^{SB} \leftarrow S_0$ and $S_2^{SB} \leftarrow S_0$ transitions of the torsionally disordered subpopulation. These calculations should only be considered on a qualitative basis, as the calculated transition energies remain significantly larger (0.35 eV) than the experimental one, even including the solvent. Additionally, a proper description of the disorder should take the distribution of the torsional angle of all three branches into account.

First experimental evidence of the inhomogeneous nature of the ground-state population comes from the comparison of the absorption, fluorescence, and excitation spectra of CV in a polyvinylbutyral (PVB) film, in which the nonradiative decay of the excited state of CV is strongly slowed down (Figures 2 and S2). The absence of the shoulder in the emission spectrum is consistent with the fact that fluorescence originates from S_1^{D3} and S_1^{SB} only, whereas the absorption band is additionally due
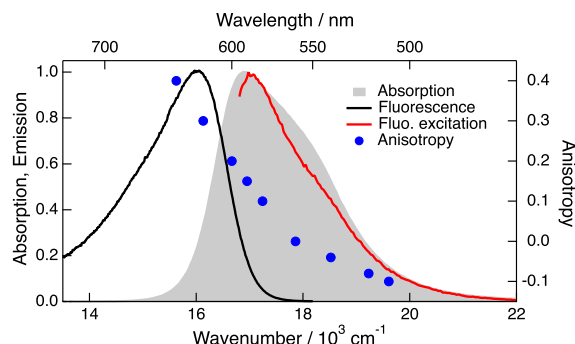

Figure 2. Stationary absorption, fluorescence (530 nm excitation), and excitation (600 nm emission) spectra measured with CV in a PVB film and anisotropy obtained from time-resolved fluorescence measurements.

to the transition to S_2^{SB}. As shown in Figure S3, the fluorescence spectrum upon red-edge excitation (≥600 nm) is red-shifted relative to those obtained upon shorter-wavelength excitation. This suggests that the red-shifted fluorescence arises mostly from the S_1^{SB} state. The excitation spectrum also depends on the wavelength at which fluorescence is detected (Figures 2 and S4). The excitation spectrum of the red-edge fluorescence (≥650 nm) is similar to the absorption spectrum, whereas the excitation spectrum monitored at the band maximum is blue-shifted relative to the absorption maximum (580 vs 595 nm) and does not exhibit the shoulder (Figure 2). This indicates that symmetric molecules can be predominantly excited by irradiating around the center of the absorption band, whereas the symmetry-broken molecules can be preferentially excited by irradiating on either the red ($S_1^{SB} \leftarrow S_0$) or the blue side of the band ($S_2^{SB} \leftarrow S_0$). Previous studies in various solvents pointed to an attenuation of the shoulder upon decreasing temperature.[18,22] We repeated such measurements in ethanol and PVB, and observed significant narrowing and intensity increase of the absorption band in liquid ethanol upon decreasing the temperature to 160 K (Figure S5). By contrast, the band shape in PVB remains essentially unchanged upon going from room temperature to 100 K (Figure S5). The band narrowing in ethanol can be explained by a decrease of torsional disorder at lower temperatures and, thus, a decrease of the $S_1^{SB}-S_2^{SB}$ gap. The quantum-chemical calculations suggest that the total oscillator strength of the transition to S_1^{SB} and S_2^{SB} increases with decreasing distortion (Figure S1B). The larger band intensity at low temperatures concurs with a higher oscillator strength due to a lower disorder. The absence of a temperature dependence in the PVB film indicates that thermal equilibrium cannot be achieved in a rigid environment. This is clear evidence that the torsional coordinate is responsible for inhomogeneous band broadening.

Deeper insight can be obtained by looking at the fluorescence anisotropy measured by both polarized stationary and time-resolved fluorescence spectroscopy. As a control, the same measurements were carried out with malachite green (MG) in PVB, whose S_1 state is not degenerate. The fluorescence anisotropy, r, of MG is between 0.3 and 0.4 upon excitation throughout the $S_1 \leftarrow S_0$ absorption band (Figure S6), as expected for parallel absorption and emission transition dipoles.[33] By contrast, the anisotropy at the

fluorescence band maximum of CV depends strongly on the excitation wavelength (Figures 2 and S7) and varies continuously from −0.1 at 510 nm to 0.4 at 640 nm. These r values at the two band edges are totally consistent with those expected for the symmetry-broken CV, with the value of −0.1 being close to that of −0.2 for perpendicular absorption and emission dipoles. They confirm that the absorption at the blue and red edges is due to the orthogonally oriented $S_2^{SB} \leftarrow S_0$ and $S_1^{SB} \leftarrow S_0$ transitions, respectively. The anisotropy value of 0.1, expected for the emission from a planar transition dipole, can be found at 580 nm, in perfect agreement with the wavelength deduced above for the absorption of the symmetric molecules.

We also performed transient absorption (TA) measurements with CV in butanol (BuOH) and PVB at different excitation wavelengths, 515, 550 and 615 nm, and with magic angle and parallel and perpendicular polarization of the probe light. The early magic-angle TA spectra are dominated by a negative band above 500 nm, with the red side due to stimulated emission (SE) and the blue side due to the ground-state bleach (GSB), as well as by a positive band below 500 nm that can be assigned to excited-state absorption (ESA) (Figure 3A).
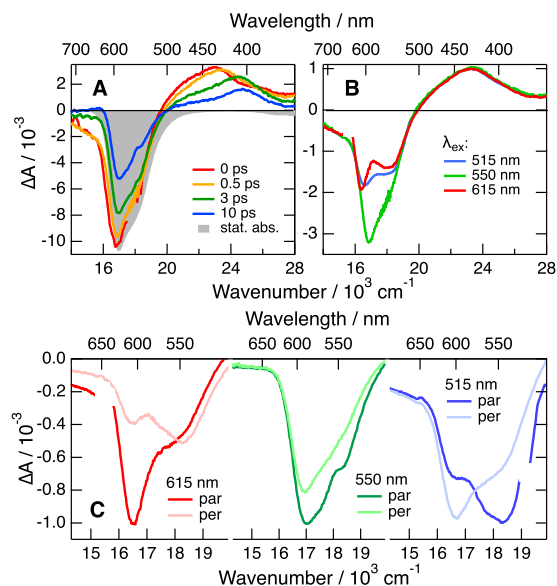

Figure 3. (A) Transient absorption spectra recorded at various time delays after 550 nm excitation of CV in butanol and negative stationary spectrum. (B) Comparison of transient spectra recorded 500 fs after excitation at different wavelengths. (C) Transient spectra recorded with parallel and perpendicular polarization 1 ps after excitation at different wavelengths.

Similar to previous observations,[21,22] the shape of the negative band depends strongly on the excitation wavelength (Figure 3B, S8 and S9): it shows two minima upon 615 and 515 nm excitation and a single one upon 550 nm excitation. In BuOH, these differences vanish within 10 ps, whereas the whole transient band decays in a few tens of ps. In PVB, these differences are still visible after 1 ns (Figure S9) and apparently persist during the whole excited-state lifetime, which is on the order of a few nanoseconds according to the time-resolved fluorescence measurements. By contrast, TA spectra in the ESA region, below 500 nm, do not show significant excitation

wavelength dependence. The overall excited-state dynamics of CV are similar to those of the other TMP dyes and are mostly controlled by large-amplitude motion along the torsional coordinate.[7,8,11,14,34]

The origin of the excitation wavelength dependence of the GSB region of the TA spectrum becomes clearer when looking at the polarized spectra in BuOH (Figure 3C). They reveal that the two minima observed upon excitation at either 615 or 515 nm are associated with perpendicular transition dipoles and correspond to the bleaches of the $S_1^{SB} \leftarrow S_0$ and $S_2^{SB} \leftarrow S_0$ bands of the distorted molecules. These bands culminate at about 605 and 540 nm, respectively. On the other hand, only weak polarization dependence is observed upon 550 nm excitation, in agreement with the fact that symmetric molecules are predominantly excited at this wavelength. These suggest that the $S_1^{D3} \leftarrow S_0$ band peaks at around 580 nm, in agreement with the fluorescence anisotropy results.

We now consider the excited-state dynamics of the different subpopulations of CV. As illustrated in Figure 4A, the early TA
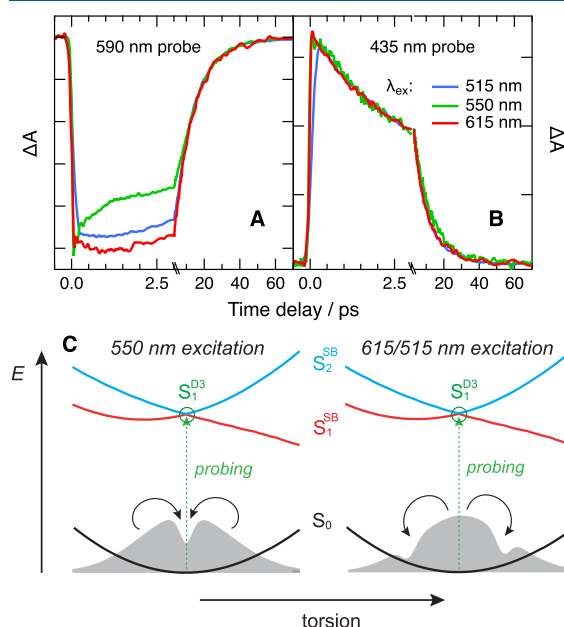

Figure 4. Temporal evolution of the transient absorption at the maximum of the stationary absorption band (A) and the ESA band (B) after excitation of CV in butanol at different wavelengths. The intensity was normalized by tail matching. (C) Effect of the re-equilibration of the ground-state population on the bleach signal of the symmetric molecules: the bleach decreases after excitation of symmetric molecules (left) and increases after exciting distorted molecules (right).

dynamics at the GSB maximum (590 nm) in BuOH depend on the excitation wavelength, the bleach increasing upon 615 and 515 nm excitation and decreasing when exciting at 550 nm. These differences can be explained in terms of the re-equilibration of the ground-state population as depicted in Figure 4C. Excitation at 550 nm depletes preferentially the (quasi-)symmetric ground-state population (left). The result-ing hole is refilled by two distinct processes: (i) the decay of the excited-state population and (ii) the re-equilibration of the distribution of the ground-state population. On the other hand,

excitation at 615/515 nm depletes preferentially distorted molecules. The corresponding holes are also refilled by excited-state decay and re-equilibration. However, the latter process decreases the population of symmetric molecules (Figure 4C, right), and therefore, the GSB signal at 590 nm becomes more negative. Once this equilibrium re-established, the dynamics do no longer depend on the excitation wavelength and reflect the decay of the excited-state. As depicted in Figure 4B, the TA dynamics at the maximum of the ESA band (435 nm), which also reflect the decay of the excited-state, do not exhibit significant excitation-wavelength dependence, except within the first ≈500 fs. Indeed, the maximum signal intensity upon 515 nm excitation is reached at a slightly later time, about 200 fs, compared to that upon 550 and 615 nm excitation. This delay is also clearly visible at 605 nm, where SE contributes significantly (Figure S10) and at 590 nm (Figure 4A), but to a lesser extent as the contribution of SE to the TA intensity is smaller. This 200 fs time delay, only present upon 515 nm excitation, is attributed to the $S_2^{SB} \rightarrow S_1^{SB}$ internal conversion after the $S_2^{SB} \leftarrow S_0$ excitation of the distorted molecules. This latter feature is also visible in the PVB film (Figure S11). However, apart from this, the early TA dynamics at 590 nm in PVB is independent of the excitation wavelength, indicating that the re-equilibration of the ground-state population is not taking place in a rigid environment, where large amplitude motion is inhibited. This difference between BuOH and PVB is strong evidence that torsional disorder is the main origin of the inhomogeneous broadening of the lowest-energy absorption band of CV. The dynamics in the GSB and ESA regions suggest a slower excited-state decay upon 550 nm excitation in PVB (Figure S11). This is consistent with the TCSPC data which indicate that the fluorescence lifetime upon excitation at the center of the band is about 15% longer than upon excitation at the edges (Figure S12). This difference might be due to the smaller S_1-S_0 gap of the distorted molecules and hence to a faster internal conversion.

All of the results presented here allow drawing a clear picture of the nature of the lowest-energy absorption band of CV and of the origin of its shoulder. This picture combines several features of the previous hypotheses. As proposed by Lewis et al.,[16] the torsional coordinate is responsible for the shoulder. However, there is no equilibrium between two well-defined structures but rather a broad distribution of geometries that can be sorted into two groups, symmetric and distorted, because of their distinct absorption spectra. Consequently, three different transitions contribute to the absorption band of CV, with the shoulder being mostly due to the $S_2^{SB} \leftarrow S_0$ transition of distorted molecules. As torsional disorder decreases, the splitting of the excited state becomes smaller and the shoulder is less pronounced. Although solvation energy and interactions with the counterion may vary with the degree of distortion[14] and, thus, modulate the relative energies of the S_1^{D3}, S_1^{SB} and S_2^{SB} states, solvent/counterion are not the main factors for the inhomogeneous broadening of the band and the presence of the shoulder. In a broader context, such inhomogeneous broadening due to torsional disorder offers interesting perspectives for an excitation-wavelength dependent photochemistry.

ASSOCIATED CONTENT

Data Availability Statement

The data can be downloaded from https://doi.org/10.26037/yareta:qkufv7qezngl7fl55yzrgaa53y

SI **Supporting Information**

This material is available free of charge via the Internet at http://pubs.acs.org/. The Supporting Information is available free of charge at https://pubs.acs.org/doi/10.1021/acs.jpclett.3c01038.

> Experimental details, additional results, quantum-chemical calculations, stationary spectra, transient absorption spectra, and time-resolved fluorescence data (PDF)

> Transparent Peer Review report available (PDF)

AUTHOR INFORMATION

Corresponding Author

    Eric Vauthey − *Department of Physical Chemistry, University of Geneva, CH-1211 Geneva, Switzerland;* orcid.org/0000-0002-9580-9683; Email: eric.vauthey@unige.ch

Authors

    Jihad Sissaoui − *Department of Physical Chemistry, University of Geneva, CH-1211 Geneva, Switzerland*
    Darya S. Budkina − *Department of Physical Chemistry, University of Geneva, CH-1211 Geneva, Switzerland*

Complete contact information is available at:
https://pubs.acs.org/10.1021/acs.jpclett.3c01038

Notes

The authors declare no competing financial interest.

REFERENCES

(1) Thetford, D. *Kirk-Othmer Encyclopedia of Chemical Technology*; Blackwell Wiley: Hoboken, NJ, 2013; pp 1−19.

(2) Joffre, M.; Yaron, D.; Silbey, R. J.; Zyss, J. Second Order Optical Nonlinearity in Octupolar Aromatic Systems. *J. Chem. Phys.* **1992**, *97*, 5607−5615.

(3) Lee, Y.-K.; Jeon, S.-J.; Cho, M. Molecular Polarizability and First Hyperpolarizability of Octupolar Molecules: Donor-Substituted Triphenylmethane Dyes. *J. Am. Chem. Soc.* **1998**, *120*, 10921−10927.

(4) Xu, Q.-H.; Ma, Y.-Z.; Fleming, G. R. Different Real and Imaginary Components of the Resonant Third-Order Polarization Revealed by Optical Heterodyne Detected Transient Grating Spectroscopic Studies of Crystal Violet: Model and Experiment. *J. Phys. Chem. A* **2002**, *106*, 10755.

(5) Rao, Y.; Guo, X.-m.; Tao, Y.-S.; Wang, H.-f. Observation of the Direct S2 → S_0 Two-Photon Fluorescence between 370 and 480 nm and the Hyperpolarizability of Crystal Violet (CV) from Spectrally Resolved Hyper-Rayleigh Scattering Measurement. *J. Phys. Chem. A* **2004**, *108*, 7977−7982.

(6) Campo, J.; Painelli, A.; Terenziani, F.; Van Regemorter, T.; Beljonne, D.; Goovaerts, E.; Wenseleers, W. First Hyperpolarizability Dispersion of the Octupolar Molecule Crystal Violet: Multiple Resonances and Vibrational and Solvation Effects. *J. Am. Chem. Soc.* **2010**, *132*, 16467−16478.

(7) Magde, D.; Windsor, M. W. Picosecond Internal Conversion in Crystal Violet. *Chem. Phys. Lett.* **1974**, *24*, 144−148.

(8) Sundström, V.; Gillbro, T. Effects of Solvent on TMP Photophysics. Transition from no Barrier to Barrier Case, Induced by Solvent Properties. *J. Chem. Phys.* **1984**, *81*, 3463−3474.

(9) Duxbury, D. F. The Photochemistry and Photophysics of Triphenylmethane Dyes in Solid and Liquid Media. *Chem. Rev.* **1993**, *93*, 381.

(10) Nagasawa, Y.; Ando, Y.; Kataoka, D.; Matsuda, H.; Miyasaka, H.; Okada, T. Ultrafast Excited State Deactivation of Triphenylmethane Dyes. *J. Phys. Chem. A* **2002**, *106*, 2024−2035.

(11) Fita, P.; Punzi, A.; Vauthey, E. Local Viscosity of Binary Water +Glycerol Mixtures at Liquid/Liquid Interfaces Probed by Time-Resolved Surface Second Harmonic Generation. *J. Phys. Chem. C* **2009**, *113*, 20705−20712.

(12) Li, G.; Magana, D.; Dyer, R. B. Direct Observation and Control of Ultrafast Photoinduced Twisted Intramolecular Charge Transfer (TICT) in Triphenyl-Methane Dyes. *J. Phys. Chem. B* **2012**, *116*, 12590−12596.

(13) Laptenok, S. P.; Addison, K.; Heisler, I. A.; Meech, S. R. Excited State Structural Dynamics in Higher Lying Electronic States: S2 State of Malachite Green. *Chem. Phys. Lett.* **2014**, *607*, 43−46.

(14) Wu, E. C.; Ge, Q.; Arsenault, E. A.; Lewis, N. H. C.; Gruenke, N. L.; Head-Gordon, M. J.; Fleming, G. R. Two-Dimensional Electronic-Vibrational Spectroscopic Study of Conical Intersection Dynamics: an Experimental and Electronic Structure Study. *Phys. Chem. Chem. Phys.* **2019**, *21*, 14153−14163.

(15) Lovell, S.; Marquardt, B. J.; Kahr, B. Crystal Violet's Shoulder. *J. Chem. Soc., Perkin Trans.* **1999**, *2*, 2241−2247.

(16) Lewis, G. N.; Magel, T. T.; Lipkin, D. Isomers of Crystal Violet Ion. Their Absorption and Re-emission of Light. *J. Am. Chem. Soc.* **1942**, *64*, 1774−1782.

(17) Lueck, H. B.; McHale, J. L.; Edwards, W. D. Symmetry-Breaking Solvent Effects on the Electronic Structure and Spectra of a Series of Triphenylmethane Dyes. *J. Am. Chem. Soc.* **1992**, *114*, 2342−2348.

(18) Korppi-Tommola, J.; Kolehmainen, E.; Salo, E.; Yip, R. W. The Temperature-Dependent Red-Shift of the Visible Absorption Spectra of Crystal Violet in Alcohol Solutions. *Chem. Phys. Lett.* **1984**, *104*, 373−377.

(19) Clark, F. T.; Drickamer, H. G. High-Pressure Study of Triphenylmethane Dyes in Polymeric and Aqueous Media. *J. Phys. Chem.* **1986**, *90*, 589−592.

(20) Ben-Amotz, D.; Harris, C. B. Torsional Dynamics of Molecules on Barrierless Potentials in Liquids. I. Temperature and Wavelength Dependent Picosecond Studies of Triphenylmethane Dyes. *J. Chem. Phys.* **1987**, *86*, 4856−4856.

(21) Ishikawa, M.; Maruyama, Y. Femtosecond Spectral Hole-Burning of Crystal Violet in Methanol. New Evidence for Ground State Conformers. *Chem. Phys. Lett.* **1994**, *219*, 416−420.

(22) Maruyama, Y.; Ishikawa, M.; Satozono, H. Femtosecond Isomerization of Crystal Violet in Alcohols. *J. Am. Chem. Soc.* **1996**, *118*, 6257−6263.

(23) Lewis, L. M.; Indig, G. L. Solvent Effects on the Spectroscopic Properties of Triarylmethane Dyes. *Dyes Pigm.* **2000**, *46*, 145−154.

(24) Loison, C.; Antoine, R.; Broyer, M.; Dugourd, P.; Guthmuller, J.; Simon, D. Microsolvation Effects on the Optical Properties of Crystal Violet. *Chem. Eur. J.* **2008**, *14*, 7351−7357.

(25) Sluch, M. I.; Godt, A.; Bunz, U. H. F.; Berg, M. A. Excited-State Dynamics of Oligo(p-phenyleneethynylene): Quadratic Coupling and Torsional Motions. *J. Am. Chem. Soc.* **2001**, *123*, 6447−6448.

(26) Beeby, A.; Findlay, K. S.; Low, P. J.; Marder, T. B.; Matousek, P.; Parker, A. W.; Rutter, S. R.; Towrie, M. Studies of the S1 State in a Prototypical Molecular Wire Using Picosecond Time-Resolved Spectroscopies. *Chem. Commun.* **2003**, 2406−7.

(27) Magyar, R. J.; Tretiak, S.; Gao, Y.; Wang, H. L.; Shreve, A. P. A Joint Theoretical and Experimental Study of Phenylene-Acetylene Molecular Wires. *Chem. Phys. Lett.* **2005**, *401*, 149−156.

(28) Beeby, A.; Findlay, K. S.; Goeta, A. E.; Porrès, L.; Rutter, S. R.; Thompson, A. L. Engineering a Twist in 9,10-Diethynylanthracenes by Steric Interactions. *Photochem. Photobiol. Sci.* **2007**, *6*, 982−986.

(29) Roy, K.; Kayal, S.; Ravi Kumar, V.; Beeby, A.; Ariese, F.; Umapathy, S. Understanding Ultrafast Dynamics of Conformation Specific Photo-Excitation: A Femtosecond Transient Absorption and Ultrafast Raman Loss Study. *J. Phys. Chem. A* **2017**, *121*, 6538−6546.

(30) Soederberg, M.; Dereka, B.; Marrocchi, A.; Carlotti, B.; Vauthey, E. Ground-State Structural Disorder and Excited-state Symmetry Breaking in a Quadrupolar Molecule. *J. Phys. Chem. Lett.* **2019**, *10*, 2944−2948.

(31) Fureraj, I.; Budkina, D. S.; Vauthey, E. Torsional Disorder and Planarization Dynamics: 9,10-Bis(phenylethynyl)anthracene as a Case Study. *Phys. Chem. Chem. Phys.* **2022**, *24*, 25979−25989.

(32) Yanai, T.; Tew, D. P.; Handy, N. C. A New Hybrid Exchange-Correlation Functional using the Coulomb-Attenuating Method (CAM-B3LYP). *Chem. Phys. Lett.* **2004**, *393*, 51−57.

(33) Valeur, B. *Molecular Fluorescence: Principles and Applications*; Wiley-VCH Verlag: Weinheim, Germany, 2001.

(34) Yoshizawa, M.; Suzuki, K.; Kubo, A.; Saikan, S. Femtosecond Study of S2 Fluorescence in Malachite Green in Solutions. *Chem. Phys. Lett.* **1998**, *290*, 43−48.

SUPPORTING INFORMATION:

Torsional Disorder, Symmetry Breaking, and the Crystal Violet Shoulder Controversy

Jihad Sissaoui, Darya S. Budkina, and Eric Vauthey[*]

Department of Physical Chemistry, University of Geneva, CH-1211 Geneva, Switzerland.

E-mail: eric.vauthey@unige.ch

Contents

List of Figures

S3

74

S4

S1 Experimental

S1.1 Samples

The dyes crystal violet (CV) chloride and malachite green (MG) oxalate were purchased from Sigma Aldrich and used without further purification. The solvents, 1-butanol (BuOH), ethanol and dichloromethane were purchased from Acros Organics and were used as received. The polyvinylbutyral (PVB, Mowital B60 H) films were prepared by mixing a dye solution in dichloromethane with a polymer solution in the same solvent. This solution was then poured into a glass cylinder placed on a glass plate and left in the fume hood overnight until complete evaporation. The resulting films were placed under vacuum for about a week to eliminate the remaining solvent. They were then compressed between two quartz windows. The absorbance at the band maximum was kept between 0.1 and 0.2 for the stationary measurements. For the transient absorption experiments, the absorbance was between 0.1 and 0.2 at the excitation wavelength.

S1.2 Stationary spectroscopy

Electronic absorption spectra were recorded using a Cary 50 spectrometer. Measurements at different temperatures were carried out using an Oxford OptistatDN cryostat. Stationary fluorescence spectra were measured using a Horiba Fluorolog 322 spectrofluorometer. They were corrected using a set of secondary emissive standards.[2]

S1.3 Time-resolved fluorescence

Fluorescence lifetime measurements with MG and CV in PVB films were performed using the time-correlated single-photon counting (TCSPC) technique. Two excitation light sources were used: a tunable picosecond laser source (NKT photonics SuperK COMPACT with SuperK SELECT tunable multiline filter) and a pulsed laser diode (PicoQuant Prima). The excitation light was focused on the film. The fluorescence was then collected with an

S5

optical fiber using a Schwarzschild objective, then spectrally filtered with a Horiba Triax-190 imaging spectrograph with 1200 lines/mm grating. The spectrally dispersed light exiting the spectrograph was focused on a single-photon avalanche diode (Micro Photon Devices, MPD-100-CTE) with the help of an elliptic mirror (Horiba, 1427C). The time-correlated single photon counting was performed with a PicoHarp-300 (PicoQuant). Time-resolved fluorescence anisotropy measurements were performed by recording fluorescence with the analyser set either parallel or perpendicular to the excitation beam polarization. The G-factor was determined by tail matching method with the fluorescence decays of an oxazine solution.

S1.4 Electronic transient absorption spectroscopy

The transient absorption (TA) measurements were performed with a setup based on an 5 kHz amplified Ti:Sapphire system (solstice Ace, Spectra Physics) producing 35 fs pulses centred at 800 nm, described in detail previously.[3,4] The pump pulses were produced by TOPAS-Prime combined with NirUVis module (Light Conversion) and were compressed to less than 150 fs at the sample position. The pump intensity on the sample was 0.15-0.75 mJ/cm^2. For measurements with the polymer films, the samples were continuously moved laterally and vertically to avoid irradiation on the same spot. Probing was achieved from 320 to 750 nm using white light pulses generated in a 3 mm CaF$_2$ plate. The polarization of the pump and probe pulses was controlled with a combination of polariser and half waveplate.

S6

S2 Quantum-chemical calculations

All calculations were carried out at the density functional theory (DFT) or time-dependent (TD) DFT using the CAM-B3LYP functional,[5] and the 6-31g(d,p) basis set, as implemented in the Gaussian16 (Rev. B) software.[6] This functional was used because of the charge-transfer character of the lowest electronic excited states of CV. The calculations were performed in the gas phase as well as in water using the polarisable continuum model. Apart from the transition energies that were systematically smaller in water, the results were qualitatively the same in both environments.
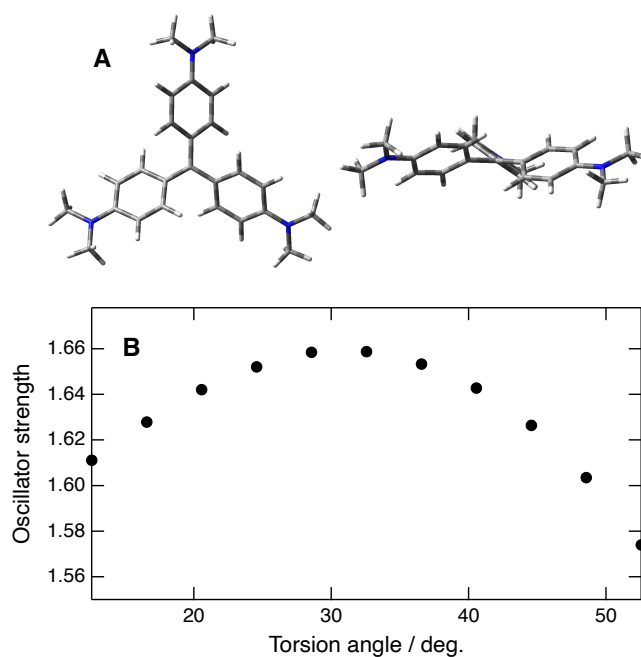
Figure S1: A) Ground-state energy minimum geometry of CV calculated at the DFT level (CAM-B3LYP/6-31g(d,p)). B) Sum of the calculated oscillator strength of the $S_1 \leftarrow S_0$ and $S_2 \leftarrow S_0$ transitions as a function of torsional angle of one of the branches.

S7

S3   Stationary spectroscopy
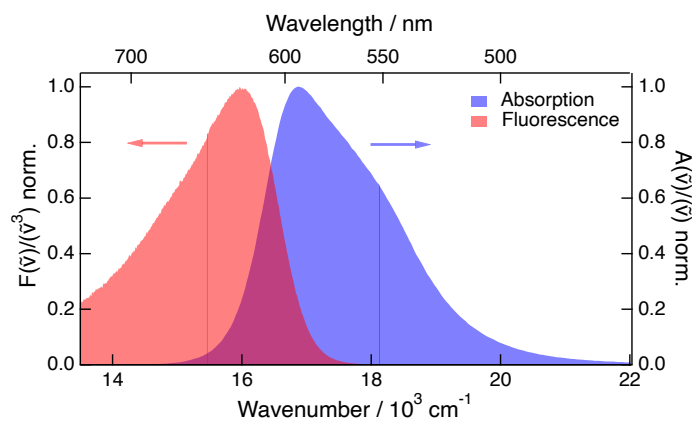
Figure S2: Stationary absorption and fluorescence (530 nm excitation) spectra of CV in a PVB film in the transition-dipole representation.[1]
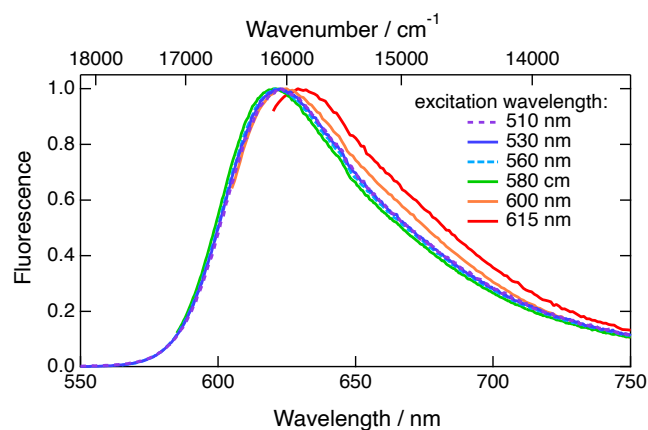
Figure S3: Intensity-normalised fluorescence spectra recorded with CV in a PVB film at different excitation wavelengths.

S8
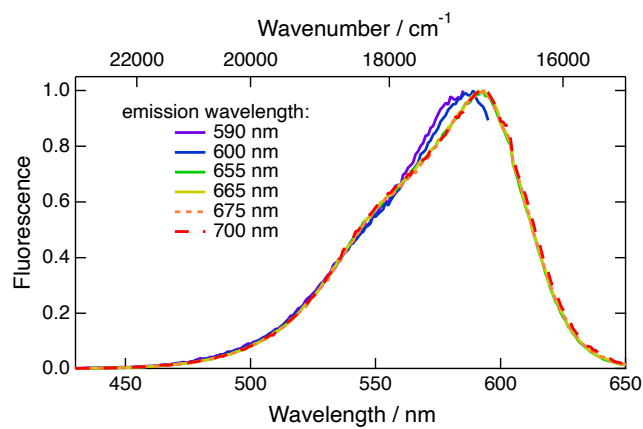
Figure S4: Intensity-normalised excitation spectra recorded with CV in a PVB film at different emission wavelengths.
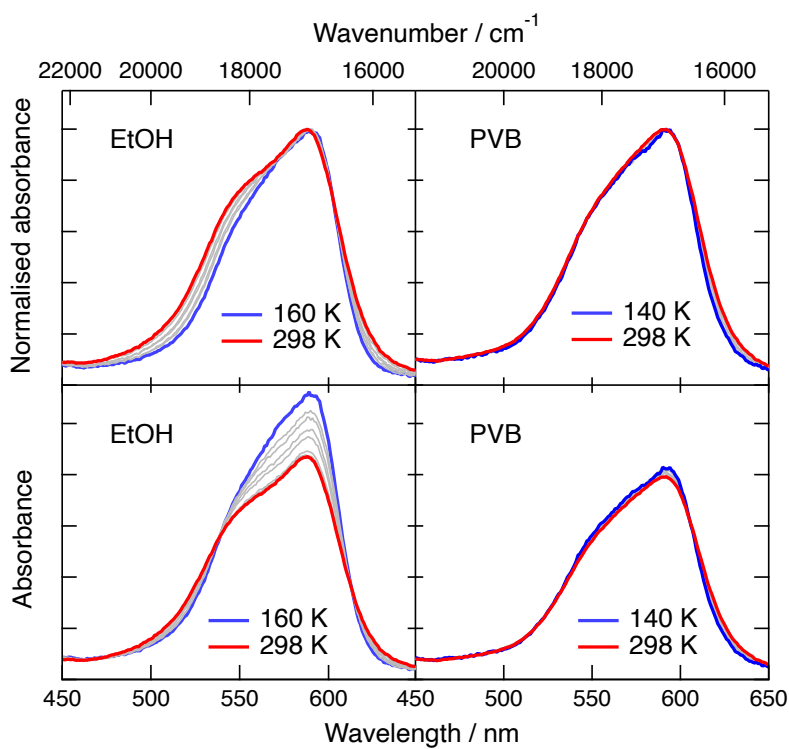
Figure S5: Intensity-normalised (top) and non-normalised (bottom) absorption spectra recorded with CV in ethanol (EtOH, left) and PVB film (right).

S9
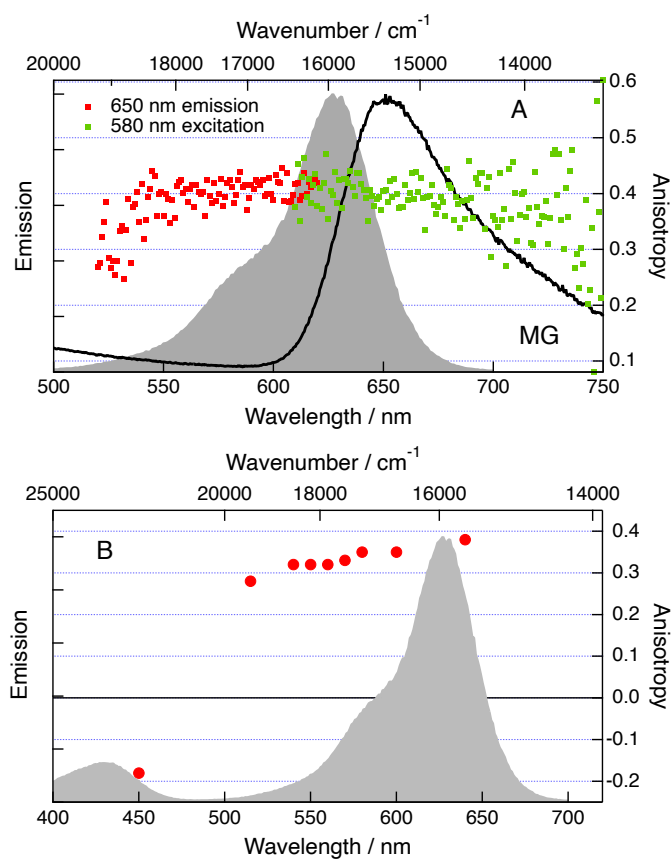
Figure S6: Excitation spectrum at 710 nm and emission spectrum (600 nm excitation) measured with malachite green (MG) in a PVB film together with the fluorescence anisotropy determined from stationary (A) and time-resolved (B) measurements.
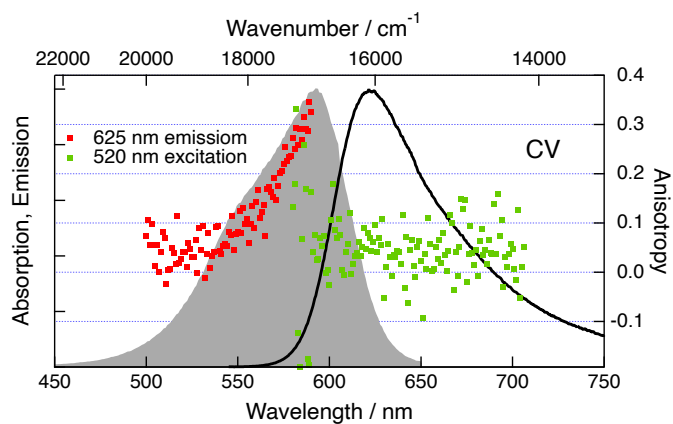
Figure S7: Excitation spectrum at 655 nm and emission spectrum (540 nm excitation) measured with CV in a PVB film together with the fluorescence anisotropy determined from stationary measurements.

S11

S4   Electronic transient absorption spectroscopy
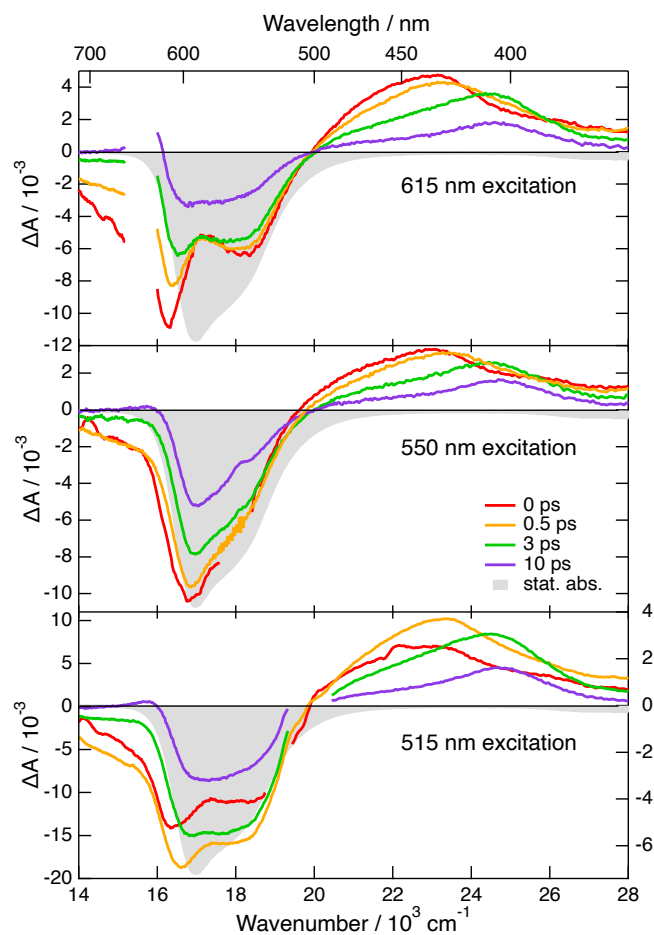
Figure S8: Transient-absorption spectra recorded at various time delays after excitation of CV in butanol at different wavelengths.
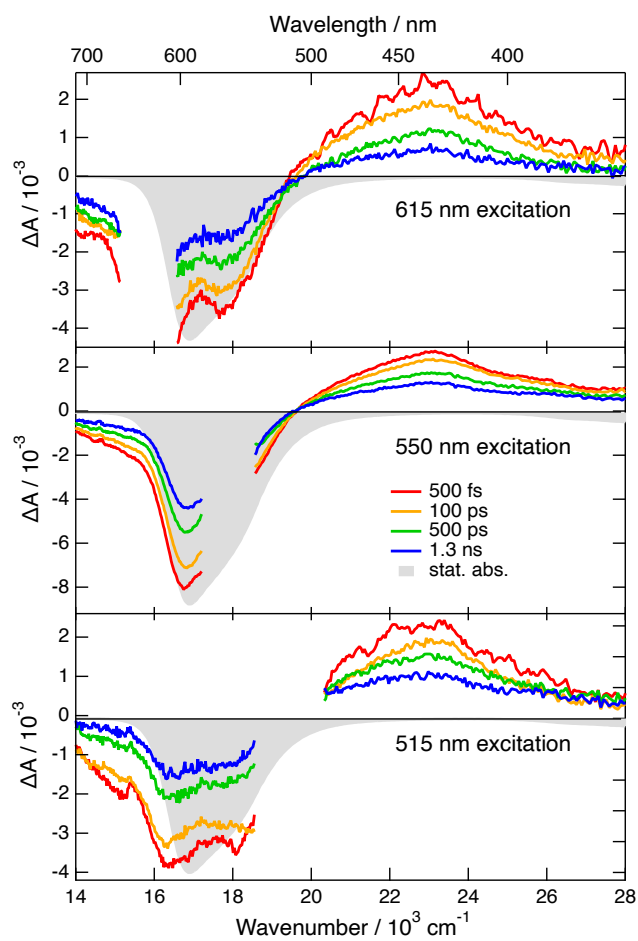
Figure S9: Transient-absorption spectra recorded at various time delays after excitation of CV in a PVB film at different wavelengths.
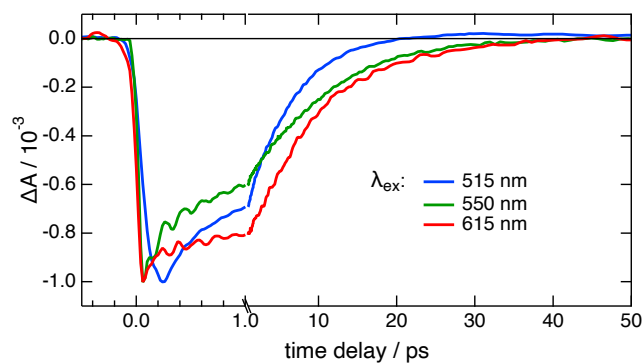
Figure S10: Temporal evolution of the transient absorption in the stimulated emission region (605 nm) after excitation of CV in butanol at different wavelengths.
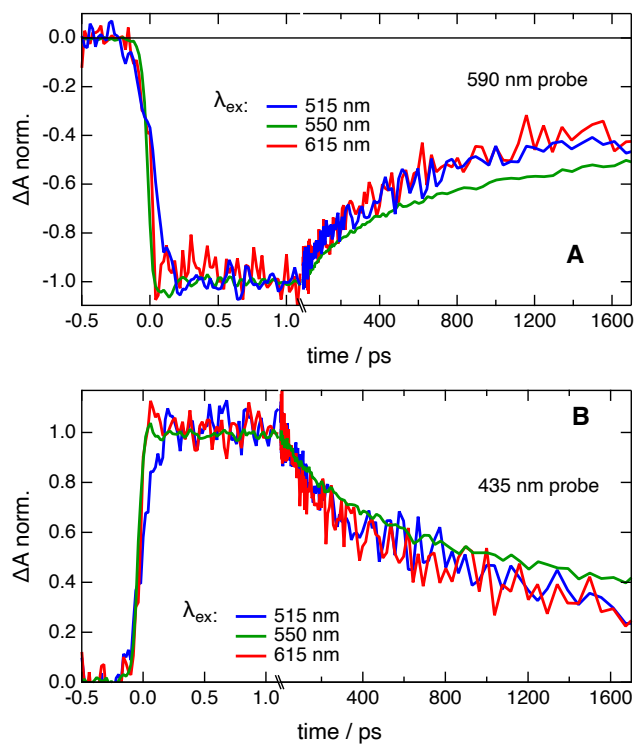
Figure S11: Temporal evolution of the transient absorption at the maximum of the stationary absorption band (A) and the ESA band (B) after excitation of CV in PVB film at different wavelengths.

S14

84

S5   Time-resolved fluorescence
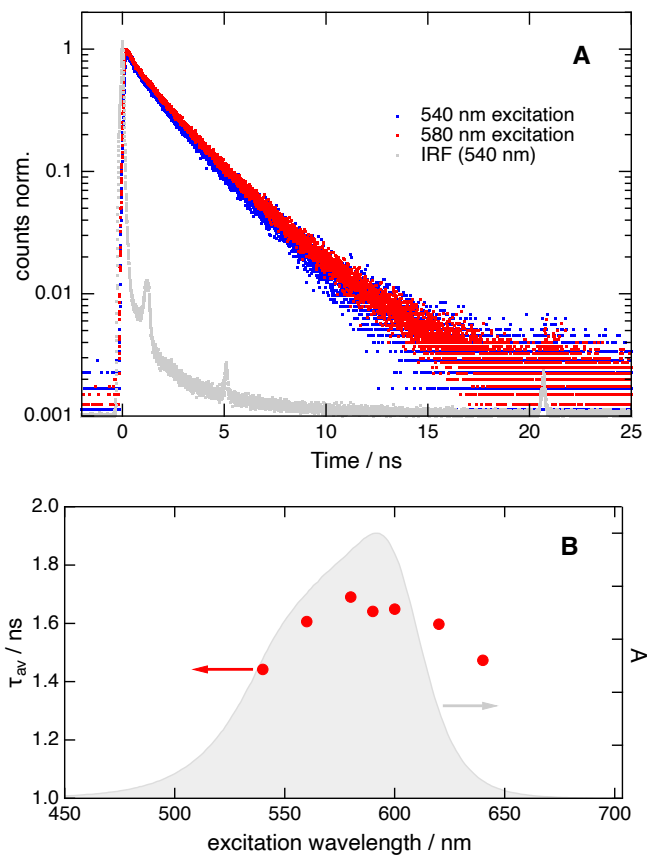
Figure S12: A)TCSPC profiles recorded at 680 nm after excitation of CV in a PVB film at 540 and 580 nm and instrument response function for 540 nm excitation. B) Amplitude-average fluorescence lifetime of CV in a PVB film as a function of the excitation wavelength and absorption spectrum. Error on the lifetime: ±5%.

S15

85

References

(1) Angulo, G.; Grampp, G.; Rosspeintner, A. Recalling the Appropriate Representation of Electronic Spectra. *Spectrochim Acta A* **2006**, *65*, 727–31.

(2) Gardecki, J. A.; Maroncelli, M. Set of Secondary Emission Standard for Calibration of the Spectral Responsivity in Emission Spectroscopy. *Appl. Spectrosc.* **1998**, *52*, 1179–1189.

(3) Aster, A.; Licari, G.; Zinna, F.; Brun, E.; Kumpulainen, T.; Tajkhorshid, E.; Lacour, J.; Vauthey, E. Tuning Symmetry Breaking Charge Separation in Perylene Bichromophores by Conformational Control. *Chem. Sci.* **2019**, *10*, 10629–10639.

(4) Beckwith, J. S.; Aster, A.; Vauthey, E. The Excited-State Dynamics of the Radical Anions of Cyanoanthracenes. *Phys. Chem. Chem. Phys.* **2022**, *24*, 568–577.

(5) Yanai, T.; Tew, D. P.; Handy, N. C. A New Hybrid Exchange-Correlation Functional using the Coulomb-Attenuating Method (CAM-B3LYP). *Chem. Phys. Lett.* **2004**, *393*, 51–57.

(6) Frisch, M. J.; Trucks, G. W.; Schlegel, H. B.; Scuseria, G. E.; Robb, M. A.; Cheeseman, J. R.; Scalmani, G.; Barone, V.; Petersson, G. A.; Nakatsuji, H. et al. Gaussian 16 Rev. B.01. **2016**,

S16

Chapter 6

Photophysics of Methyl Orange in Heterogeneous Media

6.1 Introduction

Azobenzenes and their derivatives are among the most investigated dyes due to their unique photochemical properties, most notably their ultrafast trans-to-cis isomerization [1]. These attributes have enabled their use in diverse applications spanning from biology [2–5] to data storage [6–8], and even molecular machines [9–11].

Despite the vast existing literature in this field, the nature of the photoisomerization mechanism continues to attract significant research interest. An enhanced understanding of this phenomenon could expedite advancements in the development of its diverse applications. The mechanism of the trans-to-cis isomerization, which could occur through torsion around the central double bond or through an in-plane bending motion known as hula-twist , has been a matter of long-standing debate[12–15].However, a recent study on the photoisomerization efficiency in push-pull azobenzenes has recognized the torsional mechanism as the sole productive route, since structures attributable to the inversion mechanism were never detected in their TD-DFT simulations[16].

According to the historical classification of azobenzene derivatives based on the energy spacing between the two first excited states, methyl orange (MO) (Figure 6.1) falls into the category of push-pull azobenzenes [1]. In its electronic ground state, it is found almost exclusively in its trans conformation. Photo-excitation to the S_1 or S_2 state leads to a conversion of a certain percentage of the excited molecules to the cis conformation, which then thermally relaxes back to the more thermodynamically stable trans configuration over a span of milliseconds to seconds [1]. Due to its high non-linear response, it has also been employed as a second harmonic generation probe [17–19].

Investigations into the excited state dynamics of methyl orange in diverse solvents using ultrafast time-resolved fluorescence and transient absorption in the UV and IR regions have been conducted in our group [20]. Findings suggest significant variances depending on the hydrogen bond strength of the solvents, which were

attributed to hydrogen bond interactions between the solvent and the azo nitrogen atoms.

In this study, we probe the influence of a confined environment on the isomerization dynamics and yields, both at liquid/liquid interfaces using second harmonic generation and in bulk using transient absorption techniques.
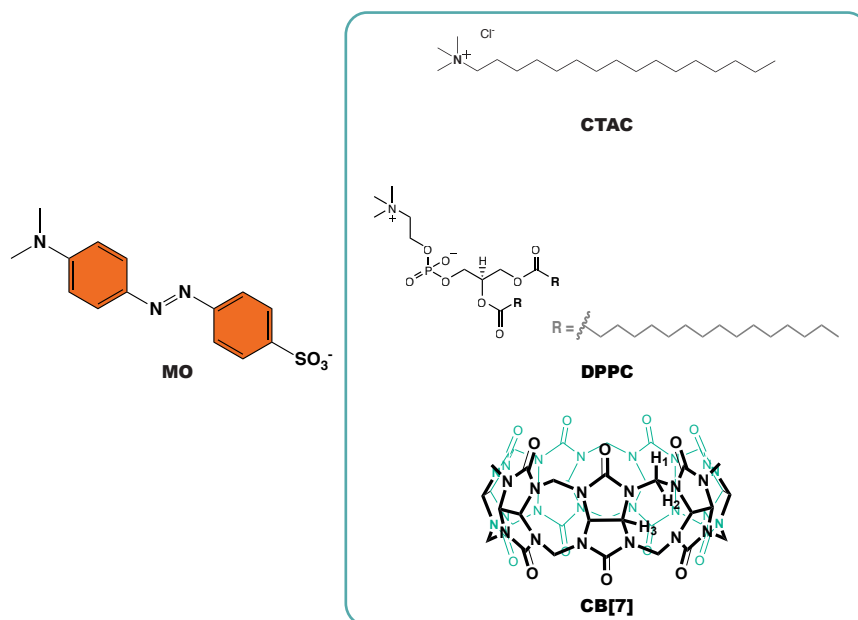
Figure 6.1: Structure of MO, DPPC, CTAC and CB[7]

Three systems designed for molecular confinement at the interface are investigated: a surfactant (CTAC), a phospholipid (DPPC) (which are expected to enhance order and confinement), and a macrocycle CB[7] (a barrel-like structure with a hollow cavity capable of encapsulating small molecules or parts of larger ones based on size, shape, and electronic compatibility). Previous studies have indicated the binding affinity of methyl orange and other azobenzene dyes to CB[7] [21–23]. We explore the excited state dynamics as well as the orientation and localization of methyl orange at the interface. In the bulk, transient absorption measurements with CTAC and CB[7] are conducted, where the concentration of CTAC is high enough to form micelles, thus creating another confined environment where the dye can intercalate. Both SSHG and TA show a significant impact of confinement on the photophysics of MO. MD simulations, performed by Professor Eric Vauthey, shed further light on these dynamics.

6.2 Results and Discussions

6.2.1 Stationary Electronic Absorption
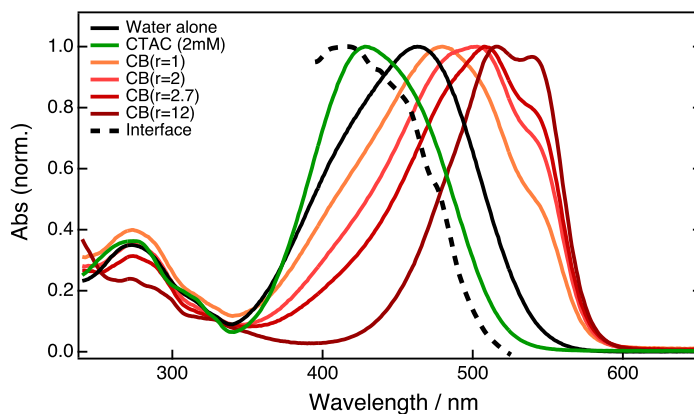
Figure 6.2: Normalised electronic absorption spectra of MO in the presence of CTAC and CB[7] in water

Figure 6.2 shows the normalized electronic absorption spectra of MO in neat water with the addition of either CTAC or CB[7]. The spectra consist of two bands: a weak band in the UV at 275 nm and a more intense band above 350 nm, the maximum of which varies between 428 nm and 515 nm depending on the nature and concentration of the added co-solutes. Upon the addition of CTAC, a 35 nm (1770 cm^{-1}) blue shift is observed. This shift can be explained by the fact that the CTAC concentration used in our experiment (2 mM) exceeds the reported values for the critical micelle concentration (CMC) in water, approximately 1-1.3 mM [24, 25]. Above these concentrations, micelles begin to spontaneously form, creating a new environment with different properties where the dye can intercalate. A previous study from our group demonstrated that the hydrogen bond interactions between MO and solvents result in a red shift of the absorption band [20]. The observed blue shift could be explained if the dye is intercalated in the micelle, effectively shielding the molecule from water. This is comforted by MD simulation results, which show that when micelles are present, the dye intercalates within the micelle. This effectively shields the molecule from water, as shown in Figure 6.3.
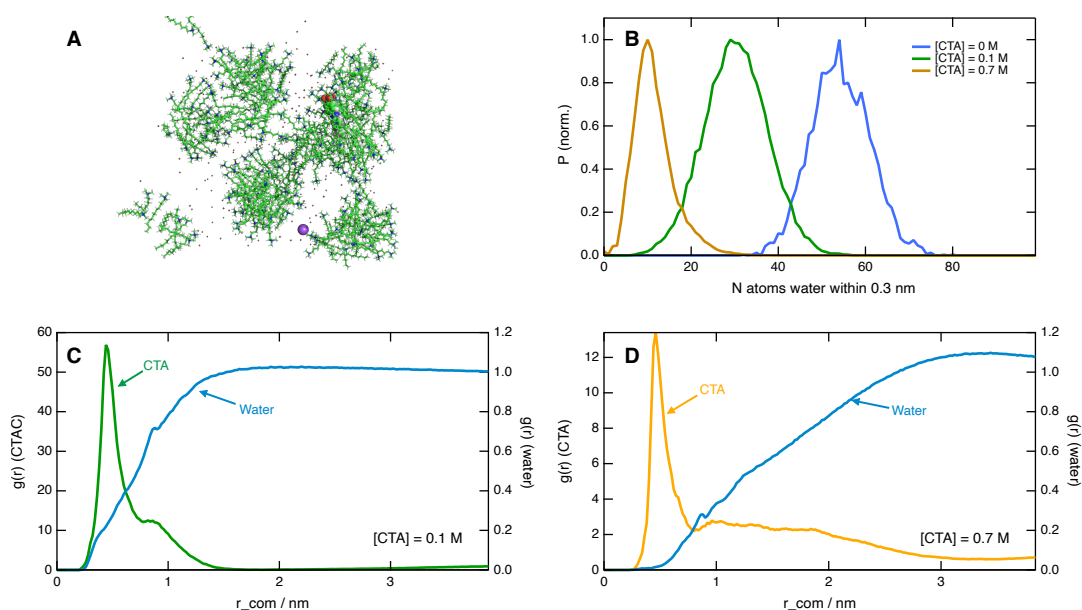
Figure 6.3: (A) A snapshot illustrating the intercalation of the dye in a CTA micelle. (B) The probability of finding water atoms in the vicinity of MO. (C and D) The radial distribution function, defining the probability of finding a particle at a distance r_{com} from the center of mass of the MO, for a low (0.1 M) (C) and high (0.7 M) (D) concentration of CTA.

On the other hand, the addition of CB[7] induces a red shift of the spectrum and results in the emergence of a shoulder on the red side of the spectrum, which becomes more pronounced as the CB[7] concentration increases. Besides the red shift, the spectrum becomes narrower, and the band intensity rises with increasing CB[7] concentration, as depicted in Figure 6.4. At the highest CB[7] concentration, the spectrum has a maximum around 516 nm, comparable to the maximum observed in the most protic solvent, 1,1,1,3,3,3-hexafluoro-2-propanol, from our previous study [20]. The interaction of MO with CB[7] can occur in several ways. Given the hydrophobic components present in methyl orange, such as benzene rings, azo group, and a dimethylamino group, these could be expected to be encapsulated within the cavity. Conversely, the sulfonate group, which displays electrostatic repulsion with the carbonyl portal of CBs, is likely to remain outside. When protonated, the guest molecule's protonated part may form hydrogen bonds with the portal.

The binding of MO and CBs has been explored via Single Crystal X-ray Diffraction and NMR spectroscopy [21]. The findings suggest that the protonation state of the anionic part of MO greatly influences the binding mode. Protonated methyl orange was deeply inserted into the cavity, stabilized by hydrogen bonding at the portal and hydrophobic and dispersion interactions inside the cavity. In contrast, the anionic methyl orange was pushed towards the cavity's exterior due to the electrostatic repulsion between the azo group and the portal oxygen. Therefore, predicting the precise positioning of methyl orange relative to CB[7] in a complex is quite challenging.
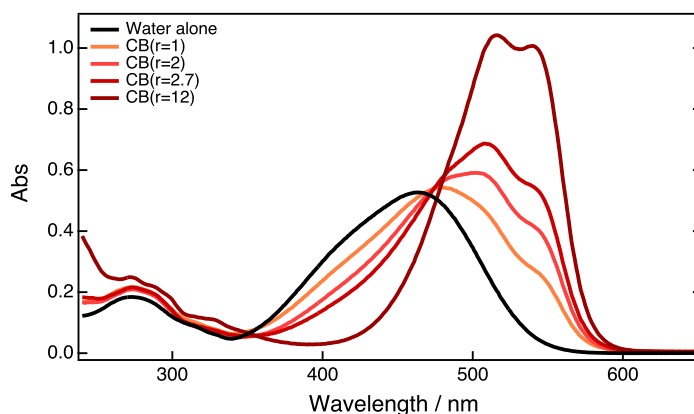
Figure 6.4: Electronic spectra of MO in the presence of CB[7] in water

6.2.2 Localization and Orientation of the Dye at the Interface

Polarization-resolved measurements were conducted at various interfaces to gain insight into the behavior and orientation of the dye at the interface in the presence of various co-solutes. The experiment was carried out at a 840 nm, where the signal is enhanced by two-photon resonance. We tested three different co-solutes: DPPC, CTAC, and CB[7], in addition to a pure water/dodecane interface. The orientation of the dye was estimated from the relative magnitudes of the $\overset{\leftrightarrow}{\chi}^{(2)}$ tensor elements, which were extracted from the measured data.

For the MO dye, we assumed that the hyperpolarizability tensor is dominated by the β_{zzz} element, where z represents the direction of the MO transition dipole moment. This assumption is safe considering that our experiments were performed near the $\pi - \pi^*$ electronic resonance. Azobenzene dyes have a $n - \pi^*$ transition close to the $\pi - \pi^*$ transition, and for a push-pull azobenzene, the two states are very close. However, the contribution of the $n - \pi^*$ transition to the hyperpolarizability tensor is significantly weaker than that of the $\pi - \pi^*$ transition due to both a lower oscillator strength and decreased charge transfer. This was confirmed in a recent Density Functional Theory (DFT) study that systematically investigated the linear and nonlinear optical properties of methyl orange in its acidic and alkaline forms [26].

The tilt angle θ obtained from the analysis of the polarization data is the angle between the transition dipole involved in the resonance and the normal to the interface. The angle θ for MO at the neat water/dodecane interface, obtained from polarization-resolved SHG measurements (see Figure 6.5), is approximately 44°. This angle is close to the values reported in a study of MO at water/dichloroethane (DCE) interfaces: 43° and 34° for the hydrated and dehydrated forms of MO at the interface, respectively [17]. However, the SHG spectrum measured at the water/DCE interface showed two distinct bands attributed to the coexistence of the two forms at the

Figure 6.5: Polarization-resolved SH (Second Harmonic) profiles recorded at *p* (red), *s* (blue), and 45 (green) geometries at 420 nm with MO at a concentration of 200 *μ*M at the dodecane/water interface. The solid lines represent the best fits.

water/DCE interface. In contrast, the spectrum measured at the dodecane/water interface shown in Figure 6.2 is quite different. Although the spectrum was measured only within a limited window, it displays a single blue-shifted band compared to the SSHG spectrum shown in the study by Rinuy et al. [17] and the electronic absorption spectrum of MO in water. This can be compared with the MO electronic spectrum measured in acetonitrile in our group's previous study [20]. These differences can be rationalized in terms of the dye's location. The dye was found to be primarily located in the dodecane phase at the dodecane/water interface, with only the sulfonic acid group located in water, thus limiting the hydrogen bond interactions between the azo group and water, as we can see from the MD simulations (Figure 6.6)

Figure 6.6: Left: Density profiles of water, dodecane, and MO. The interface is located at z = 0 nm. Right: MD snapshots illustrating the location of the dye at the dodecane/water interface.

The results obtained from analyzing all polarization curves with different co-solutes are reported in Table 6.1.

MO Orientation in the Presence of DPPC, CTAC, and CB[7]

To acquire a deeper understanding of the impact of order and confinement on the photophysics and isomerization of MO, we conducted an investigation into its behavior at the dodecane/DPPC/water interface. The polarization-resolved measurements were carried out with a mean molecular area of $60\,\mathring{A}^2$. Higher surface coverages were also investigated but resulted in a decrease and then a loss of signal. Since MO is an anionic dye, the charge of the phospholipid plays a role in its adsorption due to Coulombic interactions. For example, upon adding a phospholipid like DPPG (Dipalmitoylphosphatidylglycerol), which has a headgroup that carries a negative charge due to the deprotonation of the phosphate group, the signal is lost, most likely because of the Coulombic repulsion of the anionic dye from the interfacial region. DPPC, on the other hand, consists of a phosphatidylcholine headgroup, which is zwitterionic and carries both a positive charge on the quaternary ammonium group and a negative charge on the phosphate group. However, even if the overall charge of DPPC is neutral, the signal is lost at higher surface coverages, and those high concentrations could not be investigated. Figure 6.7 shows the polarization curves in the presence of DPPC. The overall observed signal is of the same order of magnitude compared to the bare water/dodecane interface, which points to a similar dye population at the interfacial region. However, this can only be considered quantitatively since the signal intensity is proportional to both the population and the average orientation.

In fact, in the presence of the DPPC, the tilt angle decreases to $33°$, pointing to a more perpendicular orientation of the dye at the interface. This can be due to the intercalation of the dye between the phospholipid tails. A similar effect was observed with other organic dyes in previous studies [27, 28].

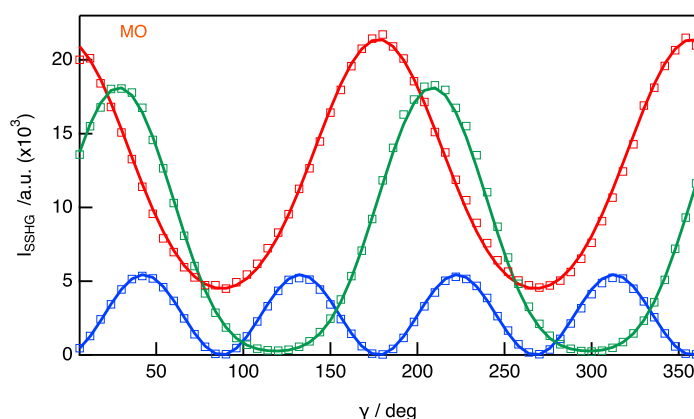**Figure 6.7:** Polarization-resolved SH profiles recorded at p (red), s (blue), and 45 (green) geometries at 420 nm with MO at a concentration of 200 μM and DPPC ($60\,\mathring{A}^2$) at the dodecane/DPPC/water interface. The solid lines are best fits.

MO was also investigated in the presence of CTAC. CTA is a cationic surfactant

that is widely used in many applications in the field of chemistry. Due to its amphiphilic nature, CTAC exhibits surfactant properties and adsorbs at solid-liquid or air-liquid interfaces, such as the dodecane/water interface in our case. In this scenario, the hydrophobic alkyl chains tend to interact with the dodecane layer, while the charged headgroups face the water. This adsorption phenomenon leads to the formation of a monolayer or multilayer of CTAC molecules at the interface, allowing us to investigate the dye in a confined environment.

The concentrations used here were much lower than the critical micelle concentration (CMC) values of CTAC found in the literature [24, 25]. At these concentrations, we would expect the formation of a monolayer. A study on the adsorption of CTAB at the interface with various alkanes, including dodecane, has shown that the adsorption of the surfactant results in the ousting of alkane molecules from the adsorbed layer, and a very small decrease in the interfacial tension is observed [29]. Nevertheless, the formation of some bilayer patches cannot be fully discarded.

The idea we have of the dye's location at the interface is supported by MD simulations, which reveal that the MO is intercalated within the CTA layer, as shown in Figure 6.8.
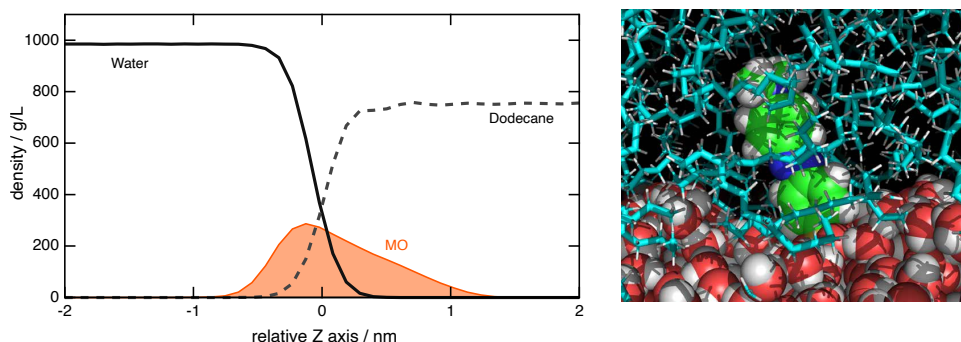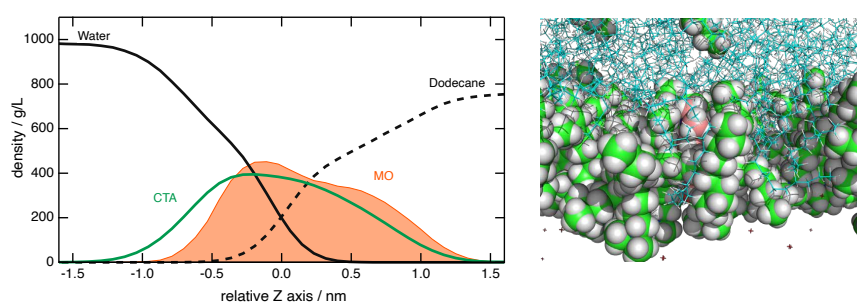

Figure 6.8: Left: Density profiles of water, dodecane, CTAC and MO. The interface is located at z = 0 nm. Right: MD snapshots illustrating the location of the dye at the dodecane/water interface in presence of CTAC (MO: orange, CTAC : green, DOD: blue, H_2O not shown).

Figure 6.9 shows the polarization-resolved SHG measurements with different CTAC volume concentrations. Upon the addition of CTAC, an approximately 20-fold enhancement of the signal is observed. The cationic surfactant has a high affinity for the interface, resulting in the Coulombic attraction of the anionic dye towards the interfacial region, which gives the enhanced signal. However, the signal starts to decrease at around 7 µM bulk concentration and even more at 11 µM, which is most likely due to the competition for adsorption between the dye and CTAC at the interface, favoring the surfactant.
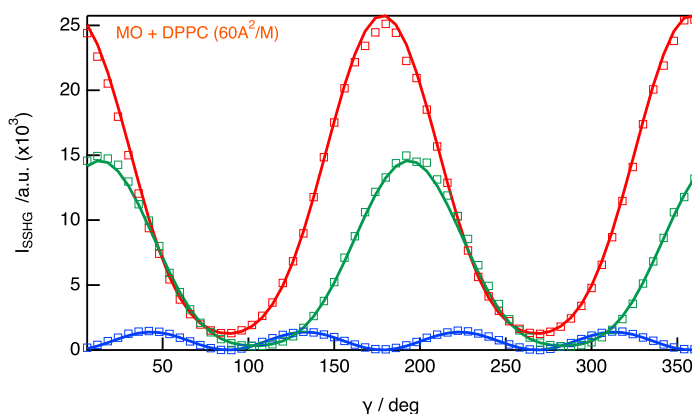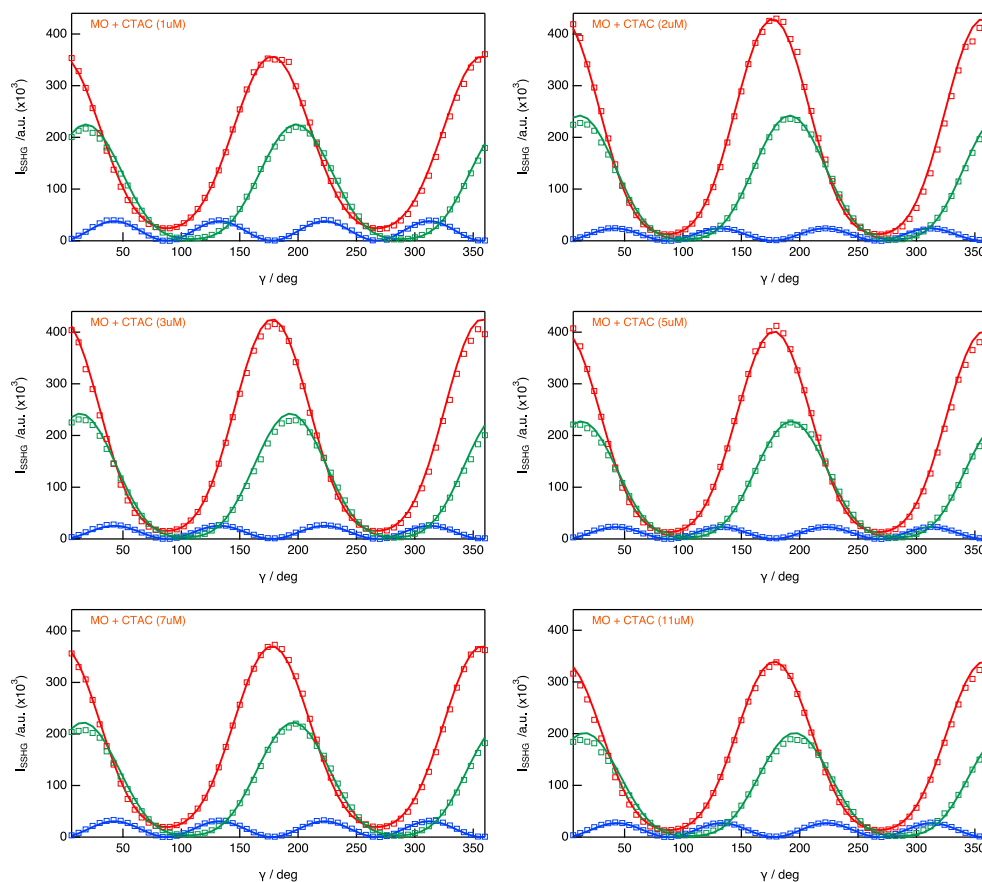
Figure 6.9: Polarization-resolved SH profiles recorded at p (red), s (blue), and 45 (green) geometries at 420 nm with MO at a concentration of 200 µM and various concentrations of CTAC at the dodecane/CTAC/water interface. The solid lines are best fits.

The average dye orientation at the interface also changes in the presence of the surfactant. The tilt angle decreases to $30°$, which, similarly to the DPPC case, reflects the intercalation of the dye in the surfactant monolayer.

The tilt angle decreases to $35°$ at 1 µM bulk concentration and then decreases to $30°$ at 2 µM concentration. The angle stays essentially constant even with increasing concentration, as we can see in Table 6.1.

The study also involved examining the effect of CB[7] at the interface. CB[7], known for its unique cavity-like structure, exhibits interesting host-guest properties. It has a hydrophobic interior cavity lined with carbonyl groups, while the exterior is hydrophilic. This combination of hydrophobic and hydrophilic regions enables CB[7] to selectively bind and encapsulate guest molecules within its cavity through non-covalent interactions such as hydrogen bonding, hydrophobic interactions, and π-π stacking.

In this study, we aimed to observe the formation of a CB[7]-MO complex, where CB[7] encapsulates the MO molecule, and understand its impact on MO adsorption and dynamics at the interface. The polarization-resolved SSHG data for two volume

concentrations of CB[7] are shown in Figure 6.10. The tilt angle of MO at the interface remains around $47°$ for both CB[7] concentrations, indicating that the dye lies slightly flatter at the interface.
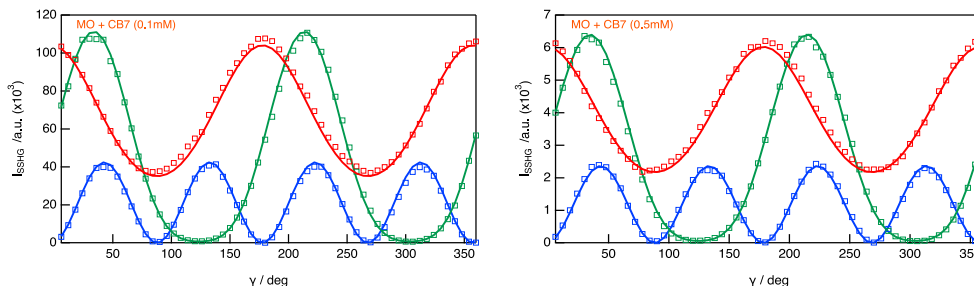
Figure 6.10: Polarization-resolved SH profiles recorded at p(red), s(blue), and 45(green) geometries at 420nm with MO at a concentration of 200 μM and two concentrations of CB[7] at the dodecane/CTAC/water interface. The solid lines represent the best fits.

6.2.3 Excited-State Dynamics at the Interface
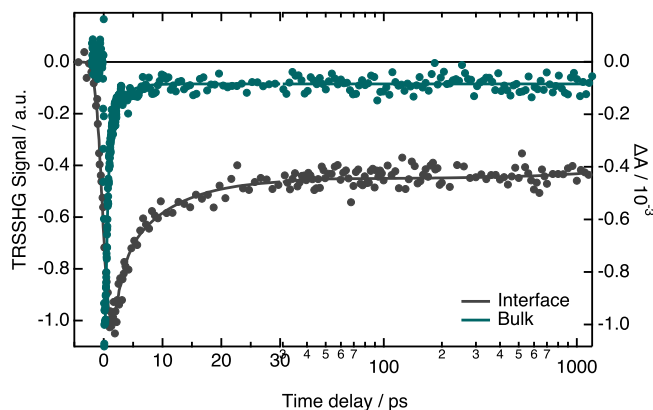
Figure 6.11: Comparison of time profiles recorded by transient absorption in bulk water and TRSSHG at the dodecane/water interface after 500 nm excitation

In addition to the polarization-resolved measurements, time-resolved SSHG measurements were conducted on the same systems to understand how the excited state dynamics of MO are influenced. Azobenzene dyes such as MO exhibit a rapid trans-to-cis photoisomerization. Figure 6.11 presents the TR-SSHG profile measured at 420nm following 500nm excitation at the dodecane/water interface. The time-dependence of the TA signal at 460nm after a 500nm excitation is shown for comparison. In MO's case, the SSHG signal resonates with $S_2 \leftarrow S_0$ or $S_1 \leftarrow S_0$ as the S_1 and S_2 are closely spaced in energy. In both scenarios, the decrease in signal upon excitation is due to the depletion of the ground state in the trans form, and the recovery mainly reflects the repopulation of this ground state, although contributions from higher states cannot be ruled out. In this instance, the signal recovery can be

c or *mma*	$\chi^{(2)}_{ZXX}/\chi^{(2)}_{XXZ}$	$\chi^{(2)}_{ZZZ}/\chi^{(2)}_{XXZ}$	*D*	θ / $^{\circ}$
dodecane/water				
200 μM	0.94 ± 0.01	2.08 ± 0.02	0.52 ± 0.01	43.6 ± 0.2
dodecane/DPPC/water				
60 $\mathring{A}^2$	0.99 ± 0.02	4.58 ± 0.04	0.69 ± 0.01	33.3 ± 0.3
dodecane/CTAC/water				
1 μM	0.82 ± 0.02	3.24 ± 0.07	0.66 ± 0.01	35.4 ± 0.4
2 μM	0.75 ± 0.04	4.48 ± 0.2	0.75 ± 0.01	30.0 ± 0.7
3 μM	0.81 ± 0.04	4.43 ± 0.2	0.72 ± 0.01	31.4 ± 0.6
5 μM	0.78 ± 0.02	4.44 ± 0.2	0.74 ± 0.01	30.0 ± 0.3
7 μM	0.82 ± 0.02	3.6 ± 0.1	0.69 ± 0.01	33.7 ± 0.3
11 μM	0.73 ± 0.02	3.75 ± 0.08	0.72 ± 0.01	32.0 ± 0.4
dodecane/CB[7]/water				
100 μM	0.94 ± 0.02	1.63 ± 0.02	0.46 ± 0.01	47.0 ± 0.3
500 μM	0.99 ± 0.01	1.66 ± 0.02	0.45 ± 0.01	47.5 ± 0.2

Table 6.1: Results from the analysis of the polarization-resolved SSHG data of MO with the different co-solutes. The global fit was performed on all three polarization components. The errors are obtained from the weighted fit procedure with 99% confidence interval using the inverse of the data standard error as weight and propagating the error through the various equations. The tilt angle θ was deduced assuming a Dirac distribution and a single dominant element of the $\overset{\leftrightarrow}{\beta}$ tensor.

reproduced with the sum of three exponential functions with time constants and amplitudes listed in Table 6.2.

An energy level scheme is shown in Figure 6.12, which is adapted from [20]. This energy level scheme provides a comprehensive representation of the electronic transitions involved and can account for the ensemble of the data. In the case of the trans form of the molecular isomer (MO), upon excitation, the population preferentially populates the S_2 $\pi\pi^*$ state. Subsequently, rapid internal conversion takes place, leading to the S_1 $n\pi^*$ state. Within the S_1 state, the excited population undergoes vibrational relaxation while progressing towards a conical intersection. At this conical intersection, two pathways become available: one involves returning to the trans ground state (referred to as Path **A**), while the other leads to the cis ground state (referred to as Path **B**).

In Figure 6.11 The fast decay likely reflects the decay of the trans excited state, followed by a long-lived plateau indicating an incomplete recovery of the ground state due to the conversion of excited trans molecules to the cis form. These data suggest that the photoisomerization efficiency is significantly higher at the water/dodecane interface compared to bulk water.
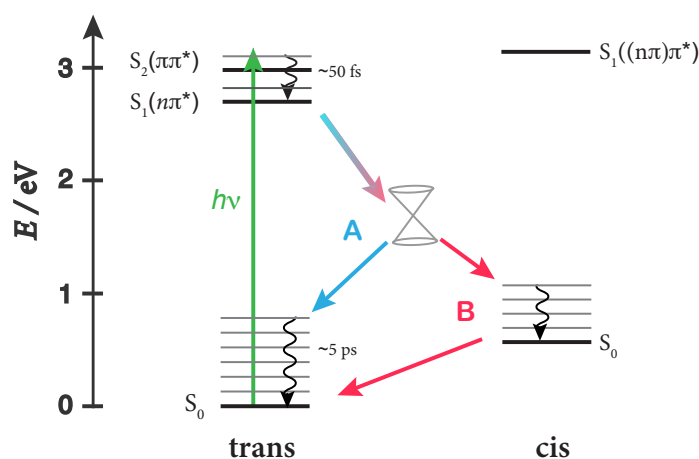
Figure 6.12: Energy level scheme illustrating the photocycle of MO in the trans form, adapted from [20].

Excited State Dynamics at Different Interfaces

For deeper insight into the properties of the adsorbed MO dyes at the interface, TR-SSHG measurements were performed with the same co-solutes as for the polarization-resolved measurements. For all the time traces, the signal was reproduced using three exponential functions, with the long-time constant (>20 ns) kept the same as for the bare dodecane/water interface, and accounting for the plateau.

At dodecane/DPPC/water and dodecane/CB[7]/water interfaces, no significant changes in dynamics were observed except for the smallest CB[7] concentration (0.1mM), where a minor alteration is seen (i.e., the short time component increases

slightly). Nevertheless, the signal was fairly noisy, and the sample with a higher concentration of CB[7] does not confirm this change and aligns closely with the results obtained at the bare dodecane/water interface.
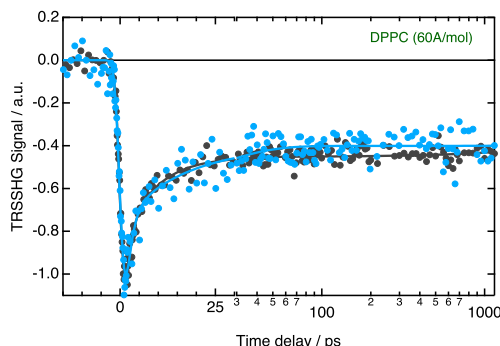
Figure 6.13: Time-resolved SSHG signal profiles recorded at 420nm after 500nm excitation of MO at the dodecane/water interface in the presence of DPPC
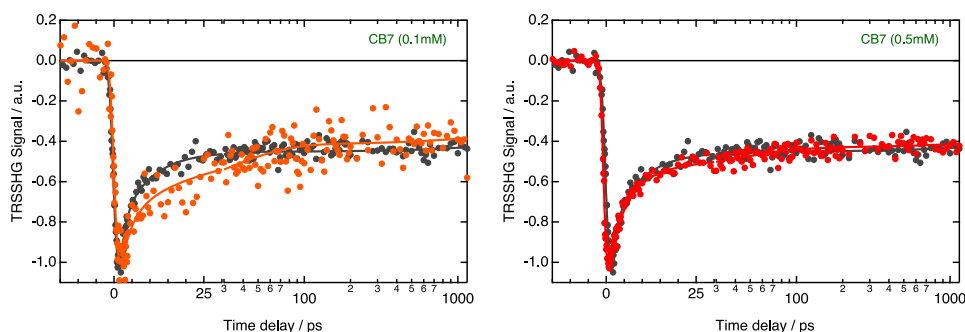
Figure 6.14: Time-resolved SSHG signal profiles recorded at 420nm after 500nm excitation of MO at the dodecane/water interface in the presence of CB[7]

On the other hand, when CTAC is added, a systematic change is observed. The long-lived plateau is less pronounced, and the ground-state recovery occurs relatively faster. Moreover, the fast components of the decay become slower with the addition of the surfactant (Figure 6.15).

A recent computational study of the photoisomerization of azobenzene embedded in a DPPC lipid membrane demonstrated that in this case, two photoisomerization mechanisms depend on the starting isomer: a torsional mechanism for the trans-to-cis isomerization and a Hula twist mechanism for the cis-to-trans isomerization [30]. Here, the presence of the DPPC membrane impedes the cis isomer from reaching the optimal dihedral angle, and the trans-to-cis photoisomerization is not fully equilibrated. The environment was shown to slow down the trans to cis isomerization due to stronger interaction of the trans isomer, i.e., through hydrophobic interactions with the tails of the DPPC membranes.
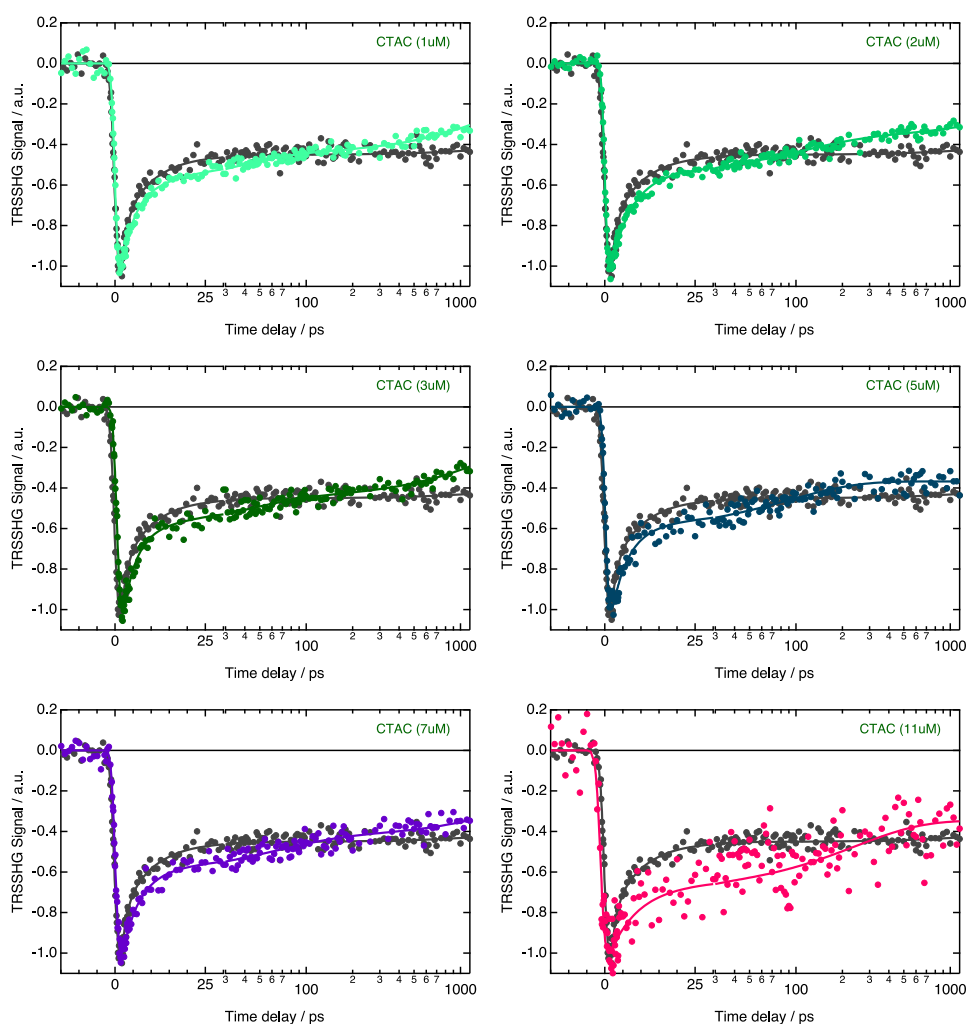
Figure 6.15: Time-resolved SSHG signal profiles recorded at 420nm after 500nm excitation of MO at the dodecane/water interface in the presence of various concentrations of CTAC

The interpretation of the TR-SSHG signal recovery is not straightforward. The absence of a plateau and the relatively rapid recovery can be attributed to two possible factors: (i) back isomerization from cis to trans (path **B**), or (ii) a fraction of the excited state population which is still decaying due to the restricted environment created by the surfactant (path **A**). The latter scenario appears more plausible. In the presence of surfactants, the MO is most likely to be intercalated within the surfactant layer, as supported by the polarisation measurements and the MD simulations. This intercalation results in a more constrained environment for the MO, which could potentially lead to a slower decay of the S_1 state along path **A**. Additionally, we cannot rule out the possibility of a plateau that could potentially be reached at longer times beyond the resolution of our experimental setup, its presence would indicate a lower photoisomerization efficiency in the presence of CTAC. However, according to ref [30], calculations show that for an azobenzene embedded in a DPPC membrane, the S_1 state decays within 8-10 ps whether it goes to the ground state or to the

c or *mma*	τ_1 (ps)	A_1	τ_2 (ps)	A_2	τ_3 (ns)	A_3
dodecane/water						
200 μM	1.1	48.7	8.3	25.2	>20	26.1
dodecane/DPPC/water						
60 $\mathring{A}^2$	1.2	57.6	14.5	20.4	>20	22
dodecane/CTAC/water						
1 μM	6.1	53.9	190	14.7	>20	31.4
2 μM	6	52.3	133	18.2	>20	29.5
3 μM	5.4	54.1	191.4	1	>20	35
5 μM	4.5	48.8	83.4	19.9	>20	31.3
7 μM	7	52.2	219.6	15.1	>20	32.7
11 μM	7.7	38.6	231.3	29.4	>20	31.9
dodecane/CB[7]/water						
100 μM	3.3	37.7	29.1	29.1	>20	33.2
500 μM	4.3	48.7	33.7	15.9	>20	35.5

Table 6.2: Time constants obtained from the multi-exponential weighted fit applied to the time-resolved SSHG data from MO. Exponential functions convolved with a Gaussian function were employed to simulate the instrument response function. The time resolution of the experiment is approximately between 1 to 2 ps

cis form, which is relatively faster compared to our experimental observations.

It's also important to note that contributions to this signal from other states cannot be discounted. To better understand the TR-SSHG results, transient absorption (TA) measurements of MO with CTAC and CB[7] were performed and are presented in the following section.

6.2.4 TA measurements

Figure 6.16 shows the TA spectra measured at different time delays after excitation at either 500 nm (a) or 532 nm (b) of MO in water. Both TA spectra exhibit similar transient features. Four distinct spectral regions can be distinguished: a positive band below 400 nm and around 550 nm, and two negative bands at 460 nm and above 620 nm. Within the first 1.5 ps, the positive band below 400 nm and the negative band above 620 nm decay entirely. Afterwards, the positive band at 550 nm decays within a few ps, and the TA spectrum becomes dominated by the negative band at 460 nm assigned to the ground-state bleach, which remains unchanged up to 1 ns, as seen clearly in Figure 6.16c.

When comparing the kinetics at the two excitation wavelengths, a slightly lower proportion of the ground-state bleach persists when exciting at 532 nm compared to 500 nm. This disparity could suggest a variation in the quantum yield of isomerization at these particular wavelengths. Additionally, in a previous study by our group [20], a more noticeable residual ground-state bleach was observed when exciting at 400 nm compared to 530 nm.
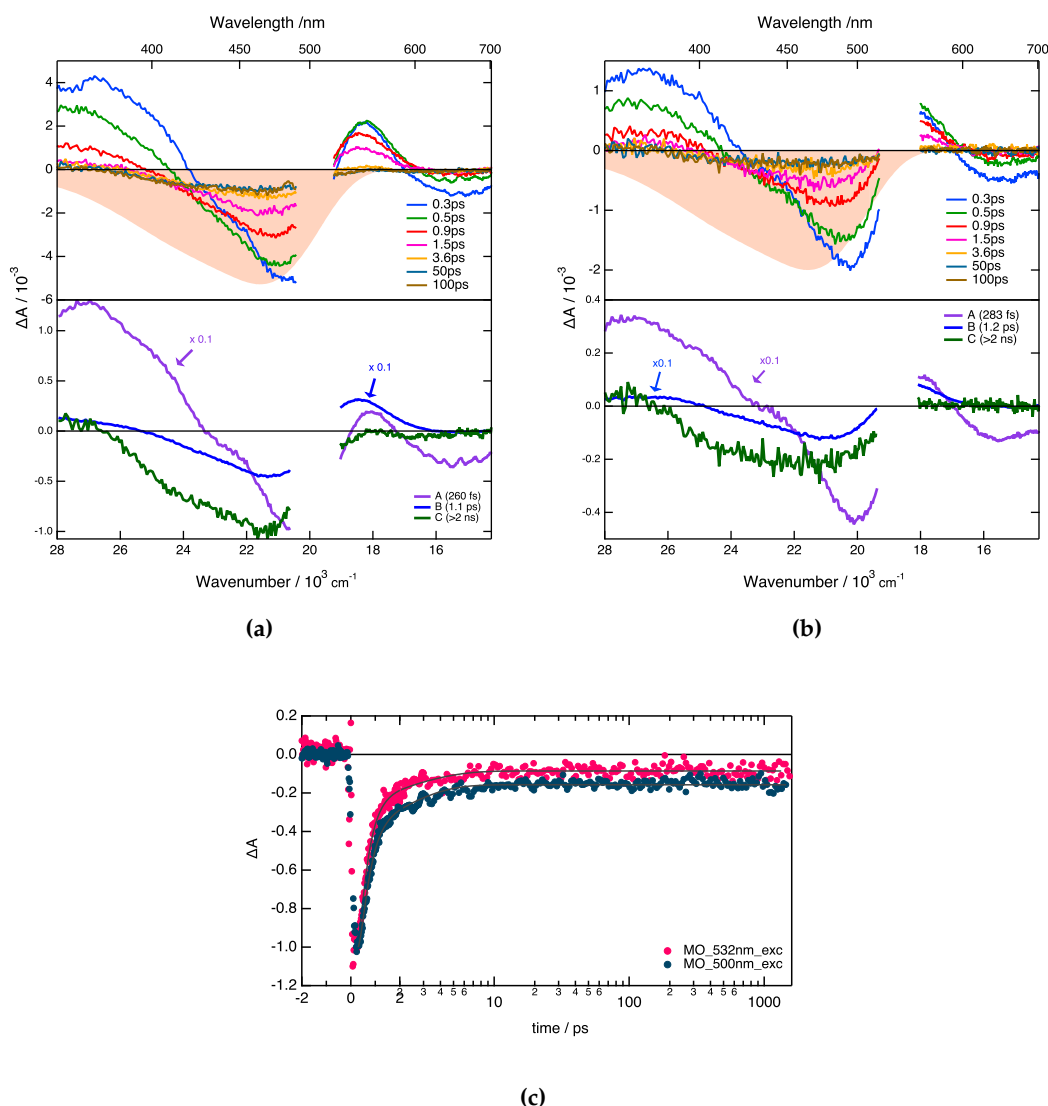
Figure 6.16: Transient absorption spectra recorded at various time delays after excitation at (a) 500 nm and (b) 532 nm of MO in water and the negative stationary spectrum. (c) Comparison between single wavelength kinetics at 480 nm for the two excitation wavelengths.

The data analysis for the following TA spectra was performed at time delays greater than 0.2-0.3 ps. A series of three successive exponential steps was found sufficient to accurately reproduce the TA dynamics. The resulting evolution-associated difference absorption spectra (EADS) are also presented. These EADS were not attributed to a single state species, and the time constants were not assigned to specific processes; instead, they can only be considered as representative time scales.

For the MO samples, the obtained results are consistent with our previous study. In summary, EADS C reveals a prolonged depletion of the ground-state population, which is attributed to the formation of the cis form of MO. EADS A exhibit a similar timescale as the lifetime of the S_1 state. Furthermore, the negative feature above 620 nm can be attributed to the overlap of stimulated emission with the positive band

at 540 nm, while the band around 400 nm corresponds to excited-state absorption. Consequently, EADS A is primarily influenced by the contribution of the S_1 state. EADS B was associated with a vibrationally hot ground state, characterized by a positive band resulting from induced absorption on the red side of the bleach.

Similar TA measurements were performed in the presence of CB[7] and CTAC. Figure 6.17 shows the TA results obtained with CB[7] at an MO and CB[7] concentration ratio of 1, as shown in Figure 6.2. The spectral features appear similar; however, the negative band in the red region of the TA spectrum is more pronounced at early times and likely overlaps with the positive feature around 570 nm, resulting in a slow rise at very short timescales. Within 1.5 ps, the negative band corresponding to the ground-state bleach exhibits some structure compared to the MO measurements in solution. This negative feature decays almost entirely, leaving only a very small residual plateau observed at longer times, as shown in Figure 6.17b. This small residual plateau was also observed in previous measurements in HFP.
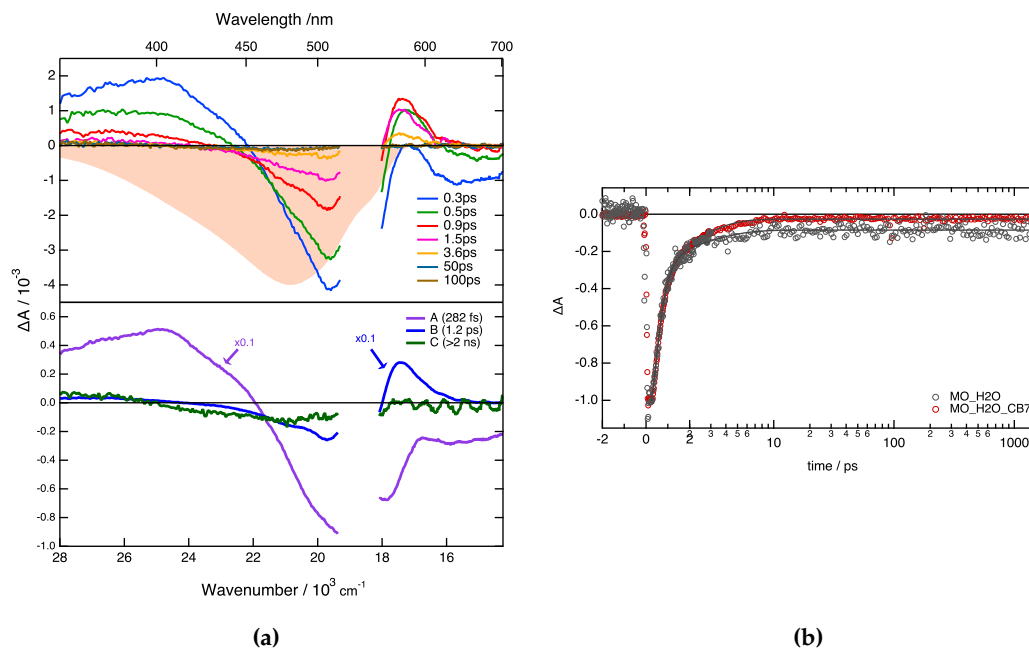
Figure 6.17: (a) Transient absorption spectra recorded at various time delays after 532 nm excitation of MO in water in the presence of CB[7] and the negative stationary spectrum. (b) Comparison between single wavelength kinetics taken in the bleach for MO alone or in the presence of CB[7].

Figure 6.18 shows the results obtained from the TA measurements of MO in the presence of CTAC at a concentration of 2 mM. The TA spectrum obtained in this case is quite different. Only three spectral regions can be distinguished, and the negative feature above 620 nm observed in MO alone is not present in this TA data. The TA spectra exhibit a broad positive band above 550 nm, which decays within 49 ps. The other positive band, present below 420 nm, reaches its maximum at 0.3 ps and then decays slowly until it reaches a plateau at around 50 ps, showing no

significant changes thereafter. The negative feature, attributed to the ground-state bleach, exhibits a small rise within the first 500 fs, followed by a decay on the same timescales as the positive feature below 400 nm. A plateau is reached within 200 ps and remains unchanged for the rest of the experimental time, as can be seen in Figure 6.18b.

(a)	**(b)**
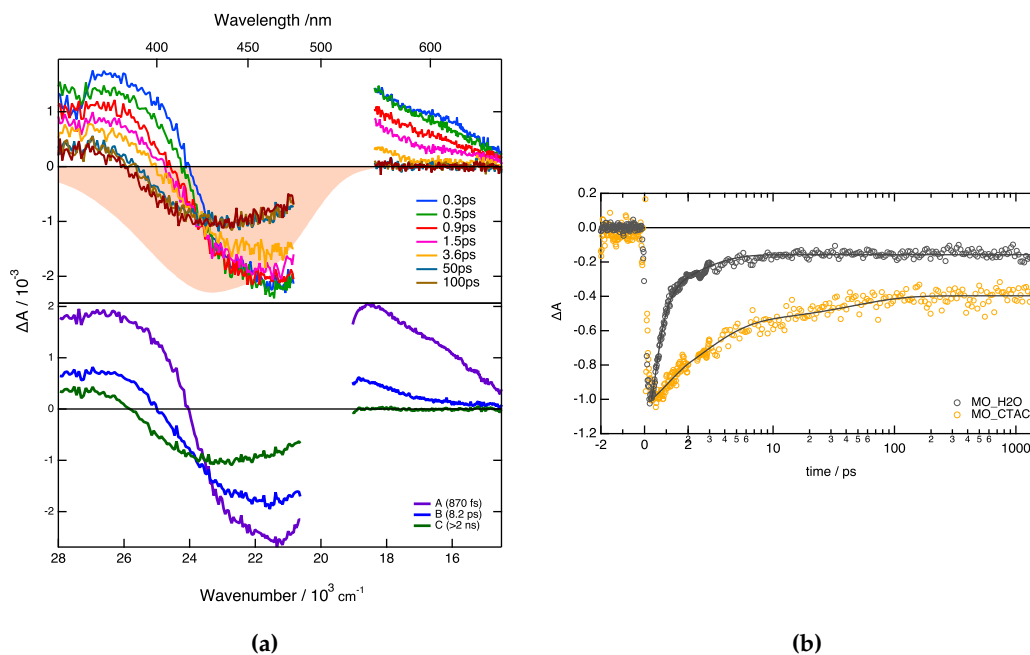
Figure 6.18: (a) Transient absorption spectra recorded at various time delays after 500 nm excitation of MO in water in the presence of 2 mM CTAC and the negative stationary spectrum. (b) Comparison between single wavelength kinetics taken in the bleach for MO alone or in the presence of CTAC.

To gain further insight into the rotational dynamics of MO in the micelle environment, we calculated the rotational correlation functions (rcf) from the MD simulations. These results are shown in Figure 6.19..
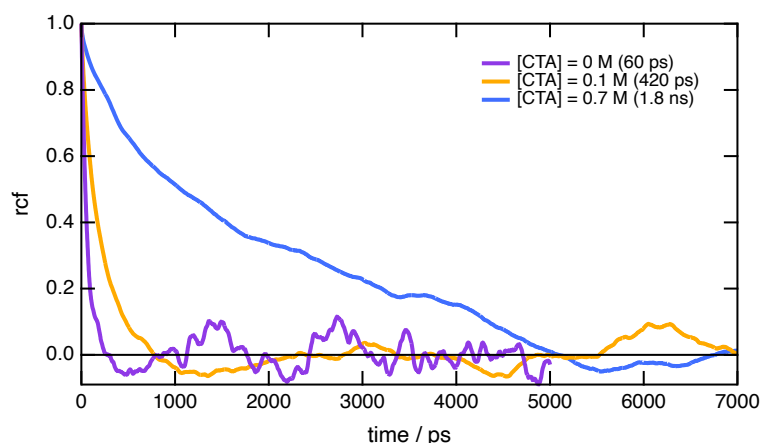
Figure 6.19: The rotational correlation function (RCF) at different CTA concentrations. The rotational correlation time (τ) obtained by fitting the rcf time dependence to an exponential decay function is shown in brackets.

The time dependence of the rcf for MO in water and in the presence of two concentrations of CTA is shown. We observe that for MO in water, the rcf displays a rapid decay with a rotational correlation time of 60 ps. This time increases to 204 ps with the lowest concentration of CTA (0.1 M). At a higher concentration of CTA (0.7 M), the rcf significantly slows down, with a rotational correlation time of 1.8 ns. This indicates that the motion of the molecule within the micelle is substantially restricted. This observation aligns with the slowdown of the faster component and the larger plateau seen in the TA data.

6.3 Conclusion

The objective of this study was to investigate how various environments affect the photophysics and photoisomerization of MO. Our results indicate that the environment plays a significant part in the photophysics of MO. The first observation was that the efficiency of photoisomerization is greater at the interface than in bulk water. As we know from previous work [20], the solvent's hydrogen bond donating ability can affect photoisomerization efficiency. The higher photoisomerization efficiency at the interface might be due to the dye predominantly located in the dodecane phase, which constitutes a less protic environment, as predicted by molecular dynamics (MD) simulations. Other factors, such as polarity, might also have an impact and cannot be ruled out.

Upon adding CTAC to bulk water, a slowdown of the faster component was observed along with a larger plateau, suggesting an increased photoisomerization efficiency. As previously mentioned, the dye is expected to intercalate into the CTA micelle, as predicted by MD simulations. The changes in the dynamics could be due to the constrained environment experienced by the dye, which might affect the

large amplitude motion on the S_1 potential energy surface or changes in the environment's polarity or hydrogen bonding ability. It's noteworthy that the dynamics and photoisomerization of MO intercalated in the micelle closely match those measured at the interface. The lifetimes (0.9ps/8.2ps/>2ns) and (1.1ps/8.3ps/>20ns) in the micelle and at the bare dodecane/water interface respectively are relatively similar. The photoisomerization efficiency is also very comparable. This observation suggests that the environment in the micelle may be quite similar to the one at the interface and the results from the water/dodecane and the bulk in presence of CTAC appear consistent. The introduction of CTAC at the water/dodecane interface leads to changes that do not seem to be concentration-dependent. One noticeable change is the alteration in the plateau, which is not yet fully understood.

The addition of CB[7] at the interface appears to have minimal effect. In the bulk, the efficiency of isomerization decreases, and an inhomogeneous band is observed in the ground state bleach, suggesting the possible existence of distinct populations —Maybe one that interacts with CB[7] and another that does not-. To obtain further insights, future transient absorption measurements at different wavelengths and various concentrations of CB[7] are planned to gather more information.

While our study provides important insights into the photoisomerization efficiency of the dye in various environments. We can't conclude anything about the specific isomerization mechanism at work. Whether the process is dominated by rotational or inversion transitions remains unclear from our current results. A mechanism such as inversion, as suggested by Rau [31], is expected to show little dependency on friction. Interestingly, the dynamics at the water interface are slower by a factor of 5-7 compared to the bulk. This factor aligns with findings from previous studies conducted by our group [32, 33], where chromophores exhibit a friction-dependent non-radiative decay. The constrained environment investigated here seems to have a significant influence on the large amplitude motion of MO but other mechanisms could also be at play. Future studies are planned to further elucidate the isomerization process.

Bibliography

(1) Bandara, H. M. D.; Burdette, S. C. *Chem. Soc. Rev.* **2012**, *41*, 1809–1825.

(2) A. Beharry, A.; Andrew Woolley, G. *Chem Soc Rev* **2011**, *40*, 4422–4437.

(3) Bozovic, O.; Jankovic, B.; Hamm, P. *Nat Rev Chem* **2022**, *6*, 112–124.

(4) Magni, A.; Bondelli, G.; Paternò, G. M.; Sardar, S.; Sesti, V.; D'Andrea, C.; Bertarelli, C.; Lanzani, G. *Phys. Chem. Chem. Phys.* **2022**, *24*, 8716–8723.

(5) Goulet-Hanssens, A.; Barrett, C. J. *J. Polym. Sci.* **2013**, *51*, 3058–3070.

(6) Zarins, E.; Balodis, K.; Ruduss, A.; Kokars, V.; Ozols, A.; Augustovs, P.; Saharovs, D. *Opt. Mater.* **2018**, *79*, 45–52.

(7) Spiridon, M. C.; Iliopoulos, K.; Jerca, F. A.; Jerca, V. V.; Vuluga, D. M.; Vasilescu, D. S.; Gindre, D.; Sahraoui, B. *Dyes Pigm.* **2015**, *114*, 24–32.

(8) Gindre, D.; Boeglin, A.; Fort, A.; Mager, L.; Dorkenoo, K. D. *Opt. Express, OE* **2006**, *14*, 9896–9901.

(9) Erbas-Cakmak, S.; Leigh, D. A.; McTernan, C. T.; Nussbaumer, A. L. *Chem. Rev.* **2015**, *115*, 10081–10206.

(10) Choi, Y.-J.; Kim, J.-T.; Yoon, W.-J.; Kang, D.-G.; Park, M.; Kim, D.-Y.; Lee, M.-H.; Ahn, S.-k.; Jeong, K.-U. *ACS Macro Lett.* **2018**, *7*, 576–581.

(11) Aprahamian, I. *ACS Cent. Sci.* **2020**, *6*, 347–358.

(12) Amirjalayer, S.; Buma, W. J. *Chem. Eur. J.* **2019**, *25*, 6252–6258.

(13) Chang, C.-W.; Lu, Y.-C.; Wang, T.-T.; Diau, E. W.-G. *J. Am. Chem. Soc.* **2004**, *126*, 10109–10118.

(14) Fregoni, J.; Granucci, G.; Coccia, E.; Persico, M.; Corni, S. *Nat Commun* **2018**, *9*, 4688.

(15) Henzl, J.; Mehlhorn, M.; Gawronski, H.; Rieder, K.-H.; Morgenstern, K. *Angew. Chem. Int. Ed.* **2006**, *45*, 603–606.

(16) Aleotti, F.; Nenov, A.; Salvigni, L.; Bonfanti, M.; El-Tahawy, M. M.; Giunchi, A.; Gentile, M.; Spallacci, C.; Ventimiglia, A.; Cirillo, G.; Montali, L.; Scurti, S.; Garavelli, M.; Conti, I. *J. Phys. Chem. A* **2020**, *124*, 9513–9523.

(17) Rinuy, J.; Piron, A.; Brevet, P. F.; Blanchard-Desce, M.; Girault, H. H. *Chem. Eur. J.* **2000**, *6*, 3434–3441.

(18) Piron, A.; Brevet, P. F.; Girault, H. H. *J. Electroanal. Chem.* **2000**, *483*, 29–36.

(19) Olaya, A. J.; Brevet, P.-F.; Smirnov, E. A.; Girault, H. H. *J. Phys. Chem. C* **2014**, *118*, 25027–25031.

(20) Nançoz, C.; Licari, G.; Beckwith, J. S.; Soederberg, M.; Dereka, B.; Rosspeintner, A.; Yushchenko, O.; Letrun, R.; Richert, S.; Lang, B.; Vauthey, E. *Phys. Chem. Chem. Phys.* **2018**, *20*, 7254–7264.

(21) He, S.; Sun, X.; Zhang, H. *J. Mol. Struct.* **2016**, *1107*, 182–188.

(22) Kommidi, S. S. R.; Smith, B. D. *Molecules* **2022**, *27*, 5440.

(23) Wu, J.; Isaacs, L. *Chem. Eur. J.* **2009**, *15*, 11675–11680.

(24) Neumann, M. G.; Schmitt, C. C.; Iamazaki, E. T. *Carbohydr. Res.* **2003**, *338*, 1109–1113.

(25) Li, D.; Li, H.; Fu, Y.; Zhang, J.-L.; Li, W.; Han, Y.-C.; Wang, L. *Colloid J* **2008**, *70*, 747–752.

(26) Pimenta, Â. C. M.; Andrade-Filho, T.; Manzoni, V.; Del Nero, J.; Gester, R. *Theor Chem Acc* **2019**, *138*, 27.

(27) Licari, G.; Beckwith, J. S.; Soleimanpour, S.; Matile, S.; Vauthey, E. *Phys. Chem. Chem. Phys.* **2018**, *20*, 9328–9336.

(28) Licari, G.; Cwiklik, L.; Jungwirth, P.; Vauthey, E. *Langmuir* **2017**, *33*, 3373–3383.

(29) B. Fainerman, V.; V. Aksenenko, E.; Mucic, N.; Javadi, A.; Miller, R. *Soft Matter* **2014**, *10*, 6873–6887.

(30) Osella, S.; Granucci, G.; Persico, M.; Knippenberg, S. *J. Mater. Chem. B* **2023**, *11*, 2518–2529.

(31) Rau, H.; Lueddecke, E. *J. Am. Chem. Soc.* **1982**, *104*, 1616–1620.

(32) Fita, P.; Fedoseeva, M.; Vauthey, E. *Langmuir* **2011**, *27*, 4645–4652.

(33) Richert, S.; Mosquera Vazquez, S.; Grzybowski, M.; Gryko, D. T.; Kyrychenko, A.; Vauthey, E. *J. Phys. Chem. B* **2014**, *118*, 9952–9963.

Chapter 7

Photoinduced Electron Transfer in a Porphyrin Fullerene Dyad at a Liquid Interface
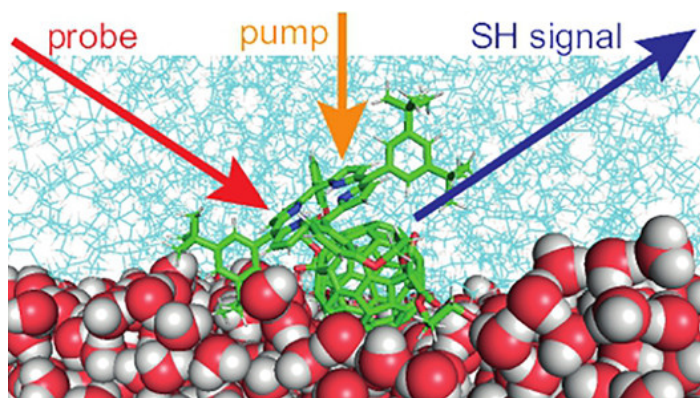
Article

Photoinduced Electron Transfer in a Porphyrin−Fullerene Dyad at a Liquid Interface

Jihad Sissaoui, Alexander Efimov, Tatu Kumpulainen,* and Eric Vauthey*

Read Online

ACCESS | Metrics & More | Article Recommendations | SI Supporting Information

ABSTRACT: The excited-state properties of an amphiphilic porphyrin−fullerene dyad and of its porphyrin analogue adsorbed at the dodecane/water interface are investigated by using surface second-harmonic generation. Although the porphyrin is formally centrosymmetric, the second-harmonic spectra of both compounds are dominated by the intense Soret band of the porphyrin. Polarization-selective measurements and molecular dynamics simulations suggest an angle of about 45° between the donor−acceptor axis and the interfacial plane, with the porphyrin interacting mostly with the nonpolar phase. Time-resolved measurements reveal a marked concentration dependence of the dynamics of both compounds upon Q-band excitation, indicating the occurrence of intermolecular quenching processes. The significant differences in dynamics and spectra between the dyad and the porphyrin analogue are explained by a self-quenching of the excited dyad via an intermolecular electron transfer.
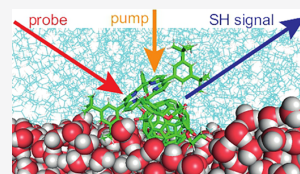
INTRODUCTION

Interfaces between two immiscible liquids are involved in many areas of science and technology.[1−7] Because the molecules experience an asymmetry of forces at the interface, their orientation is not isotropic, giving rise to properties that can significantly differ from those of the two constituting liquids. This, in turn, can have a strong impact on the chemical reactivity. These specific properties of liquid interfaces are exploited in "on-water" chemistry, where reactions between organic reactants are accelerated in the presence water.[8−13] However, the current understanding of the chemical dynamics at liquid interfaces is still limited. This is mostly due to their typical thickness of 1−2 nm and, consequently, to the extremely small number of molecules in this region relative to those in the bulk phases. Therefore, the spectroscopic response from the interface is usually buried in the response arising from the bulk, unless a surface-selective technique is used.

Herein, we report on our investigation of the excited-state properties of an electron donor−acceptor dyad at the dodecane/water interface using surface second-harmonic generation (SSHG). Despite the relevance of interfacial charge-transfer processes, this technique has still been rarely applied for studying the dynamics of photoinduced electron transfer at liquid interfaces.[14,15] SSHG is selective to the interface between two isotropic media as it probes the second-order nonlinear optical susceptibility, $\overleftrightarrow{\chi}^{(2)}$, which, under the dipolar approximation, is zero in centrosymmetric materials.[16−21] The magnitude of the tensor elements of $\overleftrightarrow{\chi}^{(2)}$ is strongly frequency dependent, and its spectrum consists of bands arising from one- and two-photon resonances. We exploit the electronic resonance enhancement so that the second-harmonic (SH) signal originates only from the dyad and not from dodecane or water molecules.

Dyad **1** consists of a free-base tetraphenylporphyrin (H$_2$TPP) doubly linked to a C$_{60}$ fullerene (Chart 1). Substitution on the porphyrin and fullerene subunits confers an amphiphilic character, as shown by a previous study, where Langmuir−Blodgett monolayers of this dyad were prepared.[22] According to previous time-resolved studies,[23−25] local excitation of the porphyrin subunit is followed by the ultrafast

Chart 1. Structures of Dyad 1 and the Porphyrin-Only Analogue 2

4723
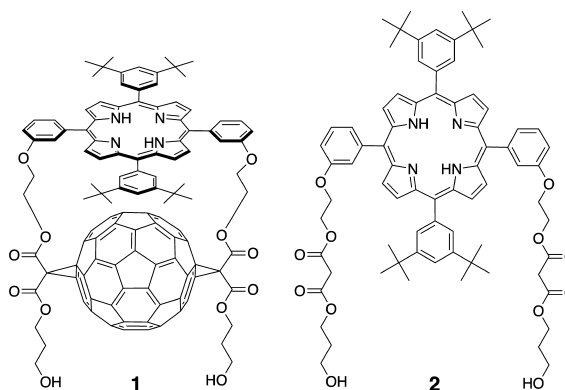
population of a delocalized excited state interpreted as an exciplex.[26] In polar solvents, the latter evolves in a few picoseconds into a charge-separated state with a subnanosecond lifetime. In nonpolar media, the exciplex decays back to the ground state on a few nanoseconds time scale.

We compare the excited-state dynamics of the dyad with those of the donor porphyrin analogue (**2**, Chart 1) using time-resolved SSHG. Information on the orientation of these two molecules at the interface is obtained by using both polarized SSHG and molecular dynamics (MD) simulations. The results suggest that the excited-state dynamics of both compounds at the interface is dominated by self-quenching processes, which, in the case of the dyad, involve intermolecular charge separation. In this respect, these interfacial dynamics differ significantly from those measured in solution.

■ METHODS

Samples. The synthesis of dyad **1** and of the reference compound **2** was reported in ref 27. Dodecane (>99%) was purchased from Alfa Aesar. Water was purified by using a Milli-Q Reference system before use.

The samples were prepared by adding a specific volume (between 0.5 and 7 μL) of a 0.1 mM solution of the dye in CHCl$_3$ on the lower aqueous phase located in a $4 \times 4 \times 4$ cm^3 cubic quartz cell. Dodecane was slowly added after ~10 min, allowing the CHCl$_3$ to evaporate. All measurements were performed at room temperature.

Surface Second-Harmonic Generation. *Experimental Setup.* The SSHG setup was based on a 1 kHz amplified Ti:sapphire system (Solstice, Spectra-Physics) and was described in detail before.[28,29] Briefly, the SSHG probe pulses (100 fs, 0.7 μJ, and 130 μm $\times$ 340 μm spotsize at the interface) were generated with a collinear optical parametric amplifier (Topas C, Light Conversion) and were focused onto the interface with an angle of incidence just above the critical angle for total internal reflection, which amounts to about 70° for the dodecane/water interface between 350 and 1200 nm. Their polarization was controlled with a half-wave plate. The conventional notation for the polarization is used: p for parallel polarization with respect to the plane of incidence and s for perpendicular polarization and 45°. The reflected pulses were guided through a combination of irises, filters, and spectrograph to eliminate the reflected probe light before reaching a CCD camera (Newton 920, Andor). No SH signal could be detected at the dodecane/water interface without the dye.

Stationary Second-Harmonic (SH) Spectra. Stationary SH spectra were recorded by scanning the wavelength of the probe pulses with 5 nm steps. They were measured at $\gamma = 45°/s$ polarization geometry. The spectra were corrected by using the SH spectrum from a Al mirror immersed in dodecane.[30] The resulting spectral intensity is termed I_{SH}. The SH spectra are usually displayed by using $\sqrt{I_{SH}}$, as this quantity is proportional to the concentration of harmonophores.

Polarization-Resolved SSHG. For polarization-selective measurements, the polarization angle of the incident beam at 860 or 840 nm, γ, was controlled with a half-wave plate mounted on a motorized rotatory stage, and a given polarization component of the steady-state SH signal was selected by using a wire-grid polarizer.[30] The resulting signal intensity is termed I_{SH}.

Time-Resolved SSHG. For TR-SSHG measurements, a pump pulse channel that can be delayed with respect to the probe pulse was added to the SSHG setup. The pump pulses were at 520 nm (80 fs, 0.8 μJ, and 180 μm $\times$ 500 μm spotsize at the interface) and were generated with a noncollinear optical parametric amplifier (Topas White, Light Conversion). This wavelength corresponds to the Q$_y$ transition of the porphyrin subunit. These pulses were circularly polarized to avoid photoselection and were focused on the interface from the top by using a combination of spherical and cylindrical lenses and overlapped with the probe pulses. As a consequence, the SH signal is resonant with the Soret band transition of the porphyrin subunit.

The TR-SSHG profiles were recorded by using the 45°/s polarization, where the signal intensity is the highest. No significant dependence of the dynamics on the polarization was observed. To correct for the fluctuations of the probe beam intensity, a chopper was used to reduce the pump pulse repetition rate by a factor of 2 relative to the probe pulse. The reflected SH signal was directed onto the spectrograph entrance slit by using a mirror mounted on a galvanometer oscillating at the same frequency (500 Hz). The SH signals coming from the pumped and the nonpumped sample hit different spots on the CCD camera and were measured separately. The TR-SSHG profiles were processed by taking the square root of the pumped SH signal intensity divided by the square root of the nonpumped signal intensity, and were then normalized, so that it changes from 1 to 0 upon photoexcitation. As the SSHG is purely resonant, the resulting signal, $S(t)$, directly reflects the photoinduced changes in population.

Molecular Dynamics (MD) Simulations. MD simulations were performed by using GROMACS 2021.2.[31] The topology files for **1** and **2**, based on the AMBER99SB-ILDN force field,[32,33] were generated by using the Antechamber Python parser interface (ACPYPE) tool,[34] with as input the optimized structures obtained from DFT quantum-chemical calculations (B3LYP/6-31G+d)[35] as implemented in the Gaussian 16 package.[36] For the dyad **1**, the force field parameters of the fullerene were taken from ref 37. The atomic charges were determined from CHELPG fits of the electrostatic potential obtained from the DFT calculations.[38] The TIP3P model was used for water,[39] whereas for dodecane, the atom types obtained from ACPYPE were changed to distinguish two different sets of carbon and hydrogen types for the CH$_3$ and CH$_2$ groups with the Lennard-Jones parameters taken from ref 40. Without this modification, the simulated dodecane freezes at room temperature.[41] A periodic rectangular box ($6 \times 6 \times 11$ nm^3) with two dodecane/water interfaces was used for the simulations. It contained 512 dodecane molecules and either 5850 water molecules and two dyads or 5906 water molecules and two porphyrin-only dyes **2**. Simulations were performed at constant pressure and temperature (295 K) with 2 fs steps for 40−150 ns. Further details on the simulation parameters can be found in the Supporting Information.

■ RESULTS AND DISCUSSION

Origin of the SH Signal. The stationary SH spectra recorded with **1** and **2** at the dodecane/water interface are compared with their electronic absorption spectra in CHCl$_3$ in Figure 1. The SH spectra are dominated by a band peaking at 428 nm, which can be assigned to an electronic resonance associated with the Soret band of the H$_2$TPP subunit. The larger width of this SH band compared to the corresponding
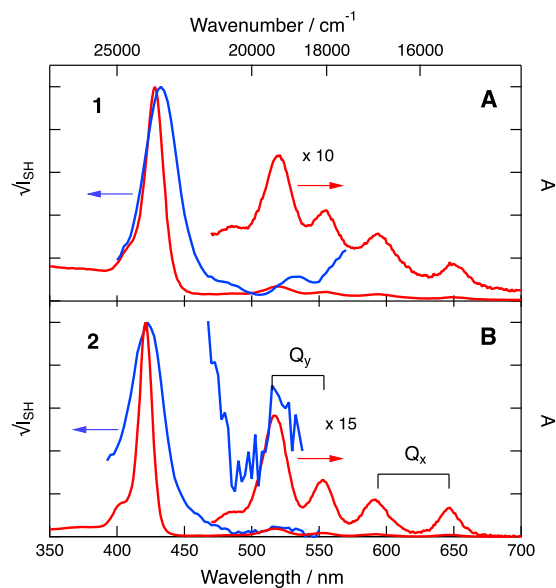
Figure 1. Stationary electronic absorption and SH spectra recorded with **1** (A) and **2** (B) in CHCl$_3$ and at the dodecane/water interface.

Orientation at the Interface. Polarization-resolved SSHG measurements were performed to get information about the orientation of **1** and **2** at the interface. Figure 2 shows

Figure 2. Polarization-resolved SH profiles recorded at γ/x (x = p, 45, or s) geometries with **1** (A, 430 nm) and **2** (B, 420 nm) at the dodecane/water interface. The solid lines are best fits of eqs S2−S4.

absorption band is mostly due to the ∼10 nm spectral width of the SH probe pulse.

Both the SH and absorption bands of the dyad **1** are red-shifted by about 400 cm^{-1} relative to those of the reference porphyrin **2**. Furthermore, the absorption band of **1** is markedly broader than that of **2**, that is, 930 versus 620 cm^{-1}. The Soret band is due to two quasi-degenerate porphyrin transitions,[42] and the larger width with **1** was attributed to interactions with the fullerene subunit, which lead to an increased energy splitting of these two transitions.[23] In principle, centrosymmetric molecules like porphyrins do not have any nonzero element of the hyperpolarizability tensor, $\vec{\beta}$, and should thus not give any SH signal.[43] However, the SH response from porphyrins is well-documented[44−48] and has been explained by structural distortions in the asymmetric interfacial environment, resulting in nonzero tensor elements of $\vec{\beta}$. Moreover, the dyad is not centrosymmetric, and according to quantum-chemical calculations described in the Supporting Information (section S2), it has a nonzero $\vec{\beta}$. The same is also true for **2** because of the long-chain substituents that are oriented toward the aqueous phase. These calculations suggest that $\vec{\beta}$ becomes particularly large when the SHG signal is resonant with the Soret band transitions, in agreement with the observations. The SH spectra of both **1** and **2** show also weaker features above 500 nm that can be associated with the Q bands. The relative intensity of these features is significantly larger for **1** than for **2**. This could be attributed to perturbations of the electronic structure of the porphyrin due to the presence of the fullerene subunit and/or to a contribution to the SH signal from the fullerene, which has electronic resonances in this spectral region.[49]

Independently of the origin of the difference between the electronic absorption and SH spectra, these results confirm that both **1** and **2** are located at the interface and are responsible for the measured SH signal. This is further confirmed by the absence of a signal without dye at the dodecane/water interface.
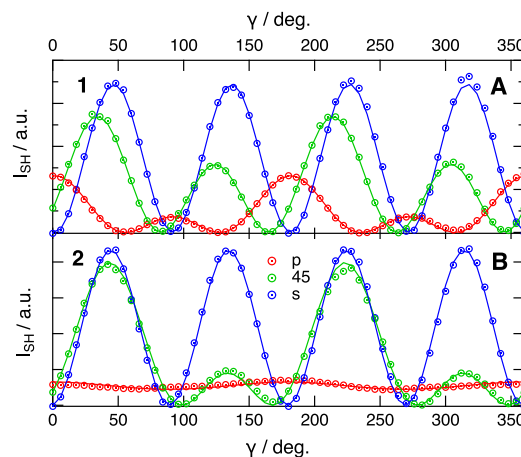
polarization profiles obtained upon measuring the intensity of three polarization components of the SH signal, namely parallel (p), perpendicular (s), and at 45° relative to the plane of incidence, as a function of the polarization angle of the probe field, γ. The p and 45° profiles recorded with **1** and **2** are markedly distinct. They point to differences in the symmetry of the second-order nonlinear susceptibility tensor:[16,17]

$$\vec{\chi}^{(2)} \propto N\langle\vec{\beta}\rangle \qquad (1)$$

where N is the surface density of the dyes and the angle brackets denote orientational averaging. Analysis of these profiles allows for the determination of the relative magnitude of the three independent nonzero tensor elements of $\vec{\chi}^{(2)}$ (see the Supporting Information section S1 for details).[17,50−53] The latter can, in turn, be used to estimate the orientation parameter D:

$$D = \frac{\langle\cos^3\theta\rangle}{\langle\cos\theta\rangle} \qquad (2)$$

where θ is the tilt angle between the transition dipole moment associated with the resonance probed by SSHG and the normal to the interface. To do this, the dominant elements of the hyperpolarizability tensor have to be known. Given that the SH signal is due to the porphyrin subunit, chemical intuition suggests that the dominant tensor elements should be associated with the porphyrin plane, where the transition dipoles are located. This is confirmed by quantum-chemical calculations of $\vec{\beta}$ ($-2w, w, w$) with $2w$ corresponding to the Soret band transition frequency, which suggest that the dominant tensor elements are β_{zzz} and β_{zxx}, with the molecular-frame axes x and z located in the plane (see the Supporting Information, section S2). With this definition, θ is the angle between the porphyrin plane and the normal to the interface.

Analysis of the polarization curves, assuming a delta distribution of the tilt angle, yields θ values of 45° and 56°

for **1** and **2**, respectively. This indicates that the orientation of the dyad **1** is such that its porphyrin subunit lies less flat at the interface than the reference **2**.

Figure 3A depicts snapshots of **1** and **2** at the dodecane/water interface taken from 40 to 150 ns MD simulations. Both

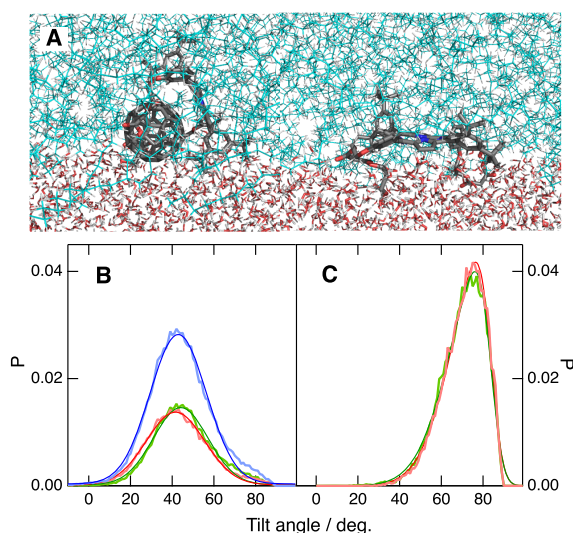**Figure 3.** Snapshots from MD simulations of the dyad **1** and the porphyrin reference **2** at the dodecane/water interface (A); distributions of tilt angle θ obtained from two 100 ns (for **1**, B) and 40 ns (for **2**, C) trajectories. The blue curve in (B) is the sum of the two distributions.

molecules were initially inserted in the aqueous phase and moved to the interface within 1 ns. After this period, they remained adsorbed at the interface during the whole simulation time. These snapshots reveal that the porphyrin and the fullerene subunits of the dyad, both of which are hydrophobic, are mostly located in the dodecane phase and that interaction with the aqueous phase occurs mainly via the two hydrophilic chains. This is confirmed by density profiles (Figure S3) which indicate that the density associated with **1** is not distributed symmetrically relative to the interface plane but is centered on the dodecane side.

The most probable orientation of the dyad with the porphyrin plane at about 40° from the interface normal minimizes the contact of the two hydrophobic subunits with water while keeping the end of both arms in an aqueous environment. Figure 3B shows histograms of the tilt angle θ of **1** extracted from the last 100 ns of two 150 ns trajectories. The small differences between these two distributions point to slow fluctuations of the orientation, which would require very long simulation times to be properly sampled. Given the similarity of these two distributions, we assume that their sum, also presented in this figure, accounts reasonably well for the orientation of the dyad. It can be reproduced by using a Gaussian function centered at 43° with a 13° root-mean-square (rms) width.

In the case of the analogue **2**, 40 ns trajectories were sufficient to obtain identical histograms of the tilt angle, with a maximum at 76° (Figure 3C). They can be reproduced by using a skewed Gaussian function with a rms width of 16°. As illustrated in Figure 3A, the porphyrin plane of **2** lies almost

flat at the interface, with the hydrophilic chains penetrating in the aqueous subphase. Although slightly centered on the dodecane side, the density profile of dye **2** extends less in this phase than that of the dyad (Figure S3).

The difference of tilt angle deduced from the polarization curves and the MD simulations of **2** can to a large extent be explained by the assumption of a delta distribution of θ, which is not supported by the MD simulations. As discussed by Simpson and Rowlen,[54] a Gaussian distribution of θ centered at 76° with a width of 16° should give an apparent tilt angle of about 60° when assuming delta distribution (Figure S1). This is in better agreement with the 56° value determined from the polarization profiles. The effect of a distribution decreases as the center of this distribution approaches 39.2°.[54] For this reason, a 13° wide distribution of θ around 43°, as found for the dyad, should give a similar apparent angle (Figure S1).

Excited-State Dynamics. Figure 4A shows time-resolved (TR) SH profiles, $S(t)$, recorded at 430 nm upon 520 nm
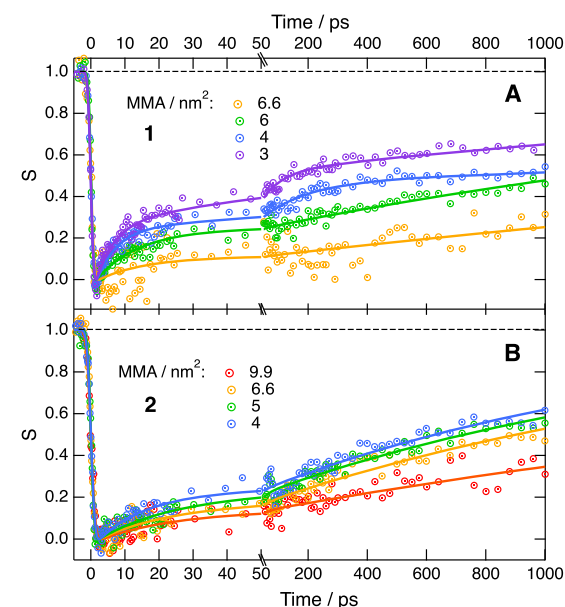
Figure 4. Time-resolved SSHG signal, $S(t)$, profiles recorded at 430 nm (**1**) or 420 nm (**2**) after 520 nm excitation of the dyad **1** (A) or the porphyrin analogue **2** (B) at different concentrations, expressed in mean molecular area (MMA), at the dodecane/water interface. The solid lines are best multiexponential fits.

excitation of the dyad **1** at different concentrations at the water/dodecane interface. Those measured with **2** at 420 nm are shown for comparison (Figure 4 B). As mentioned above, $S(t)$ reflects the photoinduced change in population. This approximation is valid here because the signal is purely resonant.

As an alternative to concentration, we use the mean molecular area (MMA), that is, the interfacial area available per dye molecule, calculated by assuming that all dyes are adsorbed. Full coverage of the interface can be estimated to correspond to a MMA of about 3 nm².[22]

For both molecules, photoexcitation in the Q-band region leads to a prompt decrease of the SH intensity. The ensuing recovery dynamics of $S(t)$ are accelerated with increasing dye

concentration for both **1** and **2**. At the lowest concentration (highest MMA), the signal recovers by only about 20−30% after 1 ns. As the concentration is increased (MMA decreased), the amount of recovery becomes larger due to the presence of fast components. For the dyad, these faster dynamics of $S(t)$ can be reproduced by using exponential functions with ~5 and ~100 ps time constants (Table S3). For the reference **2**, a single-exponential function with an ~20 ps time constant is sufficient to reproduce the initial dynamics. At a given concentration, the signal recovery 1 ns after excitation is systematically smaller for the dyad than for the reference.

As the stationary SH signal in the 420−430 nm region is resonant with the Soret band transition, its intensity is proportional to the square of the ground-state population, namely, $I_{SH} \propto |N_{S_0}\langle\beta_{S_0}\rangle|^2$, where β_{S_0} is the hyperpolarizability tensor of the dye in the electronic ground state. Photoexcitation at 520 nm in the Q_y band of the porphyrin leads to the population of the S_1 state, which can then either decay back to the ground state or populate another state X. The signal intensity is

$$I_{SH}(t) \propto |N_{S_0}(t)\langle\beta_{S_0}\rangle + N_{S_1}(t)\langle\beta_{S_1}\rangle + N_X(t)\langle\beta_X\rangle|^2$$

where N_i and β_i are the population and hyperpolarizability tensor of state i, respectively. Given that directly after excitation only the S_0 and the S_1 states are populated, the decrease of the SH intensity, hence of $S(t)$, indicates that $\beta_{S_0} > \beta_{S_1}$. This agrees with electronic transient absorption measurements, which demonstrate that H_2TPP has relatively weak $S_n \leftarrow S_1$ absorption between 440 and 700 nm.[55,56] The recovery of the signal could have two origins: (1) the repopulation of the ground state or (2) the population of a state X with $\beta_X > \beta_{S1}$ at the probe wavelength.

The excited-state dynamics of the reference compound in bulk solution can be expected to be similar to those of H_2TPP; namely, the S_1 state decays via internal conversion and fluorescence to the ground state and via intersystem crossing (ISC) to the T_1 state. In toluene, the fluorescence lifetime of H_2TPP amounts to 12.8 ns and its triplet yield to 0.8.[57] On the other hand, a fluorescence lifetime of 7.9 ns was measured with **2** in CHCl₃ (Figure S7). On the basis of this, the $S(t)$ signal measured with **2** should recover by <20% within 1 ns. The faster dynamics measured experimentally, and especially its strong concentration dependence is most probably because of aggregation phenomena. MD simulations with two molecules **2** inserted in the aqueous phase show that after adsorption they diffuse close to each other and remain side by side at the interface, interacting mostly via their hydrophilic chains (Figures S6 and S7). This mutual orientation of the porphyrins favors dipolar excitonic coupling and should, thus, significantly affect the excited-state properties. Khairutdinov and Serpone showed that aggregates of free-base porphyrins in aqueous environments are hardly fluorescent because of efficient internal conversion on the 30−200 ps time scale.[58] This study revealed that these aggregates also absorb in both the Soret and Q-band regions. The fast dynamic component measured with **2** could, thus, be due to the ground-state recovery of photoexcited aggregates. The faster than expected nanoseconds recovery of the SH intensity could be due to the quenching of excited monomers by nearby aggregates, a phenomenon that is well-known for xanthene dyes, such as rhodamines, both in bulk solution and at liquid interfaces.[59−62]

Turning now to the dyad, MD simulations with two dyads **1** located in the aqueous subphase point to aggregation as well (Figures S4 and S5). These simulations suggest that the C_{60} subunits are relatively close, while the porphyrins are located on opposite sides with their planes making an angle of about 80°. Such mutual orientation with near orthogonal porphyrin planes point to negligible dipolar excitonic coupling, contrary to the analogue **2**.

As depicted in Figure 4A, the TR-SSHG profiles measured with **1** also depend on the concentration but nevertheless differ from those recorded with **2**. Investigations of the excited-state dynamics of **1** in solution revealed that photoexcitation of the porphyrin moiety is followed by the population of an exciplex-like state in 150 fs in both polar and nonpolar solvents.[23,24] In the latter, this exciplex decays back to the ground state on a few nanoseconds time scale. In the polar benzonitrile, the exciplex transforms in 6.6 ps into a charge-separated state, with the hole and the electron on the H_2TPP and C_{60} subunits, respectively. This charge-separated state was found to recombine back to the ground state in 450 ps. The exciplex was mostly detected by its fluorescence which is distinct from that of the porphyrin.[23] However, no strong spectroscopic signature could be found in the transient electronic absorption spectrum. As a consequence, one can assume that photoexcitation of the dyad at the dodecane/water interface also leads to sub-picoseconds population of the exciplex. The slow recovery of the signal at low concentration would be consistent with the nanoseconds decay of the exciplex. Its acceleration upon increasing concentration suggests the occurrence of an intermolecular process that could speed up the repopulation of the ground state and/or lead to the population of another state, X, with $\beta_X > \beta_{S_1}$ at the probe wavelength.

To have a better insight into this, transient SH spectra were recorded between 400 and 480 nm with the pump pulses on. Figure 5A shows that 20 and 100 ps after excitation the
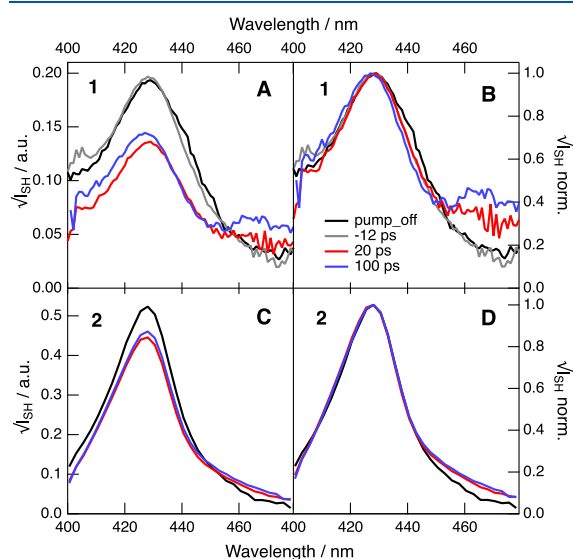

Figure 5. SH spectra (A, C) and intensity-normalized SH spectra (B, D) recorded at different times after 520 nm excitation of the dyad **1** (A, B) and the porphyrin-only reference **2** (C, D) at the dodecane/water interface (MMA = 4 nm²).

amplitude of the Soret band is significantly reduced, in agreement with the TR-SH profiles, and a new band, more visible at a 100 ps delay, is present above 450 nm. The presence of this band, which is not observed with the reference **2** (Figure 5C), is a strong indication of the population of a state X with a nonzero β at the probe wavelength. On the basis of the results in bulk solutions,[23,24] the state X is interpreted as the charge-separated state, with the SH band above 450 nm attributed to the radical cation of the porphyrin subunit.[63,64] The MD simulations suggest that the dyads are mostly surrounded by dodecane. Therefore, they should not experience a local field commensurate with that of a polar solvent. In such case, the exciplex can be expected to decay to the ground state on the nanoseconds time scale without undergoing charge separation (CS), in agreement with the TR-SH data at low concentration. We hypothesize that at higher concentrations intermolecular CS between an excited dyad and a dyad in the ground state takes place, with the hole and the electron located on two different molecules (Figure 6). On the
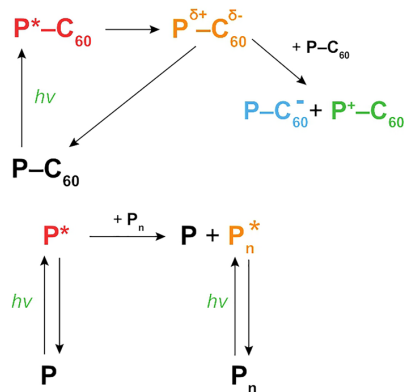

Figure 6. Schemes illustrating the most relevant processes upon photoexcitation of the dyad **1** (top) and the porphyrin reference **2** (bottom) at the dodecane/water interface. P stands for the porphyrin and P_n for porphyrin aggregates. For the sake of simplicity, the vertical arrow from P* to P also includes the intersystem crossing to the triplet state and its ensuing decay to the ground state. The ground-state equilibrium for aggregation is also omitted.

basis of this, the fast recovery components of $S(t)$ present at higher concentrations should mostly reflect the dynamics of this intermolecular CS. The latter process should also be favored by the aggregation suggested by the MD simulations (Figures S4 and S5) with the relatively close proximity of another C_{60} moiety facilitating electron hopping.

Intramolecular charge recombination (CR) in benzonitrile was reported to take place with a 450 ps time constant.[23,24] The time window of the TR-SSHG experiment does not allow measuring the entire signal recovery. However, intermolecular CR can be expected to be significantly slower than intramolecular CR. Given the relatively high concentration of adsorbed molecules, hopping of the charges to adjacent dyads can in principle compete with geminate recombination.

The interfacial dynamics, summarized in Figure 6, can be compared with that reported for solid films of the dyads prepared with the Langmuir–Blodgett (LB) technique.[22] A CS time constant of 2 ns was estimated from the exciplex lifetime. The authors determined from time-resolved photoelectric measurements that CR occurs on multiple time scales and that

the decay of the charge-separated state follows a power law time dependence, $f(t) \propto t^{-\beta}$, with β around 0.25. Such behavior is indicative of lateral diffusion of the charges in the film. Similarly, transient absorption measurements on solid LB films of a dyad similar to **1** but with a phthalocyanine donor revealed intermolecular CS occurring in 35 ps, with CR taking place on the microseconds time scale.[65]

Therefore, the excited-state dynamics proposed here for the dyad at the dodecane/water interface occurs in a regime that is between that found in bulk solutions, where intermolecular interactions are negligible and solvation drives CS, and that in solid films where there is no formal solvent and intermolecular interactions are dominant.

■ CONCLUSIONS

We have investigated the excited-state properties of an amphiphilic electron donor–acceptor dyad at the dodecane/water interface. Polarization-resolved SSHG measurements supported by MD simulations revealed significantly different orientations for the dyad and the porphyrin reference at the interface. The orientation is dictated by the presence of the hydrophobic fullerene subunit, which causes the dyad to be almost entirely surrounded by dodecane. The location of the dyad at the interface has strong consequence on its excited-state dynamics because intramolecular charge separation is not operative in such a low-polarity environment. Instead, photoexcitation of the dyad leads to the population of an excited state with modest charge-transfer character that decays back to the ground state. However, because the amphiphilic dyad adsorbs efficiently, interfacial concentrations enabling self-quenching processes can be easily reached. On the basis of the SH spectra recorded after photoexcitation, the acceleration of the TR-SH signal recovery observed upon increasing concentration is attributed to an intermolecular charge separation between two dyads.

This investigation illustrates how chemical reactivity at liquid interfaces can differ from that in bulk solution. In addition to favoring intermolecular processes, liquid interfaces also allow for some control of the orientation and position of the adsorbates upon addition of hydrophilic or hydrophobic substituents at specific locations. For example, adding stronger hydrophilic groups on the dyad investigated here could shift its position toward an environment that might be sufficiently polar to enable intramolecular charge separation.

■ ASSOCIATED CONTENT

ⓈI Supporting Information

The Supporting Information is available free of charge at https://pubs.acs.org/doi/10.1021/acs.jpcb.2c02405.

> Analysis of the polarization-resolved SSHG data, calculation of the hyperpolarizability, MD simulations, time-resolved fluorescence, analysis of the time-resolved SSHG data (PDF)

■ AUTHOR INFORMATION

Corresponding Authors

Tatu Kumpulainen − *Department of Chemistry/Nanoscience Center, University of Jyväskylä, 40014 Jyväskylä, Finland;* ⓞ orcid.org/0000-0001-9469-9294; Email: tatu.s.kumpulainen@jyu.fi

Eric Vauthey − *Department of Physical Chemistry, University of Geneva, 1205 Geneva, Switzerland;* ⦿ orcid.org/0000-0002-9580-9683; Email: eric.vauthey@unige.ch

Authors

Jihad Sissaoui − *Department of Physical Chemistry, University of Geneva, 1205 Geneva, Switzerland*

Alexander Efimov − *Faculty of Engineering and Natural Sciences, Tampere University, 33100 Tampere, Finland;* ⦿ orcid.org/0000-0003-4671-3009

Complete contact information is available at:
https://pubs.acs.org/10.1021/acs.jpcb.2c02405

Notes

The authors declare no competing financial interest.

All data can be downloaded from 10.26037/yareta:vo4jtzixorg2jmpw2r2syq3tc4.

■ **REFERENCES**

(1) Ball, P. Water as an Active Constituent in Cell Biology. *Chem. Rev.* **2008**, *108*, 74−108.

(2) Volkov, A. G. E. *Liquid Interfaces in Chemical, Biological, and Pharmaceutical Applications*; Marcel Dekker: New York, 2009.

(3) Girault, H. H. In *Electroanalytical Chemistry*; Bard, A. J., Zoski, C. G., Eds.; 2010; Vol. 23, pp 1−104.

(4) Liu, S.; Li, Q.; Shao, Y. Electrochemistry at Micro- and Nanoscopic Liquid/Liquid Interfaces. *Chem. Soc. Rev.* **2011**, *40*, 2236−2253.

(5) Benjamin, I. Reaction Dynamics at Liquid Interfaces. *Annu. Rev. Phys. Chem.* **2015**, *66*, 165−188.

(6) Divya, V.; Sangaranarayanan, M. V. Nanomaterials at Liquid/Liquid Interfaces. A Review. *J. Nanosci. Nanotechnol.* **2015**, *15*, 6863−6882.

(7) Zarbin, A. J. G. Liquid-Liquid Interfaces: a Unique and Advantageous Environment to Prepare and Process Thin Films of Complex Materials. *Mater. Horiz.* **2021**, *8*, 1409−1432.

(8) Narayan, S.; Muldoon, J.; Finn, M. G.; Fokin, V. V.; Kolb, H. C.; Sharpless, K. B. 'On Water': Unique Reactivity of Organic Compounds in Aqueous Suspension. *Angew. Chem., Int. Ed.* **2005**, *44*, 3275−3279.

(9) Klijn, J. E.; Engberts, J. B. F. N. Fast Reactions 'On Water'. *Nature* **2005**, *435*, 746−747.

(10) Jung, Y.; Marcus, R. A. On the Theory of Organic Catalysis 'on Water'. *J. Am. Chem. Soc.* **2007**, *129*, 5492−5502.

(11) Kitanosono, T.; Kobayashi, S. Reactions in Water Involving the 'On-Water' Mechanism. *Chem.—Eur. J.* **2020**, *26*, 9408−9429.

(12) Cortes-Clerget, M.; Yu, J.; Kincaid, J. R. A.; Walde, P.; Gallou, F.; Lipshutz, B. H. Water as the Reaction Medium in Organic Chemistry: from our Worst Enemy to our Best Friend. *Chem. Sci.* **2021**, *12*, 4237−4266.

(13) Walker, R. A. Faster Chemistry at Surfaces. *Nat. Chem.* **2021**, *13*, 296−297.

(14) McArthur, E. A.; Eisenthal, K. B. Ultrafast Excited-State Electron Transfer at an Organic Liquid/Aqueous Interface. *J. Am. Chem. Soc.* **2006**, *128*, 1068−1069.

(15) Fedoseeva, M.; Richert, S.; Vauthey, E. Excited-State Dynamics of Organic Dyes at Liquid-Liquid Interfaces. *Langmuir* **2012**, *28*, 11291−11301.

(16) Eisenthal, K. B. Liquid Interfaces Probed by Second-Harmonic and Sum-Frequency Spectroscopy. *Chem. Rev.* **1996**, *96*, 1343−1360.

(17) Brevet, P.-F. *Surface Second Harmonic Generation*; Presses Polytechniques et Universitaires Romandes: Lausanne, 1997.

(18) Simpson, G. J. New Tools for Surface Second-Harmonic Generation. *Appl. Spectrosc.* **2001**, *55*, 16A−32A.

(19) Richert, S.; Fedoseeva, M.; Vauthey, E. Ultrafast Photoinduced Dynamics at Air/Liquid and Liquid/Liquid Interfaces. *J. Phys. Chem. Lett.* **2012**, *3*, 1635−1642.

(20) Tian, C. S.; Shen, Y. R. Recent Progress on Sum-Frequency Spectroscopy. *Surf. Sci. Rep.* **2014**, *69*, 105−131.

(21) Tran, R. J.; Sly, K. L.; Conboy, J. C. Applications of Surface Second Harmonic Generation in Biological Sensing. *Annu. Rev. Anal. Chem.* **2017**, *10*, 387−414.

(22) Vuorinen, T.; Kaunisto, K.; Tkachenko, N. V.; Efimov, A.; Lemmetyinen, H.; Alekseev, A. S.; Hosomizu, K.; Imahori, H. Photoinduced Electron Transfer in Langmuir-Blodgett Monolayers of Porphyrin-Fullerene Dyads. *Langmuir* **2005**, *21*, 5383−5390.

(23) Chukharev, V.; Tkachenko, N. V.; Efimov, A.; Guldi, D. M.; Hirsch, A.; Scheloske, M.; Lemmetyinen, H. Tuning the Ground-State and Excited-State Interchromophore Interactions in Porphyrin-Fullerene π-Stacks. *J. Phys. Chem. B* **2004**, *108*, 16377−16385.

(24) Chukharev, V.; Tkachenko, N. V.; Efimov, A.; Lemmetyinen, H. Effect of Central Metal on Intra-Molecular Exciplex of Porphyrin-Fullerene Double Linked Dyad. *Chem. Phys. Lett.* **2005**, *411*, 501−505.

(25) Lemmetyinen, H.; Tkachenko, N. V.; Efimov, A.; Niemi, M. Temperature Independent Ultrafast Photoinduced Charge Transfer in Donor-Acceptor Pairs Forming Exciplexes. *J. Phys. Chem. C* **2009**, *113*, 11475−11483.

(26) Kesti, T. J.; Tkachenko, N. V.; Vehmanen, V.; Yamada, H.; Imahori, H.; Fukuzumi, S.; Lemmetyinen, H. Exciplex Intermediates in Photoinduced Electron Transfer of Porphyrin-Fullerene Dyads. *J. Am. Chem. Soc.* **2002**, *124*, 8067−8077.

(27) Efimov, A.; Vainiotalo, P.; Tkachenko, N. V.; Lemmetyinen, H. Efficient Synthesis of Highly Soluble Doubly-Bridged Porphyrin-Fullerene Dyad. *J. Porphyrins Phthalocyanines* **2003**, *07*, 610−616.

(28) Fedoseeva, M.; Fita, P.; Vauthey, E. Excited-State Dynamics of Charged Dyes at Alkane/Water Interfaces in the Presence of Salts and Ionic Surfactants. *Langmuir* **2013**, *29*, 14865−14872.

(29) Richert, S.; Mosquera Vazquez, S.; Grzybowski, M.; Gryko, D. T.; Kyrychenko, A.; Vauthey, E. Excited-State Dynamics of an Environment-Sensitive Push-Pull Diketopyrrolopyrrole: Major Differences between the Bulk Solution Phase and the Dodecane/Water Interface. *J. Phys. Chem. B* **2014**, *118*, 9952−9963.

(30) Licari, G.; Brevet, P.-F.; Vauthey, E. Fluorescent DNA Probes at Liquid/Liquid Interfaces Studied by Surface Second Harmonic Generation. *Phys. Chem. Chem. Phys.* **2016**, *18*, 2981−2992.

(31) Abraham, M. J.; Murtola, T.; Schulz, R.; Pall, S.; Smith, J. C.; Hess, B.; Lindahl, E. GROMACS: High Performance Molecular Simulations through Multi-Level Parallelism from Laptops to Supercomputers. *SoftwareX* **2015**, *1−2*, 19−25.

(32) Hornak, V.; Abel, R.; Okur, A.; Strockbine, B.; Roitberg, A.; Simmerling, C. Comparison of Multiple Amber Force Fields and Development of Improved Protein Backbone Parameters. *Proteins* **2006**, *65*, 712−25.

(33) Lindorff-Larsen, K.; Piana, S.; Palmo, K.; Maragakis, P.; Klepeis, J. L.; Dror, R. O.; Shaw, D. E. Improved Side-Chain Torsion Potentials for the Amber ff99SB Protein Force Field. *Proteins* **2010**, *78*, 1950−8.

(34) Sousa da Silva, A. W.; Vranken, W. F. ACPYPE - AnteChamber PYthon Parser InterfacE. *BMC Res. Notes* **2012**, *5*, 367.

(35) Lee, C.; Yang, W.; Parr, R. G. Development of the Colle-Salvetti Correlation-Energy Formula into a Functional of the Electron Density. *Phys. Rev. B* **1988**, *37*, 785−789.

(36) Frisch, M. J.; Trucks, G. W.; Schlegel, H. B.; Scuseria, G. E.; Robb, M. A.; Cheeseman, J. R.; Scalmani, G.; Barone, V.; Petersson, G. A.; Nakatsuji, H.; et al. *Gaussian 16*, Rev. B.01; Gaussian Inc.: 2016.

(37) Monticelli, L. On Atomistic and Coarse-Grained Models for C60 Fullerene. *J. Chem. Theory Comput.* **2012**, *8*, 1370−1378.

(38) Chirlian, L. E.; Francl, M. M. Atomic Charges Derived from Electrostatic Potentials: A Detailed study. *J. Comput. Chem.* **1987**, *8*, 894−905.

(39) Jorgensen, W. L.; Chandrasekhar, J.; Madura, J. D.; Impey, R. W.; Klein, M. L. Comparison of Simple Potential Functions for Simulating Liquid Water. *J. Chem. Phys.* **1983**, *79*, 926−935.

(40) Jambeck, J. P.; Lyubartsev, A. P. Derivation and Systematic Validation of a Refined all-Atom Force Field for Phosphatidylcholine Lipids. *J. Phys. Chem. B* **2012**, *116*, 3164−79.

(41) Licari, G.; Cwiklik, L.; Jungwirth, P.; Vauthey, E. Exploring Fluorescent Dyes at Biomimetic Interfaces with Second Harmonic Generation and Molecular Dynamics. *Langmuir* **2017**, *33*, 3373−3383.

(42) Gouterman, M.; Wagniere, G. H.; Snyder, L. C. Spectra of Porphyrins: Part II. Four Orbital Model. *J. Mol. Spectrosc.* **1963**, *11*, 108−127.

(43) Boyd, R. *Nonlinear Optics*, 3rd ed.; Academic Press: Orlando, FL, 2008.

(44) Nagatani, H.; Piron, A.; Brevet, P.-F.; Fermin, D. J.; Girault, H. H. Surface Second Harmonic Generation of Cationic Water-Soluble Porphyrins at the Polarized Water| 1,2-Dichloroethane Interface. *Langmuir* **2002**, *18*, 6647−6652.

(45) Nagatani, H.; Samec, Z.; Brevet, P.-F.; Fermin, D. J.; Girault, H. H. Adsorption and Aggregation of meso-Tetrakis(4-carboxyphenyl)-porphyrinato Zinc(II) at the Polarized Water| 1,2-Dichloroethane Interface. *J. Phys. Chem. B* **2003**, *107*, 786−790.

(46) Fujiwara, K.; Monjushiro, H.; Watarai, H. Total Internal Reflection Second-Harmonic Generation Spectrometer System Optimized for the Liquid/Liquid Interface. *Rev. Sci. Instrum.* **2005**, *76*, 023111.

(47) Kruk, N. N. Nonlinear Optical Properties of Tetrapyrrole Compounds and Prospects for their Application (a Review). *J. Appl. Spectrosc.* **2008**, *75*, 461−482.

(48) Lin, L.; Wang, T.; Lu, Z.; Liu, M.; Guo, Y. In Situ Measurement of the Supramolecular Chirality in the Langmuir Monolayers of Achiral Porphyrins at the Air/Aqueous Interface by Second Harmonic Generation Linear Dichroism. *J. Phys. Chem. C* **2014**, *118*, 6726−6733.

(49) Pavlovich, V. S.; Shpilevsky, E. M. Absorption and Fluorescence Spectra of C60 Fullerene Concentrated Solutions in Hexane and Polystyrene at 77−300 K. *J. Appl. Spectrosc.* **2010**, *77*, 335−342.

(50) Tamburello-Luca, A. A.; Hebert, P.; Brevet, P. F.; Girault, H. H. Resonant-Surface Second-Harmonic Generation Studies of Phenol Derivatives at Air/Water and Hexane/Water Interfaces. *J. Chem. Soc., Faraday Trans.* **1996**, *92*, 3079−3085.

(51) Simpson, G. J.; Westerbuhr, S. G.; Rowlen, K. Molecular Orientation and Angular Distribution Probed by Angle-Resolved Absorbance and Second Harmonic Generation. *Anal. Chem.* **2000**, *72*, 887−898.

(52) Doughty, B.; Rao, Y.; Kazer, S. W.; Kwok, S. J.; Turro, N. J.; Eisenthal, K. B. Probing the Relative Orientation of Molecules Bound to DNA through Controlled Interference using Second-Harmonic Generation. *Proc. Natl. Acad. Sci. U. S. A.* **2013**, *110*, 5756−5758.

(53) Svechkarev, D.; Kolodezny, D.; Mosquera-Vazquez, S.; Vauthey, E. Complementary Surface Second Harmonic Generation and Molecular Dynamics Investigation of the Orientation of Organic Dyes at a Liquid/Liquid Interface. *Langmuir* **2014**, *30*, 13869−13876.

(54) Simpson, G. J.; Rowlen, K. L. An SHG Magic Angle: Dependence of Second Harmonic Generation Orientation Measurements on the Width of the Orientation Distribution. *J. Am. Chem. Soc.* **1999**, *121*, 2635−2636.

(55) Rodriguez, J.; Kirmaier, C.; Holten, D. Optical Properties of Metalloporphyrin Excited States. *J. Am. Chem. Soc.* **1989**, *111*, 6500−6506.

(56) Banerji, N.; Bhosale, S. V.; Petkova, I.; Langford, S. J.; Vauthey, E. Ultrafast Excited-State Dynamics of Strongly Coupled Porphyrin/Core-Substituted-Naphthalenediimide Dyads. *Phys. Chem. Chem. Phys.* **2011**, *13*, 1019−1029.

(57) Taniguchi, M.; Lindsey, J. S.; Bocian, D. F.; Holten, D. Comprehensive Review of Photophysical Parameters (ϵ, Φ_f, τ_s) of Tetraphenylporphyrin (H2TPP) and Zinc Tetraphenylporphyrin (ZnTPP) - Critical Benchmark Molecules in Photochemistry and Photosynthesis. *J. Photochem. Photobiol. C* **2021**, *46*, 100401.

(58) Khairutdinov, R. F.; Serpone, N. Photoluminescence and Transient Spectroscopy of Free Base Porphyrin Aggregates. *J. Phys. Chem. B* **1999**, *103*, 761−769.

(59) Penzkofer, A.; Lu, Y. Fluorescence Quenching of Rhodamine 6G in Methanol at High Concentration. *Chem. Phys.* **1986**, *103*, 399−405.

(60) Isak, S. J.; Eyring, E. M. Fluorescence Quantum Yield of Cresyl Violet in Methanol and Water as a Function of Concentration. *J. Phys. Chem.* **1992**, *96*, 1738−1742.

(61) Fita, P.; Fedoseeva, M.; Vauthey, E. Hydrogen-Bond-Assisted Excited-State Deactivation at Liquid/Water Interfaces. *Langmuir* **2011**, *27*, 4645−4652.

(62) Fedoseeva, M.; Letrun, R.; Vauthey, E. Excited-State Dynamics of Rhodamine 6G in Aqueous Solution and at the Dodecane/Water Interface. *J. Phys. Chem. B* **2014**, *118*, 5184−5193.

(63) Paliteiro, C.; Sobral, A. Electrochemical and Spectroelectrochemical Characterization of Meso-Tetra-Alkyl Porphyrins. *Electrochim. Acta* **2005**, *50*, 2445−2451.

(64) Aleman, E. A.; Manriquez Rocha, J.; Wongwitwichote, W.; Godinez Mora-Tovar, L. A.; Modarelli, D. A. Spectroscopy of Free-Base N-Confused Tetraphenylporphyrin Radical Anion and Radical Cation. *J. Phys. Chem. A* **2011**, *115*, 6456−6471.

(65) Lehtivuori, H.; Kumpulainen, T.; Efimov, A.; Lemmetyinen, H.; Kira, A.; Imahori, H.; Tkachenko, N. V. Photoinduced Electron Transfer in Langmuir-Blodgett Monolayers of Double-Linked Phthalocyanine-Fullerene Dyads. *J. Phys. Chem. C* **2008**, *112*, 9896−9902.

📖 Recommended by ACS

SUPPORTING INFORMATION:

Photoinduced Electron Transfer in a

Porphyrin-Fullerene Dyad at a Liquid Interface

Jihad Sissaoui,[†] Alexander Efimov,[‡] Tatu Kumpulainen,[*,¶] and Eric Vauthey[*,†]

†*Department of Physical Chemistry, University of Geneva, 30 Quai Ernest-Ansermet, Geneva, Switzerland*

‡*Faculty of Engineering and Natural Sciences, Tampere University, Korkeakoulunkatu 8, Tampere, Finland*

¶*Department of Chemistry/Nanoscience Center, University of Jyväskylä, Survontie 9 C, Jyväskylä, Finland*

E-mail: tatu.s.kumpulainen@jyu.fi; eric.vauthey@unige.ch

Contents

List of Figures

List of Tables

S4

S1   Analysis of the polarisation profiles

The macroscopic nonlinear optical susceptibility, $\overset{\leftrightarrow}{\chi}^{(2)}$, is a second-rank tensor containing 27 elements. For liquid interfaces, only seven non-zero elements, three of which being independent, have to be considered: $\chi^{(2)}_{ZZZ}$, $\chi^{(2)}_{ZXX} = \chi^{(2)}_{ZYY}$ and $\chi^{(2)}_{XXZ} = \chi^{(2)}_{XZX} = \chi^{(2)}_{YYZ} = \chi^{(2)}_{YZY}$, where the subscripts are the Cartesian coordinates in the laboratory frame, with X and Y being in the interfacial plane, and Y and Z being in the plane of incidence of the optical beam. The dependence of the SH intensity linearly polarized at an angle Γ on the polarization angle of the probe field, γ , is given by:[2,3]

$$I_{\text{SH}}(\gamma, \Gamma) = C \left| a_1 \chi^{(2)}_{XXZ} \sin 2\gamma \sin \Gamma + \left(a_2 \chi^{(2)}_{XXZ} + a_3 \chi^{(2)}_{ZXX} + a_4 \chi^{(2)}_{ZZZ} \right) \cos^2 \gamma \cos \Gamma + \right.$$
$$\left. + a_5 \chi^{(2)}_{ZXX} \sin^2 \gamma \cos \Gamma \right|^2 I_{\text{pr}}^2, \tag{S1}$$

where $a_1, \ldots, a_5$ are optical coefficients that depend on the Fresnel factors. These coefficients were calculated as described in ref. 2 using the following experimental values:

$$n_{1,dod} = 1.42, \quad n_{2,water} = 1.33, \quad n_m = 1.378.$$

The polarization-resolved SSHG measurements were carried out at three different output polarizations, namely Γ=0° (p), 45°, and 90° (s) allowing the relative magnitude and sign of the three independent susceptibility elements to be extracted. The following expressions can be obtained from eq.S1:

$$I_{\text{SH}}(\gamma, 0°) \propto \left| \left(a_2 \chi^{(2)}_{XXZ} + a_3 \chi^{(2)}_{ZXX} + a_4 \chi^{(2)}_{ZZZ} \right) \cos^2 \gamma + a_5 \chi^{(2)}_{ZXX} \sin^2 \gamma \right|^2 , \tag{S2}$$

$$I_{\text{SH}}(\gamma, 45°) \propto \left| a_1 \chi^{(2)}_{XXZ} \sin 2\gamma + \left(a_2 \chi^{(2)}_{XXZ} + a_3 \chi^{(2)}_{ZXX} + a_4 \chi^{(2)}_{ZZZ} \right) \cos^2 \gamma + a_5 \chi^{(2)}_{ZXX} \sin^2 \gamma \right|^2 , \tag{S3}$$

$$I_{\text{SH}}(\gamma, 90°) \propto \left| a_1 \chi^{(2)}_{XXZ} \sin 2\gamma \right|^2 . \tag{S4}$$

These three equations were used in a least-squares curve-fitting analysis of the experimental data to obtain the ratios of the susceptibility elements.

S5

The macroscopic second-order nonlinear susceptibility is related to the hyperpolarizability tensor $\overset{\leftrightarrow}{\beta}$:

$$\overset{\leftrightarrow}{\chi}{}^{(2)} = \frac{1}{\varepsilon_0} N \langle \overset{\leftrightarrow}{T} \rangle \overset{\leftrightarrow}{\beta}, \tag{S5}$$

where N is the number of chromophores per unit area and $\langle \overset{\leftrightarrow}{T} \rangle$ is the averaged transformation tensor allowing the transformation from the molecular frame to the lab frame. Based on quantum-chemical calculations of the hyperpolarisability described in the next section, the dominant elements of hyperpolarizability tensor of the dyad **1** and the porphyrin **2** are β_{zzz} and β_{zxx}, with the x and z axes located in the plane. In this case, the tensor elements of $\overset{\leftrightarrow}{\chi}{}^{(2)}$ are related to the $\overset{\leftrightarrow}{\beta}$ tensor elements as:

$$\chi^{(2)}_{XZX} = \frac{N}{2\epsilon_0} \left[\langle \sin^2 \theta \cos \theta \rangle \beta_{zzz} - \langle \sin^2 \psi \cos \theta \sin^2 \theta \rangle \beta_{zxx} \right], \tag{S6}$$

$$\chi^{(2)}_{ZXX} = \frac{N}{2\epsilon_0} \left[\langle \sin^2 \theta \cos \theta \rangle \beta_{zzz} - \langle \sin^2 \psi \cos \theta \sin^2 \theta \rangle \beta_{zxx} + \langle \cos \theta \rangle \beta_{zxx} \right], \tag{S7}$$

$$\chi^{(2)}_{ZZZ} = \frac{N}{\epsilon_0} \left[\langle \cos^3 \theta \rangle \beta_{zzz} - \langle \sin^2 \psi \cos \theta \sin^2 \theta \rangle \beta_{zxx} \right], \tag{S8}$$

where θ is the tilt angle, i.e. the angle between the molecular z axis and the laboratory Z axis, and ψ a second Euler angle associated with the rotation of the molecular plane around the z axis.

Assuming a random distribution of the angle ψ, the orientational parameter D is expressed as :

$$D = \frac{\chi^{(2)}_{ZZZ} - \chi^{(2)}_{ZXX} + \chi^{(2)}_{XZX}}{\chi^{(2)}_{ZZZ} - \chi^{(2)}_{ZXX} + 3\chi^{(2)}_{XZX}} = \frac{\langle \cos^3 \theta \rangle}{\langle \cos \theta \rangle}$$

If we consider a Dirac distribution of the angle θ, the D parameter becomes $D = \cos^2 \theta$.

S6
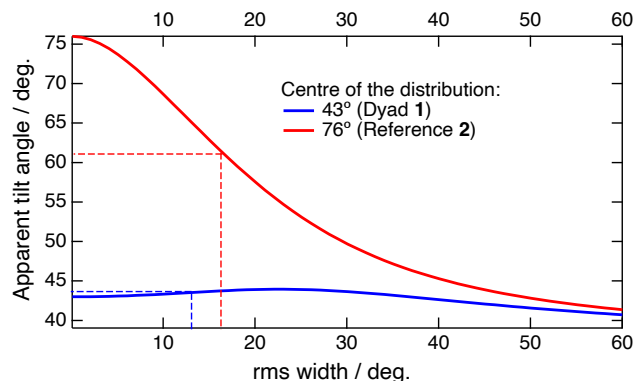
Figure S1: Estimation of the apparent tilt angle, θ, when assuming a delta distribution for a 16° wide distribution around 76° (red) and a 13° wide distribution around 43° (blue). See reference 1 for details.

S2 Quantum-chemical calculations of the hyperpolarisability

Molecules **1** and **2** were first optimised at the B3LYP/6-31G+d level. The vertical electronic transitions were then calculated using time-dependent DFT (B3LYP/6-31G). The transition corresponding to the Soret band was identified at 394.5 nm for **1** and 375 nm for **2**. These values were used to calculate the frequency-dependent hyperpolarisability for SHG, $\overset{\leftrightarrow}{\beta}(-2w; w, w)$, as implemented in Gaussian 16,[4] with w corresponding to 689 and 650 nm for **1** and **2**, respectively. The static polarisability, $\overset{\leftrightarrow}{\beta}(0; 0, 0)$, was also calculated for comparison. The vector components of $\overset{\leftrightarrow}{\beta}(-2w; w, w)$ and $\overset{\leftrightarrow}{\beta}(0; 0, 0)$ are listed in Table S1. The relevant tensor elements of $\overset{\leftrightarrow}{\beta}(-2w; w, w)$ for C_{2v} symmetry are listed in Table S2. The orientation of the molecular coordinates is illustrated in Figure S2.

Table S1: Calculated vector components of the hyperpolarisability for SHG, $\beta(-2w; w, w)$, and of the static hyperpolarisability, $\beta(0; 0, 0)$, in 10^{-30} esu. For 1 and 2, w corresponds to 689 and 650 nm, respectively.

molecule	$\beta_x(-2w; w, w)$	$\beta_y(-2w; w, w)$	$\beta_z(-2w; w, w)$	$\beta_x(0; 0, 0)$	$\beta_y(0; 0, 0)$	$\beta_z(0; 0, 0)$
1	900	120	1500	2	17	3
2	3340	360	5950	14	20	4

S7

Table S2: Calculated elements of $\beta(-2w; w, w)$ relevant for C_{2v} symmetry (in 10^{-30} esu). For 1 and 2, w corresponds to 689 and 650 nm, respectively.

molecule	β_{xxz}	β_{zxx}	β_{zzz}	β_{yyz}	β_{zyy}
1	45	120	550	43	14
2	80	2500	3050	5	44
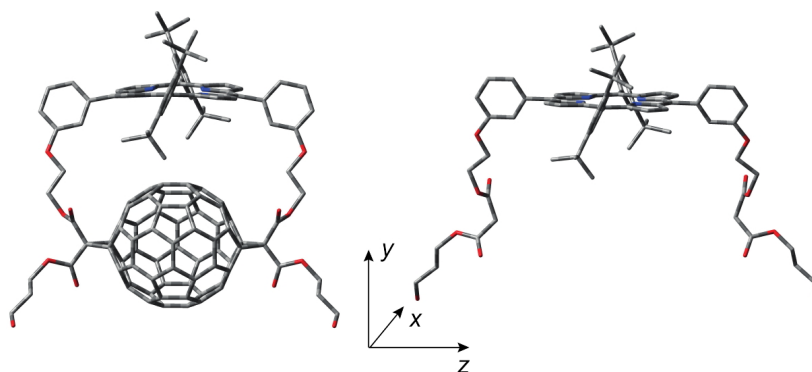
Figure S2: Orientation of the molecular coordinates.

These results indicate that the dominant elements of $\overset{\leftrightarrow}{\beta}$ responsible for the SHG signal in the Soret band region involve the porphyrin xz plane. They also reveal that, whereas the out-of-plane y vector component is dominant in the static hyperpolarisability, $\overset{\leftrightarrow}{\beta}(0;0,0)$, it becomes of minor importance in the frequency-dependent $\overset{\leftrightarrow}{\beta}(-2w; w, w)$, when the SHG signal is resonant with the intense Soret transitions located in the xz plane.

S3 Molecular dynamics simulations

Non-bonded interactions were evaluated with a cutoff of 1.4 nm, and long-range electrostatic interactions were accounted for by the particle mesh Ewald method,[5] with 0.12 nm grid spacing and forth-order interpolation. A long-range dispersion correction for energy was also included. The LINCS algorithm[6] was used to constrain the bonds of all system components with the exception of water, for which the SETTLE algorithm was applied.[7] The equilibration of the system was ensured by inspecting the total energy drift, the dye

S8

contacts with the interface, and the density profiles at the two distinct interfaces of the box. The isothermal-isobaric ensemble, NPT, was used for all productions with the v-rescale thermostat at 295 K,[8] and the Parrinello-Rahman barostat using coupling constants of 0.5 ps and 3 ps respectively.[9] The pressure was controlled semi-isotropically so that the x-y and z dimensions of the simulation box were allowed to fluctuate independently of each other, keeping the total pressure constant.[9] The coupled pressure in the z direction (normal to the interfacial plane) was always 1 atm. The XZ pressure was set to a negative value of -85 atm in order to compensate for a large surface tension, which would cause explosion of the box in the Z direction.[10]
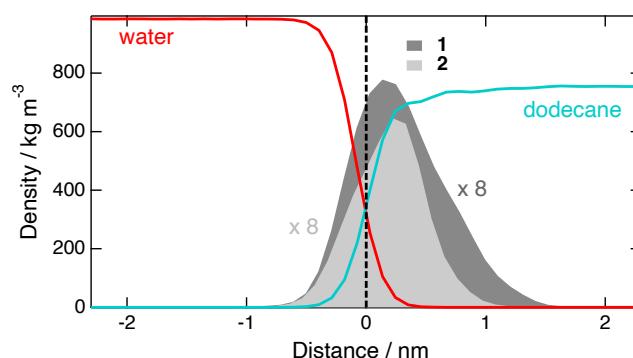
Figure S3: Density profiles obtained from MD simulations of the dyad **1** and the porphyrin analogue **2** at the dodecane/water interface.

In order to investigate possible aggregation at the interface, MD simulations we carried out upon inserting two dye molecules close to a dodecane/water interface. Both were found to adsorb rapidly at the interface within about 1 ns. Several tens of ns simulations were then carried out. The centre to centre distance between the two dyes was determined by taking the average of the 16 distances between each four N atoms of each molecules.

The time evolution of the distance between two dyads **1** is illustrated in Figure S4. After significant fluctuations during the first 65 ns of the simulation, the center-to-center distance between the two porphyrin sub-units remains almost constant, around 1.45 nm. As depicted

S9

by the snapshots in Figure S5, this distance corresponds to a geometry where the two C_{60} are relatively close, while the two porphyrins are further apart, located on opposite sides, with an angle of about 80° between the molecular planes. This mutual orientation does not change significantly from 65 ns until the end of the trajectory. Such geometry does not favour excitonic coupling between the porphyrins and, thus, aggregation should not lead to significant changes in the electronic absorption spectrum. However, we cannot exclude that the small red shift of the Soret band in the SH spectra relative to the electronic absorption spectrum (Figure 1) is due to aggregation. Based on this, the electronic excited state should be mostly localised on one dyad and not over the whole aggregate.
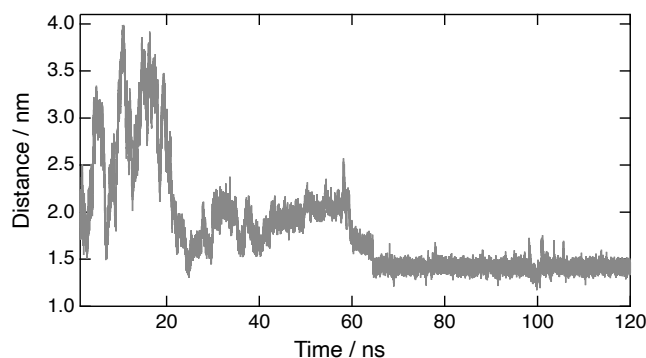
Figure S4: Time evolution of the centre-to-centre distance between two porphyrin sub-units of the dyads **1** at a dodecane/water obtained from MD simulations.
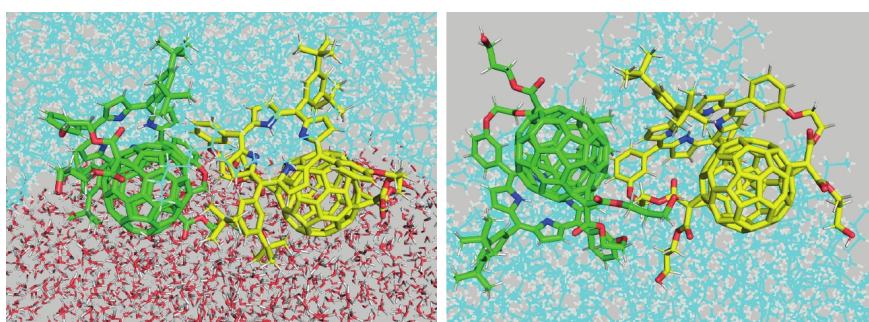
Figure S5: MD simulations snapshots illustrating two dyads **1** at the dodecane/water interface with a centre-to-centre distance of 1.46 nm between the two porphyrin sub-units. Left: side view; Right: top view.

The time evolution of this distance between two porphyrin dyes **2** is shown in Figure S6.

S10

After 20 ns, the two molecules remain in contact at a centre-to-centre distance of less than 1.3 nm. MD snapshots with two molecules at a distance of 1.28 nm are shown in Figure S7. The molecular planes remain almost parallel from about 20 ns until the end of the trajectory.
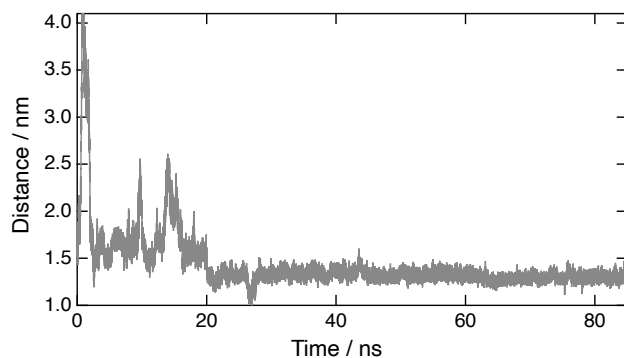
Figure S6: Time evolution of the centre-to-centre distance between two porphyrin analogues **2** adsorbed at a dodecane/water obtained from MD simulations.
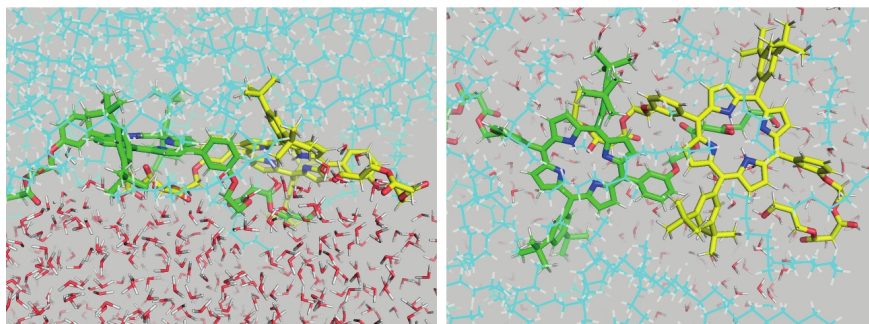
Figure S7: MD simulations snapshots illustrating two porphyrin analogues **2** adsorbed at the dodecane/water interface with a centre-to-centre distance of 1.3 nm Left: side view; Right: top view.

S4   Time-resolved fluorescence

Time-resolved fluorescence measurements were carried out using a time-correlated single photon counting setup described earlier.[11] Excitation was carried out at 395 nm using a laser diode (Picoquant, LDH-P-C 400b).

S11
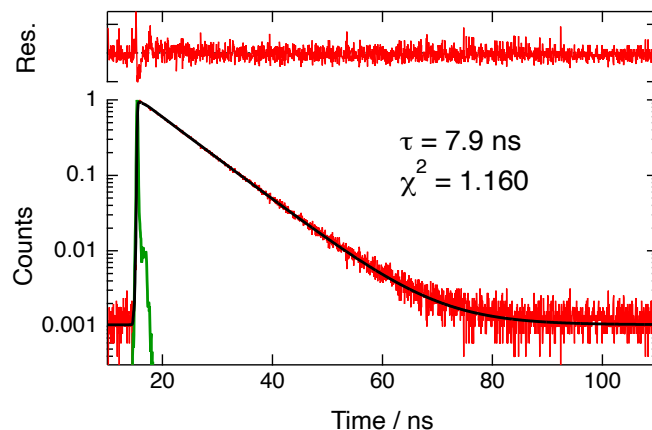
Figure S8: Fluorescence decay measured by time-correlated single photon counting with **2** in CHCl$_3$, upon 395 nm excitation.

S5 Analysis of the TR-SSHG data

The time-resolved SSHG signal, S(t), was analysed by iterative reconvolution of the instrument response function (IRF) with the sum of two or three exponential functions. The IRF was described by a Gaussian function centred at time 0 with an adjustable width. From the fit, the full width at half maximum of the IRF is below 1 ps. The best fits are shown in Figure 4 of the main text, whereas the best-fit parameters are listed in Tables S3 and S4. The error on the time constants is of the order of ±15%. Given the 0-1 ns time window of the experiment, time constant > 2 ns cannot be determined with reliability.

Table S3: Time constants, τ_i, and relative amplitudes A_i, obtained from a multiexponential analysis of the time-resolved SSHG signal, $S(t)$, measured upon photoexcitation of the dyad 1 at the dodecane/water interface. (MMA: mean molecular area).

MMA / nm^2	6.6	6	4	3
τ_1/ ps (A_1)	13 (0.12)	12 (0.26)	6 (0.30)	5 (0.32)
τ_2/ ps (A_2)			150 (0.21)	70 (0.24)
τ_3/ ns (A_3)	> 2 (0.88)	> 2 (0.74)	> 2 (0.49)	> 2(0.44)

S12

129

Table S4: Same as in Table S3 but for the porphyrin analogue 2.

MMA / nm^2	9.9	6.6	5	4
τ_1/ ps (A_1)	21 (0.14)	20 (0.16)	21 (0.20)	14 (0.24)
τ_2/ ns (A_2)	> 2 (0.86)	1.7 (0.84)	1.5 (0.79)	1.4 (0.76)

References

(1) Simpson, G. J.; Rowlen, K. L. An SHG Magic Angle: Dependence of Second Harmonic Generation Orientation Measurements on the Width of the Orientation Distribution. *J. Am. Chem. Soc.* **1999**, *121*, 2635–2636.

(2) Brevet, P.-F. *Surface Second Harmonic Generation*; Presses polytechniques et universitaires romandes: Lausanne, 1997.

(3) Nagatani, H.; Piron, A.; Brevet, P.-F.; Fermin, D. J.; Girault, H. H. Surface Second Harmonic Generation of Cationic Water-Soluble Porphyrins at the Polarized Water—1,2-Dichloroethane Interface. *Langmuir* **2002**, *18*, 6647–6652.

(4) Frisch, M. J.; Trucks, G. W.; Schlegel, H. B.; Scuseria, G. E.; Robb, M. A.; Cheeseman, J. R.; Scalmani, G.; Barone, V.; Petersson, G. A.; Nakatsuji, H. et al. Gaussian 16 Rev. B.01. **2016**,

(5) Darden, T.; York, D.; Pedersen, L. Particle Mesh Ewald: An N x log(N) Method for Ewald Sums in Large Systems. *J. Chem. Phys.* **1993**, *98*, 10089–10092.

(6) Hess, B.; Bekker, H.; Berendsen, H. J. C.; Fraaije, J. G. E. M. LINCS: A Linear Constraint Solver for Molecular Simulations. *J. Comput. Chem.* **1997**, *18*, 1463–1472.

(7) Miyamoto, S.; Kollman, P. A. Settle: An analytical version of the SHAKE and RATTLE algorithm for rigid water models. *J. Comput. Chem.* **1992**, *13*, 952–962.

(8) Bussi, G.; Zykova-Timan, T.; Parrinello, M. Isothermal-isobaric molecular dynamics using stochastic velocity rescaling. *J. Chem. Phys.* **2009**, *130*, 074101.

(9) Parrinello, M.; Rahman, A. Polymorphic Transitions in Single-Crystals - a New Molecular-Dynamics Method. *J. Appl. Phys.* **1981**, *52*, 7182–7190.

(10) Licari, G.; Cwiklik, L.; Jungwirth, P.; Vauthey, E. Exploring Fluorescent Dyes at Biomimetic Interfaces with Second Harmonic Generation and Molecular Dynamics. *Langmuir* **2017**, *33*, 3373–3383.

(11) Muller, P.-A.; Högemann, C.; Allonas, X.; Jacques, P.; Vauthey, E. Deuterium Isotope Effect on the Charge Recombination Dynamics of Contact Ion Pairs Formed by Electron Transfer Quenching in Acetonitrile. *Chem. Phys. Lett.* **2000**, *326*, 321–327.

S14

Chapter 8

General Conclusions

The aim of this thesis was to deepen our understanding of the properties of interfaces between two immiscible liquids. We focused particularly on the photochemical reactivity of molecules adsorbed at these interfaces, both in the presence and absence of added co-solutes that can alter interfacial properties.

Several chapters in this thesis tackle specific aspects of liquid interfaces.

Chapter 3 investigates interfaces with room temperature ionic liquids, showing that adding these ionic liquids to an aqueous subphase changes interfacial behavior. The overall charge of the interface depends on both components of the ionic liquid. This knowledge could be helpful in fine-tuning liquid interface properties and open up many applications for these solvents. In this study, malachite green served as our molecular probe due to its robust second harmonic response and well-documented photophysics in bulk and at the interface.

In Chapter 4, we examine crystal violet, a dye from the same family as malachite green. This dye could potentially offer orientational information, which is difficult to achieve with malachite green. Chapter 5 further investigates the nature of crystal violet's lowest-energy electronic absorption band and the origin of its high-energy shoulder. The study suggests that torsional disorder in the ground state results in inhomogeneous broadening of the absorption band, providing valuable insights into the spectroscopic behavior of crystal violet and its potential as a probe at interfaces.

Chapter 6 delves into the excited state dynamics and photoisomerization of Methyl Orange (MO) in different environments, including liquid/liquid interfaces and bulk solutions. The findings show that the environment significantly impacts MO's photophysics and the efficiency of photoisomerization. We noticed variations in photoisomerization efficiency and dynamics between the interface and bulk environments, offering key insights into the isomerization process.

Chapter 7 covers the excited-state properties of an amphiphilic electron donor-acceptor dyad at the dodecane/water interface. The presence of a hydrophobic fullerene subunit significantly affects the dyad's orientation at the interface and its excited-state dynamics. The dyad's efficient adsorption at the interface enables intermolecular charge separation, emphasizing the crucial role of liquid interfaces in facilitating unique chemical reactivity.

Through the comprehensive investigations outlined in this thesis, we hope to have made a modest yet impactful contribution to the growing understanding of liquid interfaces and their potential applications. The primary aim has been to elucidate the complex environment that these interfaces present.

Looking to the future, further progress in understanding liquid interfaces is anticipated through continued research in surface nonlinear optics and the employment of other techniques. However, SSHG techniques have not yet been exploited to their full potential and substantial enhancements are needed for them to match the efficacy of techniques used to study photoinduced processes in the bulk phase.

Lastly, it's essential to acknowledge the cumulative efforts that made the experimental findings of this thesis possible. Over the years, numerous predecessors have fine-tuned and enhanced the SHG setup, making it a reliable and valuable tool for the study of interfaces

Appendices

Appendix A

Additional Measurements at Dodecane/Phospholipid/Water Interface

In order to examine the impact of ordering and confinement on various dyes adsorbed at the liquid interface, we conducted additional Second Harmonic Generation (SHG) experiments at water/dodecane interfaces. To achieve ordering, we used different phospholipids, as monolayers of phospholipids at a dodecane-water interface can serve as simplified models of biological membranes. Our objective was to explore the orientation and excited state dynamics of environment-sensitive dyes at the interface, using second harmonic generation as a tool to gain a more comprehensive understanding of the behavior of organic molecules at liquid/liquid interfaces.

In this study, we present the results obtained with two dyes that have previously been investigated in our research group. The first dye is an aminostilbazolium dye (DiA), which has demonstrated excited state dynamics dependent on the viscosity of the upper phase. We employed this dye to quantify the friction of the local dodecane/phospholipid/water environment.These experimental measurements were carried out jointly with my former colleague, Dr. Darya Budkina. The second dye is a diketopyrrolopyrrole derivative (DPP), which exhibits excited state dynamics influenced by the hydrogen-bond donating ability of the environment.

The results of the experiments conducted on these two dyes are outlined in Sections 1 and 2 of this appendix, respectively.

A.1 Excited-State Reactivity at Liquid/Phospholipid/Water Interfaces

A.1.1 Introduction

Aminostilbazolium, commonly known as hemicyanine, belongs to a class of organic compounds characterized by a conjugated aromatic system. These compounds exhibit solvatochromic behavior, meaning they are sensitive to changes in solvent polarity. Additionally, they have a high second order nonlinear optical susceptibility which makes them suitable for second harmonic generation. Aminostilbazolium derivatives find applications in fluorescence microscopy, imaging, sensing, nonlinear optical devices, and biological labeling [1–7] . The properties and functionalities of these compounds can be tailored through chemical modifications, allowing for specific applications and desired characteristics.

In a previous study carried out in our group, the properties of an amphiphilic dye, 4-(4-(dihexadecylamino)styryl)-N-methylpyridinium (DiA) (Figure A.1), were studied in the bulk and at interfaces. This molecule undergoes efficient nonradiative deactivation via large amplitude motion. This study revealed that the decay time of the excited state of DiA at interfaces increases with the viscosity of the apolar phase, which consists of n-alkanes of different lengths, but remains unaffected by the viscosity of the polar phase composed of water/glycerol mixtures. This indicates that the nonradiative deactivation is associated with the twist of the dialkylaniline group, predominantly located in the apolar phase.

DiA is an amphiphilic molecule, and when present at the interface between two immiscible liquids, it orients almost perpendicularly with the charged pyridinium head in the polar phase and the dialkylaniline end in the apolar phase. In our study, we focused on investigating DiA at the interface in the presence of phospholipids, as this could provide valuable information about the location of the dye in the presence of lipids.

We selected two lipids, namely dipalmitoylphosphatidylcholine (DPPC) and di-oleoylphosphatidylcholine (DOPC) Figure A.1, to study the changes in orientation and the effects of confinement and packing on DiA at the interface. DPPC, with its saturated fatty acid chains, allows for closer and more ordered packing, resulting in a more rigid membrane structure. On the other hand, DOPC, with its unsaturated fatty acid chains, introduces kinks that hinder tight packing and promote fluidity in the membrane [8] . These differences in packing contribute to the distinct physical properties and behaviors exhibited by DPPC and DOPC membranes .

Our experimental results include polarization-resolved SSHG, SSHG spectra, and time-resolved SSHG (TR-SSHG) experiments performed on interfaces containing DiA in the presence of varying amounts of DOPC and DPPC. These results are presented in the following sections.
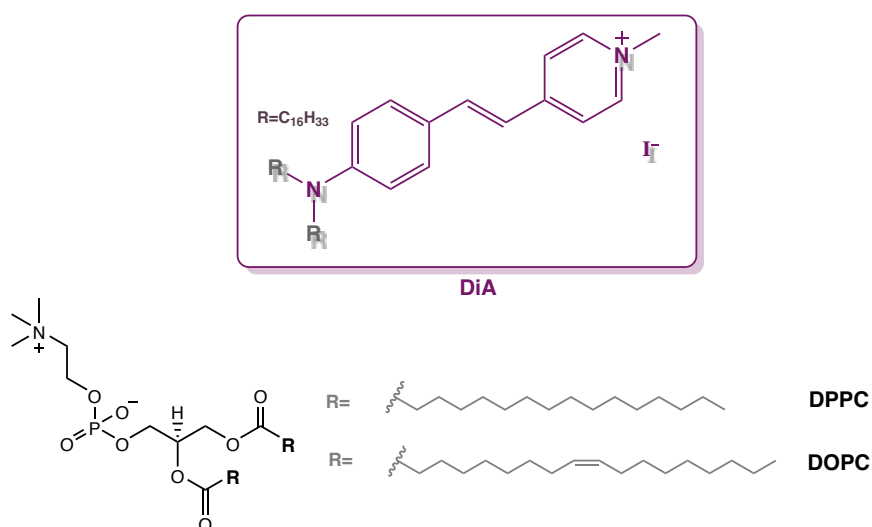
Figure A.1: Structure of the DiA dye and the used phospholipids

A.1.2 Experimental Results

Steady State Absorption
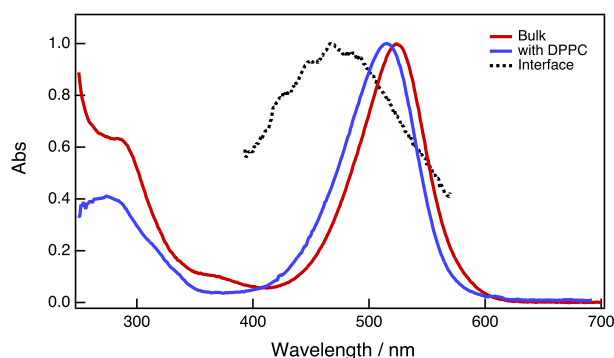
Figure A.2: Normalized electronic spectra of DiA in chloroform (red), in the presence of phospholipids (blue), and the SSHG spectrum at the dodecane/water interface (dashed line).

The steady state absorption spectrum of DiA reveals an intense band at 525 nm, with less intense bands appearing in the UV portion of the spectrum as shown in Figure A.2. The surface second harmonic generation (SSHG) spectra predominantly consist of a broad band centered at 470 nm, which is shifted relative to the absorption spectrum. When DPPC is added to the solution, a small blue shift is observed. The blue shift is most likely due to the change in the refractive index upon the addition of DPPC.. The absorbance of the lipids is predominantly in the UV region, below 300 nm. DiA, as a hemicynaine dye, is known to exhibit substantial solvatochromism, with the presence of donor-acceptor systems making the charge transfer bands highly solvent-sensitive [9]. TD-DFT gas-phase calculations were performed on an analogue of DiA, where the long alkyl chains were replaced with an

ethyl group. The calculations predict that the first transition is at 439.28 nm, originating from the transition between the highest occupied molecular orbital (HOMO) and the lowest unoccupied molecular orbital (LUMO), and is predominantly along the long axis of the molecule.
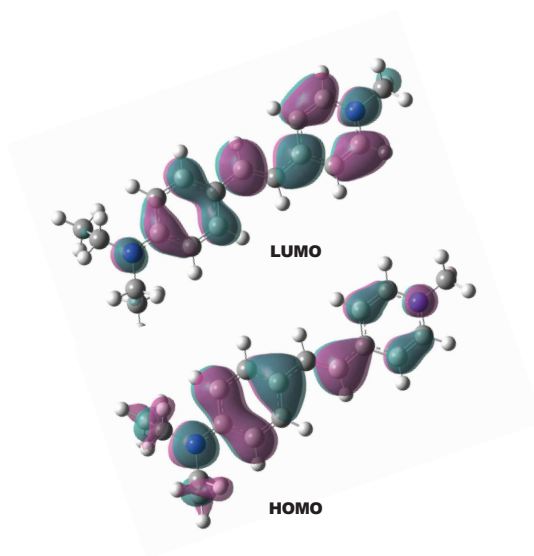
Figure A.3: Frontier molecular orbitals of DiA computed at the CAM-B3LYP/6-31G(d,p) level of theory.The long alkyl chains on the N atom were replaced by ethyl groups.

SHG Results

The SHG spectrum of DiA was measured at the dodecane/phospholipids/water interface using DOPC and DPPC phospholipids at varying surface coverages. The results can be seen in Figure A.4. Even the slightest presence of lipids induces observable changes. The spectral band undergoes a blue shift, paralleling observations in the electronic absorption spectra, and a feature at approximately 430 nm seems to rise upon adding either DPPC or DOPC. This blue shift might be due to changes in the interface properties, due to the introduction of lipids and that could account for the spectral changes.

Nevertheless, the formation of aggregates is also a possibility. The blue shift can be explained by the formation of H-type aggregates as this DiA is known to spontaneously form chiral domains and H-type aggregates at the air/water interfaces [10–13].

Noticing these spectral changes, we were motivated to investigate different regions of the spectrum to potentially discern distinct conformations and subpopulations. Subsequent polarization measurements were conducted at fundamental wavelengths of 800 nm, 940 nm, 960 nm, and 1060 nm, roughly corresponding to the blue edge, the band maximum, and the red edge of the spectrum, respectively. This was done in an effort to obtain information about the orientation of DiA at the interface in the presence of phospholipids. Three different sets of polarization (p, s,

(a)

(b)
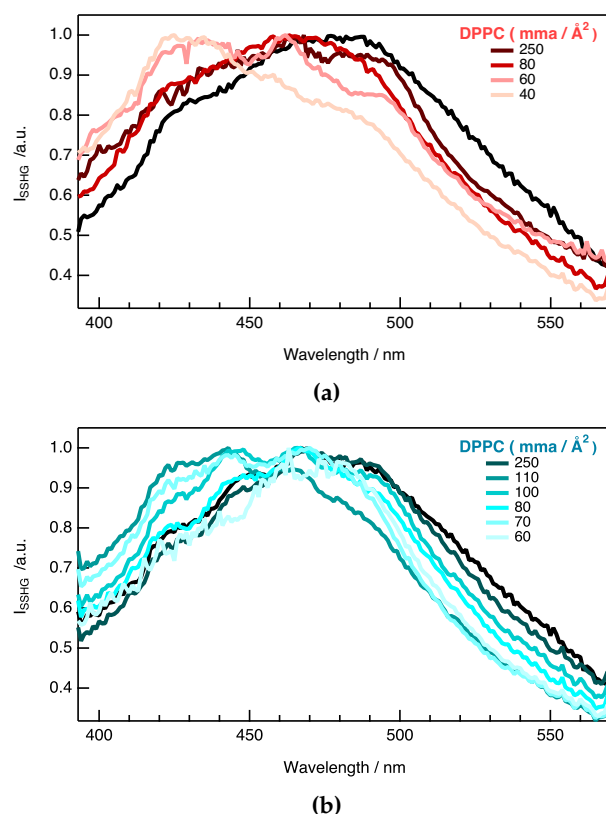
Figure A.4: SSHG spectra of DiA at the dodecane/interface (black line) and in the presence of phospholipids with decreasing mma at the corresponding interfaces: (a) DPPC and (b) DOPC.

and 45) were measured, and the analysis incorporated all three, with the exception of samples without lipids where only s and 45 polarizations were used.

As depicted in Figure A.5, the polarization curves of DiA at 800nm significantly change upon the addition of DPPC. Notably, the p-polarization, illustrated in red, undergoes a substantial visual transformation.

Same experiments were conducted at 940 nm, 960 nm, and 1060 nm for DPPC and DOPC. The analysis of these curves enabled us to extract the tilt angle θ, which represents the angle between the transition dipole moment of DiA responsible of the resonance enhancement and the normal to the interface. The results are depicted in Figure A.6, and the extracted fit parameters (for measurements at 800nm and 940nm) are presented in Table A.1.

For both lipids and at all probe wavelengths, the angle decreases with the addition of phospholipids. This implies that the DiA orientation becomes more perpendicular, likely due to the dye's intercalation in the phospholipid layer, and as the mma per lipid decreases. The packing of the lipids becomes tighter, making the dye's orientation increasingly perpendicular. In all samples, the initial tilt angle θ is larger when probing with longer wavelengths. This can possibly indicate that the molecules contributing to the red side of the SSHG spectrum lie flatter on the
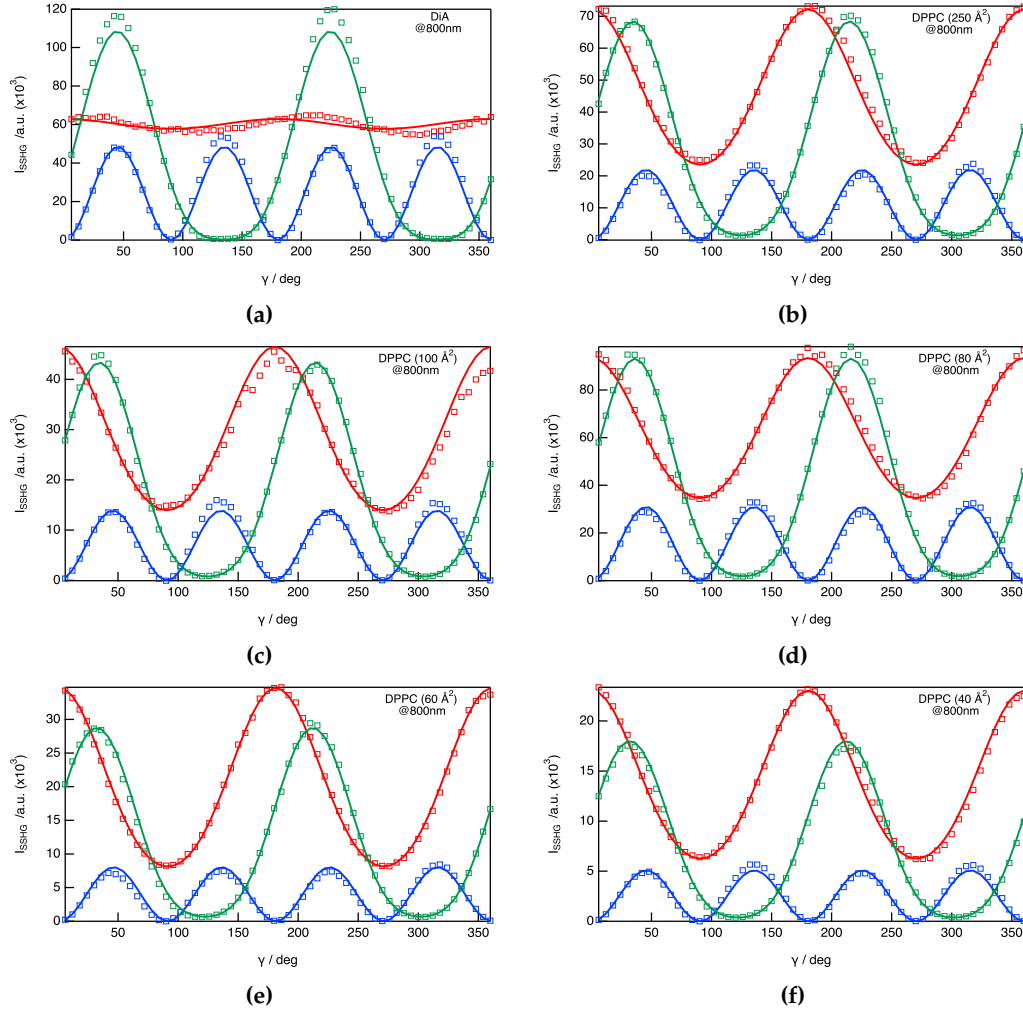
Figure A.5: Polarization-resolved SSHG data at the dodecane/DPPC/water interface varying the mma per lipid . The output polarization components are color-coded as follows: red for p-polarization, blue for s-polarization, and green for 45 degrees. Best fit curves are represented by solid lines.
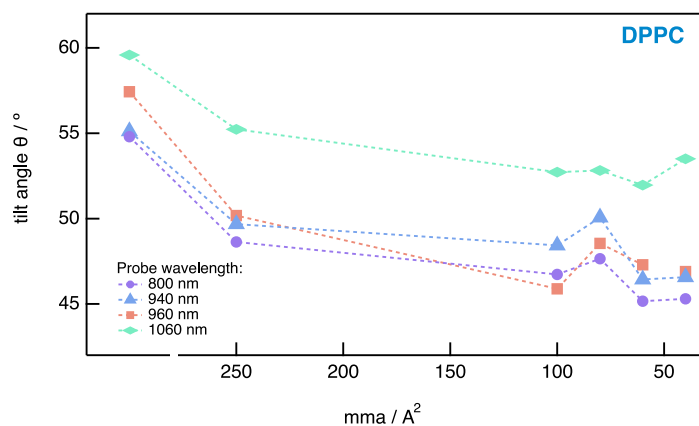
(a)
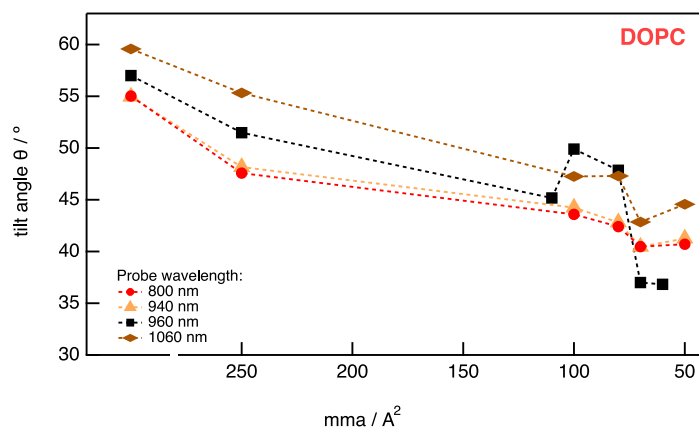
(b)

Figure A.6: Mean tilt angle of DiA at the interface as a function of the mean molecular area per lipid molecule for (a) DPPC and (b) DOPC. The amount of dye was kept constant throughout the experiments. The dashed lines are for visual guidance.

interface than those absorbing on the blue side. The trend and angle changes are consistent across several experiments.

Figure A.6 demonstrates that the trend is predominantly linear, with a slight increase in the observed angle at an mma of $80\,\overset{\circ}{A}^2$. This increase is present at all wavelengths. For DOPC, a deviation from the trend is observed when probing at 960nm and 1060nm. Despite the experimental reproducibility of these results, a definitive explanation has yet to be established.

Overall, the change in the tilt angle appears more significant with DOPC compared to DPPC. DOPC has longer, unsaturated acyl chains, while DPPC has shorter, saturated acyl chains. Therefore, the layer formed by DOPC is more disordered and can probably occupy more space, possibly pushing the dye to adopt a more perpendicular orientation.

mma/Å^2	$\chi^{(2)}_{ZXX}/\chi^{(2)}_{XXZ}$	$\chi^{(2)}_{ZZZ}/\chi^{(2)}_{XXZ}$	D	θ / $^\circ$
DPPC at 800 nm				
No phospholipid	1.12 ± 0.03	1.17 ± 0.03	0.34 ± 0.01	54.2 ± 0.5
250	1.07 ± 0.02	1.90 ± 0.04	0.46 ± 0.05	46.7 ± 0.3
100	1.03 ± 0.04	1.90 ± 0.04	0.48 ± 0.01	33.3 ± 0.3
80	1.09 ± 0.03	1.81 ± 0.04	0.45 ± 0.01	47.6 ± 0.4
60	1.04 ± 0.01	2.18 ± 0.03	0.51 ± 0.01	44.3 ± 0.2
40	1.14 ± 0.06	2.23 ± 0.03	0.49 ± 0.01	45.4 ± 0.3
DPPC at 940 nm				
No phospholipid	0.93 ± 0.10	0.94 ± 0.04	0.33 ± 0.01	54.6 ± 0.7
250	1.01 ± 0.04	1.60 ± 0.04	0.44 ± 0.01	48.4 ± 0.6
100	1.11 ± 0.02	1.76 ± 0.06	0.40 ± 0.01	50.2 ± 0.5
80	0.95 ± 0.03	1.31 ± 0.03	0.40 ± 0.01	50.2 ± 0.5
60	1.10 ± 0.03	2.06 ± 0.05	0.48 ± 0.01	45.96 ± 0.41
40	1.05 ± 0.02	1.89 ± 0.06	0.47 ± 0.01	46.5 ± 0.4
DOPC at 800 nm				
No phospholipid	1.12 ± 0.03	1.25 ± 0.03	0.35 ± 0.01	53.2 ± 0.4
250	1.09 ± 0.03	1.95 ± 0.04	0.47 ± 0.01	46.7 ± 0.4
100	1.08 ± 0.03	2.23 ± 0.06	0.50 ± 0.01	44.7 ± 0.4
80	1.06 ± 0.04	2.77 ± 0.08	0.56 ± 0.01	41.2 ± 0.5
60	1.06 ± 0.03	2.72 ± 0.06	0.56 ± 0.01	41.4 ± 0.4
40	1.01 ± 0.04	2.79 ± 0.08	0.58 ± 0.01	40.3 ± 0.6
DOPC at 940 nm				
No phospholipid	0.90 ± 0.08	0.95 ± 0.06	0.34 ± 0.02	54.0 ± 1.4
250	1.14 ± 0.05	1.94 ± 0.07	0.46 ± 0.01	47.3 ± 0.8
100	1.08 ± 0.04	2.07 ± 0.07	0.49 ± 0.01	45.3 ± 0.5
80	1.17 ± 0.05	2.76 ± 0.11	0.54 ± 0.01	42.7 ± 0.8
60	1.13 ± 0.08	2.84 ± 0.11	0.55 ± 0.01	41.8 ± 1.1
40	1.03 ± 0.04	2.42 ± 0.09	0.54 ± 0.01	42.6 ± 0.7

Table A.1: Results from the analysis of the polarization-resolved SSHG data of DiA with the different added phospholipids at 800nm and 940nm. The global fit was performed on all three polarization components except for the samples without lipids where only the s and 45 components were used. The errors are obtained from the weighted fit procedure with 99% confidence interval using the inverse of the data standard error as weight and propagating the error through the various equations. The tilt angle θ was deduced assuming a Dirac distribution and a single dominant element of the $\overset{\leftrightarrow}{\beta}$ tensor.

Figure A.7: Time-resolved SSHG signal profiles recorded at 400nm after 520nm excitation of DiA at the dodecane/water interface in the presence of DPPC

Figure A.8: Time-resolved SSHG signal profiles recorded at 400nm after 520nm excitation of DiA at the dodecane/water interface in the presence of DOPC

Excited State Dynamics at the Interface

Time-resolved SSHG measurements (TR-SSHG) were conducted on the same system to investigate any potential changes in the excited state dynamics. We used probe wavelengths of 800 nm and 940 nm. Probing the red edge of the spectrum is difficult due to the presence of scattered light from the excitation source.

Figure A.7 illustrates the TR-SSHG profiles measured following the $S_1 \leftarrow S_0$ excitation of the dye at the dodecane/phospholipid/water interface. In these profiles, the signal recovery reflects the repopulation of the ground state. A notable slowing down in the dynamics is observed when the DiA is intercalated within the DPPC layer. A similar effect was detected with DOPC; the overall recovery is slower, but the effect appears slightly larger compared to DPPC. When probing at 940nm, all samples—regardless of the type of phospholipid—exhibit a delayed rise followed by a monoexponential decay. The results of this analysis are summarized in Table A.2.

Transient Absorption (TA) measurements in ACN were conducted in an attempt
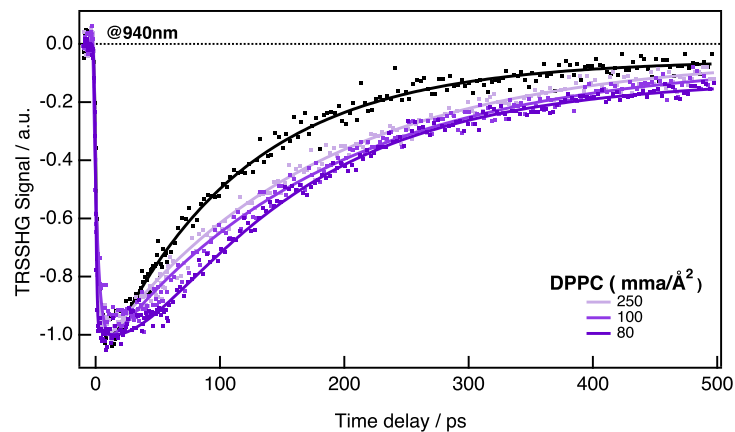
Figure A.9: Time-resolved SSHG signal profiles recorded at 470nm after 520nm excitation of DiA at the dodecane/water interface in the presence of DPPC

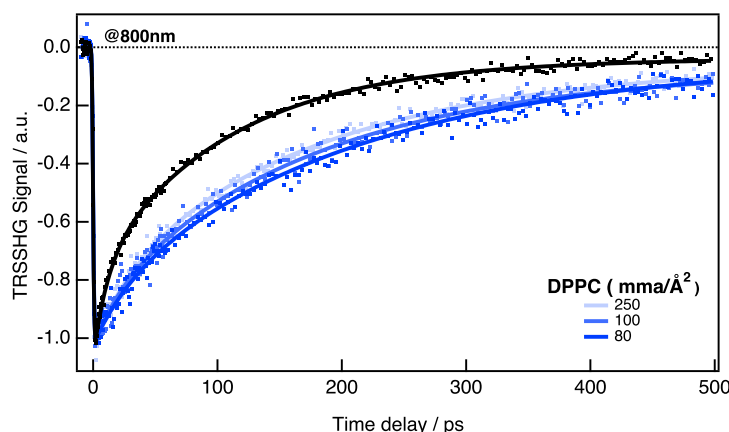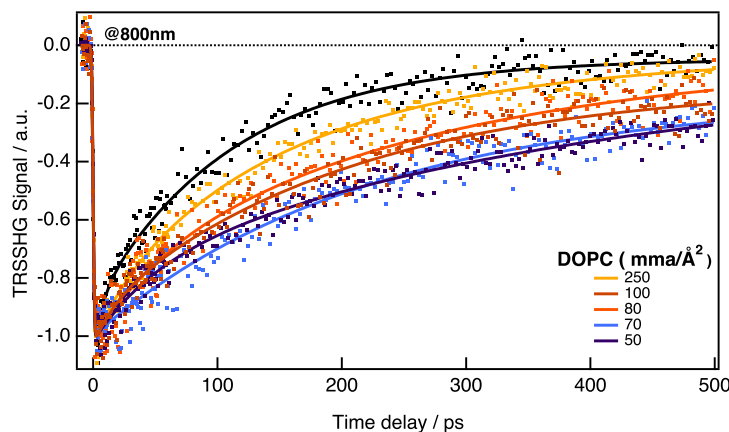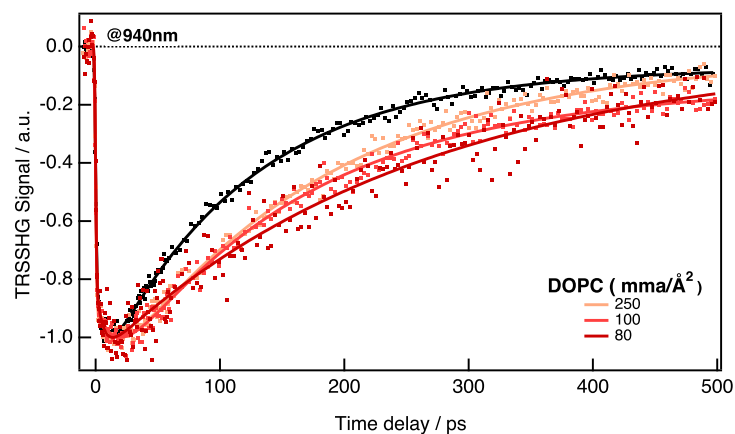

Figure A.10: Time-resolved SSHG signal profiles recorded at 470nm after 520nm excitation of DiA at the dodecane/water interface in the presence of DOPC

mma/Å^2	τ_1 (ps)	A_1	τ_2 (ps)	A_2
DPPC at 800 nm				
No phospholipid	32 ± 5	-0.47 ± 0.04	173 ± 12	-0.53 ± 0.04
250	59.5 ± 9.5	-0.4 ± 0.08	278 ± 34	-0.6 ± 0.1
100	62 ± 22	-0.37 ± 0.1	291 ± 46	-0.63 ± 0.1
80	57 ± 27	-0.27 ± 0.1	266 ± 29	-0.73 ± 0.1
DPPC at 940 nm				
No phospholipid	2.8 ± 2.5	0.49 ± 0.04	137 ± 5	-1
250	5.4 ± 2.7	0.30 ± 0.01	188 ± 5	-1
100	12 ± 6	0.25 ± 0.08	193 ± 7	-1
80	20 ± 3	0.33 ± 0.1	128 ± 28	-1
DOPC at 800 nm				
No phospholipid	64 ± 28	-0.57 ± 0.28	227 ± 104	-0.43 ± 0.3
250	65 ± 27	-0.42 ± 0.18	261 ± 61	-0.58 ± 0.19
100	128 ± 25	-0.6 ± 0.12	400 ± 14	-1.0 ± 0.1
80	56 ± 5	-0.25 ± 1.7	300 ± 66	-0.75 ± 0.2
DPPC at 940 nm				
No phospholipid	3.0 ± 2.2	0.33 ± 0.01	156 ± 4	-1
250	12 ± 5	0.25 ± 0.04	189 ± 5	-1
100	8 ± 5	0.25 ± 0.08	233 ± 8	-1
80	5.1 ± 4.1	0.28 ± 0.1	256 ± 14	-1

Table A.2: Time constants were derived from a biexponential weighted fit applied to the time-resolved SSHG data of DiA in the presence of lipids. We employed exponential functions convolved with a Gaussian function to simulate the instrument response function. The experimental time resolution is approximately 1 to 2 ps

to understand the delayed rise observed in the SSHG spectra, as demonstrated in Figure A.11. The spectra primarily feature a positive band below 470 nm and two negative bands at 500 nm and 590 nm, which shift towards longer wavelengths over time. The positive band can be ascribed to excited state absorption, whereas the negative bands are attributable to bleach and stimulated emission. This spectral data was analysed globally using a sum of three exponential functions.

Upon inspecting the TA spectrum, a disparity between the dynamics at 400 nm and 470 nm is noticeable. These wavelengths correspond to the probe wavelengths utilised in the SHG study. It can be observed that there is no dynamics or shift at 400 nm, unlike at 470 nm where dynamics on the time scale of solvent relaxation can be seen. This could potentially be related to the rise observed in the SSHG measurement at 940 nm.

In a previous study conducted by our group, it was observed that the decay time of the excited states of DiA increased with the viscosity of the apolar phase [14]. Consistent with these findings, our experiments demonstrate similar results. The addition of lipids leads to an increase in the time constants, which is expected as it enhances the order and rigidity of the interface. The previous study also determined that the rotation of the dialkylaniline group was the main mode associated with the non-radiative deactivation of these molecules [14]. This means that the dialkylaniline group in this study is also located in the non-polar phase and intercalated in the phospholipid membrane.
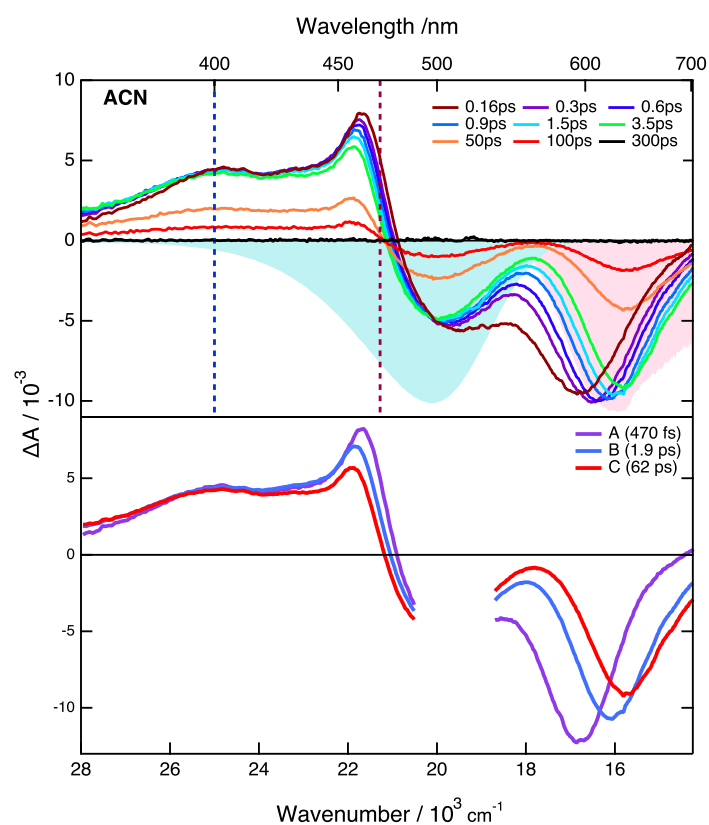
Figure A.11: Transient absorption spectra recorded at various time delays after 520 nm excitation of DiA in acetonitrile. The shaded area are the negative stationary spectra.

A.2 Hydrogen Bond Interactions at Liquid/Liquid Interfaces in the Presence of Phospholipids

In order to further understand the interactions between organic molecules and phospholipid membranes, particularly their location within the membranes, we conducted experiments to investigate the excited state dynamics of a diketopyrrolopyrrole derivative (DPP) shown in Figure A.12.

Figure A.12: Chart 2. Structure of the DPP dye and the used phospholipids

The dye has been designed with two oligoethylene glycol chains to facilitate water solubility, and push-pull groups, which includes dialkylamino and nitrile substituents that allow for SHG measurements. A previous study in our group has shown that the excited state lifetime of DPP decreases significantly as the hydrogen-donating ability of the environment increases.[15]

It was also observed that DPP has the ability to form hydrogen bonds at the interface, as evidenced by the increased lifetime when going from a dodecane/water to a dodecane/heavy-water interface.

In this study, we performed second harmonic generation (SHG) measurements to investigate the orientation, spectra, and dynamics of DPP at interfaces in the presence of six different types of phospholipids with varying head groups and fatty acid chains (see Figure A.12). The aim was to gain insight into the specific location of the dye at the interface and to determine whether it is shielded or capable of interacting with water molecules. The results presented in this section serve as a preliminary exploration. A more comprehensive understanding would greatly benefit from further

Figure A.13: Normalized electronic spectra of DPP in chloroform (purple) and the SSHG spectrum at the dodecane/water interface (dashed line).

research, particularly through the use of Molecular Dynamics (MD) simulations.

A.2.1 Experimental Findings

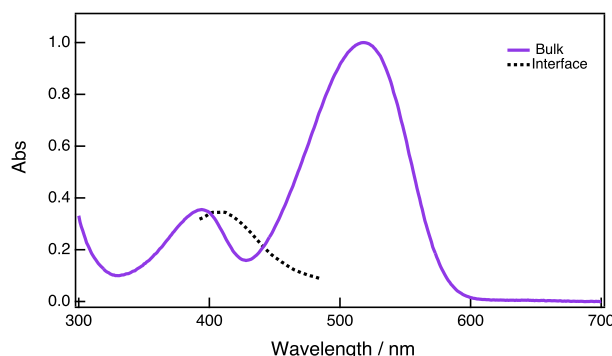Figure A.13 displays the electronic absorption and emission spectra of DPP1 in chloroform. The absorption spectrum is primarily characterized by a broad and intense band peaking at 517 nm, accompanied by a secondary band at 395 nm. The stationary Second Harmonic Generation (SSHG) spectrum, recorded at the dodecane/water interface with 1 nmol of the dye deposited on the interface, is represented by dashed lines. The partially measured spectrum appears to reach its maximum at approximately 407 nm. The SSHG measurements, which will be presented, were conducted at a fundamental wavelength of 800 nm to coincide with the band's maximum and to enhance the signal. For the time-resolved SSHG, the excitation was at 520 nm.

Polarization-resolved SSHG measurements were performed in the presence of various phospholipids and at different surface coverages to obtain information about the dye's orientation at the interface. Although the polarization curves are not displayed here, the extracted tilt angle θ, the angle between the long molecular axis and the interface, is shown in Figure A.14 for all experiments. It's worth noting that the surface coverages used in these experiments are considerably lower than those used in the DiA measurements, for instance. Significant variations start to occur from a mean molecular area (mma) of $650 \, \text{Å}^2$, with no SHG signal detected at mean molecular areas lower than $100 \, \text{Å}^2$. This finding is not unexpected, considering the dye's affinity for the interface is lower than that of the phospholipids, resulting in a competition that favors the latter, potentially pushing the dye away from the interface.

Before the addition of lipids, the initial tilt angle of DPP is approximately 70°, indicating that the molecule predominantly lies flat at the interface. This observation is consistent with previous Molecular Dynamics (MD) simulations, which demonstrate these molecules' tendency to lie flat at the interface, with the poly(ethylene glycol) chains immersed in the aqueous phase and the DPP interacting with both
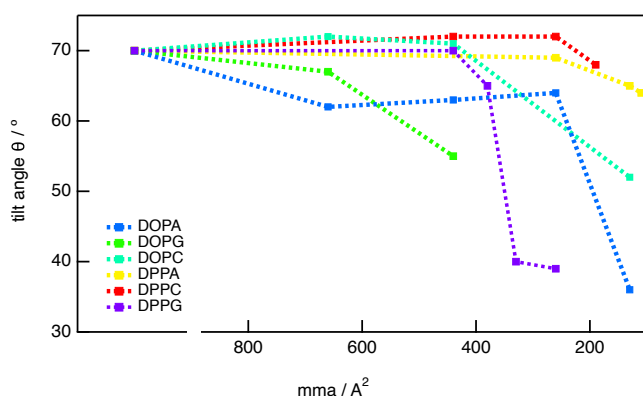
Figure A.14: Mean tilt angle of DiA at the interface as a function of the
mean molecular area per lipid molecule for (a) DPPC and (b) DOPC.
The amount of dye was kept constant throughout the experiments.
The dashed lines are for visual guidance.

phases. However, the tilt angle significantly decreases upon the introduction of
phospholipids, except in the case of DPPC and DPPA where only a slight change
is noted. The most profound impact on the orientation was witnessed with DPPG
and DOPA, where the angle diminishes to under $40°$, suggesting a more perpendic-
ular orientation of the dye.

Both Time-Resolved Second Harmonic Generation (TR-SSHG) measurements and
steady state SSHG spectrum were also recorded. These results are presented in Fig-
ures Figure A.15 to Figure A.20. Analysis of the data reveals that the dynamics
slightly accelerate upon the addition of a small quantity of any phospholipid. How-
ever, at higher concentrations (assuming sufficient signal for the measurement), the
dynamics suddenly slow down. This trend is especially noticeable in the case of
DPPC, DOPC, and DOPG. Nevertheless, the signal-to-noise ratio is quite low, yet
the trend remains distinct. The spectrum also exhibits some blue shift upon the ad-
dition of certain phospholipids. This is particularly noticeable in the case of DOPG.

The initial acceleration of dynamics could suggest that the molecule is in a more
hydrogen-donating environment. This may be because it is in greater contact with
water, or due to the properties of the lipids themselves, particularly those carrying
a glycerol and a carboxyl group, both of which are capable of forming hydrogen
bonds. At higher concentrations, the diminishing signal could imply that the dye is
likely being repelled from the interface. The simultaneous slowing of the dynamics
could imply that the remaining dye molecules at the interface are perhaps shielded
from water, being intercalated within the lipid layer.

No discernible trend has emerged from the various Second Harmonic Genera-
tion (SHG) experiments conducted. For example, the phospholipids that induced
the most significant changes in dye orientation did not necessarily show the largest
changes in the dynamics or spectra. This adds a layer of complexity to the interpreta-
tion of the data, suggesting that other, currently unidentified or not fully understood
factors may be at play. A definitive correlation has not yet been established between

(a) (b)

Figure A.15: (a) Time-resolved SSHG signal profiles recorded at 400nm after 520nm excitation of DPP and (b) SSHG spectra of DPP at the dodecane/water interface in the presence of various amounts of DPPC. The black line represents the interface without lipids.

(a) (b)

Figure A.16: (a) Time-resolved SSHG signal profiles recorded at 400nm after 520nm excitation of DPP and (b) SSHG spectra of DPP at the dodecane/water interface in the presence of various amounts of DOPC. The black line represents the interface without lipids.
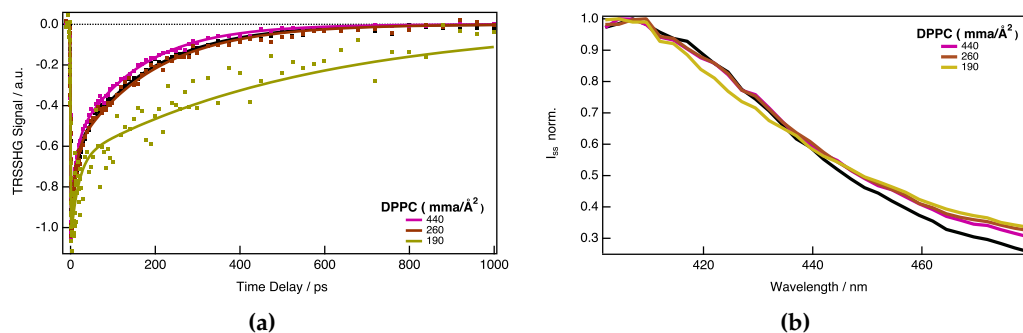

(a) (b)
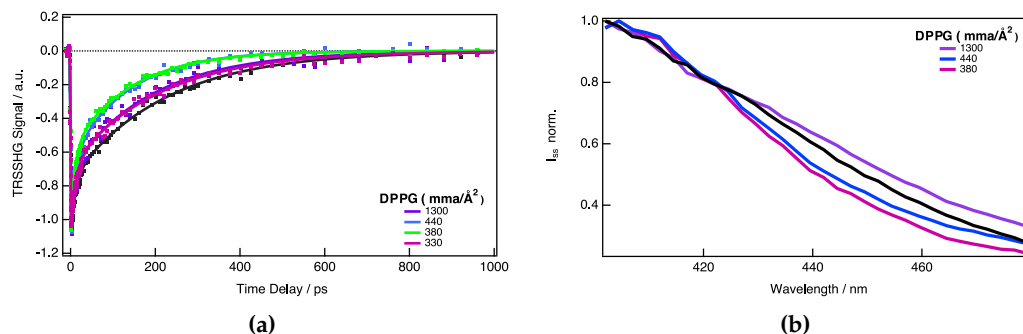
Figure A.17: (a) Time-resolved SSHG signal profiles recorded at 400nm after 520nm excitation of DPP and (b) SSHG spectra of DPP at the dodecane/water interface in the presence of various amounts of DPPG. The black line represents the interface without lipids.
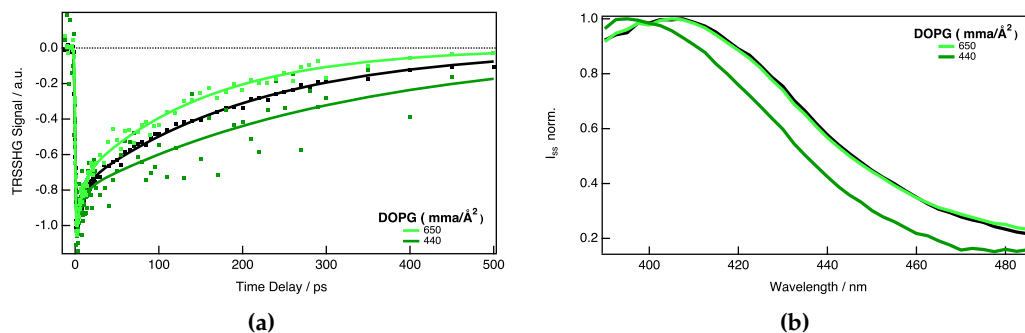
Figure A.18: (a) Time-resolved SSHG signal profiles recorded at 400nm after 520nm excitation of DPP and (b) SSHG spectra of DPP at the dodecane/water interface in the presence of various amounts of DOPG. The black line represents the interface without lipids.
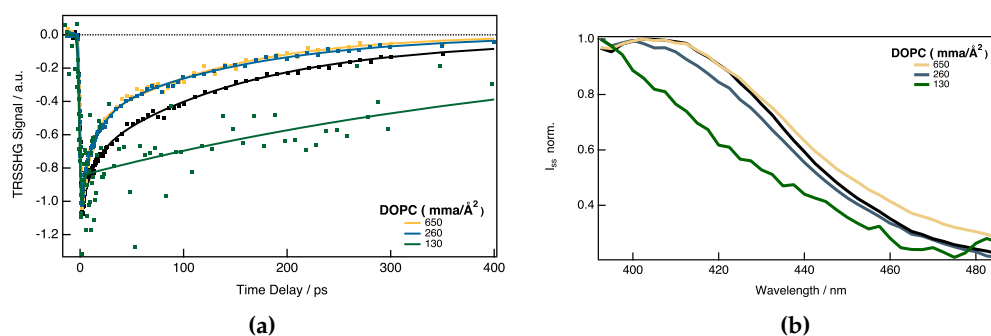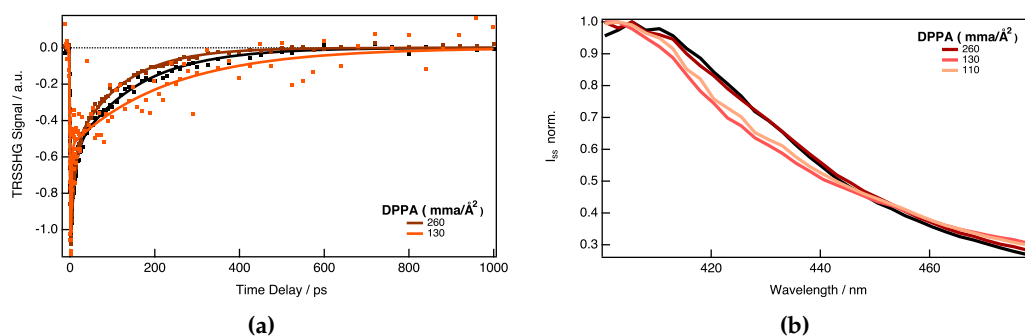

Figure A.19: (a) Time-resolved SSHG signal profiles recorded at 400nm after 520nm excitation of DPP and (b) SSHG spectra of DPP at the dodecane/water interface in the presence of various amounts of DPPA. The black line represents the interface without lipids.
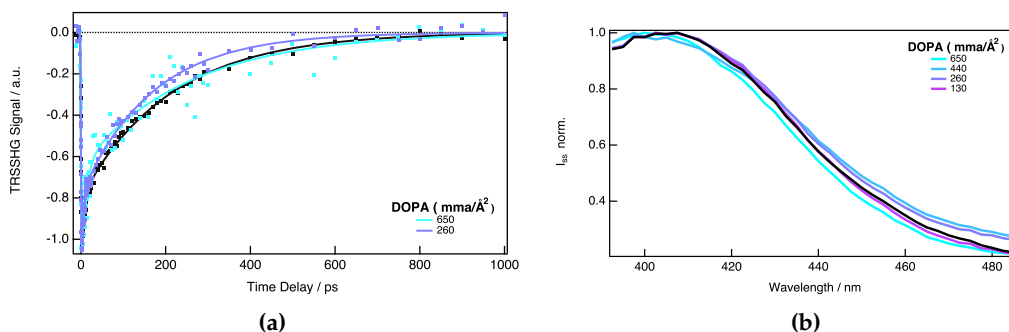
Figure A.20: (a) Time-resolved SSHG signal profiles recorded at 400nm after 520nm excitation of DPP and (b) SSHG spectra of DPP at the dodecane/water interface in the presence of various amounts of DOPA. The black line represents the interface without lipids.

the dye's behavior and the properties of different phospholipids' head and tail structures. Given these results, computational simulations could be invaluable in exploring potential underlying mechanisms and giving more insight into the interaction of the dye with the phospholipids and its position. Further integrated work, combining both experimental and simulation approaches, is essential to elucidate these observed behaviors and their relationships with the phospholipids' properties.

Bibliography

(1) Dahal, D.; Pokhrel, S.; McDonald, L.; Bertman, K.; Paruchuri, S.; Konopka, M.; Pang, Y. *ACS Appl. Bio Mater.* **2019**, *2*, 4037–4043.

(2) Ephardt, H.; Fromherz, P. *J. Phys. Chem.* **1989**, *93*, 7717–7725.

(3) Hall, R. C.; Lindsay, G. A.; Kowel, S. T.; Hayden, L. M.; Anderson, B. L.; Higgins, B. G.; Stroeve, P.; Srinivasan, M. P. In *Advances in Nonlinear Polymers and Inorganic Crystals, Liquid Crystals and Laser Media*, SPIE: 1988; Vol. 0824, pp 121–125.

(4) Li, B.; Kou, J.; Mei, H.; Gu, X.; Wang, M.; Xie, X.; Xu, K. *Anal. Methods .* **2020**, *12*, 4181–4184.

(5) Mishra, A.; Behera, R. K.; Behera, P. K.; Mishra, B. K.; Behera, G. B. *Chem. Rev.* **2000**, *100*, 1973–2012.

(6) Shindy, H. A. *Dyes and Pigments* **2017**, *145*, 505–513.

(7) Wang, Y.-N.; Xu, B.; Qiu, L.-H.; Sun, R.; Xu, Y.-J.; Ge, J.-F. *Sens. Actuators B* **2021**, *337*, 129787.

(8) Andrade, C. A. S.; Baszkin, A.; Santos-Magalhães, N. S.; Coelho, L. C. B. B.; de Melo, C. P. *J Colloid Interface Sci* **2005**, *289*, 379–385.

(9) Panigrahi, M.; Patel, S.; Mishra, B. K. *J. Mol. Liq.* **2013**, *177*, 335–342.

(10) Gassin, P.-M.; Martin-Gassin, G.; Benichou, E.; Brevet, P.-F. *J. Phys. Chem. C* **2014**, *118*, 1135–1141.

(11) González-Delgado, A. M.; Giner-Casares, J. J.; Rubia-Payá, C.; Pérez-Morales, M.; Martín-Romero, M. T.; Brezesinski, G.; Camacho, L. *J. Phys. Chem. C* **2011**, *115*, 9059–9067.

(12) Xu, Z.; Lu, W.; Bohn, P. W. *J. Phys. Chem.* **1995**, *99*, 7154–7159.

(13) Lusk, A. L.; Bohn, P. W. *J. Phys. Chem. B* **2001**, *105*, 462–470.

(14) Martin-Gassin, G.; Villamaina, D.; Vauthey, E. *J. Am. Chem. Soc.* **2011**, *133*, 2358–2361.

(15) Richert, S.; Mosquera Vazquez, S.; Grzybowski, M.; Gryko, D. T.; Kyrychenko, A.; Vauthey, E. *J. Phys. Chem. B* **2014**, *118*, 9952–9963.

Appendix B

Experimental Details

Samples

The dyes Malachite Green (MG) and Crystal violet (CV) used in Chapter 4 were purchased from Sigma Aldrich, Methyl Orange (MO) used in Chapter 6 was purchased from Thermo Scientific Chemicals and were used without further purification. Typically, a 2 mM stock solution of the dye in water is used to make the samples. In Appendix A, 4-(4-(dihexadecylamino)styryl)-N-methylpyridinium iodide (DiA) used was purchased from INTERCHIM, diketopyrrolopyrrole derivative (DPP1) was obtained from the group of Prof. D. Gryko (Warsaw, Poland), and the synthesis was described in the literature [1] and were used as received. For DiA and DPP, a 2mM stock solution of the dye in CHCl$_3$ (Chloroform, Acros Organics, 99.9%) was prepared.

Dodecane (99%), ACN (Acetonitrile, 99+%, for spectroscopy) were purchased from Acros organics. Cyclohexane-D12 (Dodecadeutero-cyclohexane, ≥99.6 atom % D) was purchased from Sigma-Aldrich. For all experiments, water was purified using a Milli-Q purification system.

The surfactant CTAC (Hexadecyltrimethylammonium Chloride, 99%) was purchased from Acros Organics and was dissolved in water at the desired concentration for all experiments. DPPA (1,2-dipalmitoyl-sn-glycero-3-phosphate), DPPC (1,2-dipalmitoyl-sn-glycero-3-phosphocholine), DPPG (1,2-dipalmitoyl-sn-glycero-3-phospho-(1'-rac-glycerol)), and DOPA (1,2-dioleoyl-sn-glycero-3-phosphate), DOPC (1,2-dioleoyl-sn-glycero-3-phosphocholine), DOPG (1,2-dioleoyl-sn-glycero-3-phospho-(1'-rac-glycerol)) were purchased from Avanti Polar Lipids.

CB[7] used in Chapter 6 was obtained from the group of Dr. A. Fürstenberg. The synthesis of CB[7] was made following the procedure of Nau and coworkers [2].

The samples for second-harmonic generation (SSHG) measurements were prepared using the following steps:

- 10 mL of aqueous dye solution was poured into a $4 \times 4 \times 4 \, \text{cm}^3$ quartz cell if the dye was soluble in water. If the dye was not soluble in water, a desired amount of the dye was dissolved in CHCl$_3$ and deposited on the water's surface. In

this case, the mixture was left for approximately 10 minutes to allow $CHCl_3$ to evaporate.

- 12 mL of dodecane was then slowly added to the solution.

- For experiments involving CTAC and CB[7], both substances were added to the aqueous solution in the desired concentration.

- For experiments involving phospholipids, a specific amount of phospholipid was dissolved in $CHCl_3$ and deposited on the surface of the 10 mL aqueous dye solution if the dye was soluble in water. If the dye needed to be deposited at the interface, a desired amount of the dye and the phospholipid were mixed before depositing the mixture on the water's surface. This mixture was then left for approximately 10 minutes to allow the $CHCl_3$ to evaporate.

Bulk spectroscopy

Steady State Spectroscopy

Steady state measurements were performed in a 1mm quartz cuvette at room temperature unless specified. The electronic absorption spectra were recorded using a Varian Cary 50 UV-vis spectrophotometer. All the measurements are corrected with a proper baseline. Electronic spectra were measured before and after the SSHG and the TA experiments to check any degradation of the sample.

Transient Absorption Spectroscopy

Transient electronic absorption measurements were performed using a setup previously described in detail [3] [4]. The setup was based on an amplified Ti:Sapphire system (Spectra-Physics, Solstice Ace) that produced 30 fs pulses at a repetition rate of 5 kHz centered at 800 nm. Part of the amplifier output was used to pump an optical parametric amplifier (TOPAS Prime) to generate excitation pulses at either 500 nm or 532 nm. The irradiance on the samples ranged from 0.15 to 0.75 µJ. Probing was achieved from 320 to 750 nm using white-light pulses generated by focusing 800 nm pulses on a CaF_2 plate. The full width at half maximum of the instrument response function was 70 fs. The excitation beam's polarization was set at the magic angle with respect to the probe beam. The solutions were kept in 1 mm cuvettes and bubbled with argon.

SSHG Measurements

The square root of the SSHG intensity was taken for all the SSHG spectra and time-resolved measurements as it is proportional to the number of molecules at the interface. The maximal photoinduced change in the time-resolved traces was set to -1.

The SSHG spectra were recorded by scanning the TOPAS-C with 2-5 nm steps. the spectra were corrected for the setup's wavelength dependence by referencing the SSHG signal measured with a protected-silver mirror or a UV-enhanced aluminum-coated mirror immersed in dodecane depending on the probe range of interest. (see reflectance in Figure B.1)
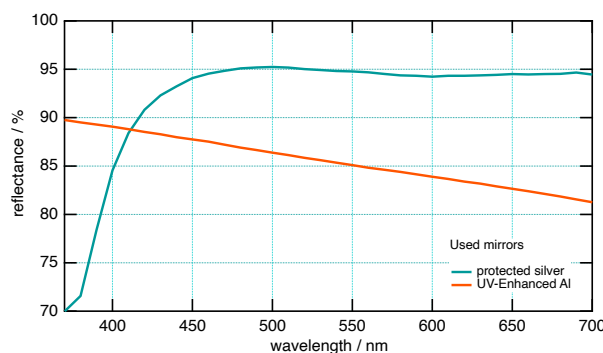
Figure B.1: The reflectance from the protected silver and UV-enhanced aluminum mirrors which were used as a reference for the SSHG spectra measurements.

In the spectra measured for Chapter 4, Cyclohexane-D12 was used as a substitute for Dodecane. This substitution was made because Dodecane absorbs fundamental light at wavelengths above 1100 nm, as shown in Figure B.2.
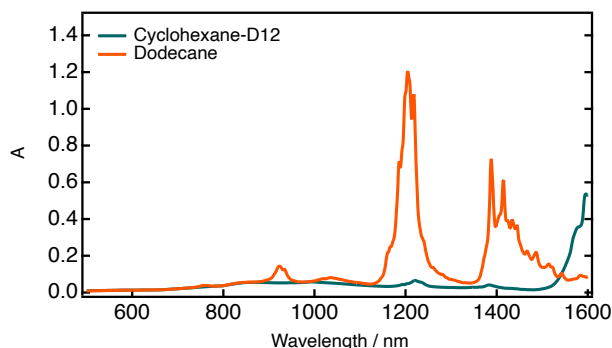
Figure B.2: Comparison of absorbance between Dodecane and Cyclohexane-D12, the measurements were taken in a 1 cm cuvette.

Bibliography

(1) Richert, S.; Mosquera Vazquez, S.; Grzybowski, M.; Gryko, D. T.; Kyrychenko, A.; Vauthey, E. *J. Phys. Chem. B* **2014**, *118*, 9952–9963.

(2) Koner, A. L.; Nau, W. M. *Supramol. Chem.* **2007**, *19*, 55–66.

(3) Beckwith, J. S.; Aster, A.; Vauthey, E. *Phys. Chem. Chem. Phys.* **2021**, *24*, 568–577.

(4) Aster, A.; Licari, G.; Zinna, F.; Brun, E.; Kumpulainen, T.; Tajkhorshid, E.; Lacour, J.; Vauthey, E. *Chem. Sci.* **2019**, *10*, 10629–10639.

List of Abbreviations and Symbols

Abbreviations:

A	Absorbance
B	Magnetic field
c	Speed of light
COM	**C**enter **O**f **M**ass
CR	**C**harge **R**ecombination
CS	**C**harge **S**eparation
D	**D**isplacement or orientational parameter
DFT	**D**ensity **F**unctional **T**heory
E	Electric field or energy
EADS	**E**volution **A**ssociated **D**ecay **S**pectra
ESA	Excited-**S**tate **A**bsorption
FWHM	**F**ull **W**idth at **H**alf **M**aximum
GS	**G**round **S**tate
GSB	**G**round **S**tate **B**leach
HOMO	**H**ighest **O**ccupied **M**olecular **O**rbital
IC	**I**nternal **C**onversion
IRF	**I**nstrument **R**esponse **F**unction
ISC	**I**nter**s**ystem **C**rossing
IVR	**I**ntramolecular **V**ibrational **R**elaxation
LUMO	**L**owest **U**noccupied **M**olecular **O**rbital
MD	**M**olecular **D**ynamics
mma	**M**ean **m**olecular **a**rea
MO	**M**olecular **O**rbital
n	Refractive index
NOPA	**N**on-**C**ollinear **O**ptical **P**arametric **A**mplifier
OPA	**O**ptical **P**arametric **A**mplification
P	Polarization
S$_0$	Ground State
S$_n$	n^{th}-Excited State

SSHG	**S**urface **S**econd **H**armonic **G**eneration
TA	**T**ransient **A**bsorption
TCSPC	**T**ime-**C**orrelated **S**ingle **P**hoton **C**ounting
TDM	**T**ransition **D**ipole **M**oment
TIR	**T**otal **I**nternal **R**eflection
TR	**T**ime-**R**esolved
UV	**U**ltra**v**iolet
UV-Vis	**U**ltraviolet-**Vis**ible
VC	**V**ibrational **C**ooling
VER	**V**ibrational **E**nergy **R**elaxation

Symbols:

$\mathbf{X}$, $\vec{X}$	Vector
$\overset{\leftrightarrow}{X}$	Tensor
$\hat{X}$	Unit Vector or Operator
$\tilde{X}$	Complex Quantity
s, p, m	90°, 0°, and 45° Polarization Angle with Respect to the Plane of Incidence of the Fundamental or Harmonic Wave
β	First Hyperpolarizability
γ	Polarization Angle of Fundamental Beam
Γ	Polarization Angle of the Second Harmonic Beam
δ	Dirac Delta-Function
λ	Wavelength
τ	Time Constant
$\chi^{(n)}$	n^{th}-Order Optical Susceptibility
ω	Angular Frequency of the Fundamental Light Beam